Transport-theoretical Description of Nuclear Reactions

O. Buss, T. Gaitanos, K. Gallmeister, H. van Hees, M. Kaskulov, O. Lalakulich,
A. B. Larionov[1], T. Leitner, J. Weil, U. Mosel

Institut für Theoretische Physik, Universität Giessen, Germany

Abstract

In this review we first outline the basics of transport theory and its recent generalization to off-shell transport. We then present in some detail the main ingredients of any transport method using in particular the Giessen Boltzmann-Uehling-Uhlenbeck (GiBUU) implementation of this theory as an example. We discuss the potentials used, the ground state initialization and the collision term, including the in-medium modifications of the latter. The central part of this review covers applications of GiBUU to a wide class of reactions, starting from pion-induced reactions over proton and antiproton reactions on nuclei to heavy-ion collisions (up to about $30\,A\mathrm{GeV}$). A major part concerns also the description of photon-, electron- and neutrino-induced reactions (in the energy range from a few $100\,\mathrm{MeV}$ to a few $100\,\mathrm{GeV}$). For this wide class of reactions GiBUU gives an excellent description with the same physics input and the same code being used. We argue that GiBUU is an indispensable tool for any investigation of nuclear reactions in which final-state interactions play a role. Studies of pion-nucleus interactions, nuclear fragmentation, heavy-ion reactions, hypernucleus formation, hadronization, color transparency, electron-nucleus collisions and neutrino-nucleus interactions are all possible applications of GiBUU and are discussed in this article.

Keywords: Transport theory, Hadron-induced reactions, Heavy-ion collisions, Antiproton-induced reactions, Photonuclear reactions, Lepton-induced reactions

Contents

---

[1]Also at the National Research Center "Kurchatov Institute", Moscow, Russia

1. Introduction and Motivation

Any reaction involving nuclear targets poses a challenge to nuclear theory. Nuclear many-body effects come into play not only in the reaction mechanism, but also in the reaction amplitude and the description of final-state interactions. These many-body effects in general evolve dynamically during the course of a reaction and thus require a time-dependent framework for their description. For the experimenters the challenge is to draw conclusions from observed asymptotic particle yields, spectra and distributions on the interactions or the state of the matter during early stages of the collision. A well-known example is that of ultra-relativistic heavy-ion collisions. There the main aim is to investigate the properties of a transient state of matter, the quark-gluon plasma, involving quite different degrees of freedom than those being present both in the initial and the final states of the reaction, with the help of asymptotic, 'normal' free particles. Another example is given by the production of hadrons on nuclear targets using high-energy electron beams. Here the aim is to understand time scales in hadronization and the search for the phenomenon of color transparency in hadron- or electron-induced reactions, where the observed final particle yield must be used to reconstruct the nuclear interactions in a very early stage of the reaction. This is very much the same as the challenge in the studies of short-range correlations between nucleons in nuclei which must be inferred from the final outgoing particles. A final example is that of neutrino-nucleus reactions, where the nuclear response must be understood in order to extract neutrino-oscillation parameters from so-called long-baseline experiments. Common to all these quite different reactions and physics questions is the need to understand quantitatively the final-state interactions experienced by the outgoing particles. Somewhat simpler are

determinations of total inclusive cross sections. Here final-state interactions enter only into the first interaction amplitude, but nevertheless they do determine in this way the total cross sections.

The question then arises, which theoretical framework can be used to describe all these various reaction types. It is obvious that any reaction that preserves the phase coherence of the nuclear target can only be described by a quantum-mechanical reaction theory. An example is the coherent photoproduction of mesons on nuclear targets. However, as soon as the final state is not fully specified there are other options for their description available. The extreme case in this class is the total inclusive cross section with an elementary projectile without any information on specific final states of the target. An example is given by the total photoabsorption cross section on nuclei. Here quantum-mechanical reaction theory can be used with its standard approximations, such as the impulse approximation with plane or distorted waves. The quantum mechanics of the nuclear many-body system enters here into the wave functions of the initial and final states. These can be approximated at various degrees of sophistication; approximations for these states can range from Fermi-gas descriptions over shell-model wave functions up to very sophisticated results of state-of-the-art nuclear many-body calculations. The same inclusive process can also be treated by transport theory by modeling the collision term for the first, initial interaction by using a plane wave approximation. Indeed, results of such calculations for fully inclusive cross sections often show an agreement with data as good as that achieved in more sophisticated quantum mechanical approximation schemes. A more complicated case is the investigation of semi-inclusive reactions, i.e., reactions, where one outgoing particle is measured in detail, with many other particles and an excited nuclear target being present. For this reaction type also quantum-mechanical approximations have been used that describe the final state again by an optical-model wave function. However, while such an ansatz may be quite appropriate for the description of total cross sections it must fail in its description of, e.g., final-state energy distributions of knocked-out particles. The optical model can describe – through its imaginary part of the potential – the loss of flux of these particles when they traverse the nuclear target, but it contains no information where the lost particles go. It can also not describe any side feeding of reaction channels, where the final observed particle is not the one that was originally produced, nor can it describe energy distributions in situations, where the primary particles are being slowed down by final-state interactions. Semi-inclusive reactions, that in addition often involve many particles in the final state, thus present a problem for quantum-mechanical approximations. Here, transport theory is the method of choice. Such a theory can in principle handle all final-state channels with many interacting particles present and includes naturally the processes of rescattering, absorption or side feeding; its applicability is in general given if the many-body final state evolves incoherently.

This has been recognized quite early. Precursors of present-day transport theories were Monte-Carlo (MC) generators written to describe the final-state interactions in reactions of nucleons with nuclear targets. While the earliest suggestion of such methods goes back to Serber [1], the method has then been picked up by, among others, Metropolis *et al.* [2], Bertini [3], and Cugnon [4]. In 1983 Carruthers and Zachariasen gave a very complete description of quantum collision theory [5]. Later on, with the advent of heavy-ion reactions, first practical implementations were developed to describe the dynamical evolution of a colliding nucleus-nucleus system [6, 7, 8, 9, 10] while taking into account the hadronic potentials and the equation of state of nuclear matter within the Boltzmann-Uehling-Uhlenbeck (BUU) theory. These codes thus went beyond the simple MC generators used until then that could not account for potential effects on the propagation of particles. The GiBUU code, to be discussed later in this article, has its origins in this era; it started with applications to heavy-ion reactions (see [8, 11, 12] and further refer-

ences therein). With the availability of ultra-relativistic heavy-ion beams at the AGS, the CERN SPS, RHIC, and the LHC this field has flourished ever since. Models such as IQMD [13, 14], relativistic BUU [15, 16], UrQMD [17], RQMD [18], HSD [19] (which grew out of an early predecessor version of GiBUU), and many other transport models (for a comprehensive list see Ref. [20]) are still widely used to extract properties of hot and dense matter from the final state observables.

On the other hand, little (with protons as projectiles) or no work involving transport-theoretical methods had been done on the description of inclusive or semi-inclusive reactions on nuclei with elementary projectiles, where simple (sometimes oversimplified) approximations such as the Glauber treatment of final-state interactions prevailed. The first attempt to use transport-theoretical methods for the description of elementary processes on nuclei was an investigation of inclusive pion-nuclear reactions [21] in an MC calculation. A first calculation within the framework of a BUU theory of pion and η photoproduction off nuclei was performed by the Giessen group in [22] with the same code that had been originally developed to describe heavy-ion collisions. Since then BUU theory has been used by that group to analyze a wide class of nuclear reactions involving elementary projectiles such as hadrons or electrons, photons, and neutrinos.

The Giessen Boltzmann-Uehling-Uhlenbeck (GiBUU) transport model, which grew out of these early studies, is a method and simulation code for hadron-, photon-, electron-, neutrino-, and heavy-ion-induced reactions on nuclei. It is based on a coupled set of semi-classical kinetic equations, which describe the dynamics of a hadronic system explicitly in phase space and in time. The initial state of the hadronic system either directly corresponds to the experimental conditions (meson-nucleus, hadron-nucleus, and heavy-ion collisions) or is obtained via external models (photon-, electron-, and neutrino-nucleus reactions). The relevant degrees of freedom are mesons and baryons, which propagate in mean fields and scatter according to cross sections which are appropriate for the energy range from a few $10\,\mathrm{MeV}$ to more than $100\,\mathrm{GeV}$. In the higher energy regimes the concept of pre-hadronic interactions is implemented in order to account for color transparency and formation-time effects.

The GiBUU project is aiming to provide a unified theoretical transport framework in the MeV and GeV energy regimes for all the reaction types named above. The basic parameters, e.g., particle properties and elementary cross sections, assume the same common values for all reaction types, thus allowing for a validation of the model over a wide range of phenomena and giving it some predictive power. This is what makes GiBUU unique among all the other transport codes. The detailed comparison with many different experimental results also allows one to get a feeling for the inherent systematic uncertainties of the method, which are often unknown in other approaches. At the same time, the GiBUU model contains a number of options like on-shell vs. off-shell particle propagation, non-relativistic vs. relativistic mean fields, various treatments of the nuclear ground state etc. That also makes GiBUU a quite flexible theoretical toolkit, allowing to describe a given reaction on various levels of sophistication. The code itself is available under public license from [23].

The purpose of this article is, on one hand, to set out the general framework of transport theory and its practical implementation. In that sense many of the methods and ingredients to be described can be found also in transport codes for heavy-ion reactions. On the other hand, a specific implementation of transport theory is used to describe the power of the method in its application to various physics questions and to very different reaction types. Such a implementation is provided by the GiBUU transport code, developed by the authors mainly to describe interactions of elementary projectiles with nuclear targets [23].

In the first part of this paper, in section 2, we briefly describe the theoretical basis of any transport theory, going back to the seminal work of Kadanoff and Baym [24] and to the later derivation of relativistic quantum kinetic equations by Botermans and Malfliet [25] that provided the theoretical basis for off-shell transport; we will also outline the approximations that lead to the BUU transport equations that are actually being used. A particular point here is the discussion of our treatment of off-shell transport of quasi-particle degrees of freedom with broad mass spectra, which presents a major development in practical implementations of transport theory during the last decade. In the following section 3 we describe in some detail the actual ingredients of the GiBUU model. Although similar ingredients can be found in any transport implementation we felt it necessary to discuss here as many details as possible in order to make the physics in the GiBUU model transparent. Only then can meaningful conclusions be drawn from detailed comparisons with other transport approaches and, more importantly, from analyses of experimental results.

Section 4 then contains the center piece of this article, a discussion of physics results obtained with GiBUU over a wide range of nuclear reactions and energies. The reactions discussed here range from low-energy pion-nucleus interactions over heavy-ion and antiproton reactions to reactions with electrons and photons on nuclei. Finally a discussion of the very recent developments of neutrino-nucleus interactions is given, which is particularly important for neutrino long-baseline experiments. This broad coverage of very different nuclear reactions, all with the same physics input and the same code, is what sets GiBUU apart from other transport codes, mostly limited to descriptions of heavy-ion reactions. A summary then concludes this article, to be followed by several appendices that contain detailed information on the cross sections used, which may be useful also for other transport models or MC generators, and on the numerical implementation in GiBUU.

2. Transport equations

The BUU equation describes the space-time evolution of a many-particle system under the influence of mean-field potentials and a collision term, or more precisely, the time evolution of the Wigner transform of the real-time one-particle Green's function, which is a generalization of the classical phase-space density. For each particle species, within the BUU approach one obtains an additional differential equation. All these equations are coupled through the gain and loss terms, which represent scattering processes, and by the mean fields, included in the Hamilton functions. In this section, we sketch the derivation of the generalized BUU equation from nonequilibrium quantum field theory and discuss its approximations and solutions.

2.1. Nonequilibrium quantum field theory

The appropriate starting point for the derivation of transport equations from the underlying fundamental many-body-quantum theory is the Schwinger-Keldysh real-time formalism of quantum field theory. We start our derivation of a transport equation for broad resonance-like quasi-particles by a brief review of relativistic off-equilibrium quantum-field theory in the Schwinger-Keldysh real-time formalism [26, 27]. We concentrate on the motion of Dirac particles and derive the transport equations within the operator formalism. The approach of off-equilibrium many-body theory within the path-integral formalism can be found, e.g., in [28, 29].

We use the interaction picture, splitting the Hamilton operator,

$$\mathbf{H} = \mathbf{H}_0 + \mathbf{H}_i, \tag{1}$$

in a "free part", $\mathbf{H}_0$, and an "interaction part", $\mathbf{H}_i$. We assume that the equations of motion for the Dirac-field operators, $\boldsymbol{\psi}(t, \boldsymbol{x})$, evolving according to the Hamilton operator, $\mathbf{H}_0$, can be solved exactly in terms of a time evolution operator

$$
\begin{aligned}
\boldsymbol{\psi}(t, \boldsymbol{x}) &= \mathbf{A}(t, t_0)\boldsymbol{\psi}(t_0, \boldsymbol{x})\mathbf{A}^\dagger(t, t_0), \\
\mathbf{A}(t, t_0) &= \mathcal{T}_c \exp\left[\mathrm{i} \int_{t_0}^t \mathrm{d}t' \, \mathbf{H}_0(t')\right].
\end{aligned}
\tag{2}
$$

The operator, $\mathcal{T}_c$, is the usual "causal time-ordering operator", ordering time-dependent (field) operators by increasing times from right to left. In the case of fermion fields, it also includes a sign change according to the signature of the permutation necessary to bring the operators from the original order into the time-ordered sequence. The time, t_0, is the initial time, where the system is "prepared" in terms of a statistical operator, $\mathbf{R}$, which is a functional of the field operators and, in general, explicitly time dependent. Its time evolution is given by

$$
\begin{aligned}
\mathbf{R}[\boldsymbol{\psi}(t, \boldsymbol{x})] &= \mathbf{C}(t, t_0)\mathbf{R}[\boldsymbol{\psi}(t_0, \boldsymbol{x})]\mathbf{C}^\dagger(t, t_0), \\
\mathbf{C}(t, t_0) &= \mathcal{T}_c \exp\left[-\mathrm{i} \int_{t_0}^t \mathrm{d}t' \, \mathbf{H}_i(t')\right]
\end{aligned}
\tag{3}
$$

and fulfills the equation of motion,

$$
\frac{\mathrm{d}\mathbf{R}}{\mathrm{d}t} = \frac{1}{\mathrm{i}} \left[\mathbf{H}_i, \mathbf{R}\right].
\tag{4}
$$

Observable quantities are represented by self-adjoint operators, $\mathbf{O}(t)$. As functions (or functionals) of the field operators their time evolution is according to $\mathbf{H}_0$ as described in eq. (2). The expectation value of an observable is given by

$$
\langle \mathbf{O}(t) \rangle = \mathrm{Tr}\{\mathbf{R}[\boldsymbol{\psi}(t, \boldsymbol{x})]\mathbf{O}(t)\},
\tag{5}
$$

where the trace has to be taken in the Fock space of the field operators. Inserting the time evolution for the statistical operator eq. (3) one finds

$$
\langle \mathbf{O}(t) \rangle = \mathrm{Tr}\left[\mathbf{R}_0 \mathbf{C}^\dagger(t, t_0)\mathbf{O}(t)\mathbf{C}(t, t_0)\right].
\tag{6}
$$

Here, we have brought the time-evolution operator $\mathbf{C}(t, t_0)$ to the right, using the commutativity of operators under the trace operator and abbreviated the initial state by $\mathbf{R}_0 := \mathbf{R}[\boldsymbol{\psi}(t_0, \boldsymbol{x})]$. Inserting the explicit form of the time-evolution operator from eq. (3) and using

$$
\mathbf{C}^\dagger(t, t_0) = \mathcal{T}_a \exp\left[+\mathrm{i} \int_{t_0}^t \mathrm{d}t' \, \mathbf{H}_i(t')\right] = \mathcal{T}_a \exp\left[-\mathrm{i} \int_t^{t_0} \mathrm{d}t' \, \mathbf{H}_i(t')\right],
\tag{7}
$$

where $\mathcal{T}_a$ denotes the "anti-causal time-ordering operator" which orders field-operator products from left to right with increasing time arguments, leads to the *contour-ordered* time evolution of expectation values,

$$
\begin{aligned}
\langle \mathbf{O}(t) \rangle &= \mathrm{Tr}\left\{\mathbf{R}_0 \mathcal{T}_a \left[\exp\left(-\mathrm{i} \int_t^{t_0} \mathrm{d}t' \, \mathbf{H}_i(t')\right)\right] \mathbf{O}(t) \mathcal{T}_c \left[\exp\left(-\mathrm{i} \int_{t_0}^t \mathrm{d}t' \, \mathbf{H}_i(t')\right)\right]\right\} \\
&= \mathrm{Tr}\left\{\mathbf{R}_0 \mathcal{T}_C \left[\exp\left(-\mathrm{i} \int_C \mathrm{d}t' \, \mathbf{H}_i(t')\right) \mathbf{O}(t)\right]\right\}.
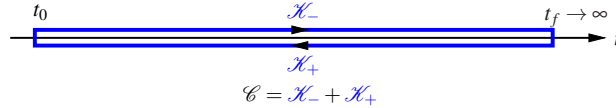\end{aligned}
\tag{8}
$$

7

Figure 1: (Color online) The Schwinger-Keldysh contour. Following the convention in [30], the two branches are denoted with $\mathcal{K}_-$ (chronological branch) and $\mathcal{K}_+$ (anti-chronological branch). The contour-ordering operator $\mathcal{T}_C$ orders operators with time arguments on the contour in the sense of the arrows from right to left. For fermionic field operators the symbol includes the usual sign change according to the signature of the permutation needed to bring the operators in the contour-ordered sequence.

In this time integral the time is defined along the *Schwinger-Keldysh contour* starting at t_0, going to a time, t_f, which is larger than any time appearing explicitly in the considered expression, $t_{\max}$, and then back in opposite direction to t_0 (see fig. 1). Note that the opposite sign in eq. (7) compared to eq. (3) is included by the opposite, i.e., "anti-chronological", integration direction on the lower branch, $\mathcal{K}_+$, of the Schwinger-Keldysh contour. The result of the expectation value eq. (8) is obviously independent of the choice of the final time, t_f, since the contributions from the upper and the lower branch of the contour for the time interval $(t_{\max}, t_f)$ cancel each other. For the following, it is convenient to let $t_f \to \infty$.

It is clear that this formalism can be extended to contour-ordered products of an arbitrary number of field operators. E.g., the exact contour n-particle-Green's function is defined by

$$i^n S_n^C(\xi_1, \ldots, \xi_n, \xi_1', \ldots, \xi_n') = \left\langle \mathcal{T}_C \psi(\xi_1)\psi(\xi_2)\cdots\psi(\xi_n)\overline{\psi}(\xi_n')\cdots\overline{\psi}(\xi_1') \right\rangle$$
$$= \mathrm{Tr}\left[\mathbf{R}_0 \mathcal{T}_C \left\{ \exp\left[-i \int_C \mathrm{d}t'\, \mathbf{H}_i(t')\right] \psi(\xi_1)\cdots\psi(\xi_n)\overline{\psi}(\xi_n')\cdots\overline{\psi}(\xi_1) \right\} \right], \tag{9}$$

while the corresponding perturbative n-particle function is defined by the leading-order perturbative approximation of the time-evolution operator,

$$i^n S_{0n}^C(\xi_1, \ldots, \xi_n, \xi_1', \ldots, \xi_n') = \left\langle \mathcal{T}_C \psi(\xi_1)\psi(\xi_2)\cdots\psi(\xi_n)\overline{\psi}(\xi_n')\cdots\overline{\psi}(\xi_1') \right\rangle_0$$
$$= \mathrm{Tr}\left[\mathbf{R}_0 \mathcal{T}_C \left\{ \psi(\xi_1)\cdots\psi(\xi_n)\overline{\psi}(\xi_n')\cdots\overline{\psi}(\xi_1) \right\} \right]. \tag{10}$$

Here, ξ_j includes the contour-time and spatial components of the four-vectors, x_j, as well as the Dirac indices α_j, i.e., $\psi(\xi_j) \equiv \psi_{\alpha_j}(x_j)$. Within this formalism the perturbative expansion of expectation values can be established in a way very similar to the usual vacuum-quantum field theory. The main difference is that time-ordering is replaced by contour ordering, and that expectation values have to be taken with respect to the initial Statistical Operator, $\mathbf{R}_0$, and not with respect to the vacuum state. Also the Wick theorem for expectation values will in general not be valid in its simple form known from vacuum quantum field theory, but only for particular forms of the initial Statistical operator, $\mathbf{R}_0$ [31], i.e., if the initial state of the system is of the form $\mathbf{R}_0 = \exp(-\mathbf{A})$, where $\mathbf{A}$ is an appropriate one-body operator. This means that many-particle correlations are neglected in the initial state.

However, the full Schwinger-Keldysh formalism cannot be applied for simulations of reactions. In fact, this formalism contains an infinite series of self-coupled equations: the one-particle Green's function is correlated with the two-particle one, the two-particle Green's function depends on the higher-order one, and so on. In that sense the Schwinger-Keldysh formalism contains all information on correlations of the many-body system. Usually one includes these many-body correlations into a self-energy. The dynamics of the highly correlated system is

then fully characterized by the Dyson equation for the one-particle Green's function, which contains the self-energy. For practical purposes one considers a truncation of the Schwinger-Dyson hierarchy on the two-particle level, and the problem is then reduced to the formulation of an approximation for the two-particle Green's function. The simplest ansatz is to neglect correlations completely, i.e., the two-particle Green's function consists of two uncorrelated one-particle Green's functions. This approach is well known as the Hartree (or by including antisymmetrization the Hartree-Fock) method. On this approach phenomenological models are based, such as the Hartree theory for quantum hadrodynamics [32]. The Dirac-Brueckner (or Dirac-Brueckner-Hartree-Fock) [25, 33] approach goes beyond the simple Hartree approximation by including a part of the two-body correlations. In the following we derive a general form of a transport equation starting from the Dyson equations for the one-particle Green's functions on the Schwinger-Keldysh contour within the Dirac-Brueckner approximation.

At first, it is more convenient to split the contour-two-point Green's functions in a matrix-like fashion [30]. The time arguments of the matrix elements are then defined on $\mathbb{R}$, and the two matrix indices denote their location at the branch of the Schwinger-Keldysh contour, leading to the following definitions for the one-particle Green's functions

$$
\begin{aligned}
\mathrm{i}S^{c}_{\alpha\beta}(x_1, x_2) &= \mathrm{i}S^{--}_{\alpha\beta}(x_1, x_2) = \left\langle \mathcal{T}_c \psi_\alpha(x_1)\overline{\psi}_\beta(x_2) \right\rangle, \\
\mathrm{i}S^{<}_{\alpha\beta}(x_1, x_2) &= \mathrm{i}S^{-+}_{\alpha\beta}(x_1, x_2) = -\left\langle \overline{\psi}_\beta(x_2)\psi_\alpha(x_1) \right\rangle, \\
\mathrm{i}S^{>}_{\alpha\beta}(x_1, x_2) &= \mathrm{i}S^{+-}_{\alpha\beta}(x_1, x_2) = \left\langle \psi_\alpha(x_1)\overline{\psi}_\beta(x_2) \right\rangle, \\
\mathrm{i}S^{a}_{\alpha\beta}(x_1, x_2) &= \mathrm{i}S^{++}_{\alpha\beta}(x_1, x_2) = \left\langle \mathcal{T}_a \psi_\alpha(x_1)\overline{\psi}_\beta(x_2) \right\rangle.
\end{aligned}
\tag{11}
$$

Here, we have written the spinor indices, α and β, explicitly. The corresponding Green's function for free particles are given in the analogous way by using the average $\langle \cdots \rangle_0$ as defined in eq. (10). As in vacuum-quantum field theory the perturbative expansion can be cast into a Feynman-diagram formalism, where expectation values of observables are given by "closed diagrams". In addition to the vacuum-Feynman rules, each vertex carries a $\pm$-contour index, and for a +-vertex an additional factor -1 has to be taken into account, which originates from the opposite integration direction over times on the +-branch of the Schwinger-Keldysh contour. By the same arguments as for the vacuum, the diagrams can be organized in classes as connected and disconnected parts, one-particle irreducible (1PI) amputated (or proper vertex parts), etc. This implies that the same (partial) resummation techniques as in the vacuum can be formally applied also in the off-equilibrium many-body case, and the corresponding Schwinger-Dyson equations can be derived.

For the derivation of transport equations, we introduce the self-energy, $-\mathrm{i}\Sigma$, as the amputated 1PI two-point function. Introducing the matrix notation,

$$
\begin{aligned}
\hat{S}_{\alpha\beta}(x_1, x_2) &= \begin{pmatrix} S^{--}_{\alpha\beta}(x_1, x_2) & S^{-+}_{\alpha\beta}(x_1, x_2) \\ S^{+-}_{\alpha\beta}(x_1, x_2) & S^{++}_{\alpha\beta}(x_1, x_2) \end{pmatrix}, \\
\hat{S}_{0\alpha\beta}(x_1, x_2) &= \begin{pmatrix} S^{--}_{0,\alpha\beta}(x_1, x_2) & S^{-+}_{0,\alpha\beta}(x_1, x_2) \\ S^{+-}_{0,\alpha\beta}(x_1, x_2) & S^{++}_{0,\alpha\beta}(x_1, x_2) \end{pmatrix}, \\
\hat{\Sigma}_{\alpha\beta}(x_1, x_2) &= \begin{pmatrix} \Sigma^{--}_{\alpha\beta}(x_1, x_2) & \Sigma^{-+}_{\alpha\beta}(x_1, x_2) \\ \Sigma^{+-}_{\alpha\beta}(x_1, x_2) & \Sigma^{++}_{\alpha\beta}(x_1, x_2) \end{pmatrix},
\end{aligned}
\tag{12}
$$

for the full and the free two-point Green's function and the self-energy, the corresponding Dyson

9

equation reads

$$\hat{S}(x_1, x_2) = \hat{S}_0(x_1, x_2) + \hat{S}_0(x_1, x_1') \odot \hat{\Sigma}(x_1', x_2') \odot \hat{S}(x_2', x_2), \tag{13}$$

where $\odot$ stands for the integration over repeated space-time arguments [34], including the matrix, $\hat{\eta} = \text{diag}(1, -1)$, acting on the contour indices, which takes into account the signs originating from the opposite direction of the +-time branch on the Schwinger-Keldysh contour. Here and in the following we do not write out the Dirac indices explicitly, if not needed.

Defining the inverse of the free Green's function as the differential operator,

$$S_{0x}^{-1} = i\partial\!\!\!/_x - m, \tag{14}$$

the equation of motion for the free matrix-Green's function can be written in the form

$$S_{0x_1}^{-1} \hat{S}_0(x_1, x_2) = \hat{\eta} \delta^{(4)}(x_1 - x_2). \tag{15}$$

Thus, from eq. (13), the matrix-Dyson equation can be cast into the following equation of motion

$$S_{0x_1}^{-1} \hat{S}(x_1, x_2) = \hat{\eta} \delta^{(4)}(x_1 - x_2) + \hat{\Sigma}(x_1, y) \odot \hat{S}(y, x_2). \tag{16}$$

For the following, another set of matrix elements than eq. (12) is more convenient,

$$
\begin{aligned}
S^{\text{ret}}(x_1, x_2) &= S^c(x_1, x_2) - S^<(x_1, x_2) = S^>(x_1, x_2) - S^a(x_1, x_2), \\
S^{\text{adv}}(x_1, x_2) &= S^c(x_1, x_2) - S^>(x_1, x_2) = S^<(x_1, x_2) - S^a(x_1, x_2), \\
\Sigma^{\text{ret}}(x_1, x_2) &= \Sigma^c(x_1, x_2) - \Sigma^<(x_1, x_2) = \Sigma^>(x_1, x_2) - \Sigma^a(x_1, x_2), \\
\Sigma^{\text{adv}}(x_1, x_2) &= \Sigma^c(x_1, x_2) - \Sigma^>(x_1, x_2) = \Sigma^<(x_1, x_2) - \Sigma^a(x_1, x_2).
\end{aligned}
\tag{17}
$$

It is easy to prove from the canonical anti-commutation relations for fermion-field operators that these Green's functions obey the boundary conditions for the retarded and advanced two-point functions. Accordingly, from eq. (16) one finds that the corresponding equations of motion only involve retarded (advanced) parts,

$$S_{0x_1}^{-1} S^{\text{ret(adv)}}(x_1, x_2) = \delta^{(4)}(x_1 - x_2) + \Sigma^{\text{ret(adv)}}(x_1, y) \odot S^{\text{ret(adv)}}(y, x_2). \tag{18}$$

For the off-diagonal elements in eq. (13), one obtains the equations,

$$S_{0x_1}^{-1} S^<(x_1, x_2) = \Sigma^{\text{ret}}(x_1, y) \odot S^<(y, x_2) + \Sigma^<(x_1, y) \odot S^{\text{adv}}(y, x_2), \tag{19}$$

which provide the space-time evolution of the single-particle properties of the particles in the system encoded in the special propagator, $S^<$. For example, the following spinor traces at equal space-time coordinates determine the vector-current and scalar densities,

$$J^\mu(x) = \left\langle \overline{\psi}(x) \gamma^\mu \psi(x) \right\rangle = -i \, \text{tr}[\gamma^\mu S^<(x, x)], \quad \rho_S(x) = \left\langle \overline{\psi}(x) \psi(x) \right\rangle = -i \, \text{tr}[S^<(x, x)]. \tag{20}$$

Later, after Wigner transformation and gradient expansion, one transforms (19) to generalized transport equations for the corresponding density distributions in phase-space together with eqs. (18) for the retarded or advanced Green's functions, which determine the spectral properties of the single-particle states [24].

2.2. Truncation schemes for the self-energies

The formula (19) provides an exact equation of motion for the one-particle Green's function. However, this set of equations requires the definition of the self-energies in terms of the exact Green's functions, involving an "infinite tower" of coupled Schwinger-Dyson equations for the complete set of n-point functions of the quantum field theory[2]. Thus, one has to choose an approximation scheme in order to cut this hierarchy of Schwinger-Dyson equations to a finite coupled set of n-point Green's and vertex functions. The usual starting point is perturbation theory, which however is not well suited for our purpose of off-equilibrium many-body theory.

The main difficulty lies in the formulation of truncation schemes which are at the same time "conserving" (i.e., obeying the conservation laws for conserved quantities like total energy, momentum, angular momentum, and charge-like quantum numbers) and are thermodynamically consistent in the equilibrium limit, i.e., bulk properties fulfill the usual Maxwell relations between the corresponding thermodynamical potentials.

A promising starting point for the derivation of transport equations for particles with large spectral widths is the use of Φ-derivable approximations, where Φ is a functional of the mean fields and exact propagators, defining self-consistent equations of motion for the mean fields and self-energies by a variational principle, which fulfill the above mentioned physical constraints. It has been shown by Baym that the derivability of the equations of motion from a functional of this kind is not only a sufficient but also a necessary condition for self-consistent approximations fulfilling all these properties [35, 36]. In recent years, the Φ-derivable-approximation technique has been used to derive transport equations, e.g., in [37, 38, 34, 39, 40] which go beyond the quasi-particle approximation, which is discussed in the next section. An investigation of a corresponding test-particle description has been given in [41, 34, 42]. A comparison of the dynamics according to the full Kadanoff-Baym equations with the corresponding off-shell transport equations has been provided, e.g., in [43, 44, 42].

For Φ-derivable approximations, the self-energy is given by the variational derivative

$$\Sigma^C(x_1, x_2) = -\mathrm{i}\frac{\delta\Phi[S^C]}{\delta S^C(x_2, x_1)}, \tag{21}$$

where the (exact) functional, $\Phi[S]$, is diagrammatically defined as the sum of all closed Feynman diagrams, where internal lines stand for full propagators, S, which cannot be disintegrated into disconnected parts by cutting two propagator lines, i.e., the two-particle irreducible (2PI) closed diagrams[3]. The functional derivative eq. (21) then leads to the skeleton expansion for the self-energy in terms of full propagators, i.e., as the sum over all self-energy diagrams with propagator lines that do not contain self-energy insertions. In this way the Φ-derivable approximation avoids double counting of diagrams automatically. In equilibrium, for the solution of the self-consistent Dyson equations for the self-energies at given temperature and chemical potential(s), at the same time Φ becomes part of the grand-canonical potential and thus leads to definitions for the thermodynamical quantities consistent with the one-particle dynamics provided by the self-consistent equations of motion for the self-energies. Of course, for practical purposes, the

---

[2]In the context of transport theory this is analogous to the well-known Boguliubov-Born-Green-Kirkwood-Yvon (BBGKY) hierarchy of multi-particle phase-space-distribution functions, which take into account multi-particle correlations to an arbitrary order.

[3]More formally the Φ functional can be defined as the interaction part of an effective action with both local and bilocal external sources [45], which provides the possibility to use Feynman-path integral methods to, e.g., derive the equations of motion or study the symmetry properties of n-particle Green's functions [46].

Φ functional has to be truncated in some way, e.g., given by the number of interaction vertices or loops since otherwise it again leads to the exact equations of motion, involving the full Schwinger-Dyson hierarchy of equations for all n-point Green's and vertex functions. Sometimes also partial resummations are used for Φ functionals, e.g., the ring-summation diagrams to obtain Landau-Fermi-liquid theory or the Dirac-Brueckner approximation given below. In this way truncation schemes are defined for which the averaged Noether currents of underlying symmetries (including energy-momentum conservation from space-time-translation invariance and current-conservation laws from (global or local) gauge symmetries) fulfill the conservation laws exactly. At the same time the self-energies obey the principle of detailed balance, and the scheme is thermodynamically consistent[4].

One example for such a scheme, leading to a transport equation for spin-symmetric nuclear matter which closely resembles the original Boltzmann equation, is the Dirac-Brueckner scheme. Following [25] it can be defined by a self-consistent set of equations for a ladder-resummed four-nucleon vertex function, Γ, and the nucleon self-energy, Σ, which itself dresses the nucleon-Green's function, S, via the Dyson Equation by

$$S^C(x_1, x_2) = S_0^C(x_1, x_2) + S^C(x_1, x_1') \odot \Sigma^C(x_1', x_2') \odot S_0^C(x_2', x_2), \tag{22}$$

$$\Sigma^C(x_1, x_2) = -i[\Gamma^C(x_1, x_1'; x_2, x_2') - \Gamma^C(x_1', x_1; x_2, x_2')] \odot S^C(x_1', x_2'), \tag{23}$$

$$\begin{aligned} \Gamma^C(x_1, x_2; x_1', x_2') = &\, U^C(x_1, x_2; x_1', x_2') \\ &+ iU^C(x_1, x_2; x_1'', x_2'') \odot S^C(x_1'', x_1''')S^C(x_2'', x_2''')\Gamma(x_1''', x_2'''; x_1', x_2'). \end{aligned} \tag{24}$$

The contour function, U^C, stands for two nucleon-meson vertices connected by a non-interacting meson propagator. The effect of meson-mean fields, i.e., the Hartree self-energy diagrams, are not taken into account explicitly but via one-point contributions to the self-energy. These contribute to the diagonal elements, Σ^{--} and Σ^{++}, of the contour-matrix self-energy (or equivalently to the retarded and advanced self-energies) and thus are implicitly included in the spectral function.

The transport equation for the Green's function, $S^<(x_1, x_2)$, which is known as Kadanoff-Baym equation, is derived from eq. (19) and its adjoint equation,

$$i\left(\partial\!\!\!/_{x_1} S^<(x_1, x_2) + S^<(x_1, x_2)\overleftarrow{\partial\!\!\!/}_{x_2}\right) - [\operatorname{Re}\Sigma^{\mathrm{ret}} \odot S^<](x_1, x_2) + [S^< \odot \operatorname{Re}\Sigma^{\mathrm{ret}}](x_1, x_2)$$
$$- [\Sigma^< \odot \operatorname{Re} S^{\mathrm{ret}}](x_1, x_2) + [\operatorname{Re} S^{\mathrm{ret}} \odot \Sigma^<](x_1, x_2) \tag{25}$$
$$= \frac{1}{2}\left\{[\Sigma^> \odot S^<](x_1, x_2) + [S^< \odot \Sigma^>]\,(x_1, x_2) - [\Sigma^< \odot S^>](x_1, x_2) - [S^> \odot \Sigma^<](x_1, x_2)\right\}.$$

The Kadanoff-Baym equation has to be supplemented by the purely retarded/advanced Dyson-like equations (18), which, as we will see below, describe the space-time evolution of the spectral properties of the particles.

In order to obtain eq. (25), we have used the relations,

$$\Sigma^{\mathrm{ret}}(x_1, x_2) = \operatorname{Re}\Sigma^{\mathrm{ret}}(x_1, x_2) + \frac{1}{2}\left(\Sigma^>(x_1, x_2) - \Sigma^<(x_1, x_2)\right), \tag{26}$$

$$\Sigma^{\mathrm{adv}}(x_1, x_2) = \operatorname{Re}\Sigma^{\mathrm{ret}}(x_1, x_2) - \frac{1}{2}\left(\Sigma^>(x_1, x_2) - \Sigma^<(x_1, x_2)\right) \tag{27}$$

---

[4]One should however note that approximations of this kind are only partial resummations of the full Dyson-Schwinger hierarchy, and the so defined self-consistent propagators and self-energies violate Ward-Takahashi identities at the order of the expansion parameter used for the truncation [46, 47].

and similar for $S^{\text{ret/adv}}(x_1, x_2)$ with $\operatorname{Re} O := \frac{1}{2}[O + \gamma^0 O^\dagger \gamma^0]$ and $\operatorname{Im} O := -\mathrm{i}(O - \operatorname{Re} O)$ for covariant spinor-matrices O. In other words, the real and imaginary parts of Dirac-spinor matrices refer to the corresponding complex coefficients in the usual decomposition into Lorentz tensors of this quantity,

$$O = O_{\text{S}} + \mathrm{i}\gamma_5 O_{\text{P}} + \gamma_\mu O_{\text{V}}^\mu + \gamma_\mu \gamma^5 O_{\text{A}}^\mu + \frac{1}{2}\sigma_{\mu\nu} O_{\text{T}}^{\mu\nu} \quad \text{with}$$

$$\gamma^5 = \gamma_5 = \mathrm{i}\gamma^0 \gamma^1 \gamma^2 \gamma^3, \quad \sigma_{\mu\nu} = \frac{\mathrm{i}}{2}\left[\gamma_\mu, \gamma_\nu\right].$$

(28)

The self-energy contour-matrix elements are determined from the Dirac-Brueckner scheme eqs. (22)–(24).

2.3. Wigner transformation and gradient expansion

To further simplify the task of approximately solving the self-consistent equations of motion for the Green's function, one aims at a reduction to a semi-classical transport equation, which admits the use of numerical approaches like Monte-Carlo test-particle simulations.

The general idea behind such reductions is the assumption that the many-body system, which is in a state where quantum correlations can be neglected, on "macroscopic" space-time scales behaves like a classical fluid. Then the Green's functions are rapidly oscillating functions of the relative coordinates, $\xi = x_1 - x_2$ ("fluctuations"), while their variations in $x = (x_1 + x_2)/2$ are slow. Thus, it is convenient to describe the two-point functions, $F(x_1, x_2)$, by their Wigner transforms[5],

$$\tilde{F}(x, p) = \int \mathrm{d}^4\xi \, \exp(\mathrm{i}p_\mu \xi^\mu) F\left(x + \frac{\xi}{2}, x - \frac{\xi}{2}\right).$$

(29)

The Wigner transform of convolution integrals can be written in terms of a Lie-derivative like operator, which resembles a relativistic generalization of the usual Poisson brackets [34]

$$\diamond(\tilde{F}_1, \tilde{F}_2) := \frac{1}{2}\left(\frac{\partial \tilde{F}_1}{\partial p_\mu}\frac{\partial \tilde{F}_2}{\partial x^\mu} - \frac{\partial \tilde{F}_1}{\partial x^\mu}\frac{\partial \tilde{F}_2}{\partial p_\mu}\right) = \frac{1}{2}\left\{\tilde{F}_1, \tilde{F}_2\right\}_{\text{pb}}.$$

(30)

Then the Wigner transform of a convolution integral reads

$$\widetilde{F_1 \odot F_2}(x, p) = \int \mathrm{d}^4\xi \, F_1\left(x + \frac{\xi}{2}, y'\right) \odot F_2\left(y', x - \frac{\xi}{2}\right)\exp(\mathrm{i}p_\mu \xi^\mu)$$

$$= \exp\left[\frac{\mathrm{i}}{2}\left(\partial_p^{(1)} \cdot \partial_x^{(2)} - \partial_x^{(1)} \cdot \partial_p^{(2)}\right)\right]\tilde{F}_1 \tilde{F}_2 =: \exp(\mathrm{i}\diamond)(\tilde{F}_1, \tilde{F}_2),$$

(31)

where $\partial_x^{(j)}$ and $\partial_p^{(j)}$ are the four-gradient operators with respect to x and p, acting on F_j ($j \in \{1, 2\}$) only. According to the above assumption of a many-body system close to a "classical state", one can neglect all gradients in the variables, x, at second and higher orders.

To derive semi-classical transport equations, the coupled equations eqs. (25)–(27) are now Wigner transformed. The convolution integrals are approximated by the first-order gradient expansion, cf. eqs. (30) and (31), assuming that the Wigner function depends only slowly on space-time and momentum

$$[\widetilde{F_1 \odot F_2}]_{\alpha\beta}(x, p) \simeq \tilde{F}_{1\alpha\beta'}(x, p)\tilde{F}_{2\beta'\beta}(x, p) + \frac{\mathrm{i}}{2}\left\{\tilde{F}_{1\alpha\alpha'}(x, p), \tilde{F}_{2\alpha'\beta}(x, p)\right\}_{\text{pb}}.$$

(32)

---

[5]The Wigner transforms, of course, inherit the Dirac-spinor-index structure from the original two-point functions.

Further, if one is only interested in the spin-averaged behavior, one can take the spinor trace of the gradient expanded Kadanoff-Baym eq. (25). Defining the Wigner form of the vector-current density by

$$F_{\mathrm{V}}^{\mu}(x, p) = -\mathrm{i}\, \mathrm{tr}[\tilde{S}^{<}(x, p)\gamma^{\mu}] \tag{33}$$

and using the trace's cyclic property one arrives at a generalized transport equation for Dirac particles,

$$\partial_{\mu}F_{\mathrm{V}}^{\mu}(x, p) - \mathrm{tr}\left\{\mathrm{Re}\,\tilde{\Sigma}^{\mathrm{ret}}(x, p), -\mathrm{i}\tilde{S}^{<}(x, p)\right\}_{\mathrm{pb}} + \mathrm{tr}\left\{\mathrm{Re}\,\tilde{S}^{\mathrm{ret}}(x, p), -\mathrm{i}\tilde{\Sigma}^{<}(x, p)\right\}_{\mathrm{pb}} = C(x, p). \tag{34}$$

Here the l.h.s. describes the non-dissipative and current conserving part of the transport, the Poisson bracket terms providing the drag- and back-flow response of the surrounding medium. The dissipative part is given by the collision term,

$$C(x, p) = \mathrm{tr}\left[\tilde{\Sigma}^{<}(x, p)\tilde{S}^{>}(x, p) - \tilde{\Sigma}^{>}(x, p)\tilde{S}^{<}(x, p)\right]. \tag{35}$$

The spectral and spinor properties of the propagator components of $\tilde{S}$ and thus those of F_{V} are determined by the retarded eq. (18) and can be quite complicated. This makes the evaluation of the traces appearing in eq. (34) quite difficult. A major simplification is thus reached by invoking the local density approximation in which the particles move locally in a homogeneous medium, with corresponding self-energies (potentials). This is in line with the gradient approximation. Furthermore, we now restrict ourselves in all of the following developments to the transport of particles assuming that the width of the particles is always much smaller than their mass. Antiparticles can be introduced as a separate particle species.

The spinor matrix of retarded and advanced propagators then simplifies to

$$\begin{aligned}
\tilde{S}^{\mathrm{ret/adv}}(x, p)\gamma^{0} &= \left\{\gamma^{0}\left[p_{\mu}\gamma^{\mu} - m - \tilde{\Sigma}^{\mathrm{ret/adv}}(x, p)\right]\right\}^{-1} \\
&= \left[p_{0} - \tilde{H}_{\mathrm{Dirac}}(x, p) - \mathrm{i}\gamma^{0}\,\mathrm{Im}\,\tilde{\Sigma}^{\mathrm{ret/adv}}(x, p)\right]^{-1},
\end{aligned} \tag{36}$$

here written in the non-covariant, i.e., Hamiltonian form with $\tilde{H}_{\mathrm{Dirac}}(x, p)$ as the corresponding hermitian Hamilton function. The above set, eqs. (34)–(36), constitutes the most general level for our transport description of Dirac particles. The extension to a multi-particle system is straightforward by either extending the internal degrees of freedom, e.g., to various flavors such as isospin, or strangeness, etc. or by adding the equations for further particles. The self-energies then provide the coupling between the various species.

If the damping terms, $\mathrm{Im}\,\tilde{\Sigma}^{\mathrm{ret}}$, are small compared to the mass gap, then $\tilde{S}^{\mathrm{ret/adv}}(x, p)\gamma^{0}$ and consequently $S^{</>}\gamma^{0}$ become approximately diagonal in the orthogonal eigen-spinors of $\tilde{H}_{\mathrm{Dirac}}(x, p)$

$$[E - \tilde{H}_{\mathrm{Dirac}}(x, E, \boldsymbol{p})]u^{r}(x, E, \boldsymbol{p}) = 0 \quad \text{with} \quad u^{r\dagger}(x, E, \boldsymbol{p})u^{r'}(x, E, \boldsymbol{p}) = \kappa\delta^{rr'}, \quad r, r' \in \{1, 2\}, \tag{37}$$

where the choice of the normalization, κ, is a matter of convention (in the case $\kappa \neq 1$, factors $1/\kappa$ have to appear in expressions explicitly using the spinors defined in eq. (37) in order to restore the normalization). We recall, that in eq. (37) the local homogeneous matter approximation is implied, i.e., it is assumed that the time and space scales, Δt and Δr, respectively, on which the Hamilton function, $\tilde{H}_{\mathrm{Dirac}}$, varies are much larger compared to the corresponding scales of variation of the single-particle wave function, i.e.,

$$\Delta t \gg E^{-1}, \quad \Delta r \gg |\boldsymbol{p}|^{-1}, \tag{38}$$

14

which is equivalent to the assumptions of the gradient expansion. The weak x-dependence of the eigen-spinors, u^r, is therefore neglected in calculating the gradient terms of the Dirac equation with respect to that of the quickly oscillating plane-wave factor $\propto \exp(-\mathrm{i}px)$.

In the next section and in section 3.1.3 we will discuss the quasi-particle case with scalar and vector potentials, $\tilde{\Sigma}_\mathrm{S}$ and $\tilde{\Sigma}_\mathrm{V}^\mu$, respectively, which are defined from the Lorentz decomposition,

$$\tilde{\Sigma}^\mathrm{ret}(x, p) = \tilde{\Sigma}_\mathrm{S}(x, p) - \gamma_\mu \tilde{\Sigma}_\mathrm{V}^\mu(x, p). \tag{39}$$

In this case,

$$\tilde{H}_\mathrm{Dirac}(x, p) = p^0 - \gamma^0(p_\mu^* \gamma^\mu - m^*) \tag{40}$$

with

$$p^{*\mu}(x, p) := p^\mu + \mathrm{Re}\,\tilde{\Sigma}_\mathrm{V}^\mu(x, p)\,, \tag{41}$$
$$m^*(x, p) := m + \mathrm{Re}\,\tilde{\Sigma}_\mathrm{S}(x, p) \tag{42}$$

being the kinetic four-momentum and the Dirac mass in the medium, respectively. Multiplying eq. (37) by γ^0 from the left and using eqs. (40)–(42), one obtains the in-medium Dirac equation,

$$[p^{*\mu}(x, E, \boldsymbol{p})\gamma_\mu - m^*(x, E, \boldsymbol{p})]u^r(x, p^*) = 0\,. \tag{43}$$

From this equation, for the given values of x and $\boldsymbol{p}$, the energy eigenvalue, E, can be found as the solution of the dispersion relation, $p^{*2} = m^{*2}$, or, for the positive-energy solutions,

$$E = E^* - \mathrm{Re}\,\tilde{\Sigma}_\mathrm{V}^0 \quad \text{with} \quad E^* := \sqrt{\boldsymbol{p}^{*2} + m^{*2}}\,, \tag{44}$$

where the kinetic three-momentum, effective mass and the real part of vector self-energy are supposed to be calculated at $p^0 = E$. Equation (44) is convenient, because it provides an analytic solution of the dispersion relation for the special case of the p^0-independent self-energies $\tilde{\Sigma}_\mathrm{S}(x, \boldsymbol{p})$ and $\tilde{\Sigma}_\mathrm{V}^\mu(x, \boldsymbol{p})$ (e.g., in the case of the nonlinear Walecka model discussed in section 3.1.3).

In the energy-spin eigenbasis $\tilde{S}^\mathrm{ret/adv}\gamma^0$ are diagonal and traces over them can easily be performed. Under the assumption of homogeneity, which is the basis for the gradient expansion, and spin saturation, other contour components of the fermionic propagator are related to $\mathrm{Im}\,\tilde{S}^\mathrm{ret}$ by a multiplicative, scalar function, $f(x, p)$, as

$$-\mathrm{i}\tilde{S}^<(x, p) = -2\,f(x, p)\,\mathrm{Im}\,\tilde{S}^\mathrm{ret}(x, p), \tag{45}$$
$$\mathrm{i}\tilde{S}^>(x, p) = -2\,[1 - f(x, p)]\,\mathrm{Im}\,\tilde{S}^\mathrm{ret}(x, p), \tag{46}$$

such that the analog of eq. (26) is satisfied. The function, $f(x, p)$, introduced in eqs. (45) and (46) is a Lorentz scalar[6]. Later on, in section 2.4.1 we will see that it represents the phase-space distribution of particles and becomes a local Fermi-Dirac distribution in the case of local equilibrium [25]. It also regulates the Pauli principle in the collision terms (cf. sections 2.4.1 and 3.3). The contour components of the propagator are thus related to each other through eqs. (45) and (46) and the contour relations (17) which also apply for the Wigner transformed propagators.

Thus also the diagonal forms of $S^{</>}\gamma^0$ are now known, and all traces in the transport equations (34) and (35) can be evaluated. The most important simplification arises from the fact that

---

[6]For a discussion of this covariance see, e.g., [48].

now all components of the vector-current density, the scalar density as well as the density of hole states can be related to just one Wigner function,

$$F(x, p) = -2f(x, p)\operatorname{tr}[\operatorname{Im}(\tilde{S}^{\operatorname{ret}}(x, p))\gamma^0] \,, \tag{47}$$

by interaction-dependent kinematical factors, i.e.,

$$F_{\mathrm{V}}^{\mu}(x, p) = \frac{p^{*\mu}}{E^*}F(x, p), \tag{48}$$

$$F_{\mathrm{S}}(x, p) = -\mathrm{i}\operatorname{tr}[\tilde{S}^{<}(x, p)] = \frac{m^*}{E^*}F(x, p). \tag{49}$$

It is important that the kinetic four-momentum in eq. (48) is taken on the effective (Dirac) mass shell, i.e., $p^{*\,0} = E^*$. The Wigner function, $F(x, p)$, has the Lorentz-transformation properties of a temporal component of a four vector. It is the generalization of the phase-space density in the sense of the Wigner representation. With the gradient expansion as a means of "coarse graining" it translates into a positive semidefinite phase-space distribution of particles, which then can be simulated with the test-particle ansatz (cf. eq. (89)). The corresponding (current) densities are retrieved upon integrating the above expressions over four-momenta with the weight, $1/(2\pi)^4$, i.e.,

$$J^{\mu}(x) = \int \frac{\mathrm{d}^4 p}{(2\pi)^4} \frac{p^{*\mu}}{E^*}F(x, p), \tag{50}$$

$$\rho_S(x) = \int \frac{\mathrm{d}^4 p}{(2\pi)^4} \frac{m^*}{E^*}F(x, p). \tag{51}$$

In the quasi-particle case the separation between particles and anti-particles is given by the sign of the vector potential (see section 3.1.3 for details).

It is important to verify that the gradient expansion does not destroy the consistency and conserving properties of the Φ-derivable approximations for the Kadanoff-Baym equations. Indeed it has been shown in [39, 40] that the transport eqs. (34)–(36) are conserving for Φ-derivable truncation schemes and admit the definition of an effective conserved current for each conserved quantity (energy, momentum, Noether charges). The effective current is identical with the expectation values of the corresponding Noether currents of the underlying symmetries. The Φ-derivable schemes also allow for a definition of the nonequilibrium entropy for the corresponding transport equations, including collision terms involving multi-particle processes beyond the $2 \leftrightarrow 2$ level, obeying the H-theorem [38]. In the general case, without assuming the quasi-particle approximation, one has to take into account the full eq. (34), including the last term on the left-hand side (l.h.s.). It turns out that this term describes the dynamics of the finite spectral width of the particles [25]. It becomes then particularly important to ensure that particles which are stable in the vacuum but have a large width in the medium due to collisional broadening fulfill their proper vacuum mass-shell conditions when they leave the medium during their dynamical evolution (e.g., to describe the "freeze-out" of hadrons in heavy-ion collisions dynamically within the transport approach).

Further, the first-order gradient expansion has to be performed consistently. This is not trivial, if the truncated Φ functional includes diagrams with more than two vertices, i.e., if the self-energy diagrams contain internal vertices that are not connected with the amputated legs. These internal vertices give rise to non-local terms before the gradient expansion, including complicated

16

memory effects (for an early discussion of the possible importance of non-Markovian effects in heavy-ion collisions, see [49]). The first-order gradient expansion can be described diagrammatically in the Wigner representation (cf. [39]) and can be applied directly to the Φ functional, leading to a local approximation, $\Phi_{\text{loc}}[x, \tilde{S}]$, where x is an arbitrary reference point, around which the gradient expansion is performed. It is clear that then Φ_{loc} consists only of loop integrals of exact propagators (and additional lines, representing space-time and four-momentum derivatives) to be taken at the reference point, x. The loops in the diagrams, including those containing the additional diagram elements for the derivatives, then stand for momentum integrals as for homogeneous systems (e.g., nuclear matter in thermal equilibrium). The self-consistent equations of motion are then given in terms of the self-energy defined by this local Φ functional,

$$- i\tilde{\Sigma}(x, p) = -\frac{\delta\Phi_{\text{loc}}[x, \tilde{S}]}{\delta\tilde{S}(x, p)}, \tag{52}$$

and the general structure of the transport equation for the Wigner function (48) reads

$$\mathcal{D}F(x, p) + \text{tr}\left\{\text{Re}\,\tilde{S}^{\text{ret}}(x, p), -i\tilde{\Sigma}^{<}(x, p)\right\}_{\text{pb}} = C(x, p)\,. \tag{53}$$

Here we have written

$$\mathcal{D}F = \{p_0 - H, F\}_{\text{pb}} \quad \text{with} \quad H = E^{*}(x, p) - \text{Re}\,\tilde{\Sigma}^{0}_{V}(x, p). \tag{54}$$

The term, $\mathcal{D}F$, contains the first Poisson bracket on the l.h.s. of eq. (34). The collision term, C, on the right-hand side (r.h.s.) of eq. (53) is defined above by eq. (35) and can be, generally, calculated via the diagrammatic rules from Φ_{loc}. In a first approximation, one can also directly express it via the elementary transition probabilities related to the experimentally measured decay widths of unstable particles and interaction cross sections in vacuum (see section 3.3 below).

Apart from the definition of the Wigner function, F, and the single-particle Hamilton function, H, the transport equation (53) has the same form as in the non-relativistic case [31, 25, 38, 41, 39].

Boson transport. For relativistic bosons the corresponding equation has been derived in refs. [50, 34, 39]. For completeness we give it here,

$$\mathcal{D}F(x, p) + \left\{\text{Re}\,\tilde{D}^{\text{ret}}(x, p), i\tilde{\Pi}^{<}(x, p)\right\}_{\text{pb}} = C(x, p)\,, \tag{55}$$

with

$$\mathcal{D}F = \left\{p^2 - m^2 - \text{Re}\,\tilde{\Pi}^{\text{ret}}(x, p), F(x, p)/2p^0\right\}_{\text{pb}}\,, \tag{56}$$

$$C(x, p) = \tilde{\Pi}^{>}(x, p)\tilde{D}^{<}(x, p) - \tilde{D}^{>}(x, p)\tilde{\Pi}^{<}(x, p)\,, \tag{57}$$

and F defined by

$$F(x, p) = 2p^0 i\tilde{D}^{<}(x, p)\,. \tag{58}$$

Here F has the same physical meaning as that in eq. (53) and D is the boson propagator. Eqs. (55), (56) differ from eqs. (53) and (54) just by the typically different appearance of the retarded polarization function, $\tilde{\Pi}^{\text{ret}}$, for bosons.

Spectral functions. From the definition of the Green's functions in terms of expectation values of field operators eq. (11) and the Fourier representation of the Heaviside unit-step function,

$$\Theta(t) = \int \frac{\mathrm{d}p_0}{2\pi} \exp(-\mathrm{i}p_0 t) \frac{\mathrm{i}}{p_0 + \mathrm{i}0} \, , \tag{59}$$

it is easy to show that the retarded and advanced Green's functions obey the dispersion relations,

$$\tilde{S}_{\alpha\beta}^{(\mathrm{ret/adv})}(x, p) = \int \mathrm{d}p_0' \frac{\hat{A}_{\alpha\beta}(x, p_0', \boldsymbol{p})}{p_0 - p_0' \pm \mathrm{i}0} \, , \tag{60}$$

with the spectral functions,

$$\hat{A}_{\alpha\beta}(x, p) = -\frac{1}{\pi} \mathrm{Im}(\tilde{S}^{\mathrm{ret}})_{\alpha\beta} = \frac{\mathrm{i}}{2\pi} [\tilde{S}_{\alpha\beta}^{>}(x, p) - \tilde{S}_{\alpha\beta}^{<}(x, p)] = \frac{\mathrm{i}}{2\pi} [\tilde{S}_{\alpha\beta}^{\mathrm{ret}}(x, p) - \tilde{S}_{\alpha\beta}^{\mathrm{adv}}(x, p)] \, . \tag{61}$$

Integrating this equation over p_0, from the canonical equal-time commutation relations for the Dirac-spinor field operators one obtains

$$\int_{-\infty}^{\infty} \mathrm{d}p_0 \, \hat{A}_{\alpha\beta}(x, p) = \gamma_{\alpha\beta}^0 \, . \tag{62}$$

It is now convenient to introduce the real-valued spectral function by taking the trace of eq. (61). Thus we define a spin-averaged spectral function,

$$A(x, p) := \frac{1}{g} \mathrm{tr}[\hat{A}(x, p)\gamma^0] = -\frac{1}{g\pi} \mathrm{tr}[\mathrm{Im}(\tilde{S}^{\mathrm{ret}}(x, p))\gamma^0] \, , \tag{63}$$

where $g = 2$ denotes the spin degeneracy. Note that $A(x, p)$ has the Lorentz-transformation properties of a temporal component of a four-vector. It can be interpreted as an energy distribution function because of eq. (62) and will be discussed further later in section 2.4.2. Since we are dealing only with the transport of particles A receives its strength mainly from positive energy states.

Using the definition of the spectral function (63) the Wigner function eq. (47) can now be rewritten as

$$F(x, p) = 2\pi g f(x, p) A(x, p) \, . \tag{64}$$

Here the spectral information contained in A has been separated out of the generalized phase-space distribution F.

2.4. Off-shell transport

Particles in the medium have a finite lifetime due to collisional broadening, even if they are stable in the vacuum. Within the local density approximation their spectral functions depend on $\rho(\boldsymbol{x})$ and p, i.e., they change over the nuclear volume, e.g., when going from high- to low-density regions. Therefore, one must ensure that particles leaving the nucleus have returned to their vacuum-pole mass (if they are stable in the vacuum like the nucleon) or to their free spectral function (for baryonic resonances, for example).

This is indeed achieved by the additional term on the l.h.s. of eq. (53) that vanishes for on-shell particles. In eq. (53), the first term includes the usual drift term, $\propto \partial H/\partial p^\mu$, as well as the Vlasov term, $\propto \partial H/\partial x_\mu$, which takes into account mean-field potentials. The second term is

not present in the quasi-particle limit. However, for broad resonances, this term becomes crucial for the validity of conservation laws in the off-equilibrium dynamics, providing the back flow of the conserved quantity from the medium into the channel described by the particular Green's function under consideration [39, 40, 42]. Unfortunately, this back-flow term causes problems in practical calculations since it cannot be easily interpreted within the test-particle ansatz for Monte Carlo simulations, because it is not proportional to F.

A possible resolution of these problems has been developed by Botermans and Malfliet [25]. In local thermal equilibrium, i.e., for the solution of the transport equation, for which the collision term vanishes identically, i.e., if $\tilde{\Sigma}^< \tilde{S}^> = \tilde{S}^< \tilde{\Sigma}^>$, we have

$$
\begin{aligned}
\tilde{\Sigma}^<_{\text{eq}}(x, p) &= i\Gamma_{\text{eq}}(x, p) f_{\text{eq}}(x, p), \\
\tilde{\Sigma}^>_{\text{eq}}(x, p) &= -i\Gamma_{\text{eq}}(x, p)[1 - f_{\text{eq}}(x, p)]
\end{aligned}
\tag{65}
$$

with

$$
\Gamma(x, p) = -2 \operatorname{Im} \tilde{\Sigma}^{\text{ret}}(x, p).
\tag{66}
$$

In the off-equilibrium case one can show that in the decomposition,

$$
\tilde{\Sigma}^<(x, p) = i\Gamma(x, p) f(x, p) + \xi(x, p),
\tag{67}
$$

the contribution of ξ to the back-flow term on the l.h.s. of eq. (53) is of higher order in the gradient expansion, i.e., it consists of second-order derivatives with respect to the space-time components, x, or of products of first-order derivatives. Thus, it is consistent with the first-order gradient expansion to neglect ξ in eq. (67) and to approximate eq. (53) by

$$
\mathcal{D}F(x, p) - \operatorname{tr}\left\{\Gamma f, \operatorname{Re} S^{\text{ret}}(x, p)\right\}_{\text{pb}} = C(x, p) .
\tag{68}
$$

Here the back-flow term becomes proportional to F (cf. eq. (64)) and can be treated within the test-particle method. Equation (68) is known as the Botermans-Malfliet form of the kinetic equation. As the Kadanoff-Baym form it admits the definition of an effective conserved current, which however deviates from the corresponding Noether-current expression by higher-order gradient terms, even if a Φ-derivable approximation is used to define the self-energies.

2.4.1. The quasi-particle limit

The spectral functions of many particles of interest in nuclear transport theory are quite narrow. For example, bound nucleons can be assumed to have spectral functions of negligible width as long as one is not looking at exclusive events connected with high-momentum tails in their wave functions. In this case it is justified to invoke the further simplifications of the quasi-particle approximation, for which the particles are assumed to be on the energy shell, i.e., their energy, $E(x, \boldsymbol{p})$, is the solution of the dispersion relation (44). Then, neglecting again anti-particles, we can approximate the spectral function (63) by a δ-function and introduce the phase-space occupation probability, $f(x, \boldsymbol{p})$, by the equation,

$$
F(x, p) = 2\pi g \delta[p_0 - E(x, \boldsymbol{p})] f(x, \boldsymbol{p}) ,
\tag{69}
$$

where it is assumed that the self-energies do not depend explicitly on p^0 (otherwise so-called Z-factors for normalization appear that contain the derivative of the self-energies with respect to p^0). Using eq. (69) allows us to rewrite the vector current of eq. (50) in the usual classical form,

$$
J^\mu(x) = g \int \frac{\mathrm{d}^3 \boldsymbol{p}}{(2\pi)^3} \frac{p^{*\mu}}{E^*} f(x, \boldsymbol{p}) .
\tag{70}
$$

Since in the quasi-particle approximation $p_0^* = E^*$, this leads to the interpretation of $gf(x, \boldsymbol{p})/(2\pi)^3$ as the phase-space density of the nucleon-quasi particles. Also this function is a Lorentz scalar for (quasi-)particles fulfilling the on-shell condition (44), leading to the current (70) as a manifestly covariant Lorentz vector, as it should be.

Since by assumption the width of the particle, Γ, is much smaller than its energy the second term on the l.h.s. of eq. (53) can be neglected since it is proportional to the width of the spectral function. Therefore, inserting eq. (69) into the kinetic equation eq. (53) leads, after performing the p^0 integration, to the transport equation for the one-particle phase-space distribution function, f,

$$
\begin{aligned}
\left[\partial_t + (\boldsymbol{\nabla}_{\boldsymbol{p}} E_{\boldsymbol{p}}) \cdot \boldsymbol{\nabla}_{\boldsymbol{r}} - (\boldsymbol{\nabla}_{\boldsymbol{r}} E_{\boldsymbol{p}}) \cdot \boldsymbol{\nabla}_{\boldsymbol{p}}\right] f(x, \boldsymbol{p}) = {} & \frac{g}{2} \int \frac{\mathrm{d}^3 \boldsymbol{p}_2 \, \mathrm{d}^3 \boldsymbol{p}_1' \, \mathrm{d}^3 \boldsymbol{p}_2'}{(2\pi)^9} \frac{m_{\boldsymbol{p}}^* m_{\boldsymbol{p}_2}^* m_{\boldsymbol{p}_1'}^* m_{\boldsymbol{p}_2'}^*}{E_{\boldsymbol{p}}^* E_{\boldsymbol{p}_2}^* E_{\boldsymbol{p}_1'}^* E_{\boldsymbol{p}_2'}^*} \\
& \times (2\pi)^4 \delta^{(3)}(\boldsymbol{p} + \boldsymbol{p}_2 - \boldsymbol{p}_1' - \boldsymbol{p}_2') \delta(E_{\boldsymbol{p}} + E_{\boldsymbol{p}_2} - E_{\boldsymbol{p}_1'} - E_{\boldsymbol{p}_2}') \\
& \times \overline{|\mathfrak{M}_{\boldsymbol{p}\,\boldsymbol{p}_2 \to \boldsymbol{p}_1'\,\boldsymbol{p}_2'}|^2} \left[f(\boldsymbol{p}_1') f(\boldsymbol{p}_2') \overline{f}(\boldsymbol{p}) \overline{f}(\boldsymbol{p}_2) - f(\boldsymbol{p}) f(\boldsymbol{p}_2) \overline{f}(\boldsymbol{p}_1') \overline{f}(\boldsymbol{p}_2')\right]
\end{aligned}
\tag{71}
$$

with $E_{\boldsymbol{p}} := E(x, \boldsymbol{p})$ and $\overline{f} = 1 - f$. The collision term of eq. (71) is written assuming a spin-saturated system of identical spin-1/2 fermions neglecting the isospin degree of freedom (cf. Eq. (6.109) in ref. [25] for the collision term for the spin-matrix phase space density). The transition matrix element squared and averaged over spins of initial particles and summed over spins of final particles is denoted as $\overline{|\mathfrak{M}_{\boldsymbol{p}\,\boldsymbol{p}_2 \to \boldsymbol{p}_1'\,\boldsymbol{p}_2'}|^2}$. The matrix element, $\mathfrak{M}_{if}$, is taken in the convention of Bjorken and Drell [51] where the spinors are normalized according to

$$
u^{r\dagger}(x, p^*) u^{r'}(x, p^*) = \frac{E^*}{m^*} \delta^{rr'} \quad \text{or} \quad \bar{u}^r(x, p^*) u^{r'}(x, p^*) = \delta^{rr'} \; .
\tag{72}
$$

Equation (71) has the typical form of a semi-classical BUU equation with a drift term containing the non-trivial space-time dependent quasi-particle dispersion relations. If meson-mean-field contributions are taken into account, the transport equation has to be closed with the corresponding mean-field equations of motion, which are themselves functionally dependent on the phase-space distribution, f.

2.4.2. Spectral functions and self-energies

In contrast to the case treated in the previous section the transport of particles with broad spectral width, for example of mesons with short lifetimes and/or collision-broadened nucleons, requires the solution of the full transport equations. In this case the quasiparticle approximation cannot be used to simplify the equations, but instead the nontrivial energy-momentum dependence of the spectral function has to be taken into account.

The spectral function (63) becomes for particle (i.e., positive energy) states (i.e., $|p^{*0} - E^*| \ll E^*$) [25]

$$
A(x, p) \approx \frac{1}{\pi} \frac{\Gamma/2}{(p_0^* - E^*)^2 + \Gamma^2/4} \; ,
\tag{73}
$$

where

$$
\Gamma := -2 \, \mathrm{Im}[(m^*/E^*) \tilde{\Sigma}_{\mathrm{S}} + (\boldsymbol{p}^*/E^*) \cdot \tilde{\boldsymbol{\Sigma}}_{\mathrm{V}} - \tilde{\Sigma}_{\mathrm{V0}}]
\tag{74}
$$

denotes the total width of a particle in the calculational frame and E^* is given by eq. (44). The four-vector, p^*, now also describes an off-shell particle, i.e., $p^{*0} \neq E^*$. Thus, within the same

approximation, the spectral function satisfies the normalization condition,

$$\int\limits_{0}^{+\infty} dp^0 A(x, p) \simeq 1 .$$ (75)

Most of the early applications of off-shell transport were in descriptions of broad vector mesons in nuclei. Therefore, the following form, suitable also for the description of bosons,

$$\mathcal{A}(x, p) = \frac{1}{\pi} \frac{\sqrt{p^{*2}} \Gamma_{\text{med}}}{[p^{*2} - m^{*2}]^2 + p^{*2} \Gamma_{\text{med}}^2} ,$$ (76)

is implemented in the GiBUU model. Here, $\Gamma_{\text{med}} = p^{*0} \Gamma / \sqrt{p^{*2}}$ is the particle width in the rest frame of this particle. This form has been widely used in hadronic transport theory [52] and nuclear matter calculations [53] and is also the one advocated by the Particle Data Group (PDG) [54]. Near the quasiparticle pole, $|p^{*0} - E^*| \ll E^*$, the Breit-Wigner spectral function (73) and the spectral function eq. (76) can be related by

$$\mathcal{A} \simeq \frac{A}{2p^{*0}}.$$ (77)

The spectral function (76) is normalized according to the condition

$$\int_{0}^{\infty} d(p^{*2}) \, \mathcal{A}(x, p) = 1,$$ (78)

where the integration is performed at constant kinetic momentum, $\boldsymbol{p}^*$, cf. eq. (41).

For simplicity, in this section and in section 2.4.3, we consider a model without a vector part of the self-energy, i.e., $p^* = p$. Defining the complex-valued quantity, Π, by

$$\text{Re} \, \Pi(x, p) := m^{*2} - m^2,$$ (79)

$$\text{Im} \, \Pi(x, p) := - \sqrt{p^2} \, \Gamma_{\text{med}},$$ (80)

one can rewrite the spectral function (76) as

$$\mathcal{A}(x, p) = -\frac{1}{\pi} \frac{\text{Im} \, \Pi}{\left[p^2 - m^2 - \text{Re} \, \Pi \right]^2 + (\text{Im} \, \Pi)^2} ,$$ (81)

which formally coincides with a bosonic spectral function with the boson polarization function, Π. Assuming the usual analyticity properties of the function, Π, in the upper part of the complex p^0-plane, we can express the real part of Π via its imaginary part by using a once-subtracted dispersion relation,

$$\text{Re} \, \Pi(x, p_0, \boldsymbol{p}) = \text{Re} \, \Pi(x, E, \boldsymbol{p}) + \frac{p_0 - E}{\pi} \, \text{PV} \int_{-\infty}^{\infty} dp_0' \frac{\text{Im} \, \Pi(x, p_0', \boldsymbol{p})}{(p_0' - E)(p_0' - p_0)} ,$$ (82)

where $E = \sqrt{\boldsymbol{p}^2 + m^{*2}}$ is the on-shell single-particle energy and PV denotes the Cauchy-principal value.

The total width of a particle in the medium is given by

$$\Gamma_{\text{med}}(x, p) = \Gamma_{\text{decay}}(x, p) + \gamma \Gamma_{\text{coll}}(x, p), \tag{83}$$

where γ denotes the Lorentz-boost factor from the nucleus rest-frame to the particle rest-frame (details are given in Ref. [55]). The decay width, Γ_{decay}, includes the Pauli blocking (Bose enhancement) factors for the outgoing fermions (bosons) (c.f. the loss term in eq. (161)). The actual parameterizations of the vacuum decay widths are described in section 3.3.1. If the invariant mass of the particle is less than the mass of its final decay products, then $\Gamma_{\text{free}} = 0$. The width of a particle with four-momentum, p, due to collisions with neutrons (n) and protons (p) in a nucleus can be evaluated in the low-density approximation as

$$\Gamma_{\text{coll}}(x, p) = \sum_{i=n,p} \int \frac{g \, d^3 \boldsymbol{p}'}{(2\pi)^3} f_i(x, \boldsymbol{p}') \sigma_i(p_0, \boldsymbol{p}, \boldsymbol{p}') v_{\text{rel}}(p_0, \boldsymbol{p}, \boldsymbol{p}') \, . \tag{84}$$

Here, v_{rel} denotes the relative velocity of the regarded particle and a nucleon with momentum, $\boldsymbol{p}'$, and f_i are the nucleon phase-space occupation probabilities (c.f. eq. (69)). The total in-medium nucleon-particle interaction cross sections, σ_i, in eq. (84) include the Pauli blocking (Bose enhancement) factors for the outgoing baryons (mesons), in contrast to the cross sections used in the GiBUU collision term, where these factors are written separately (cf. eq. (168)). Thus, the collisional width, Γ_{coll}, accounts for additional decay channels of the particle inside the nucleus.

Let us take the Δ resonance as an example. Besides the usual decay, $\Delta \to \pi N$, also the two-body and three-body interactions, $\Delta N \to \Delta N$, $\Delta N \to NN$ or $\Delta NN \to NNN$, occur in the nuclear medium. These pure in-medium interactions add to the total Δ width. On the other hand, the partial $\Delta \to \pi N$ contribution is decreased by Pauli blocking of the outgoing nucleon. Thus, the total in-medium width of the Δ resonance is determined by a delicate interplay of the new decay channels and Pauli blocking effects (cf. Ref. [56, 57] and also the discussion in Appendix B.1 before and after eq. (B.12)).

The quantity, $\text{Re} \, \Pi(x, p)$, can now be readily reconstructed from $\text{Im} \, \Pi(x, p)$ by using the dispersion relation (82). This leads to a high accuracy in the evaluation of the spectral function (see Refs. [55, 58] for further details).

2.4.3. Off-shell propagation: approximations

The kinetic equation (68) holds for stable as well as broad unstable states and thus allows, e.g., to describe the kinetics of resonances [34, 41]. For its solution we use the so-called off-shell potential (OSP) ansatz, a major simplification, that contains the relevant physics (correct transition from in-medium to in-vacuum spectral functions). Within this ansatz the effects of the second Poisson bracket on the l.h.s. of eq. (68) are absorbed into a modification of the mean-field potential.

In order to outline this method we start our discussion with the transport equation in which the back-flow term is removed

$$\{p_0 - H(x, p), F(x, p)\}_{\text{pb}} = C(x, p). \tag{85}$$

The l.h.s. of eq. (85) can explicitly be rewritten as

$$\{p_0 - H, F\}_{\text{pb}} = \left[\left(1 - \frac{\partial H}{\partial p_0}\right) \frac{\partial}{\partial t} + \frac{\partial H}{\partial \boldsymbol{p}} \frac{\partial}{\partial \boldsymbol{r}} - \frac{\partial H}{\partial \boldsymbol{r}} \frac{\partial}{\partial \boldsymbol{p}} + \frac{\partial H}{\partial t} \frac{\partial}{\partial p^0} \right] F(x, p) \tag{86}$$

22

with the single-particle Hamilton function,

$$H(x, p) = \sqrt{m^2 + \text{Re}\,\Pi(x, p_0, \boldsymbol{p}) + \boldsymbol{p}^2}\,, \tag{87}$$

where m is the pole mass of the particle species under consideration. The self-energy, Π, contains the effects of the potential; in the general off-shell case it can be explicitly dependent on p_0.

We note here that while eq. (85) is the transport equation for fermions, the analogous one for bosons (cf. eq. (55))

$$\left\{ p^2 - m^2 - \text{Re}\,\tilde{\Pi}(x, p), F(x, p)/(2p^0) \right\}_{\text{pb}} = \left\{ p_0^2 - H^2(x, p), F(x, p)/(2p^0) \right\}_{\text{pb}} = C(x, p) \tag{88}$$

reduces to the one for fermions for $|p^0 - H| \ll H$ with formally the same Hamiltonian H, provided H is not explicitly time-dependent. Thus the following considerations are also directly applicable to bosonic transport.

The generalized BUU eq. (85) can be solved numerically by using the test-particle technique, i.e., the continuous Wigner function is replaced by an ensemble of test particles represented by δ-functions,

$$F(x, p) = \lim_{n(t) \to \infty} \frac{(2\pi)^4}{N} \sum_{j=1}^{n(t)} \delta[\boldsymbol{r} - \boldsymbol{r}_j(t)]\delta[\boldsymbol{p} - \boldsymbol{p}_j(t)]\delta[p^0 - p_j^0(t)]\,, \tag{89}$$

where $n(t)$ denotes the number of test particles at time, t, and $\boldsymbol{r}_j(t)$ and $p_j(t)$ are the coordinates and the four-momenta of test particle, j, at time, t. As the phase-space density changes in time due to both, collisions and the Vlasov dynamics, also the number of test particles changes throughout the simulation: in the collision term, test particles are destroyed and new ones are created. At $t = 0$ we start with $n(0) = N \cdot A$ test particles, where A is the number of physical particles and N is the number of ensembles (test particles per physical particle). More details about the numerical treatment of the Vlasov and collision dynamics can be found in Appendix D.

Combining the time derivatives of eq. (89) and eq. (86), we find the equations of motion,

$$\frac{d\boldsymbol{r}_j}{dt} = \left(1 - \frac{\partial H}{\partial p_0}\right)^{-1} \frac{\partial H}{\partial \boldsymbol{p}}\,, \tag{90}$$

$$\frac{d\boldsymbol{p}_j}{dt} = -\left(1 - \frac{\partial H}{\partial p_0}\right)^{-1} \frac{\partial H}{\partial \boldsymbol{r}}\,, \tag{91}$$

$$\frac{dp_j^0}{dt} = \left(1 - \frac{\partial H}{\partial p_0}\right)^{-1} \frac{\partial H}{\partial t}\,. \tag{92}$$

Here the first factors on the r.h.s. are just the so-called Z-factors mentioned at the start of section 2.4.1. If $\partial H/\partial p_0 = 0$, eqs. (90) and (91) become the usual Hamilton equations of motion for stable particles. Energy conservation is enforced by eq. (92), if $\partial H/\partial t = 0$. Numerically, the generalized Hamilton equations of motion (90)-(92), are solved with a predictor-corrector algorithm (see Appendix D).

Since the Poisson-bracket term in eq. (68) has been dropped, there is, so far, nothing in eqs. (90)–(92) that restores the proper vacuum properties of a collision-broadened particle when it propagates out of the nucleus. The OSP ansatz approximately restores the proper off-shell

propagation. This idea was originally introduced in [59, 60] in the spirit of an educated guess, only taking into account the density dependence of the self-energy. An improved version has been developed in Ref. [55] with the intent to solve the non-relativistic test-particle equations of motion of [41].

To introduce the (relativistic) OSP method we start by defining the offshellness (or off-shell potential), $\Delta\mu_j^2$, of the jth test particle by

$$p_j^2 = m^2 + \text{Re}\,\Pi + \Delta\mu_j^2\ . \tag{93}$$

Thus, $\sqrt{m^2 + \text{Re}\,\Pi}$ corresponds to the in-medium pole mass and, consequently, $\Delta\mu_j^2$ is a measure of how far the test-particle invariant mass, $\mu_j = \sqrt{p_j^2}$, is off the pole[7]. Rewriting eq. (93) yields for the energy of the test particle

$$p_j^0 = \sqrt{m^2 + \text{Re}\,\Pi + \Delta\mu_j^2 + \boldsymbol{p}^2}\ . \tag{94}$$

The effects of the off-shell propagation, contained in the Poisson-bracket term in eq. (53), are thus absorbed into the off-shell potential, $\Delta\mu_j^2$.

The OSP ansatz now consists in regulating the offshellness, $\Delta\mu_j^2$, such that the vacuum behavior is restored when the particles leave the nucleus. To achieve this, the offshellness can be written as

$$\Delta\mu_j^2(\boldsymbol{r}, p) = \chi_j \tilde{\Gamma}_j(\boldsymbol{r}, p), \tag{95}$$

where the off-shell parameter, χ_j, is a constant of motion for each test particle and therefore can be calculated at the time of creation, t_0, as

$$\chi_j = \frac{\Delta\mu_j^2(\boldsymbol{r}_j(t_0), p_j(t_0))}{\tilde{\Gamma}_j(\boldsymbol{r}_j(t_0), p_j(t_0))}. \tag{96}$$

Here, $\tilde{\Gamma}_j$ is related to the total width of a particle in its $\tilde{\Gamma}_j(\boldsymbol{r}, p) = \mu_j \Gamma_{\text{tot}}(\boldsymbol{r}, p)$.

As each test particle is defined with its own off-shell parameter, we require a separate Hamilton function, H_j, for each test particle and replace

$$H = \sqrt{m^2 + \text{Re}\,\Pi + \boldsymbol{p}^2} \rightarrow H_j = \sqrt{m^2 + \text{Re}\,\Pi + \Delta\mu_j^2 + \boldsymbol{p}^2}. \tag{97}$$

Each test particle is thus propagated also under the influence of the off-shell potential, $\Delta\mu_j^2$. Note that this potential, just like χ_j, is positive for particles above the pole mass ($\mu_j > \sqrt{m^2 + \text{Re}\,\Pi}$) and negative for those below. By inserting this Hamiltonian into the generalized Hamilton equations of motion (90)-(92), one directly obtains the relativistic test-particle equations of motion given in [34]. Lehr [61] has shown that for non-relativistic particles the OSP method is equivalent to the full solution of the original Kadanoff-Baym equation as outlined in [34, 41]; for relativistic particles it approximates the full solution extremely well.

_____

[7]Remember that we suppress the particle-species index i while we keep the index j which denotes the jth test particle. For brevity, the Coulomb potential is dropped in the derivation of the OSP method, but it is taken into account in the calculations (see section 3.1.2).

Using the off-shell parameter, the relativistic equations of motion simplify to

$$\dot{\boldsymbol{r}}_j = \frac{1}{1-C_j}\frac{1}{2E_j}\left(2\boldsymbol{p}_j + \frac{\partial}{\partial \boldsymbol{p}_j}[\mathrm{Re}\,\Pi_j + \chi_j\tilde{\Gamma}_j]\right) , \tag{98}$$

$$\dot{\boldsymbol{p}}_j = -\frac{1}{1-C_j}\frac{1}{2E_j}\frac{\partial}{\partial \boldsymbol{r}_j}\left[\mathrm{Re}\,\Pi_j + \chi_j\tilde{\Gamma}_j\right] , \tag{99}$$

$$\dot{\chi}_j = 0 \tag{100}$$

$$\text{with} \quad C_j = \frac{1}{2E_j}\frac{\partial}{\partial E_j}\left[\mathrm{Re}\,\Pi_j + \chi_j\tilde{\Gamma}_j\right] , \tag{101}$$

The earlier OSP ansatz, as applied by Effenberger [60] and later by Lehr [61] and Mühlich [62], was much simpler; assuming $\Gamma_{\mathrm{med}} \approx \gamma\Gamma_{\mathrm{coll}}$ and $\Gamma_{\mathrm{coll}} \propto \rho$ they chose a linear dependence in density instead of the full in-medium width in eq. (96), which is a considerable simplification from a numerical point of view. In addition, these authors introduced a back-coupling term stemming from the influence of the OSP on the residual nucleus, which restores also the overall energy conservation. In reactions, where the nucleus stays approximately in its ground state, the back-coupling term leads only to minor modifications and can be neglected.

At first sight the implementation of the off-shell equations of motion, as given above, seems straightforward. In reality, however, a number of problems appear, which make the implementation of a fully consistent off-shell transport scheme difficult.

One such problem concerns the momentum dependence of the total widths. To describe off-shell transport in a consistent manner, one should use collisional widths in the medium which are compatible with the collision term used in the transport model. In general such a collisional width depends on the particle's momentum (relative to the medium). Also, the equations of motion shown earlier are sensitive to such momentum dependences, as they contain terms of the form $\partial\tilde{\Gamma}_j/\partial\boldsymbol{p}_j$. However, these terms can cause test particles to become superluminous. To show this, we express the width in terms of variables ($\mu = \sqrt{(p^0)^2 - \boldsymbol{p}^2}, \boldsymbol{p}$) instead of ($p^0, \boldsymbol{p}$). Then, by combining eqs. (98) and (101) and neglecting $\mathrm{Re}\,\Pi_j$ we obtain the following expression for the test-particle velocity:

$$\boldsymbol{v}_j = \dot{\boldsymbol{r}}_j = \frac{\boldsymbol{p}_j}{E_j} + \left(1 - \frac{\chi_j}{2\mu_j}\frac{\partial\tilde{\Gamma}_j(\boldsymbol{r}_j,\mu_j,\boldsymbol{p}_j)}{\partial\mu_j}\right)^{-1}\frac{\chi_j}{2E_j}\frac{\partial\tilde{\Gamma}_j(\boldsymbol{r}_j,\mu_j,\boldsymbol{p}_j)}{\partial\boldsymbol{p}_j} \tag{102}$$

If the width depends on invariant mass only and not on three-momentum the velocity simplifies to the classical expression $\boldsymbol{v}_j = \boldsymbol{p}_j/E_j$. The same always holds true for on-shell particles, which have $\chi_j = 0$. This is expected, since $\mathrm{Re}\,\Pi_j$ is neglected. However, there is a correction term $\propto \partial\tilde{\Gamma}_j/\partial\boldsymbol{p}_j$ to the classical limit for off-shell particles if the width depends on three-momentum. In addition, the velocity is not guaranteed to be smaller than the speed of light any more. This can become a problem for particles which are already highly relativistic. For them, even a small contribution from the extra term can violate the constraint, $v \leq 1$. This problem of superluminous particles has been noted already, e.g., in [63] for pion propagation. Following [60, 61, 62] we circumvent this problem by keeping only the density dependence of the width and use a momentum-independent value which fits the full one, obtained from the collision term, on average.

3. Potentials and collision terms in GiBUU

The relevant degrees of freedom in the GiBUU model are baryons, mesons, leptons, their anti-particles and the gauge bosons. The parameters for all hadrons without strangeness and charm are taken from the πN scattering phase-shift analysis of Manley and Saleski [64]; the parameters for all other particles are taken from the PDG group [65]. Besides the nucleon and the pion, also Λ, Σ, Ξ, Ω, Λ_C, Σ_C, Ξ_c, Ω_C, η, J/Ψ, K, $\bar{K}$, D, $\bar{D}$, D_s^+ and D_s^- are assumed to be stable because their lifetimes are much longer than the usual timescales for nuclear reactions. A complete list of the properties of the implemented hadrons is given in Appendix A.

Neither the leptons nor the electroweak gauge bosons (γ, $W^\pm$, Z^0) are explicitly propagated in the simulation, i.e., due to their small couplings it is assumed that they interact only once in the initial reaction (e.g., $\nu A \to \mu^- X$) or when they are produced (e.g., $\eta \to \gamma\gamma$) and that they leave the nucleus undisturbed afterwards. Gluons are also not propagated, but one may re-find them in so-called strings or pre-hadrons which carry information about gluonic excitations (for details cf. [66, 67]).

The following sections describe the potentials used in the drift term of the BUU equation, the initialization of the nuclear ground state and – in some detail – the collision terms.

3.1. Potentials

The l.h.s. of the transport equations eqs. (68), (71) and (85) describes the propagation of particles under the influence of mean-field potentials of hadronic and electromagnetic nature. The potentials determine the Hamilton function, H, for the off-shell-transport equations eqs. (68) and (85) or, for the quasi-particle approximation of eq. (71), the single-particle energy, E_p. In most implementations of BUU potentials are used only for nucleons, but there are a few investigations of in-medium corrections of hadronic self-energies [68], mainly for pions and kaons.

In GiBUU, for the nucleons the non-relativistic Skyrme-like and relativistic mean field (RMF) potentials are alternatively adopted in the quasi-particle approximation. The off-shell transport equation (85) is used with the Skyrme-like potentials only. In this section, we discuss the concrete form of the mean field potentials used in our model. The applicability of the Skyrme-like or RMF potentials depends on the physical situation under consideration.

We would like to note here, that the potentials do not only affect the particle propagation but also the collision term, e.g., via particle-production thresholds. The hadronic mean-field potentials are strong and quite sensitive to the local particle-density variations. Thus their influence on the collision integral via the energy-momentum conservation and threshold conditions in interparticle collisions is fully taken into account. However, the relatively weak and long-ranged Coulomb mean field potential does not vary much within the range of the strong interaction ~ 1 fm. Therefore, we assume that it does not affect particle reaction rates, i.e., we neglect it in the collision term.

3.1.1. Coulomb potential

We take into account the Coulomb force acting on the charged particles neglecting the Lorentz force as in our applications the latter is much smaller than the Coulomb force. In particular this holds true for hadron-induced reactions, where the bulk of the nuclear matter stays nearly at rest. Therefore, far away from the nucleus the incoming charged hadron propagates in an almost pure Coulomb field. In heavy-ion collisions, the current of charged particles, generally, exists in any frame. However, for low-energy heavy-ion collisions the Lorentz force is

suppressed with respect to the Coulomb force by a factor of $\sim (v_{\text{proj}}^{\text{cm}}/c)^2$, where $v_{\text{proj}}^{\text{cm}}$ is the projectile velocity in the center-of-mass frame of the system. For relativistic heavy-ion collisions, the Coulomb and Lorentz forces may become comparable in magnitude. But they both are of minor importance for the strongly violent dynamics of central collisions governed by inelastic production processes and the build-up of strong hadronic mean fields (see section 4.1.6).

The Coulomb potential for a given charge distribution, $\rho_c(\boldsymbol{r})$, is determined by the Poisson equation,

$$- \nabla^2 \Phi(\boldsymbol{r}) = 4\pi \rho_c(\boldsymbol{r}), \tag{103}$$

Numerically, this equation is solved using the alternating direction implicit iterative (ADI) method of Douglas [69]. The boundary conditions for the Coulomb potential are provided by the multipole expansion (cf. Appendix B of Ref. [70]).

3.1.2. Non-relativistic mean-field potentials

In the non-relativistic mean-field approach (cf. [71, 72, 73]) it is convenient to start with the energy-density functional,

$$\epsilon(x) = \int \frac{g \, \mathrm{d}^3 p}{(2\pi)^3} \sqrt{m^2 + \boldsymbol{p}^2} \left[f_n(x, \boldsymbol{p}) + f_p(x, \boldsymbol{p}) \right] + \epsilon_{\text{pot}}(x) \,, \tag{104}$$

where the first term represents the bare part of the total energy density and allows for relativistically correct kinematics, while the second term, ε_{pot}, is the potential part of the energy density. We apply the Skyrme-like potential-energy density of Welke $et\ al.$ [71], supplemented with a symmetry-energy term,

$$\begin{aligned}
\epsilon_{\text{pot}}(x) = {}& \frac{A}{2} \frac{\rho(x)^2}{\rho_0} + \frac{B}{\gamma + 1} \frac{\rho(x)^{\gamma+1}}{\rho_0^\gamma} + \frac{C}{\rho_0} \sum_{i=n,p} \sum_{j=n,p} \int \frac{g \mathrm{d}^3 p_1}{(2\pi)^3} \int \frac{g \mathrm{d}^3 p_2}{(2\pi)^3} \frac{f_i(x, \boldsymbol{p}_1) f_j(x, \boldsymbol{p}_2)}{1 + (\boldsymbol{p}_1 - \boldsymbol{p}_2)^2 / \Lambda^2} \\
& + d_{\text{symm}} \frac{(\rho_p(x) - \rho_n(x))^2}{2\rho_0} \,.
\end{aligned} \tag{105}$$

Here and in the following, $\rho_0 = 0.168\,\text{fm}^{-3}$ is the nuclear saturation density.

The single-particle Hamilton function, $H_i(x, \boldsymbol{p})$, $(i = n, p)$ — which governs the propagation of particles — is given by the functional derivative of the total energy, E, with respect to the phase-space occupation numbers,

$$\begin{aligned}
\delta E = {}& \sum_{i=n,p} \int \frac{g \mathrm{d}^3 r \mathrm{d}^3 p}{(2\pi)^3} H_i(x, \boldsymbol{p}) \, \delta f_i(x, \boldsymbol{p}) \,, \\
E = {}& \int \mathrm{d}^3 r \, \epsilon(x) \,.
\end{aligned} \tag{106}$$

Thus, we have

$$H_i(x, \boldsymbol{p}) = \sqrt{m^2 + \boldsymbol{p}^2} + U_i(x, \boldsymbol{p}) \tag{107}$$

with the single-particle potential,

$$U_i(x, \boldsymbol{p}) = U_N(x, \boldsymbol{p}) + d_{\text{symm}} \frac{\rho_p(x) - \rho_n(x)}{\rho_0} \tau_i^3 \,, \tag{108}$$

27

where $\tau_p^3 = 1$ and $\tau_n^3 = -1$. The isospin-averaged nucleon potential is

$$
\begin{aligned}
U_N(x, \boldsymbol{p}) &= \frac{U_n + U_p}{2} \\
&= A\frac{\rho(x)}{\rho_0} + B\left(\frac{\rho(x)}{\rho_0}\right)^\gamma + \frac{2C}{\rho_0}\sum_{i=n,p}\int\frac{g\,\mathrm{d}^3 p'}{(2\pi)^3}\frac{f_i(x, \boldsymbol{p}')}{1 + (\boldsymbol{p} - \boldsymbol{p}')^2/\Lambda^2}.
\end{aligned}
\tag{109}
$$

In order to reduce the computation time for calculating the momentum-dependent part of the potential eq. (109), we approximate the nucleon phase-space distribution by a Fermi distribution. This allows to evaluate the momentum integral on the r.h.s. of eq. (109) as an analytic function of $|\boldsymbol{p}|$ and of the local baryon density (see Ref. [71] for details). The six free parameters, A, B, γ, C, Λ, and d_{symm}, of the nucleon potential eq. (108), are determined from the following conditions:

- The momentum-dependent interaction should describe the phenomenological real part of a proton-nucleus optical potential and also governs the Landau effective mass at the Fermi surface (cf. [11, 74] and refs. therein) [8]

$$
(m_N^*)^{-1} = m_N^{-1} + (p_F^{(0)})^{-1}\left(\frac{\partial U_N}{\partial p}\right)_{p=p_F^{(0)}},
\tag{110}
$$

which should lie in the range $0.6\,m_N \le m_N^* \le m_N$. These conditions constrain the stiffness, C, and the range, Λ.

- The energy per nucleon in isospin-symmetric nuclear matter has a minimum at $\rho = \rho_0$ and a value of $-16\,\mathrm{MeV}$ at the minimum,

$$
\frac{\partial\epsilon(\rho, I)/\rho}{\partial\rho}\bigg|_{\rho=\rho_0,\,I=0} = 0, \quad \frac{\epsilon(\rho, I)}{\rho}\bigg|_{\rho=\rho_0,\,I=0} = -16\,\mathrm{MeV},
\tag{111}
$$

where $I \equiv (\rho_n - \rho_p)/\rho$ denotes the isospin asymmetry, and

$$
\epsilon(\rho, I) = \frac{3}{10m_N}(p_{F,n}^2\rho_n + p_{F,p}^2\rho_p) + \epsilon_{\mathrm{pot}}(\rho, I)
\tag{112}
$$

is the energy density with the Fermi momenta, $p_{F,i} = (3\pi^2\rho_i)^{1/3}$, $(i = n, p)$.

- The nuclear-matter incompressibility,

$$
K = 9\rho_0^2\,\frac{\partial^2\epsilon(\rho, I)/\rho}{\partial\rho^2}\bigg|_{\rho=\rho_0, I=0},
\tag{113}
$$

is fitted to be in the range $K = 200\text{-}380\,\mathrm{MeV}$.

---

[8]The Landau effective mass at the Fermi surface and the Dirac effective mass of the nucleon are related by $m_{\mathrm{Landau}}^{*2} = p_F^2 + m_{\mathrm{Dirac}}^{*2}$. However, to avoid complicated notations, we denote both masses simply as m^* or m_N^*. If not stated otherwise, the Dirac effective mass is used in this work.

Label	K (MeV)	m_N^*/m_N	A (MeV)	B (MeV)	C (MeV)	γ	Λ (fm^{-1})
SM	215	0.68	-108.6	136.8	-63.6	1.26	2.13
HM	380	0.68	-10.0	38.0	-63.6	2.40	2.13
S	215	1.00	-287.0	233.7	0.0	1.23	-
H	380	1.00	-124.3	71.0	0.0	2.00	-
MM	290	0.68	-29.3	57.2	-63.6	1.76	2.13

Table 1: Parameter sets for the non-relativistic mean-field potential eq. (108). The meaning of the potential labels is as follows: the first, S (soft), H (hard) or M (medium) characterizes the incompressibility modulus, K, and the second, M, if present, indicates the inclusion of the momentum-dependent part (the third term in the r.h.s. of eq. (108)) in the potential.

- The potential symmetry-energy coefficient, d_{symm}, is chosen to reproduce the parameter of the symmetry energy, $a_{symm} = 28$ MeV, in the Bethe-Weizsäcker-mass formula using the Migdal relation for symmetric nuclear matter,

$$a_{symm} = \frac{p_F^2}{6m_N} + \frac{d_{symm}}{2} \, , \tag{114}$$

which leads to $d_{symm} \simeq 30$ MeV.

Several parameter sets of the nucleon potential eq. (108) are collected in table 1.

In a similar way, the single-particle Hamilton functions of other baryons are calculated, except that for them the symmetry-energy terms are dropped. The potentials of the Δ-resonances are rescaled by $U_\Delta = 2U_N/3$ [75, 76]. The potentials of N^*-resonances are set equal to the nucleon one, i.e., $U_{N^*} = U_N$. The potentials of the $S = -1$ baryons are taken as $U_Y = U_{Y^*} = 2U_N/3$, according to a simple light-constituent-quark counting picture. At least, for the Λ-hyperon, this results in the correct potential depths. However, the empirical Σ-nucleus optical potential is strongly repulsive at normal nuclear density, which is currently a quest for microscopic theoretical models (cf. Ref. [77] and references therein). The potentials of the $S < -1$ and $C \neq 0$ baryons are neglected, since the empirical information on them is either absent or quite scarce.

In order to avoid problems with Lorentz invariance, it is very important to choose the frame, where the mean-field potentials should be calculated. For this purpose, we have chosen the local rest frame (LRF) of the nuclear medium, where the spatial components of the baryon four-current, $j^\mu = (j^0, \boldsymbol{j})$, vanish, i.e., $\boldsymbol{j} = 0$ at the space position of the particle under consideration. This choice is only possible if the antibaryons — contributing with negative sign to the baryon four-current (cf. eq. (134) below) — are not abundant. In hadron-, photon-, and lepton-induced reactions, the Hamiltonian propagation of particles is performed in the target rest frame (computational frame), which practically coincides with the LRF, since the collective motion of nuclear matter is negligible. However, even then, conserving energy in particle-particle collisions requires the determination of the potentials in the center-of-mass (c.m.) frame of the colliding particles, where the momenta of the final-state particles are chosen.

The situation becomes even more complex in the case of heavy-ion collisions, where the nuclear matter develops a space-time dependent collective-flow field. Already before the collision, due to the Lorentz-contraction[9], the baryon density inside nuclei is increased by a γ-factor.

---

[9]In the case of heavy-ion collisions, the computational frame is usually chosen as the center-of-mass frame of the colliding nuclei.

Therefore, in order to be able to apply the potential eq. (108), defined in the LRF only, one first has to perform a Lorentz transformation of the particle four-momentum to the LRF. This Lorentz transformation is not trivial since it mixes the spatial components, p, with the time component, p^0, of the particle's four-momentum. The latter, however, is not directly known since the potential is defined only in the LRF.

By using the Lorentz invariance of the quantity $E^2 - p^2$ we obtain the following equation for the determination of the particle energy E at the given momentum p:

$$E^2 - p^2 = \left(\sqrt{m^2 + p_{\mathrm{LRF}}^2} + U_i(x, p_{\mathrm{LRF}}) \right)^2 - p_{\mathrm{LRF}}^2 \,. \tag{115}$$

Here, the three-momentum in the LRF, p_{LRF}, is determined by the Lorentz boost as

$$p_{\mathrm{LRF}} = p + \gamma_{\mathrm{LRF}} \beta_{\mathrm{LRF}} \left(\frac{\gamma_{\mathrm{LRF}}}{\gamma_{\mathrm{LRF}} + 1} (\beta_{\mathrm{LRF}} \cdot p) - E \right) \,, \tag{116}$$

with $\gamma_{\mathrm{LRF}} = 1/\sqrt{1 - \beta_{\mathrm{LRF}}^2}$ and $\beta_{\mathrm{LRF}} = j_b/j_b^0$, where $j_b^\mu(x)$ is the local baryonic four-current

$$j_b(x) = \int \frac{\mathrm{d}^4 p}{(2\pi)^4} (1, \nabla_p H(x, p)) F(x, p) \,, \tag{117}$$

where $F(x, p)$ is the Wigner density of eq. (89). One observes, that in any other frame than the local rest frame the potential gets an explicit E-dependence. In the actual GiBUU implementation, we first try to find a solution of eq. (115) for the energy, E, by a Newton root-finding algorithm. If this fails, we switch to a bisection algorithm.

For the single-particle Hamiltonian, $H(x, p)$, on the l.h.s. of the transport equation (85), i.e., for the Vlasov term, the Coulomb potential of eq. (103) is added to the energy, E, calculated from eq. (115). Thus, $H(x, p) = E + e(1 + \tau^3)\Phi/2$. For the particles produced in a given elementary collision or resonance decay, the Coulomb part is directly included in eq. (115) by adding it to U_i.

3.1.3. Relativistic mean-field potentials

Another type of baryonic potentials is provided by a Relativistic Mean Field (RMF) model Lagrangian density [16, 78, 79, 80]

$$\begin{aligned}
\mathcal{L} =& \bar{\psi}[\gamma_\mu(i\partial^\mu - g_\omega\omega^\mu - g_\rho\tau\rho^\mu - \frac{e}{2}(1 + \tau^3)A^\mu) - m_N - g_\sigma\sigma]\psi \\
&+ \frac{1}{2}\partial_\mu\sigma\partial^\mu\sigma - U(\sigma) - \frac{1}{4}\Omega_{\mu\nu}\Omega^{\mu\nu} + \frac{1}{2}m_\omega^2\omega^2 \\
&- \frac{1}{4}R_{\mu\nu}R^{\mu\nu} + \frac{1}{2}m_\rho^2\rho^2 - \frac{1}{16\pi}F_{\mu\nu}F^{\mu\nu} \,,
\end{aligned} \tag{118}$$

where ψ is the nucleon field; σ, ω^μ and ρ^μ are the isoscalar-scalar ($I^G = 0^+$, $J^\pi = 0^+$), isoscalar-vector ($I^G = 0^-$, $J^\pi = 1^-$) and isovector-vector ($I^G = 1^+$, $J^\pi = 1^-$) meson fields, respectively; A^μ is the electromagnetic field. The field-strength four-tensors in eq. (118) are defined by

$$\Omega_{\mu\nu} = \partial_\mu\omega_\nu - \partial_\nu\omega_\mu \,, \tag{119}$$

$$R_{\mu\nu} = \partial_\mu\rho_\nu - \partial_\nu\rho_\mu \,, \tag{120}$$

$$F_{\mu\nu} = \partial_\mu A_\nu - \partial_\nu A_\mu \,. \tag{121}$$

Label	K (MeV)	m_N^*/m_N	g_σ	g_ω	g_ρ	g_2 (MeV)	g_3	m_σ (MeV)
NL2	210	0.83	8.5	7.54	0.0	-50.37	6.26	508.2
NL3	272	0.60	10.217	12.868	4.474	-10.431	-28.885	550.5

Table 2: Parameter sets for the RMF models commonly used and their saturation properties in terms of the compression modulus K in units of MeV and the effective mass m_N^* in units of the bare nucleon mass m_N.

The term,

$$U(\sigma) = \frac{1}{2}m_\sigma^2\sigma^2 + \frac{1}{3}g_2\sigma^3 + \frac{1}{4}g_3\sigma^4,\tag{122}$$

denotes the self-interactions of the σ-field.

The meson-nucleon coupling constants, g_σ, g_ω, and g_ρ, the meson mass m_σ, and the self-interaction coefficients, g_2 and g_3, are taken from the non-linear (NL) Walecka-model-parameter sets NL2 of Ref. [16] and NL3 of Ref. [78]) and are listed in table 2. The meson masses m_ω and m_ρ are fixed to the values 783 MeV and 763 MeV, respectively for both parameterizations. The NL2 parameterization is more appropriate to describe heavy-ion collision dynamics, while NL3 is mostly tuned to the ground-state properties of nuclei.

The Lagrange equations of motion for the mean fields read

$$[\gamma_\mu(i\partial^\mu - g_\omega\omega^\mu - g_\rho\boldsymbol{\tau}\boldsymbol{\rho}^\mu - \frac{e}{2}(1 + \tau^3)A^\mu) - m_N - g_\sigma\sigma]\psi = 0\,,\tag{123}$$

$$\partial_\mu\partial^\mu\sigma + \frac{\partial U(\sigma)}{\partial\sigma} = -g_\sigma\rho_S\,,\tag{124}$$

$$(\partial_\mu\partial^\mu + m_\omega^2)\omega^\nu = g_\omega j_b^\nu\,,\tag{125}$$

$$(\partial_\mu\partial^\mu + m_\rho^2)\boldsymbol{\rho}^\nu = g_\rho\boldsymbol{j}_I^\nu\,,\tag{126}$$

$$\partial_\mu\partial^\mu A^\nu = 4\pi e j_c^\nu\,.\tag{127}$$

The source terms on the r.h.s. of the meson-field equations eqs. (124)–(127) are the scalar density, $\rho_S = \langle\overline{\psi}\psi\rangle$, the baryon current, $j_b^\nu = \langle\overline{\psi}\gamma^\nu\psi\rangle$, the isospin current, $\boldsymbol{j}_I^\nu = \langle\overline{\psi}\gamma^\nu\boldsymbol{\tau}\psi\rangle$, and the electromagnetic current, $j_c^\nu = \frac{1}{2}(j_b^\nu + j_I^{3\,\nu})$. Here, $\langle\cdots\rangle$ denotes the expectation value, and the meson fields in eqs. (124)–(127) are treated classically. We will neglect the isospin-mixed nucleon states, which results in the conditions, $j_I^{1\,\nu} = j_I^{2\,\nu} = 0$ and $\rho^{1\,\nu} = \rho^{2\,\nu} = 0$.

The dispersion relation for a nucleon quasiparticle is obtained from the plane-wave solution of the Dirac equation (123), $\psi \propto \exp(-ipx)$,

$$(p^*)^2 - (m^*)^2 = 0\,,\tag{128}$$

where $p^* = p - V$ is the kinetic four-momentum, and $m^* = m_N + S$ is the effective mass. The vector and scalar fields are given by

$$V = g_\omega\omega + g_\rho\tau^3\rho^3 + \frac{e}{2}(1 + \tau^3)A\,,\tag{129}$$

$$S = g_\sigma\sigma\,.\tag{130}$$

The dispersion relation eq. (128) can be rewritten as

$$p^0 = \pm\sqrt{(m^*)^2 + (\boldsymbol{p} - \boldsymbol{V})^2} + V^0\,.\tag{131}$$

The nucleon is described by the positive-frequency solution (upper sign in eq. (131)). Since we treat antinucleons as a separate particle species they are also described by the positive sign in eq. (131). However, the sign of the vector potential they experience is opposite to that felt by nucleons as can be seen by using the G-parity transformation of the nucleon potentials [81] [10]. Thus, the antinucleon dispersion relation reads

$$p^0 = \sqrt{(m^*)^2 + (\boldsymbol{p} + \boldsymbol{V})^2} - V^0 \, . \tag{132}$$

The source terms in the meson-field equations eqs. (124)–(127) are expressed in terms of the on-shell particle distribution functions, $f_i(x, \boldsymbol{p})$ (cf. eq. (71)), by

$$\rho_S = \frac{g}{(2\pi)^3} \sum_{i=p,n,\bar{p},\bar{n}} \int \frac{\mathrm{d}^3 p}{p_i^{*0}} m^* f_i(x, \boldsymbol{p}) \, , \tag{133}$$

$$j_b^\mu = \frac{g}{(2\pi)^3} \int \mathrm{d}^3 p \left(\sum_{i=p,n} \frac{p_i^{*\mu}}{p_i^{*0}} f_i(x, \boldsymbol{p}) - \sum_{i=\bar{p},\bar{n}} \frac{p_i^{*\mu}}{p_i^{*0}} f_i(x, \boldsymbol{p}) \right) \, , \tag{134}$$

$$j_I^{3\mu} = \frac{g}{(2\pi)^3} \sum_{i=p,n,\bar{p},\bar{n}} \int \frac{\mathrm{d}^3 p}{p_i^{*0}} p_i^{*\mu} \tau_i^3 f_i(x, \boldsymbol{p}) \, , \tag{135}$$

The kinetic four-momentum is $p_i^* = p_i - V$ for $i = p, n$ and $p_i^* = p_i + V$ for $i = \bar{p}, \bar{n}$, where $p_i = (p_i^0, \boldsymbol{p})$. Here, p_i^0 is the single-particle Hamilton function dependent on the particle species and its isospin projection. For completeness, we will also quote a useful formula for the canonical energy momentum tensor (cf. Ref. [82, 83, 16]), $T^{\mu\nu}$, satisfying the continuity equation, $\partial_\nu T^{\mu\nu} = 0$:

$$\begin{aligned}
T^{\mu\nu} = {} & \frac{g}{(2\pi)^3} \sum_{i=p,n,\bar{p},\bar{n}} \int \frac{\mathrm{d}^3 p}{p_i^{*0}} p_i^{*\nu} p_i^\mu f_i(x, \boldsymbol{p}) \\
& + \partial^\mu \sigma \partial^\nu \sigma - \partial^\mu \omega^\lambda \partial^\nu \omega_\lambda - \partial^\mu \rho^{3\,\lambda} \partial^\nu \rho_\lambda^3 - \partial^\mu A^\lambda \partial^\nu A_\lambda \\
& - g^{\mu\nu} \left(\frac{1}{2} \partial_\lambda \sigma \partial^\lambda \sigma - U(\sigma) - \frac{1}{2} \partial_\lambda \omega_\kappa \partial^\lambda \omega^\kappa + \frac{1}{2} m_\omega^2 \omega^2 \right. \\
& \left. - \frac{1}{2} \partial_\lambda \rho_\kappa^3 \partial^\lambda \rho^{3,\kappa} + \frac{1}{2} m_\rho^2 (\rho^3)^2 - \frac{1}{2} \partial_\lambda A_\kappa \partial^\lambda A^\kappa \right) \, .
\end{aligned} \tag{136}$$

In practice, eq. (136) is used to extract the equation of state of the nuclear matter (cf. fig. 2). It is also useful for the analysis of the collective velocity profiles [84] and the approach of thermodynamical equilibrium of collective nuclear motions.

As a technical approximation, time derivatives of the meson fields are neglected in eqs. (124)–(127), while spatial derivatives are kept. The resulting equations are solved on the spatial grid by using the alternating direction implicit iterative (ADI) method of Douglas [69]. Neglecting the time derivatives also leads to some modifications in the expression for the conserved energy-momentum tensor, $T^{\mu\nu}$ (see Ref. [84] for details). The spatial components of the electromagnetic potential, A^μ, are also neglected. Thus, in fact, the Maxwell equation (127) is reduced to the Poisson equation (103) with $\Phi \equiv A^0$ and $\rho_c \equiv e j_c^0$.

---

[10]In the antiproton-nucleus reaction simulations (see section 4.1.3), we allow for the deviations from the exact G-parity symmetry for the sake of a realistic value of an antiproton optical potential.
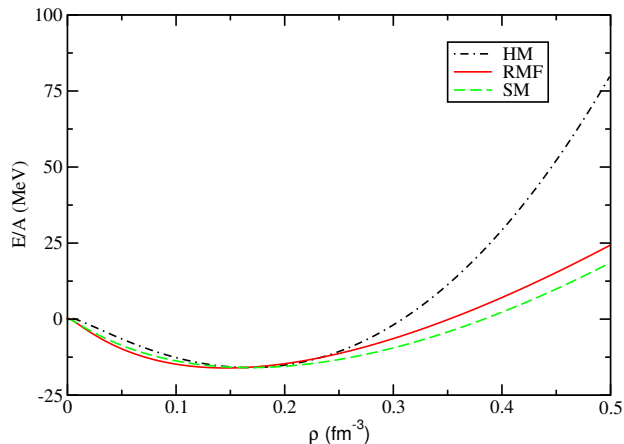
Figure 2: (Color online) Binding energy per nucleon, E/A, as function of the baryon density, ρ, for different mean-field parametrizations used in the GiBUU model: (SM) non-relativistic soft momentum-dependent Skyrme, (HM) non-relativistic hard momentum-dependent Skyrme, (RMF) non-linear Walecka model (NL2 set, [16]).

Let us briefly discuss the applicability of these approximations. A thorough consideration can be found in Refs. [85, 16, 86] (see also discussion in section 3.1.1 on the applicability of the Poisson equation). In fact, including the space and time derivatives of mesonic fields would lead to small-amplitude oscillations of these fields with a frequency $\omega = \sqrt{m^2 + \boldsymbol{k}^2}$, where m is the meson mass and $\boldsymbol{k}$ is the wave number of a field perturbation. If the process under consideration is slow with respect to the period of these oscillations, $2\pi/\omega \simeq 2.5(1.5)\,\mathrm{fm}/c$ for σ-(ω-)field in the long-wave limit $k = 0$, one can approximately average-out the time derivatives of the mesonic fields. The well known examples of such slow processes are the nuclear giant resonance vibrations or heavy-ion collisions at low and intermediate energies (below $E_{\mathrm{lab}} \simeq 1\,A\mathrm{GeV}$). The classical meson field radiation and retardation effects are disregarded in the local density approximation, when all derivatives of the mesonic fields are neglected in the meson field equations. On the other hand, in heavy-ion collisions at relativistic energies, i.e., above $E_{\mathrm{lab}} \simeq 5\,A\mathrm{GeV}$, the radiation and retardation effects might be significant [85, 16]. In the low-energy nuclear dynamics, the surface effects are important for the stability of the ground state nuclei. Including the space derivatives of the meson fields largely improves the description of a nuclear surface and, therefore, the nuclear ground state stability (see Ref. [86] and section 3.2).

3.1.4. Comparison of the non-relativistic and relativistic mean-field potentials

The key quantities, which influence the dynamical evolution in heavy-ion collisions at incident energies up to several GeV per nucleon, are the equation of state (EoS) and the optical potential. The study of the nuclear EoS has a long history. It has been pioneered by the work of Scheid, Ligensa and Greiner [88], where the compressibility of nuclear matter has been extracted from light-ion scattering data. Later, the extensive studies of different theory groups (cf. Ref. [7, 16, 71, 11, 74, 13, 89, 90, 91, 92, 93, 94, 95, 96, 97, 98, 99]) have been performed to pin down the nuclear EoS from comparison of microscopic transport simulations with experimental data on collective flow and particle production. Taking into account the realistic momentum dependence of the proton-nucleus optical potential, this resulted in values of $K \simeq 200\text{-}270\,\mathrm{MeV}$, i.e., in a relatively soft EoS. This range agrees with model analyses of data
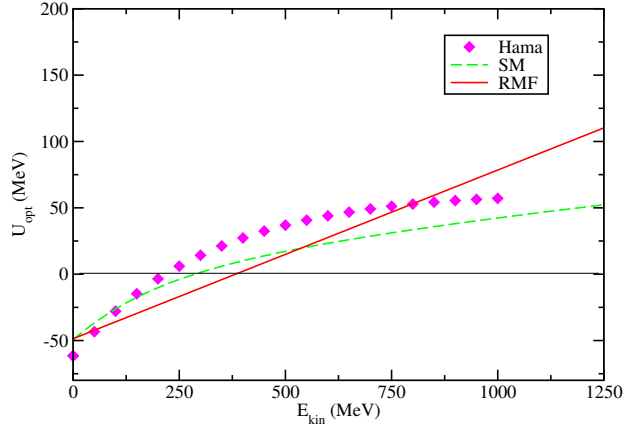
Figure 3: (Color online) Kinetic-energy dependence of the Schrödinger-equivalent optical potential for the Skyrme-like interaction (SM) and for the NL2 parameter set of the non-linear Walecka model (RMF) for baryon densities at saturation. These potentials are compared with the results of Dirac phenomenology [87].

on the giant monopole resonance in heavy nuclei [100, 101] (see also Ref. [86] and refs. therein).

The EoS of nuclear matter is defined by the density dependence of the energy per nucleon subtracting the nucleon mass. In the non-relativistic mean-field model, the EoS is calculated using eq. (112), as $E/A = \epsilon(\rho, I = 0)/\rho$. In the RMF approach the EoS is determined through the 00-component of the energy-momentum tensor, $T^{\mu\nu}$ (see eq. (136)): $E/A = T^{00}/\rho$.

For a comparison of the energy dependence between the various mean-field models (Skyrme-like and RMF) we use the Schrödinger-equivalent (SE) optical potential. For the case of the in-medium interaction of a nucleon with nuclear matter at rest the SE optical potential is derived from the in-medium dispersion relation [102]. In the RMF case, the in-medium dispersion relation reads $(E - V^0)^2 - \boldsymbol{p}^2 = (m_N + S)^2$, where the vector ($V$) and scalar ($S$) fields are given by eqs. (129) and (130), respectively. Here, E denotes the energy of a nucleon in the rest frame of the nuclear matter at a given baryon density, ρ. In the Skyrme-like potential model, the dispersion relation takes the form $(E - U_N)^2 - \boldsymbol{p}^2 = m_N^2$, where U_N denotes the isospin-averaged nucleon potential of eq. (109).

From these dispersion relations one then obtains the in-medium single-particle energy, E, of a nucleon as a function of its momentum, $\boldsymbol{p}$. Using energy conservation, i.e., setting the in-medium single-particle energy, E, equal to the asymptotic free energy, one arrives at the well known form for the SE optical potential [102], which in the RMF case reads

$$U_{\text{opt}} = \frac{E}{m_N} V^0 + S + \frac{1}{2m_N} \left[S^2 - (V^0)^2 \right] . \tag{137}$$

In the non-relativistic case, one obtains a similar equation as in eq. (137) with $S = 0$ and $V^0 = U_N$.

Figures 2 and 3 show the EoS and the kinetic-energy, dependence ($E_{\text{kin}} = E - m_N$) of the optical potential for typical parametrizations commonly adopted in the calculations, shown later on. The EoS in the SM and RMF parametrizations show a rather soft behavior at high densities. For comparison, a hard EoS (HM) is shown too. A soft density dependence is required for a reliable description of collective baryon flows and kaon abundances at SIS/GSI energies (cf. [103, 97]).

34

Also the energy dependence of the nuclear mean field is crucial for a consistent characterization of collective in-plane and out-of-plane transverse flow of matter at energies around 0.1-1 GeV per nucleon.

The non-relativistic Skyrme model predicts a saturation of the optical potential with increasing nucleon energy, which is consistent with the empirical Dirac phenomenology [87]. This originates from an explicit momentum dependence of the non-relativistic single-particle Skyrme potential, which is not present in the relativistic version. In fact, in the latter case the RMF potential rises linearly with energy. At the energies in the SIS/GSI regime, i.e., $E_{\text{lab}} \simeq 1\,A\text{GeV}$, the comparison of the Schrödinger-equivalent potential of the RMF model with the empirical data [87] is quite satisfactory. However, at higher beam energies the linear rise of the potential leads to a strong repulsion, which seems to be unphysical and limits the applicability of this simple version of the RMF model to situations where the relative motion of the components of the nuclear system is not very fast. One example of such situations is the thermalized stage of heavy-ion collisions. Due to a rather fast equilibration in momentum space the overlap region of colliding nuclei thermalizes quickly. Thus, we expect that, except for the relatively short nonequilibrium stage when the two nuclei penetrate each other, the RMF model describes the time evolution of the strongly compressed and heated nuclear system quite reliably.

3.1.5. Transport equations in the RMF model

In the case of momentum-independent fields in the spirit of a Relativistic Mean-Field (RMF) model with a scalar field, $S(x)$, and a vector field, $V^\mu(x)$, it is convenient to use the distribution function, $f^*(x, \boldsymbol{p}^*)$, in the kinetic phase space $(\boldsymbol{r}, \boldsymbol{p}^*)$. The kinetic (or effective) four-momentum $p^{*\mu}$ and the effective mass are defined, respectively, as (cf. eqs. (41) and (42))

$$p^{*\mu} = p^\mu - V^\mu \,. \tag{138}$$

and

$$m^* = m + S \,, \tag{139}$$

so that $p^{*2} = (m^*)^2$ (in-medium on-shell condition). Now, $p^0 = \sqrt{(m^*)^2 + (\boldsymbol{p}^*)^2} + V^0$ plays the role of a single-particle Hamilton function, i.e., $E_{\boldsymbol{p}} \equiv p^0$ in eq. (71).

The normalization of the distribution function, $f^*(x, \boldsymbol{p}^*)$, is such that

$$f^*(x, \boldsymbol{p}^*) \frac{g \, \mathrm{d}^3 r \, \mathrm{d}^3 p^*}{(2\pi)^3}$$

is the number of particles in a kinetic phase-space element, $\mathrm{d}^3\boldsymbol{r}\,\mathrm{d}^3\boldsymbol{p}^*$. Here, g denotes the spin-degeneracy factor. Since the Jacobian of the transformation, $(\boldsymbol{r}, \boldsymbol{p}) \to (\boldsymbol{r}, \boldsymbol{p}^*)$, fulfills

$$\det |\partial(\boldsymbol{r}, \boldsymbol{p}^*)/\partial(\boldsymbol{r}, \boldsymbol{p})| = 1 \quad,$$

we obtain $f^*(x, \boldsymbol{p}^*) = f(x, \boldsymbol{p})$. With this transformation of variables, eq. (71) can be expressed as (cf. Refs. [16, 79])

$$(p^{*0})^{-1} \left[p^{*\mu} \partial_\mu - (p^*_\mu \mathcal{F}^{\mu\alpha} - m^* \partial^\alpha m^*) \frac{\partial}{\partial p^{*\alpha}} \right] f^*(x, \boldsymbol{p}^*) = C(x, p) \,, \tag{140}$$

where $\alpha = 1, 2, 3$, $\mu = 1, 2, 3, 4$, and $\mathcal{F}^{\mu\nu} \equiv \partial^\mu V^\nu - \partial^\nu V^\mu$.

For momentum-independent scalar and vector fields, eq. (140) is solved by representing the distribution function, f^*, in terms of test particles, i.e., setting

$$f^*(x, \boldsymbol{p}^*) = \frac{(2\pi)^3}{gN} \sum_{j=1}^{n(t)} \delta^{(3)}[\boldsymbol{r} - \boldsymbol{r}_j(t)] \delta^{(3)}[\boldsymbol{p}^* - \boldsymbol{p}_j^*(t)] \,. \tag{141}$$

This test-particle representation is similar to that of the more general off-shell potential ansatz, eq. (89), except that the energy delta function, $\delta(p^0 - p_j^0)$, is integrated-out. This is because — in the RMF mode — we restrict ourselves to the quasi-particle limit.

The respective equations of motion for the centroids, $\boldsymbol{r}_j$, and kinetic momenta, $\boldsymbol{p}_j^*$, are obtained by substituting eq. (141) into eq. (140) and setting $C(x, p) = 0$, which leads to

$$\dot{\boldsymbol{r}}_j = \frac{\boldsymbol{p}_j^*}{p_j^{*0}} \,, \tag{142}$$

$$\dot{p}_j^{*\alpha} = -(p_j^{*0})^{-1}(p_{j\mu}^* \mathcal{F}^{\mu\alpha} - m^* \partial^\alpha m^*) \,, \tag{143}$$

where $p_j^{*0} = \sqrt{(m^*)^2 + (\boldsymbol{p}_j^*)^2}$, and $\alpha = 1, 2, 3$.

3.2. Nuclear ground state

The BUU equation (71) is a first-order differential equation in time. Thus, to solve this equation, the phase-space distributions of all particle species need to be known at the initial time $t = 0 \, \text{fm}/c$, in particular, the initial distribution of the nucleons within the nucleus (nuclear ground state). As discussed in the previous section, the BUU equation is treated numerically within the test-particle method, where the phase-space distribution is discretized by a finite number of test particles, see eqs. (89) and (141) for the non-relativistic and relativistic cases, respectively. This method leads to Hamilton equations of motion for the test particles, eqs. (90)–(92), (142) and (143), again for the non-relativistic and relativistic cases. In the spirit of the test-particle ansatz one has to initialize the test particles for a nucleus at the initial time. Empirical density distributions are usually adopted to initialize ground-state nuclei in transport-theoretical simulations, which might not always be consistent with the energy-density functional used for the propagation of the system. However, in some particular cases, e.g., low-energy hadron-induced reaction and fragmentation studies, a very good stability of the ground-state configurations is required, which is difficult to reach within the test-particle technique, underlying any numerical method to solve the BUU equation. Another well known problem is related to the numerical treatment of Pauli-blocking factors in the Uehling-Uhlenbeck collision integral. In this Chapter, first we give an outline of the standard-initialization procedure of nuclear ground states, before model extensions and results are presented.

3.2.1. Standard phase-space initialization

In order to prepare the phase-space density of the nuclear ground state, the coordinates of neutrons and protons are sampled according to empirical density profiles of Woods-Saxon or harmonic oscillator [104] type, for heavy or light nuclei, like ^{197}Au and ^{56}Ni or ^{12}C and ^{16}O, respectively.

The particle momenta are distributed according to a local Thomas-Fermi (LTF) approximation,

$$f_{n,p}(\boldsymbol{r}, \boldsymbol{p}) = \Theta\left[p_{F,n,p}(\boldsymbol{r}) - |\boldsymbol{p}|\right], \tag{144}$$

where the momentum distribution is given by an isotropic Fermi sphere at each point in space with the radius in momentum space determined by the local Fermi momentum,

$$p_{F,n,p}(\boldsymbol{r}) = [3\pi^2 \rho_{n,p}(\boldsymbol{r})]^{1/3}. \tag{145}$$

The normalization is chosen such that the proton and neutron densities — which serve as an input — are retrieved by

$$\rho_{n,p}(\boldsymbol{r}) = g \int f_{n,p}(\boldsymbol{r}, \boldsymbol{p}) \frac{\mathrm{d}^3 p}{(2\pi)^3}. \tag{146}$$

The single-particle phase-space densities, $f_{n,p}(\boldsymbol{r}, \boldsymbol{p})$, are then fully determined, and the momentum densities read

$$n_{n,p}(\boldsymbol{p}) = g \int f_{n,p}(\boldsymbol{r}, \boldsymbol{p}) \frac{\mathrm{d}^3 r}{(2\pi)^3} \tag{147}$$

with the normalization conditions, $\int \mathrm{d}^3 p \, n_p(\boldsymbol{p}) = Z$ and $\int \mathrm{d}^3 p \, n_n(\boldsymbol{p}) = A - Z$.

This standard method provides us with the full phase-space information at the initial time, before starting the propagation according to the Hamilton equations of motion. Smooth distributions in coordinate and momentum space are achieved by using $\sim 10^3$ test particles per nucleon, which is an important issue for the numerical treatment of mean-field gradients in the Hamilton equations of motion, for details see Appendix D.1. The smoothness of the test particle distribution in phase space is also important for numerical evaluation of the Pauli-blocking factors, $(1 - f_{n,p}(\boldsymbol{r}, \boldsymbol{p}))$, which enter the collision term of the BUU equation (see discussion related to fig. 7 and Appendix D.4.3).

In fig. 4 we show the proton density and the Fermi momentum together with the proton mean-field potential eq. (108) and the resulting Fermi energy

$$E_{F,p} = \sqrt{p_{F,p}^2 + m_N^2} + U_p(\boldsymbol{r}, p_F) \tag{148}$$

for ^{12}C, ^{16}O and ^{56}Fe as a function of the radius at the initial time $t = 0 \, \mathrm{fm}/c$. It is seen in fig. 4 that the Fermi energy varies rather strongly towards the nuclear surface and becomes very small there. This leads to problems with nuclear stability, which are addressed in the next section, where an improved initialization method is presented. A similar scheme in the non-relativistic case has been discussed in [105].

3.2.2. Improved phase-space initialization and ground-state stability

We address the problem of the ground-state stability, which is discussed in detail in Section 3.2 of Ref. [60] and in Ref. [105]. The empirical density distributions do not coincide with the ground-state density distribution corresponding to the static solution of the Vlasov equation with a local mean field potential in coordinate space. The assumed locality of the nucleon potential eq. (108) requires the ground state to be a perfect sphere of a constant density ρ_0. This discrepancy leads to oscillations of the root-mean-square radius in time (cf. e.g. Figs. 3.2 and 3.6 in [60]). It has been shown in Ref. [60] that the influence on observables in photon-induced reactions is only minor. Nevertheless, we circumvent this problem by working in the so-called "frozen" approximation, i.e., the test particles which define the initial particle distribution of the nucleus (the so-called "real particles") are not propagated and are not allowed to undergo any collisions — they are frozen. Thus, by definition, we obtain a stable ground state. This treatment is justified by the fact that in photon- and lepton-induced reactions at around 1 GeV beam energy
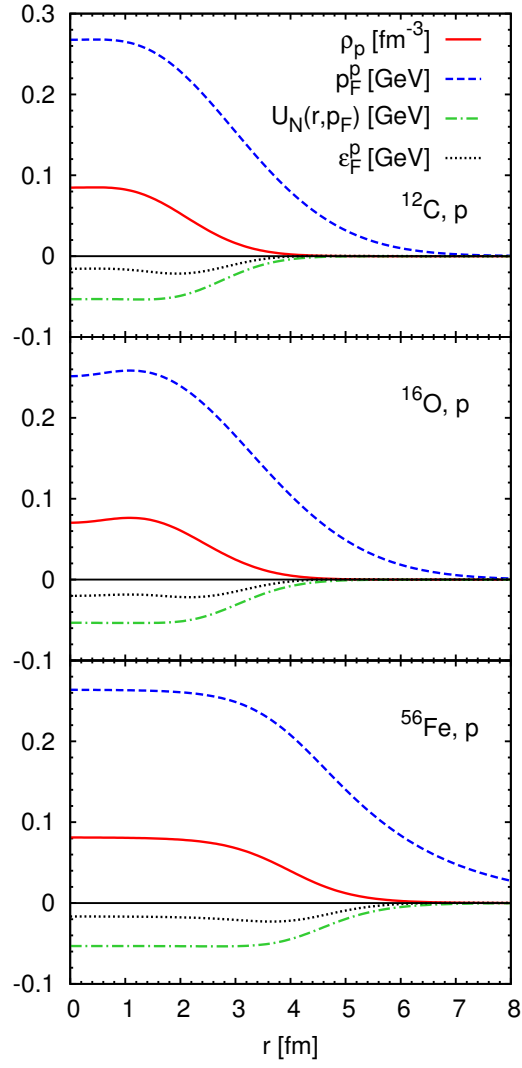
Figure 4: (Color online) The proton density, Fermi momentum, mean-field potential and Fermi energy subtracting the nucleon mass for ^{12}C, ^{16}O and ^{56}Fe as a function of radius.
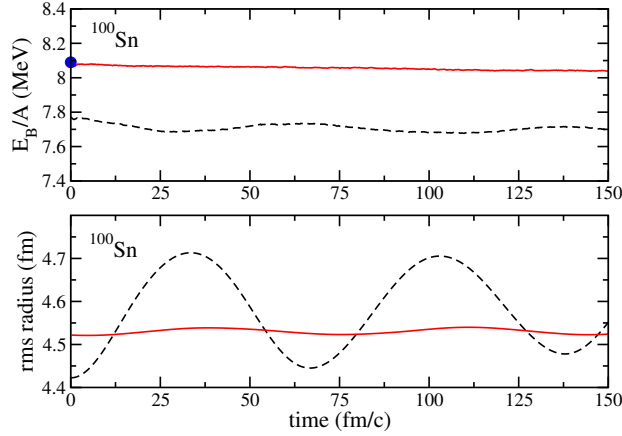
Figure 5: (Color online) Time evolution of the binding energy per nucleon (panel on the top) and root-mean square (rms) radius (panel on the bottom) for a ground state ^{100}Sn nucleus. Vlasov calculations, using the (dashed) standard initialization and the (solid) improved initialization, are shown. The filled circle in the top panel at $t = 0\,\mathrm{fm}/c$ gives the RTF-value of the binding energy. Taken from [86].

the nucleus stays close to its ground state, which means that its phase-space density stays almost constant during the simulation. Only the reaction products of the lepton-nucleon reactions are propagated and undergo final-state interactions. These test particles and also their reaction products are called "perturbative particles", and they do not affect the nucleus phase-space density (see Appendix D.2 for details).

The "frozen" approximation is not applicable to hadron-induced reactions and heavy-ion collisions at intermediate relativistic energies. Thus, a good stability of ground-state nuclei has to be achieved, in particular, when studying reactions with hadron and heavy-ion beams at low incident energies. We thus have improved the relativistic transport approach within GiBUU by performing Thomas-Fermi calculations with the same energy-density functional as that used in the dynamical evolution. The relativistic Thomas-Fermi (RTF) equations for a static nucleus with Z protons, N neutrons, i.e., $A = N + Z$ nucleons, are obtained by applying a variational principle to the total energy, $E = \int \mathrm{d}^3\boldsymbol{r}\, \epsilon(\rho_p, \rho_n)$, under the constraint of particle number conservation,

$$\delta \int \mathrm{d}^3\boldsymbol{r} \left[\epsilon(\rho_p, \rho_n) - \mu_p \rho_p(\boldsymbol{r}) - \mu_n \rho_n(\boldsymbol{r}) \right] = 0 \,. \tag{149}$$

The chemical potentials for protons and neutrons, $\mu_{p,n}$, are fixed by the conditions

$$Z = \int \mathrm{d}^3\boldsymbol{r}\, \rho_p(\boldsymbol{r}), \quad N = \int \mathrm{d}^3\boldsymbol{r}\, \rho_n(\boldsymbol{r}). \tag{150}$$

Substituting the energy-density functional, i.e., the 00-component of the energy-momentum tensor eq. (136), in eq. (149) leads to the RTF-equations for protons and neutrons,

$$p_i^0(p_{F,i}) = \mu_i, \quad (i = p, n) \tag{151}$$

Here, $p_i^0(p_{F,i})$ are the Fermi energies. They can be written explicitly as

$$
\begin{aligned}
p_p^0(p_{F,p}) &= g_\omega \omega^0 + g_\rho \rho^{30} + e A^0 + E_{F,p}^*, \\
p_n^0(p_{F,n}) &= g_\omega \omega^0 - g_\rho \rho^{30} + E_{F,n}^*,
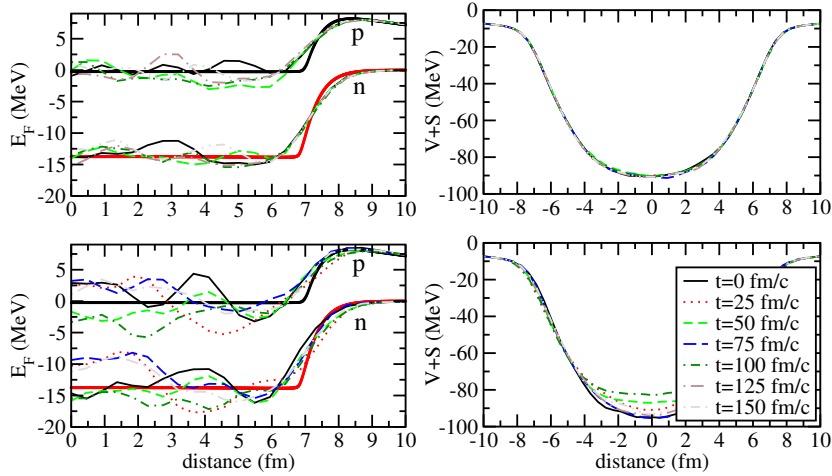\end{aligned}
\tag{152}
$$

39

Figure 6: (Color online) The Fermi energies for protons and neutrons subtracting the nucleon mass, $p^0_{p,n} - m_N$, with $p^0_{p,n}$ given by eq. (152) (left panels) and the nucleon mean-field potential, $V^0 + S$, where the vector and scalar potentials are defined by eqs. (129) and (130), (right panels) along the z-axis passing through the center of the ^{100}Sn nucleus. The thick curves in the figures on the left show the result of the RTF calculation. The other curves show the Vlasov results at different times (as indicated) using the improved initialization (upper panels) and the standard one (lower panels).

where $E^*_{F,p,n} = \sqrt{p^2_{F,p,n} + (m^*)^2}$. The Fermi energies eq. (152) are constants by definition, in contrast to the Fermi energy defined in eq. (148) for the LTF approximation. For a spherical nucleus, the RTF equations (151) together with the field equations eqs. (124)–(127) completely determine the radial dependence of the proton and neutron densities and mean fields, i.e., $\rho_{p,n}(r)$, $\sigma(r)$, $\omega^0(r)$, $\rho^{30}(r)$, and $A^0(r)$. In their solution retardation effects are neglected.

The initialization of neutron and proton densities according to the Thomas-Fermi calculation largely improves the ground-state stability in numerical simulations. As an example, figs. 5 and 6 show the time evolution of the binding energy per nucleon, the rms-radius and of the relativistic mean-field potential for Vlasov calculations.

The standard-initialization method using the empirical Woods-Saxon density distribution produces a binding energy smaller by 0.3-0.4 AMeV with respect to the RTF value of $E_B/A \simeq$ 8.1 MeV. This is expected, since the minimum of the total energy is not reached with the standard initialization. The binding energy varies with time due to numerical errors in the solution of the time-evolution eqs. (142) and (143) and field eqs. (124)–(127). For the standard initialization, the rms radius fluctuates quite strongly, even comparable in the amplitude with the real giant-monopole resonance vibrations. These artificial temporal oscillations lead also to a significant particle loss with increasing time, if collisions are included (not shown here). Applying the improved initialization, in which the same energy-density functional is used for both the initialization of the nucleus and its time propagation, stabilizes the nucleus considerably. At $t = 0$ fm/c the value of the binding energy per nucleon agrees with the corresponding RTF value, and both, the binding energy per nucleon and the rms radius, stay almost constant in time.

In relativistic transport studies the central mean-field potential consists of the sum of a large negative Lorentz-scalar and a large positive Lorentz-vector potential. Thus, small spurious density variations cause strong numerical fluctuations in the mean-field potential. This is demon-
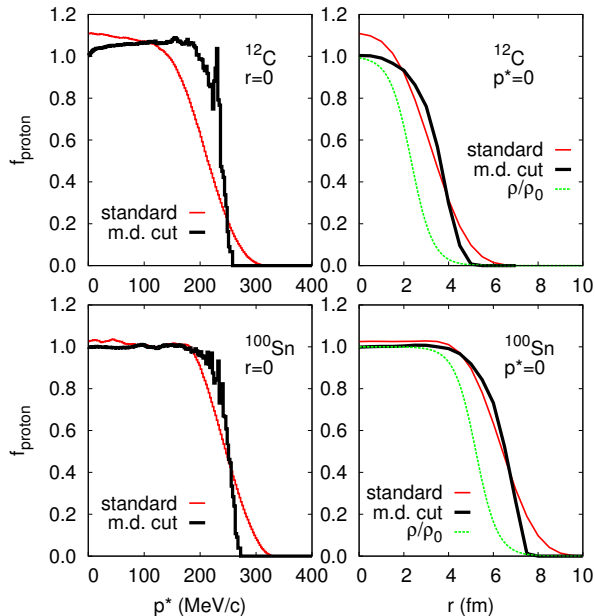
40

Figure 7: (Color online) Momentum dependence of the proton-occupation number f_{proton} in the center of ^{12}C and ^{100}Sn nuclei is shown in the upper and lower left panels, respectively. The radial dependence of f_{proton} at zero momentum for ^{12}C and ^{100}Sn is depicted in the upper and lower right panels, respectively. The results are presented for the standard (thin solid lines) and momentum-dependent (thick solid lines) radius, r_p (see Appendix D.4.3). The fluctuations of f_{proton} near the Fermi momentum, $p_F \simeq 250\,\text{MeV}/c$, are due to the finite number of test particles per nucleon, which has been set to 10000 in this calculation. The nucleon density in units of ρ_0 is shown additionally by dashed lines in the right panels. We see that at the half-central-density radius, the proton occupation number is only about 10 % below unity. Taken from [86].

strated in fig. 6 (figures on the right), where the mean-field potential is displayed as a function of the coordinate along the central z-axis. The Vlasov calculations with the standard initialization (panel on the bottom) show large fluctuations of the order of 10 %, while these fluctuations almost vanish in the calculations using the improved initialization method. Another good test of the ground state stability within the modified initialization scheme is the radial dependence of the proton- and neutron-Fermi energies, which according to the RTF model, see eq. (152), should be constant. Apart from some unavoidable numerical fluctuations the Fermi energies resulting from the dynamical Vlasov calculations are rather constant in radius and also in time within the modified initialization prescription. In particular, they fit the RTF results and are very stable around the nuclear surface. On the other hand, the dynamical calculations using the standard initialization fail to reproduce the RTF calculation and strongly fluctuate in time.

So far we have discussed the stability of ground state nuclei in Vlasov simulations, i.e., by neglecting binary collisions. The frequency of two-body collisions in a Fermi gas depends on the occupancies of the scattering final states via the hole-distribution functions $\bar{f}_i = 1 - f_i$, see the r.h.s. of the BUU equation eq. (71). Due to energy and momentum conservation, no collisions occur at zero temperature, where $f_i(\boldsymbol{r}, \boldsymbol{p}) = \Theta(p_{F,i}(\boldsymbol{r}) - |\boldsymbol{p}|)$. In test-particle simulations, however, it is impossible to model the exact $T = 0$ Fermi distribution. This causes some spurious two-

body collisions even in the ground-state nucleus. The magnitude of this effect crucially depends on the numerical treatment of Pauli blocking, which is described in Appendix D.4.3.

Thus, including two-body collisions requires a careful implementation of Pauli blocking to prevent the destruction of the ground state. To demonstrate the accuracy of the test-particle calculations, fig. 7 shows the momentum and radial dependence of the proton-occupation numbers, which are used in the evaluation of the Pauli-blocking factors, for ^{12}C and ^{100}Sn nuclei. The calculations are performed with $N = 1000$ test particles per nucleon. The simulation with the default Pauli-blocking parameters results in a rather diffuse momentum dependence, especially for the light ^{12}C nucleus. Using the momentum-dependent radius, r_p, and the reduced width of the Gaussian distribution, largely improves the momentum dependence of the occupation numbers close to the Fermi surface. The radial dependence of the occupation numbers also approximates the step function better for the calculation with the modified Pauli blocking parameters.

3.3. Collision term

In general, the collision term, $C(x, p)$, on the r.h.s. of the kinetic eqs. (68), (85) and (140) can be represented as a sum of one-, two-, three-body, etc. collisional contributions (cf. [30, 106] and refs. therein),

$$C(x, p) = C^{(1)}(x, p) + C^{(2)}(x, p) + C^{(3)}(x, p) + \cdots . \tag{153}$$

We will start with the general form of the various contributions to the collision term. At this stage, in order to keep the formulae as simple and clear as possible, the mean-field effects are ignored. They will be discussed in section 3.3.4.

From now on we will often use the invariant matrix elements $\mathcal{M}_{if}$ in the PDG convention [54], which are related to the used earlier matrix elements $\mathfrak{M}_{if}$ in the Bjorken and Drell convention [51] (cf. eq. (72)) as

$$\mathcal{M}_{if} = \mathfrak{M}_{if} \prod_j \sqrt{n_j} \quad \text{with} \quad n_j = \begin{cases} 1 & \text{if } j \text{ is a boson,} \\ 2m_j & \text{if } j \text{ is a fermion .} \end{cases} \tag{154}$$

where the product is taken over all incoming and outgoing particles.

The one-body contribution, $C^{(1)}(x, p)$, appears if the considered particle is an unstable resonance and may decay. For an illustration, let us consider the one-body collision term for the particle 1 decaying to the particles $1'$ and $2'$, taking into account the recombination $1'2' \to 1$:

$$\begin{aligned} C^{(1)}(x, p_1) = C_{\text{gain}}^{(1)}(x, p_1) - C_{\text{loss}}^{(1)}(x, p_1) = {} & \frac{\mathcal{S}_{1'2'}}{2p_1^0 g_{1'} g_{2'}} \int \frac{\mathrm{d}^4 p_{1'}}{(2\pi)^4 2p_{1'}^0} \int \frac{\mathrm{d}^4 p_{2'}}{(2\pi)^4 2p_{2'}^0} \\ & \times (2\pi)^4 \delta^{(4)}(p_1 - p_{1'} - p_{2'}) \overline{|\mathcal{M}_{1 \to 1'2'}|^2} [F_{1'}(x, p_{1'}) F_{2'}(x, p_{2'}) \overline{F}_1(x, p_1) \\ & - F_1(x, p_1) \overline{F}_{1'}(x, p_{1'}) \overline{F}_{2'}(x, p_{2'})] , \end{aligned} \tag{155}$$

where $\overline{|\mathcal{M}_{1 \to 1'2'}|^2}$ is the in-medium matrix element squared and averaged over the spin states of the initial particle and summed over the spin states of the final particles; $F_i(x, p_i)$ ($i = 1, 1', 2'$) is the Wigner function of eq. (64). In eq. (155) we have also introduced the auxiliary Wigner function,

$$\overline{F}(x, p) = \begin{cases} \mathrm{i}\, \mathrm{tr}[\tilde{S}^>(x, p)\gamma_0] = 2\pi g A(x, p)[1 - f(x, p)] & \text{for fermions,} \\ 2p^0 \mathrm{i}\tilde{D}^>(x, p) = 2\pi g A(x, p)[1 + f(x, p)] & \text{for bosons.} \end{cases} \tag{156}$$

For fermions this Wigner function describes the phase-space density of hole states and is proportional to the Pauli blocking factor, $[1 - f(x, p)]$. For bosons, the Bose enhancement factor, $[1 + f(x, p)]$, appears instead. Below these factors are denoted as $\overline{f}(x, p) = 1 \mp f(x, p)$ for outgoing fermions (-) or bosons (+). To avoid possible misunderstanding, we note that for the bosons, the spectral function which appears in eqs. (64) and (156) is defined not by eq. (63) but as $A(x, p) := 2p^0 \mathcal{A}(x, p)$ with $\mathcal{A}(x, p)$ being the spectral function given by eq. (76).

The symmetry factor, $\mathcal{S}_{1'2'}$, in eq. (155) takes into account the possible identity of the final-state particles and is defined as

$$\mathcal{S}_{1'2'\ldots N'} = \frac{1}{N_a! N_b! \ldots} , \tag{157}$$

where $a, b, \ldots$ label the different species of particles appearing in the final state, $1'2' \ldots N'$, and N_a is the number of particles of type a among the final-state particles, $1'2' \ldots N'$.

Now we introduce the vacuum decay width of the resonance as

$$\Gamma_{1 \to 1'2'}(p_1) = \frac{\mathcal{S}_{1'2'}}{2p_1^0} \int \frac{\mathrm{d}^4 p_{1'}}{(2\pi)^3 2p_{1'}^0} \int \frac{\mathrm{d}^4 p_{2'}}{(2\pi)^3 2p_{2'}^0} (2\pi)^4 \delta^{(4)}(p_1 - p_{1'} - p_{2'})$$
$$\times \overline{|\mathcal{M}_{1 \to 1'2'}|^2} A_{1'}(p_{1'}) A_{2'}(p_{2'}) . \tag{158}$$

This expression does not include the Pauli-blocking or Bose-enhancement factors for the outgoing particles. The spectral functions of the latter, $A_{1'}(p_{1'})$ and $A_{2'}(p_{2'})$, are also assumed to be the vacuum ones. In the rest frame of the resonance, after a simple calculation one can rewrite eq. (158) as

$$\Gamma_{1 \to 1'2'}(m_1) = \mathcal{S}_{1'2'} \int \mathrm{d}m_{1'}^2 \, \mathcal{A}(m_{1'}^2) \int \mathrm{d}m_{2'}^2 \, \mathcal{A}(m_{2'}^2) \frac{1}{8\pi m_1^2} \overline{|\mathcal{M}_{1 \to 1'2'}|^2} \, q(m_1; m_{1'}, m_{2'}) , \tag{159}$$

where $q(m_1; m_{1'}, m_{2'})$ is the c.m. momentum of the decay particles,

$$q(M; m_1, m_2) := \sqrt{(M^2 + m_1^2 - m_2^2)^2/(4M^2) - m_1^2} . \tag{160}$$

In eq. (159), we have used the spectral functions defined according to eq. (76) and have assumed that they depend on momentum via the mass, $m^2 = p^2$, only. Using eq. (159), we can rewrite the one-body collision term of eq. (155) in the following simple and practical form:

$$C^{(1)}(x, p_1) = \frac{m_1}{p_1^0} \Gamma_{1 \to 1'2'}(m_1) \int \frac{\mathrm{d}\Omega_{\mathrm{cm}}}{4\pi} [f_{1'}(x, p_{1'}) f_{2'}(x, p_{2'}) \overline{F}_1(x, p_1)$$
$$- F_1(x, p_1) \overline{f}_{1'}(x, p_{1'}) \overline{f}_{2'}(x, p_{2'})] , \tag{161}$$

where the expression in square brackets is averaged over the direction of the momentum of particle $1'$ in the rest frame of the decaying resonance.

The loss term of eq. (161) is modeled in the following way. For every resonance test particle of the kind 1, a MC decision is made on its decay during the time interval, $[t; t + \triangle t]$, according to the probability,

$$P_{\mathrm{decay}} = 1 - \exp\left\{\frac{-m_1 \, \Gamma_1(m_1) \, \triangle t}{p_1^0}\right\} , \tag{162}$$

where $\Gamma_1(m_1)$ is the total decay width in the rest frame of a given resonance test particle obtained by summation over all possible decay channels,

$$\Gamma_1(m_1) = \sum_{1',2'} \Gamma_{1\to 1'2'}(m_1) + \sum_{1',2',3'} \Gamma_{1\to 1'2'3'}(m_1) . \tag{163}$$

Here, the sums are taken over all two- and (for mesons only) three-body decay channels. If the resonance decays, its decay channel is selected by a MC decision with the probability proportional to the partial width of the given channel. The momenta of the outgoing particles are sampled isotropically[11] in the rest frame of the resonance. If one of the decay particles, e.g., $1'$, is a nucleon, the Pauli-blocking factor in eq. (161) is taken into account by accepting the decay event with the probability, $[1 - f_{1'}(x, \boldsymbol{p}_{1'})]$. The Pauli-blocking factors for other baryons and the Bose-enhancement factors for mesons are always neglected, since the phase-space densities of these particles are rather small in all reactions considered in this review.

The modeling of the gain term in eq. (161) and also the gain terms for the two- and three-body processes do not require special efforts. In fact, the gain terms are *automatically* included in any test-particle model simulation of the kinetic equations provided that the final-channel sampling of the corresponding loss terms is implemented in detail. E.g., the gain term in eq. (161) is modeled by the final-state sampling in the simulation of the loss terms in the kinetic equations for the particles of the kinds $1'$ and $2'$.

For the processes $12 \leftrightarrow 1'2'$ and $123 \leftrightarrow 1'2'3'$, the two- and, respectively, three-body collision terms can be written as

$$C^{(2)}(x, p_1) = C_{\text{gain}}^{(2)}(x, p_1) - C_{\text{loss}}^{(2)}(x, p_1) = \frac{\mathcal{S}_{1'2'}}{2p_1^0 g_{1'} g_{2'}} \int \frac{d^4 p_2}{(2\pi)^4 2p_2^0} \int \frac{d^4 p_{1'}}{(2\pi)^4 2p_{1'}^0} \int \frac{d^4 p_{2'}}{(2\pi)^4 2p_{2'}^0}$$
$$\times (2\pi)^4 \delta^{(4)}(p_1 + p_2 - p_{1'} - p_{2'}) \overline{|\mathcal{M}_{12\to 1'2'}|^2} [F_{1'}(x, p_{1'}) F_{2'}(x, p_{2'}) \overline{F}_1(x, p_1)$$
$$\times \overline{F}_2(x, p_2) - F_1(x, p_1) F_2(x, p_2) \overline{F}_{1'}(x, p_{1'}) \overline{F}_{2'}(x, p_{2'})] , \tag{164}$$

$$C^{(3)}(x, p_1) = C_{\text{gain}}^{(3)}(x, p_1) - C_{\text{loss}}^{(3)}(x, p_1)$$
$$= \frac{\mathcal{S}_{23} \mathcal{S}_{1'2'3'}}{2p_1^0 g_{1'} g_{2'} g_{3'}} \int \frac{d^4 p_2}{(2\pi)^4 2p_2^0} \int \frac{d^4 p_3}{(2\pi)^4 2p_3^0} \int \frac{d^4 p_{1'}}{(2\pi)^4 2p_{1'}^0} \int \frac{d^4 p_{2'}}{(2\pi)^4 2p_{2'}^0} \int \frac{d^4 p_{3'}}{(2\pi)^4 2p_{3'}^0}$$
$$\times (2\pi)^4 \delta^{(4)}(p_1 + p_2 + p_3 - p_{1'} - p_{2'} - p_{3'}) \overline{|\mathcal{M}_{123\to 1'2'3'}|^2}$$
$$\times [F_{1'}(x, p_{1'}) F_{2'}(x, p_{2'}) F_{3'}(x, p_{3'}) \overline{F}_1(x, p_1) \overline{F}_2(x, p_2) \overline{F}_3(x, p_3)$$
$$- F_1(x, p_1) F_2(x, p_2) F_3(x, p_3) \overline{F}_{1'}(x, p_{1'}) \overline{F}_{2'}(x, p_{2'}) \overline{F}_{3'}(x, p_{3'})] . \tag{165}$$

The two-body collision term, $C^{(2)}(x, p_1)$, can be expressed in terms of the differential scattering cross section $12 \to 1'2'$,

$$d\sigma_{12\to 1'2'} = (2\pi)^4 \delta^{(4)}(p_1 + p_2 - p_1' - p_2') \frac{1}{4I_{12}} \overline{|\mathcal{M}_{12\to 1'2'}|^2}$$
$$\times \mathcal{S}_{1'2'} \frac{d^4 p_1'}{(2\pi)^3 2p_{1'}^0} \frac{d^4 p_2'}{(2\pi)^3 2p_{2'}^0} A_{1'}(x, p_{1'}) A_{2'}(x, p_{2'}) , \tag{166}$$

---

[11]Exceptions are the decay $\Delta \to \pi N$, where the Δ has been produced in a πN collision, and $\rho \to \pi\pi$ for a diffractive ρ. In these two cases, the phenomenological angular distributions of the decay particles are taken into account.

where

$$I_{12} := \sqrt{(p_1 p_2)^2 - (m_1 m_2)^2} \qquad (167)$$

is the flux factor. Thus, we obtain

$$C^{(2)}(x, p_1) = \int \frac{\mathrm{d}^4 p_2}{(2\pi)^4} \int \mathrm{d}\sigma_{12 \to 1'2'} \, v_{\mathrm{rel}}[f_{1'}(x, p_{1'}) f_{2'}(x, p_{2'}) \overline{F}_1(x, p_1) \overline{F}_2(x, p_2)$$
$$- F_1(x, p_1) F_2(x, p_2) \overline{f}_{1'}(x, p_{1'}) \overline{f}_{2'}(x, p_{2'})] , \qquad (168)$$

where

$$v_{\mathrm{rel}} := \frac{I_{12}}{p_1^0 p_2^0} \qquad (169)$$

is the relative velocity of colliding particles[12]. The loss term in eq. (168) serves as a basis for various test-particle computational techniques discussed in Appendix D.4.1.

The numerical evaluation of the three-body collision term (165) is more involved [60, 107, 108, 55]. It is usually done by calculating the three-body collision rate

$$\Gamma^{(3)}(x, p_1) = C_{\mathrm{loss}}^{(3)}(x, p_1)/F_1(x, p_1) . \qquad (170)$$

Then, $\Gamma^{(3)}$ is treated as a partial width of particle 1. Therefore, the probability for particle 1 to take part in a three-body collision within the time interval $[t; t + \triangle t]$ is determined by

$$P_{3\mathrm{b}} = 1 - \exp(-\Gamma^{(3)} \triangle t) . \qquad (171)$$

Once it is decided that the particle will participate in a three-body collision, its collision partners are chosen in some close vicinity, and the final state is sampled by MC. The sampling of the final state is done microcanonically, i.e., the probability of a given momentum configuration is proportional to the corresponding phase-space volume element.

Below in this section, we address the elementary reaction processes of the GiBUU collision term. First, the vacuum decay modes of resonances are discussed. Then, we consider reactions with two and three initial-state particles. Collisions involving more than three incoming particles are neglected based on the assumption that the nuclear matter density does not reach too high values. Such multi-particle collisions might be important only at very high nuclear densities ($\sim 10\rho_0$) reached in high-energy heavy-ion collisions [79].

3.3.1. Particle decays

Decays of baryonic resonances. Our model allows the baryonic resonances to decay only into two-body final states. Overall, there are 19 different decay channels: πN, ηN, ωN, $K\Lambda$, $\pi\Delta$, ρN, σN, $\pi P_{11}(1440)$, $\rho\Delta$, $\pi\Lambda$, $\overline{K}N$, $\pi\Sigma$, $\pi\Sigma(1385)$, $\eta\Lambda$, $\overline{K}^\star N$, $\pi\Lambda(1520)$, $\pi\Xi$, $\pi\Lambda_c$, $\pi\Xi_c$. The angular momenta, L, for the final-state particles depend on the resonance and are listed in Appendix A. Following Manley and Saleski, we assume that the decay width in the rest frame of the resonance is expressed as (cf. eq. (159))

$$\Gamma_{R \to ab}(m) = \Gamma_{R \to ab}^0 \frac{\rho_{ab}(m)}{\rho_{ab}(M^0)}, \qquad (172)$$

---

[12]For relativistic particles, $v_{\mathrm{rel}} = |\mathbf{v}_1 - \mathbf{v}_2|$ only if the particles' velocities are collinear. However, for brevity, we always call the quantity defined by the r.h.s. of eq. (169) a "relative velocity".

where $m = \sqrt{p^\mu p_\mu}$ is the mass of the resonance, M^0 its pole mass and $\Gamma^0_{R\to ab}$ its decay width into a final state consisting of particles a and b at the pole mass. The function, ρ, is given by

$$\rho_{ab}(m) = \int \mathrm{d}p_a^2 \mathrm{d}p_b^2 \mathcal{A}_a(p_a^2)\mathcal{A}_b(p_b^2)\frac{p_{ab}}{m}B^2_{L_{ab}}(p_{ab}R)\mathcal{F}^2_{ab}(m) \ . \tag{173}$$

In the vacuum, the spectral functions, $\mathcal{A}$, depend only on the square of the four-momentum. The term p_{ab} denotes the c.m. momentum of the final-state products. The Blatt-Weisskopf functions, $B_{L_{ab}}$, depend on the the angular momentum L_{ab} of the final state particles a and b, on the so-called interaction radius $R = 1$ fm and on the c.m. momentum p_{ab}. Compared to Manley [64] and the implementation by Effenberger [60], we modified the large-m behavior by a cut-off function, $\mathcal{F}_{ab}(m)$. This has become necessary, because in some channels the width increased too fast with increasing mass to be used in a dispersion analysis. If the decay channel includes only stable final-state particles, this modification is not necessary ($\Rightarrow \mathcal{F}_{ab}(m) = 1$); for all other decay channels we have chosen a form factor according to Post [109] (Eq. (3.22) on page 35),

$$\mathcal{F}_{ab}(m) = \frac{\lambda_{ab}^4 + \frac{1}{4}(s_0 - M_0^2)^2}{\lambda_{ab}^4 + \left(m^2 - \frac{1}{2}(s_0 + M_0^2)\right)^2}, \tag{174}$$

where s_0 is the Mandelstam s for the threshold of the regarded process. The parameter λ has been tuned to pion scattering and is chosen to be

$$\lambda = \begin{cases} 0.85\,\mathrm{GeV} & \text{for the } \Delta\rho \text{ channel,} \\ 1.6\,\mathrm{GeV} & \text{if there is an unstable meson but no unstable baryon,} \\ 2.0\,\mathrm{GeV} & \text{if there is an unstable baryon but no unstable meson.} \end{cases} \tag{175}$$

The $\Delta\rho$ channel plays a special role, since it is the only channel with two unstable final state particles. The impact of this cut-off function is discussed in [55].

Decays of mesonic resonances. The mesonic resonances can decay into 16 different two-body decay channels ($\pi\pi$, $\pi\rho$, $K\overline{K}$, $K\pi$, $\rho\gamma$, $\pi\gamma$, $\gamma\gamma$, $D_s^+\gamma$, $D_s^-\gamma$, πD_s^+, πD_s^-, $\overline{K}\pi$, $D\gamma$, $\overline{D}\gamma$, πD, $\pi\overline{D}$) and four distinct three-body channels ($\pi^0\pi^0\eta$, $\pi^0\pi^-\pi^+$, $\pi^0\pi^0\pi^0$, $\pi^+\pi^-\eta$). For channels with two scalar final-state mesons with parity $P = -1$ (i.e., the dominant 2π, $K\overline{K}$, πK, $\pi\overline{K}$ channels), the angular momentum of the outgoing mesons must be equal to the spin of the parent resonance. Given this angular momentum, for these channels we can implement a mass-dependent partial width according to eq. (172). The widths of the other decay channels are assumed to be mass independent.

Dilepton decay. In particular, vector mesons and also baryon resonances can decay into e^+e^- pairs, so-called dileptons. The relevant expressions for decay widths are given in Appendix A.1.

3.3.2. Two-body collisions
Resonant and non-resonant processes in the low-energy region. For the two-body interactions, we distinguish a *low-energy* and a *high-energy* region. The low-energy region is dominated by resonance contributions and small non-resonant background terms. The resonance model adopted in GiBUU is reliable for baryon-meson interactions from pion-threshold up to roughly

2.3 GeV center of mass energy and for meson-meson interactions. The production cross section for $a\,b \to R$ is given by the Breit-Wigner formula,

$$
\begin{aligned}
\sigma_{ab \to R}(s) &= \sum_f F_I \frac{2J_R + 1}{(2J_a + 1)\,(2J_b + 1)} \frac{1}{S_{ab}} \frac{4\pi}{p_{ab}^2(s)} \frac{s\,\Gamma_{ab \to R}(s)\,\Gamma_{R \to f}(s)}{\left(s - m_R^2 - \mathrm{Re}\,\Pi(s)\right)^2 + s\Gamma_{\mathrm{tot}}^2(s)} \\
&= F_I \frac{2J_R + 1}{(2J_a + 1)\,(2J_b + 1)} \frac{1}{S_{ab}} \frac{4\pi}{p_{ab}^2(s)} \frac{s\,\Gamma_{ab \to R}(s)\,\Gamma_{tot}(s)}{\left(s - m_R^2 - \mathrm{Re}\,\Pi(s)\right)^2 + s\Gamma_{tot}^2(s)}
\end{aligned}
\tag{176}
$$

with

$$
S_{ab} = \begin{cases} 1 & \text{if a,b not identical} \\ \frac{1}{2} & \text{if a,b identical} \end{cases}
\tag{177}
$$

denoting the symmetry factor of a and b. The term p_{ab} denotes the c.m. momentum of particles a and b, the J_i's define the total spin of the particles and

$$
F_I = \left\langle I^a\, I_z^a;\, I^b\, I_z^b | I^R\, I_z^a + I_z^b \right\rangle^2
\tag{178}
$$

are the isospin Clebsch-Gordan coefficients squared. The term, $\Gamma_{ab \to R}$, denotes the so-called in-width. For stable particles a and b it is identical to the out-width $\Gamma_{R \to ab}$; for unstable particles the final result is given in [60] (Eq. (2.77)).

In this energy region, we have included additional *non-resonant background processes* to improve the comparison with experimental data and/or trustworthy model calculations. These background processes are treated as point-like interactions: While, e.g., the amplitude of the resonant process $\pi N \to R \to \pi N$ contains a resonance propagator, the corresponding background process $\pi N \to \pi N$ is modeled with a point-like four-particle vertex. Such background processes are defined for several channels (cf. Appendix B.3 and [55, Appendix A] for details).

For the baryon-baryon cross sections, matrix elements have been fitted to π, $\pi\pi$ and ρ^0 and strangeness production up to a c.m. energy of ca. 2.6 GeV [12]. The following processes are taken into account: $NN \leftrightarrow NN$, $NN \leftrightarrow NR$, $NN \leftrightarrow \Delta\Delta$, and the background point-like contribution $NN \to NN\pi$. Details can be found in Appendix B.1 and [55, Appendix A].

Also the meson-meson interactions are implemented in the model. This is important, in-particular, for a realistic description of strangeness production in heavy ion collisions. For details, we refer the interested reader to Appendix B.4.

High-energy processes. For high energy processes, we use Pythia [110] as an event generator. The actual implementation uses version 6.4, while former code versions used v6.2.[13] The total and elastic cross sections in the high-energy region are fitted to available data based on a model using Reggeon and Pomeron exchanges. The model separates elastic, single-diffractive, double-diffractive and non-diffractive event topologies. The choice of final state is done with the help of a fragmentation model implemented in Pythia, i.e., string fragmentation according to the LUND-String model or cluster collapses for low mass configurations.

---

[13]We have found discrepancies between these versions when describing transverse-momentum distributions of pions in $p + p$ collisions with beam energies around 10 GeV, indicating that the newer version improves the agreement with experiment [111].

Matching the high energy processes and the resonance region. Altogether, we have two models (Pythia and resonances+non-resonant background) for two different energy regimes with some overlap region. Finally, we match both models in this overlap region by introducing a "transition window", where we smoothly switch from one prescription to the other. We use a c.m. energy interval of width, 2Δ, around the center point, $\sqrt{s_0}$, in which we mix both types of events linearly. The probability for a high-energy event is then given by

$$
p_{\text{HiEnergy}}(s) = \begin{cases} 0 & \text{for} & \sqrt{s} < \sqrt{s_0} - \Delta \,, \\ \frac{\sqrt{s} - (\sqrt{s_0} - \Delta)}{2\Delta} & \text{for} & \sqrt{s_0} - \Delta < \sqrt{s} < \sqrt{s_0} + \Delta \,, \\ 1 & \text{for} & \sqrt{s_0} + \Delta < \sqrt{s} \,, \end{cases} \tag{179}
$$

where $\sqrt{s}$ is the c.m. energy, and the probability for a low-energy event is consequently $1 - p_{\text{HiEnergy}}$. We have chosen $\Delta = 0.2\,\text{GeV}$ and $\sqrt{s_0} = 2.2\,\text{GeV}$ for baryon-meson and $\sqrt{s_0} = 2.6\,\text{GeV}$ for baryon-baryon reactions. This procedure yields a smooth transition also after modifications of individual cross sections in the low- or high-energy region.

The resulting total and elastic cross section can be found for all possible incoming particles at the GiBUU homepage [23].

Detailed balance relations. The principle of detailed balance states that in the state of thermal equilibrium the number of collisions $ab \to cd$ is equal to the number of collisions $cd \to ab$, where the participating particles are characterized by their momenta only and the spin degrees of freedom are assumed to be averaged-out (c.f. Ref. [30]). This is equivalent to the following relation between the matrix elements

$$
\overline{|\mathcal{M}_{cd \to ab}|^2} = \overline{|\mathcal{M}_{ab \to cd}|^2} \,, \tag{180}
$$

where the averaging is done over spin magnetic quantum numbers of all particles. If the incoming and outgoing particles are on their mass shell, the latter equation can directly be transformed to the relation between the total cross sections of the direct and reversed processes as

$$
\sigma_{cd \to ab} = \sigma_{ab \to cd} \left(\frac{p_{ab}}{p_{cd}} \right)^2 \frac{(2J_a + 1)(2J_b + 1)}{(2J_c + 1)(2J_d + 1)} \frac{\mathcal{S}_{ab}}{\mathcal{S}_{cd}} \,, \tag{181}
$$

where the same notation as in eq. (176) is used. Equation (181) is often applied to obtain the cross sections, which can not be obtained empirically, e.g., to determine the $\pi Y \to \overline{K}N$ and $\overline{K}K \to \pi\pi$ cross sections (see Appendix B.3 and Appendix B.4).

Maintaining detailed balance in the high-energy regime is considerably more difficult and still presents a problem in many event generators. This comes about because Pythia can generate, for example, a typical DIS event, such as $1 + 1 \to n$ with $(n > 2)$, but there is no simple way to describe the time-reversed reaction where many (> 2) hadrons combine to form the simple initial state. Some progress has only been made for $3 \leftrightarrow 2$ and $3 \leftrightarrow 3$ reactions Ref. [60, 107, 108, 55].

3.3.3. Three-body collisions

The procedure of the three-body loss term modeling sketched in beginning of this section requires to know the matrix elements, $\overline{|\mathfrak{M}_{123 \to X}|^2}$. Unfortunately, the model independent information on the three-body matrix elements is restricted by the processes of the type $123 \to 1'2'$, where the detailed balance relation can be used to extract the matrix element, $\overline{|\mathfrak{M}_{123 \to 1'2'}|^2}$, from

48

the cross section of the inverse process, $1'2' \rightarrow 123$, (cf. Ref. [60]). One example of such a process is the pion absorption by two nucleons, $NN\pi \rightarrow NN$, implemented in GiBUU. It is partly due to the two-step mechanism mediated by the Δ resonance, $\pi N_1 \rightarrow \Delta$ followed by $\Delta N_2 \rightarrow NN$. However, there is also a non-negligible direct contribution to the two-nucleon pion absorption, which is related to the background, i.e., non-resonant, part of the $NN \rightarrow NN\pi$ cross section important near threshold (cf. fig. B.50). The process, $NN \rightarrow NN\pi$, has been extensively studied in several experiments over the last twenty years[112, 113, 114, 115, 116, 117, 118]. We have, therefore, constructed well defined background cross sections on top of the resonance contributions for all possible isospin channels. Another three-body process implemented in GiBUU is the Δ resonance absorption by two nucleons, $NN\Delta \rightarrow NNN$. The rate for the this process is based on the model of Oset *et al.* [56].

A somewhat different, geometrical, approach to many-body collisions have been developed in Ref. [106] and optionally implemented in GiBUU in Ref. [79] for the three-body initial states. Further details on the three-body processes in GiBUU can be found in Ref. [60, 79, 55]. The influence of the three-body collisions on particle production in heavy-ion collisions is discussed in section 4.1.6.

3.3.4. Reactions in the medium

Besides the modification of the collision rate via the Pauli-blocking term, the presence of potentials modifies the in-medium kinematics and has to be considered in the collision term. After addressing Pauli blocking, we discuss the general aspects of in-medium cross sections for the hadron-hadron collisions with arbitrary hadronic final states. Finally, we consider the resonance processes, where the in-medium modification of the resonance width has also to be taken into account.

Pauli blocking and Bose enhancement. For reactions, for which the nucleus stays close to its ground state, e.g., in low-energy photon and lepton induced events, Pauli blocking is approximated by the condition that each momentum state below the Fermi momentum is Pauli blocked. However, in heavy-ion collisions and reactions induced by pions, protons, leptons, or photons (which deposit high energies within the target nucleus) one has to simulate the Pauli blocking dynamically. This requires to determine the nucleon phase space occupation number at the position and momentum of the nucleon in the final state of scattering or resonance decay. The numerical calculation of the nucleon phase space occupation number and the discussion of its accuracy are given in section 3.2.2 and in Appendix D.4.3 (see fig. 7 and eqs. (D.22),(D.23)). The Pauli blocking for the other baryons than nucleons as well as the Bose enhancement for the mesons are always neglected due to presumably low phase space occupancies of these particles.

General aspects of cross section modifications. Here, we will discuss the influence of the mean field on the two-body collision term. The differential in-medium cross section of the scattering $12 \rightarrow 1'2'$ is defined as (cf. eq. (166) for the vacuum case)

$$d\sigma^*_{12 \rightarrow 1'2'} = (2\pi)^4 \delta^{(4)} \left(p_1 + p_2 - p'_1 - p'_2 \right) \frac{n_1^* n_2^* n_{1'}^* n_{2'}^*}{4I_{12}^*} \overline{|\mathfrak{M}_{12 \rightarrow 1'2'}|^2}$$
$$\times \mathcal{S}_{1'2'} \frac{d^4 p'_1}{(2\pi)^3 2p_{1'}^{*0}} \frac{d^4 p'_2}{(2\pi)^3 2p_{2'}^{*0}} A_{1'}(x, p_{1'}) A_{2'}(x, p_{2'}) ,$$

(182)

where

$$I_{12}^* := \sqrt{(p_1^* p_2^*)^2 - (m_1^* m_2^*)^2}$$

(183)

49

is the in-medium flux factor, $\overline{|\mathfrak{M}_{12 \to 1'2'}|^2}$ is the in-medium matrix element squared and averaged over spins of initial particles and summed over spins of final particles, and $\mathcal{S}_{1'2'}$ is a symmetry factor for final particles (see eq. (177)). Equation (182) explicitly uses the matrix element in the Bjorken and Drell normalization [51] with

$$
n_j^* = \begin{cases} 1 & \text{if } j \text{ is a boson,} \\ 2m_j^* & \text{if } j \text{ is a fermion .} \end{cases}
\tag{184}
$$

While the final results of any consistent field-theoretical calculation should not depend on the choice of the bispinor normalization, we prefer the normalization of Bjorken and Drell when discussing the in-medium effects, since, due to the dimensionless Dirac bispinors ($\bar{u}u = 1$), the matrix elements become less sensitive to the nuclear medium. This normalization is also the preferred one for the Dirac-Brueckner calculations of the in-medium cross sections (cf. Ref. [119, 53]).

This leads to the following expression for the two-body collision term (cf. expressions for the on-shell particles with mean fields, eq. (71), and for off-shell particles without mean fields, eq. (168)):

$$
\begin{aligned}
C^{(2)}(x, p_1) = \int \frac{\mathrm{d}^4 p_2}{(2\pi)^4} \int \mathrm{d}\sigma_{12 \to 1'2'}^* \, v_{\text{rel}}^* \, [f_{1'}(x, p_{1'}) f_{2'}(x, p_{2'}) \overline{F}_1(x, p_1) \overline{F}_2(x, p_2) \\
- F_1(x, p_1) F_2(x, p_2) \overline{f}_{1'}(x, p_{1'}) \overline{f}_{2'}(x, p_{2'})] =: C_{\text{gain}}^{(2)} - C_{\text{loss}}^{(2)} ,
\end{aligned}
\tag{185}
$$

where

$$
v_{\text{rel}}^* := \frac{I_{12}^*}{E_1^* E_2^*}
\tag{186}
$$

is the in-medium relative velocity of the colliding particles. In other words, in order to obtain the in-medium collision term, one should replace $p \to p^*$ and $m \to m^*$, i.e., the bare vacuum four-momenta — by the kinetic ones and the bare vacuum masses — by the effective ones, everywhere except for the energy-momentum conserving δ-function, where the in-medium canonical four-momenta should appear at the place of the bare vacuum momenta.

In a similar way, the loss terms for more complicated processes like $12 \to 1'2' \cdots N'$ are given by

$$
C_{\text{loss}}(x, p_1) = \int \frac{\mathrm{d}^4 p_2}{(2\pi)^4} \int \mathrm{d}\sigma_{12 \to 1'2'...N'}^* v_{\text{rel}}^* F_1(x, p_1) F_2(x, p_2) \prod_{i=1'}^{N'} \overline{f}_i(x, p_i) .
\tag{187}
$$

The differential cross section of the transition $12 \to 1'2' \cdots N'$ reads

$$
\begin{aligned}
\mathrm{d}\sigma_{12 \to 1'2'...N'}^* = (2\pi)^4 \delta^{(4)} \left(p_1 + p_2 - \sum_{i=1'}^{N'} p_i \right) \frac{n_1^* n_2^* \prod_{i=1'}^{N'} n_i^*}{4 I_{12}^*} \overline{|\mathfrak{M}_{12 \to 1'2'...N'}|^2} \\
\times \mathcal{S}_{1'2'...N'} \prod_{i=1'}^{N'} A_i(p_i) \frac{\mathrm{d}^4 p_i}{(2\pi)^3 2 p_i^{*0}} ,
\end{aligned}
\tag{188}
$$

where we have included the spectral functions (see eq. (63)) for the general case of broad resonances in the final state.

50

In practice, however, it is impossible to evaluate the in-medium cross section (188) for all possible collision types. In most cases, suitable parametrizations of experimentally measured cross sections or theoretically predicted cross sections on the basis of boson-exchange and resonance models (cf. [120, 121, 122, 123]) are used in transport model simulations. All these (semi-) empirical approaches provide us with the vacuum cross sections, $\sigma^{\text{vac}}_{12 \to 1'2'...N'}$. Since the latter depend on the bare invariant energy $\sqrt{s_{\text{free}}}$ and possibly other parameters (such as masses etc.) defined in vacuum, the problem arises how to use these vacuum cross sections for collisions that take place in the nuclear medium, in the presence of mean-field potentials acting on initial and final particles.

We first consider hadron-hadron collisions. Assuming that the potential energy of incoming resonance and outgoing final states is exactly the same, one could view the potential as a background field, which should not affect the reaction rates. For example, consider a momentum independent potential and an elastic $N_1 N_2 \to N_{1'} N_{2'}$ scattering process. In this case the potential energy is exactly conserved during the reaction. One then defines a potential-corrected, so-called "free", c.m. energy

$$s_{\text{free}} = (p_{1,\text{free}} + p_{2,\text{free}})^2 \, , \qquad (189)$$

where

$$p_{\text{free}} = (\sqrt{m^2 + \boldsymbol{p}^{\,2}}, \boldsymbol{p}) \qquad (190)$$

and uses this to read off the cross section at this energy from its vacuum parametrization. This is the prescription used in most transport codes for treating hadron-hadron collisions. There are some intricacies involved in actually determining the quantity s_{free} which are discussed in Appendix D.4.2.

The definition (189) relies on the particle's three-momenta but not on the total in-medium energy of colliding particles. The latter, however, is important for endothermic threshold processes, where particles are produced, like, e.g., for meson production in baryon-baryon collisions. In this case, one can use a prescription similar to the one applied in Ref. [97, 124] for the treatment of in-medium thresholds in kaon production processes

$$\sqrt{s_{\text{free}}} = \sqrt{s^*} - (m_1^* - m_1) - (m_2^* - m_2) \qquad (191)$$

which is used in the RMF calculations (see Appendix D.4.2 for a short derivation) with $s^* \equiv (p_1^* + p_2^*)^2$.

For electroweak processes special care has to be taken for treating the first, initial reaction of the incoming particle (electron, photon, neutrino) with the nucleon bound in a potential and moving in the Fermi sea. For such reactions the high-energy cross sections all depend linearly on the energy of the incoming particle so that any error in calculating the "free" c.m. energy results in a major effect on the cross section at higher energy. In this case it is most natural to Lorentz-transform first into the rest frame of the Fermi-moving bound nucleon. Indeed this is the procedure widely used in the literature for treating inclusive inelastic scattering cross sections for leptons with nuclei [125, 126]. Since here the free (vacuum) cross sections in the rest frame of the Fermi-moving nucleon depend on the product mE (cf. eq. (C.37)), given by $(s - m^2 + Q^2)/2$, it is suggestive to use the relation

$$s_{\text{free}} = s^* + m^2 - (m^*)^2 \qquad (192)$$

where s^* has to be calculated with the properly boosted incoming energy.

51

Since transition rates enter the collision terms in the BUU equation it is reasonable to require that the collision rate of quasi-particles ($\propto \rho^2 \sigma^* v_{\text{rel}}^*$) and not the cross section, is the same as in vacuum [60]. Therefore, with non-relativistic potentials, the cross sections are calculated as

$$\sigma_{12 \to 1'2'...N'}^* = \frac{v_{\text{rel}}}{v_{\text{rel}}^*} \sigma_{12 \to 1'2'...N'}^{\text{vac}} , \tag{193}$$

where $v_{\text{rel}} = |\boldsymbol{v}_{1,\text{free}} - \boldsymbol{v}_{2,\text{free}}|$ is the relative velocity calculated in the c.m. frame with vacuum kinematics, i.e., $\boldsymbol{v}_{\text{free}} = \boldsymbol{p}_{\text{free}}/p_{\text{free}}^0$. To estimate the effect of the flux correction factor in eq. (193), let us consider the collision between two nucleons on the Fermi surface. Then, $v_{\text{rel}}/v_{\text{rel}}^* \simeq m_N^*/m_N \simeq 0.7$, where m_N^* is the Landau effective mass (see eq. (110) and table 1). So, the flux correction alone gives an in-medium reduction of the nucleon-nucleon cross section due to the factor of $\sim m_N^*/m_N$.

One may wish to evaluate the in-medium structure of the differential cross section (188) in more detail [79, 127]. It is convenient to perform this in the RMF model. A reasonable assumption, which has some support from the correlated basis [128] and Dirac-Brueckner [53] calculations of the in-medium elastic $NN \to NN$ scattering cross sections, is to use the vacuum matrix element $|\mathfrak{M}_{12 \to 1'2'...N'}|^2$. Assuming that the particles in the final state are on their mass shell, this results in the relation

$$\sigma_{12 \to 1'2'...N'}^*(\sqrt{s^*}) = \mathcal{F} \sigma_{12 \to 1'2'...N'}^{\text{vac}}(\sqrt{s_{\text{free}}}) \tag{194}$$

between the vacuum and in-medium-modified cross sections for the process, $12 \to 1'2'...N'$, where

$$\mathcal{F} = \frac{n_1^* n_2^* n_{1'}^* n_{2'}^* \ldots n_{N'}^*}{n_1 n_2 n_{1'} n_{2'} \ldots n_{N'}} \frac{I_{12}}{I_{12}^*} \frac{\Phi_{N'}(\sqrt{s^*}; m_{1'}^*, m_{2'}^*, \ldots, m_{N'}^*)}{\Phi_{N'}(\sqrt{s_{\text{free}}}; m_{1'}, m_{2'}, \ldots, m_{N'})} \tag{195}$$

is the modification factor. Here, we used the N-body phase-space volume (cf. eq. (D.18)),

$$\Phi_N(M; m_1, m_2, \ldots, m_N) = \int d\Phi_N(\mathcal{P}; p_1, p_2, \ldots, p_N) \tag{196}$$

with the mass-shell constraints $m_i^2 = p_i^2$ ($i = 1, 2, \ldots, N$) and $M^2 = \mathcal{P}^2$. E.g., the two-body phase-space volume is given by

$$\Phi_2(M; m_1, m_2) = \frac{\pi q(M; m_1, m_2)}{(2\pi)^6 M} . \tag{197}$$

For the valuation of the higher-dimensional phase-space volumes, we use alternatively either the exact recurrence relations [129] or approximate expressions from [130] accurate at the level of a few percent. The latter are substantially reducing the computational time. The vacuum and in-medium flux factors entering eq. (195) are expressed as

$$I_{12} = q(\sqrt{s_{\text{free}}}; m_1, m_2) \sqrt{s_{\text{free}}} , \tag{198}$$

$$I_{12}^* = q(\sqrt{s^*}; m_1^*, m_2^*) \sqrt{s^*} . \tag{199}$$

It is also important to note, that, in the derivation of eq. (194), we have assumed that the sum of vector fields for incoming and outgoing particles is the same. This allows us to replace the canonical four-momenta in the energy-momentum conserving δ-function by the kinetic ones, since $p_1 + p_2 - \sum_{i=1'}^{N'} p_i = p_1^* + p_2^* - \sum_{i=1'}^{N'} p_i^*$.

52

The in-medium modification of the cross sections according to eqs. (194) and (195) is most efficient for the baryon-baryon collisions. In this case, the particles 1, 2, 1', 2' are baryons and the other particles 3', ..., N', if present, are mesons. Thus, we have

$$\mathcal{F} \propto \frac{m_1^* m_2^* m_{1'}^* m_{2'}^*}{m_1 m_2 m_{1'} m_{2'}} . \tag{200}$$

Since $m^* < m$, the baryon-baryon cross sections are reduced in the nuclear medium according to this simple picture. This effect is especially strong at high baryon densities reached in heavy-ion collisions (see section 4.1.6). We also expect on the basis of eqs. (194) and (195), that the in-medium modifications of the baryon-meson and meson-meson cross sections should be less pronounced due to the smaller powers of the ratio m^*/m.

In the limit of low-energy elastic scattering, $NN \to NN$, the modification factor, $\mathcal{F}$, can be easily calculated. The in-medium correction factor of eq. (195) can be simplified by using eqs. (197)–(199),

$$\mathcal{F} = \left(\frac{m_N^*}{m_N}\right)^4 \frac{s_{\text{free}}}{s^*} . \tag{201}$$

Then, since $s_{\text{free}} \simeq (2m_N)^2$ and $s^* \simeq (2m_N^*)^2$ at low collision energies, one has $\mathcal{F} \simeq \left(\frac{m_N^*}{m_N}\right)^2$ (cf. [128, 53, 131, 132]).

Once the partial cross sections of all final states are calculated for a given two-body collision, a particular final state f is selected by MC sampling according to the probability,

$$P_f = \frac{\sigma_f}{\sum_{f'} \sigma_{f'}} . \tag{202}$$

The MC decision for the momenta and, for the broad particles, for the masses of the final state particles is performed according to the algorithm presented in Appendix D.5.

Resonance production. The resonance cross sections deserve special consideration, since it has a structure which allows us to take into account the in-medium modifications of the resonance mass and width.

As follows from the general cross-section formula (188), the production cross section for a resonance, R, in a collision of two particles, a and b, can be written as

$$\sigma_{ab \to R} = \frac{\pi n_a n_b n_R}{2 I_{ab}} \overline{|\mathfrak{M}_{ab \to R}|^2} \mathcal{A}_R(p_R) . \tag{203}$$

The spectral function of the resonance can be, in general, the in-medium one (cf. eq. (81)). All the other quantities on the r.h.s. of eq. (203) are taken always at their vacuum values, for simplicity reasons[14]. Due to detailed balance, the same matrix element determines also the vacuum-decay width in the rest frame of the resonance,

$$\Gamma_{R \to ab}^{\text{vac}}(\mu) = \frac{n_a n_b n_R}{8\pi \mu^2} \frac{(2J_a + 1)(2J_b + 1)}{2J_R + 1} \overline{|\mathfrak{M}_{ab \to R}|^2} p_{ab}(\mu) S_{ab} , \tag{204}$$

---

[14]Since, in our model, a resonance can be formed only in baryon-meson or in meson-meson collisions, the in-medium modifications are not expected to be strong anyway (see discussion after eq. (200)).

where μ is the vacuum mass of the resonance R, and $p_{ab}(\mu) := q(\mu; m_a, m_b)$ is the c.m. momentum of particles a and b, cf. eq. (160).

For the calculation with non-relativistic potentials, the value of μ is determined from the known in-medium canonical four-momenta of the colliding particles, a and b, by imposing the conservation of energy and momentum,

$$\boldsymbol{p}_a + \boldsymbol{p}_b = \boldsymbol{p}_R, \tag{205}$$

$$E_a + E_b = E_R = \sqrt{\boldsymbol{p}_R^2 + \mu^2} + U_R(x, \boldsymbol{p}_R), \tag{206}$$

where all energies and three-momenta are calculated in the LRF. Since energy and momentum of the resonance are fixed by conservation laws, the solution of eq. (206) with respect to μ can be easily done and *does not* require iterations, in contrast to the general case of the particle energy calculation (see section 3.1.2). By expressing the squared matrix element in eq. (203) via the decay width eq. (204), one obtains

$$\sigma_{ab \to R} = \frac{2J_R + 1}{(2J_a + 1)(2J_b + 1)\mathcal{S}_{ab}} \frac{4\pi^2}{p_{ab}^2(\mu)} \mu \Gamma_{R \to ab}^{\mathrm{vac}}(\mu) \mathcal{A}_R(p_R), \tag{207}$$

or, by using eq. (81) for the spectral function,

$$\sigma_{ab \to R} = \frac{2J_R + 1}{(2J_a + 1)(2J_b + 1)\mathcal{S}_{ab}} \frac{4\pi}{p_{ab}^2(\mu)} \frac{\mu \Gamma_{R \to ab}^{\mathrm{vac}}(\mu)(- \operatorname{Im} \Pi(p_R))}{(p_R^2 - m_R^2 - \operatorname{Re} \Pi(p_R))^2 + (\operatorname{Im} \Pi(p_R))^2}. \tag{208}$$

In the case of the RMF-mode, the calculations of the resonance-production cross section, $\sigma_{ab \to R}$, is somewhat modified: The real part of the resonance self-energy $\operatorname{Re} \Pi$ is neglected. The invariant energy, $\sqrt{s}$, which fully determines the cross section in the vacuum given by the Breit-Wigner formula (176), is replaced by the "free" invariant energy (191). The flux correction is dropped. Overall, this simulates the usual vacuum Breit-Wigner formula for the resonance cross section in the simplest possible way.

Resonance decays. Due to detailed balance, the partial decay widths of the resonance in its rest frame, $\Gamma_{R \to cd}$, and the resonance cross section $\sigma_{cd \to R}$ are not independent. Therefore, the partial decay widths of resonances are calculated consistently within the assumptions made in the previous paragraph. Thus, we set

$$\Gamma_{R \to cd}(p_R) = \begin{cases} \Gamma_{R \to cd}^{\mathrm{vac}}(\mu) & \text{if there exists a solution to the equation, } p_R = p_c + p_d, \\ 0 & \text{otherwise,} \end{cases} \tag{209}$$

where μ is the vacuum mass of the resonance determined at its production time in a collision $ab \to R$ according to eqs. (205) and (206). Within this assumption, we do not include modifications of the final-state phase space, except that we reject decay events, where we can not fulfill energy and momentum conservation given the initial four-momentum, p_R. E.g., if $\mu > m_c + m_d$, then $\Gamma_{R \to cd}^{\mathrm{vac}}(\mu) > 0$. However if simultaneously $\sqrt{p_R^2} < m_c^* + m_d^*$, where m_c^* and m_d^* are the effective masses of particles c and d with zero momenta in the resonance rest frame, then the event must be rejected[15].

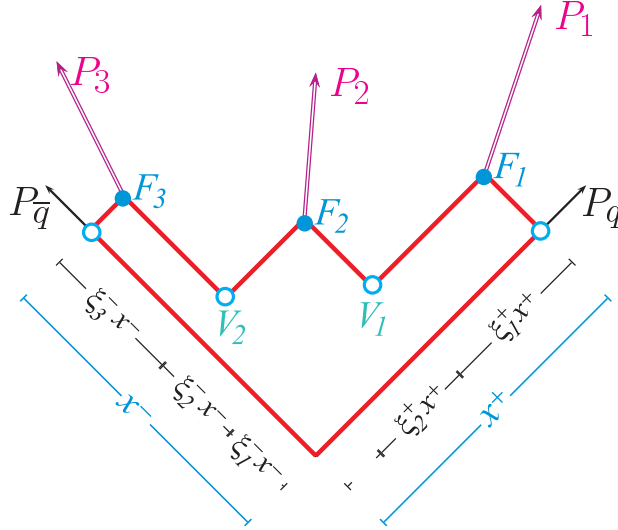[15]In the RMF-mode calculations, in the latter condition, we replace p_R by p_R^*.

Figure 8: (Color online) A sketch of the fragmentation of a one-dimensional $q\bar{q}$-string (in the rest frame of the string). The P_x denote momenta, while V_i indicate string-breaking vertices (production points) and the F_i the yoyo-formation points of the hadrons. While in principle all vectors are four-dimensional, in this sketch the horizontal axis is the x-axis and the vertical coordinate represents the time, t. Fractions of the light cone coordinates $x^{\pm}$ are also indicated. Taken from [66].

3.4. Hadronization

As already explained in section 3.3.2, in the case of high-energy collisions the final state is not known a priori. It is given via the Lund string fragmentation as provided by the JETSET part of the PYTHIA package [110]. Here one or more strings are formed by the quarks, antiquarks and diquarks produced by the hard interactions on the partonic level. These strings fragment by creating new quark–antiquark pairs in between. From these, the resulting mesons and baryons are built up. In fig. 8 we sketch this mechanism for the case of a simple 1+1-dimensional quark–antiquarks string.

As can be seen in this figure, we have to distinguish two classes of particles: Resulting directly from the fragmentation, any meson or baryon may consist of 0, 1, 2 or even 3 ("leading") partons, which build up the initial string configurations. Particles with 0 leading partons are called "secondary" or "non-leading" particles.

As elaborated in [66], in every event during the MC calculations and for each final particle we extract three 4D-points in PYTHIA: First, two string breaking points correspond usually to two production points. The meeting point of the quark/antiquark lines starting at these two string breaking points is then identified with the hadron-formation point. We label the production points by P_1 and P_2 and the formation point by F; the corresponding times are t_{P_1}, t_{P_2} and t_F. In fig. 8 we illustrate this for a simple $(1+1)$ case: "V_1" and "V_2" correspond to the two production points of particle 2, while "F_2" indicates its formation point. In the following we will always identify the "production time" of a particle with the "first" string breaking, i.e. $t_P = \min(t_{P_1}, t_{P_2})$.

Particles with 0 leading partons, i.e. the "non-leading" particles, all have non-vanishing production times, while "leading" particles have at least one parton line directly connected with the hard interaction point and also have at least one production time which is zero in all frames.

55

We now assume, that particles before their *production* may not interact, while they interact with their full cross section after their *formation*. Particles before formation we call "pre–hadrons". We have shown in Ref. [133] that only a linear increase of the cross section between these two times is compatible with data. In that sense the formation time could also be viewed as an expansion time during which the prehadronic system expands to its physical ground-state radius, with a correspondingly larger cross section. This then makes it possible to investigate color transparency (CT) effects within GiBUU.

4. Application to Nuclear Reactions

In this section we discuss applications of GiBUU to various quite different reaction types of present interest. We start out with reactions involving hadrons, i.e. pions, protons, antiprotons and heavy-ions, as projectiles. In a second subsection we discuss the applications of GiBUU to electron scattering on nuclei, covering both quasi-elastic scattering and pion production. We also discuss here studies of hadronization in high-energy electron-nucleus collisions. This subsection is followed by a discussion of meson-production on nuclei with real photons. At the end we cover a relatively new topic, the investigation of neutrino-nucleus interactions the understanding of which is necessary for extracting information from neutrino long-baseline experiments.

4.1. Hadronic Reactions

The interaction of pions and nucleons is a crucial cornerstone of every hadronic transport approach. Both particle species are most abundant in all reaction types and, therefore, very important within the coupled-channel calculations. To benchmark our description of pion-nucleon interactions we thus discuss first pion-induced reactions which set the stage for the discussion of pion production in heavy-ion, antiproton, electron-, neutrino- and photon-induced processes.

4.1.1. Low-energy pions

In this Section we try to answer the key question how far down in pion energy a transport model such as GiBUU is applicable since at low energies the de Broglie wavelength become large and the semi-classical treatment should start to break down.

To describe reactions such as close-to-threshold-$\pi\pi$ production in photon-induced reactions [134, 135], we aim to a description of low-energetic pions with kinetic energies down to 30 MeV. Already in earlier works of Salcedo *et al.* [136], with a simulation of pion propagation in nuclear matter, and of Engel *et al.* [137], with a precursor of our present simulation, pions with kinetic energies of 85-300 MeV have been investigated in transport models. As motivated above, we now investigate even less energetic pions. Therefore, we carefully account for Coulomb corrections in the initial channel of π-induced processes and improve the description of the threshold behavior of the cross sections as compared to earlier implementations. Additionally, a momentum-dependent hadronic pion potential, A_π^0, shown in the left panel of fig. 9 has been implemented [138, 139, 140, 141]. This potential shows a repulsive nature at low momenta, which is due to the S-wave interactions of pions and nucleons, whereas the P-wave Δ-hole excitations lead to an attractive contribution, which dominates the higher momentum. With Coulomb and hadronic potentials, the single-particle-Hamilton function for the pion becomes

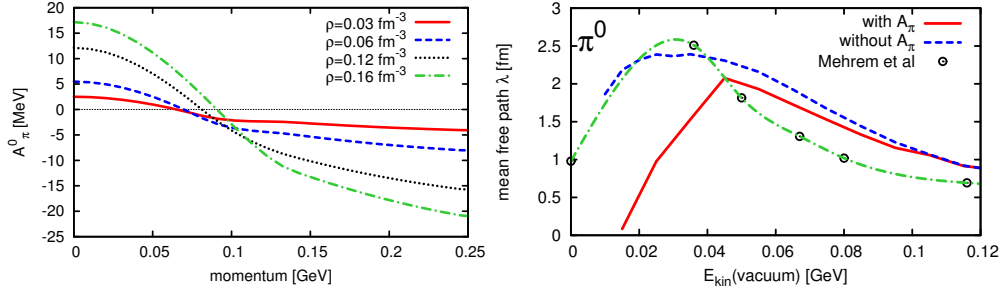$$H_\pi = \sqrt{\boldsymbol{p}_\pi^2 + m_\pi^2} + A_\pi^0 + V_C \; . \tag{210}$$

Figure 9: (Color online) Left panel: Hadronic potential, A_π^0, of the pion as a function of pion momentum for symmetric-nuclear-matter density at different densities. Right panel: Mean-free path of a neutral pion in symmetric nuclear matter at $\rho_0 = 0.168\,\mathrm{fm}^{-3}$ with (solid line) and without (dashed line) hadronic potential for the pion versus pion kinetic energy. The quantum-mechanical calculation by Mehrem *et al.* [142] is shown as circles linked by a dashed-dotted line. Source: Taken from [55].

Pion mean free path. The effect of including the hadronic potential becomes visible in the mean-free path of the pion in nuclear matter. A proper discussion of the mean-free path is obviously important in the analysis of experiments with final-state pions that are produced inside the nuclear medium. After having extracted the width of the pion in the nuclear-matter-rest frame directly from our numerical simulation, the mean free path is obtained by $\lambda = v/\Gamma$. Therefore one must consider the modifications of both the decay width, Γ, and the velocity, v, due to the potentials.

The velocity of the pions in nuclear matter (in the classically allowed region $E_\pi - m_\pi = E_{\mathrm{kin}} > A_\pi^0 + V_C$) is given by Hamilton's equation,

$$v_i = \frac{\partial H_\pi}{\partial p_\pi^i} = \frac{p_{\pi i}}{\sqrt{\boldsymbol{p}_\pi^2 + m_\pi^2}} + \frac{\partial A_0^\pi}{\partial p_\pi^i}\,. \tag{211}$$

At low pion-kinetic energies this velocity, as compared to the vacuum one, decreases sharply with decreasing kinetic energies, because the second term in eq. (211) is always negative. This, in turn, results in the sharp decrease of the mean-free path, as compared to the simulation without hadronic potentials. This is shown in fig. 9, where the mean-free path is plotted as a function of the pion momentum. At larger values of the pion momentum the effects of width and velocity just compensate each other.

As a benchmark for our model, the result of Mehrem *et al.* [142] obtained within the quantum-mechanical framework, solving the full dispersion relation, is also shown in fig. 9. As already mentioned, including the hadronic potential in our model considerably decreases the mean free path at low pion momenta. At even lower momenta, where the hadronic potential becomes repulsive with $A_\pi^0 + V_C > E_{\mathrm{kin}}$ the semi-classical model breaks down, while quantum mechanical calculations allow for tunneling, i.e., propagation into such classically forbidden regions. Indeed, the comparison with the results of Mehrem in fig. 9 shows that the semiclassical transport theory works rather well down to kinetic energies of about 30 MeV, but break down for lower ones.

Our study of the density dependence of the mean-free path [140] has shown, that it is highly nonlinear at low energies. This non-linearity is generated by the $NN\pi \to NN$ process, which to first order depends quadratically on the density, and by the implicit density dependence in the medium modifications. We conclude, that the naive low-density approximation is qualitatively and quantitatively not reliable in the energy regime of $E_{\mathrm{kin}} \lesssim 70\,\mathrm{MeV}$, where multi-body

57

collisions, potential effects, and Pauli-blocking are important.

Since the mean free path is not directly observable, it is ultimately an open question whether a transport description gives a reasonable mean-free path for the pion. This can only be answered by experiment. A test of our model assumptions will, therefore, be the absorption cross sections which we address next.

Pion absorption and quasi-elastic scattering. Low-energy pion scattering experiments have been conducted extensively with elementary targets (e.g. [143, 144, 145, 146]). However, there exist only a few data points for pions scattering off complex nuclei [147, 148, 149, 150, 151, 152, 153]. Our results on reaction and charge-exchange cross sections are presented in [140, 55]. They show a good agreement with the few data points existing for ^{12}C and ^{209}Bi [150, 151].

Also for pion absorption, shown in fig. 10, we achieve good agreement with existing data. Comparing the curves in fig. 10 obtained without any potential to those with the Coulomb potential included, we see that the Coulomb potential alone has only a small influence for light nuclei, but is very important at low energies for heavy nuclei. Its long range leads to a sizable deformation of the trajectories already long before the pions reach the nucleus. When one includes the hadronic potential for the pion, another overall effect sets in. Once the pion enters the nucleus it is affected by the short-range hadronic potential, which amounts to -40 MeV at high momenta and to $+20$ MeV at low momenta, as well as the Coulomb potential which amounts to roughly ± 10 MeV in a medium-size nucleus, and to roughly ± 20 MeV in the case of a ^{207}Pb nucleus. At very low energies the two potentials nearly compensate for the negative pion, while they add up to a strongly repulsive potential in the case of a π^+.

All results discussed above have been obtained using the parallel-ensemble scheme (see Appendix D.4.1). In fig. 10, we observe deviations between the results from the superior local-ensemble scheme (box size=0.5 fm^3) compared to those from the parallel ensemble scheme. The local ensemble scheme produces less absorption at higher energies and more absorption at lower energies. The overall agreement with the data is slightly improved.

As an overall conclusion, we find that it is critical to include Coulomb corrections. On top, the absorption cross sections are sensitive to the hadronic potential of the pion, in particular to the real part of the self-energy in the medium. As we have already seen in fig. 9, the mean-free path is quite insensitive to the hadronic potential except at very low energies. We thus conclude that the modification of the trajectories of the pion is the main effect of the hadronic potential. In its repulsive regime the hadronic potential pushes the pion outwards, and the overall path of the pion inside the nucleus becomes shorter. The probability of absorption is therefore decreased. The attractive behavior at larger energies causes the opposite effect.

The overall agreement to data is satisfactory in spite of some discrepancies, especially for the ^{12}C and ^{27}Al nuclei. Considering the fact that the pions have very large wave lengths at such low energies, the success of the semi-classical BUU model is quite astonishing. Due to the large wave length one expects also many-body correlations and quantum interference effects to be important. Many-body effects are partially included via the mean fields acting on pions and baryons and the modification of the Δ width. Besides this we included only $1 \leftrightarrow 2$, $2 \leftrightarrow 2$ and $2 \leftrightarrow 3$ body processes in the collision term. We take the success as an evidence that no higher order correlations are necessary to describe pion absorption.

Double charge exchange. Pionic double charge-exchange (DCX) in πA scattering is a very interesting reaction. The fact that DCX requires at least two nucleons makes it a very sensitive
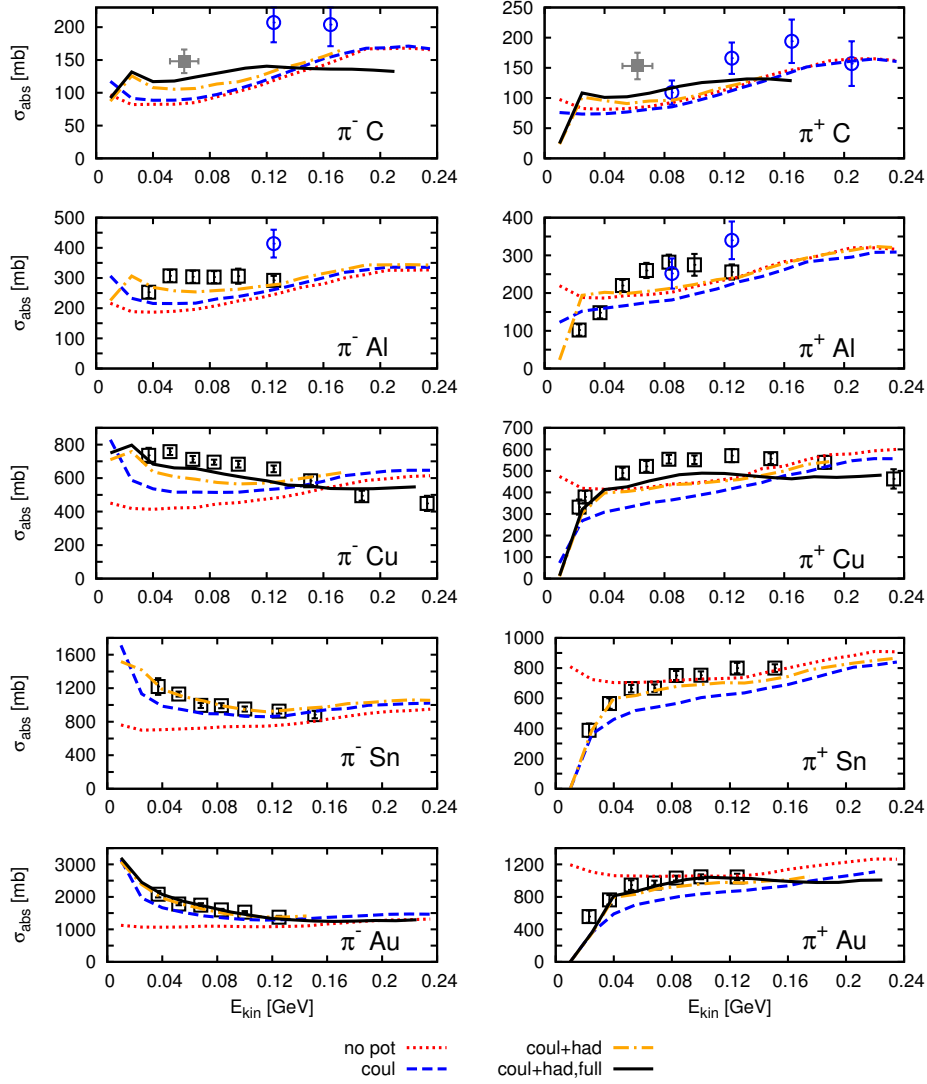
Figure 10: (Color online) Pion absorption on nuclei as a function of pion kinetic energy, depending on the choice of potentials for the pion. The data points are taken from [150] (open circles), [152] (open squares) and [153] (full squares). The dotted line represents a calculation without Coulomb potential and hadronic potential for the pion such that the pion feels no potentials, all other particle species are propagated under consideration of all potentials. All other lines are obtained with the Coulomb potential for the pion included. The dashed-dotted line additionally includes a hadronic potential for the pion. Finally, the solid line has been obtained using all potentials and, in contrast to the other results, in a full-ensemble calculation. Source: Taken from [55].

benchmark for pion rescattering and absorption. This reaction has received a considerable attention in the past (see for instance [154] and references therein). The mechanism of two sequential single-charge exchanges has traditionally succeeded to explain the main features of this reaction [155, 156] at low energies, although the contribution of the $A(\pi, \pi\pi)X$ reaction becomes progressively important as the energy increases [157, 158]. At higher (~ 1 GeV) energies, the sequential mechanism becomes insufficient to account for the reaction cross section [159, 160]. Extensive experimental studies performed at LAMPF has lead to high precision data for double-differential cross sections on $_3^4$He [161] and heavier nuclei (^{16}O, ^{40}Ca, ^{208}Pb) [162] for kinetic energies of the incoming pions of $E_{kin} = 120$-270 MeV.

Hüfner and Thies [163] have explored for the first time the applicability of the Boltzmann equation in πN collisions and achieved qualitative agreement with data on single- and double-charge exchange using some simplifying assumptions of averaged cross sections and averaged potentials. The work by Vicente *et al.* [157] is based on the cascade model described in [136]. There a microscopic model for πN scattering has been used as input for the pion-reaction rates in the simulation. In Ref. [157], pion DCX off ^{16}O and ^{40}Ca nuclei was explored and fair quantitative agreement with the data was achieved.

In our work [138, 55] we explore DCX on heavier nuclei, comparing with the data measured by Wood *et al.* [162]. We also address the scaling of the total cross section discussed by Gram *et al.* [164]. To focus only on single-pion rescattering, we consider incoming pion energies below $E_{kin} = 180$ MeV; above this energy, 2π production becomes prominent and DCX does not happen necessarily in a two-step process anymore. Due to the small mean free path of the incoming pions, the process is mostly sensitive to the surface of the nucleus. Therefore, we will discuss and compare two widely used numerical schemes for the solution of the Boltzmann equation: the *parallel-ensemble method* employed in the BUU models [165, 166, 90, 11] and in the Vlasov-Uehling-Uhlenbeck model [167]; and the *full-ensemble method* used in the Landau-Vlasov [168], Boltzmann-Nordheim-Vlasov [169, 170] and Relativistic BUU [93, 171] models, see Appendix D.4.1. Both schemes are based on the test-particle representation of the single-particle phase-space density, but they differ in the locality of the scattering processes. In the following, we first compare both schemes and, thereafter, point out the impact of neutron skins. Finally, the transport results are confronted with the experimental data obtained at LAMPF by Wood *et al.* [162].

In the non-discretized version of the BUU equation, the interactions are strictly local in space-time. Utilizing the so called *test-particle ansatz* to solve the problem numerically, this is no longer the case since usually cross sections in the collision terms are converted into interaction distances. The fact that the DCX reaction depends considerably on the spatial distributions of protons and neutrons implies that it is also sensitive to the degree of locality of the scattering processes. Thus we need to elaborate on this degree of locality of the scattering processes in our simulation. In Appendix D.4.1 we have introduced the concept of the parallel-ensemble approximation, which is expected to break down for large interaction volumes, ΔV_{ij}. In the energy regime under consideration, the incoming pions interact strongly with the nucleons so that the total cross section can reach more than 200 mb. Consequently, the reaction volume, ΔV_{ij}, exceeds 5 fm^3 for a typical time-step size $\Delta t = 0.25$ fm/c. The parallel-ensemble approximation is, therefore, questionable in this energy regime, and thus we evaluate this approximation scheme by comparison to the full-ensemble method, which is numerically more time consuming. In [138] and in [55] the results of both methods were compared. While the results from both methods are consistent with each other for the ^{40}Ca nucleus and within the statistical uncertainties also more or less for ^{16}O, some major discrepancy was found for the $\pi^+\text{Pb} \rightarrow \pi^- X$ reaction, in particular at
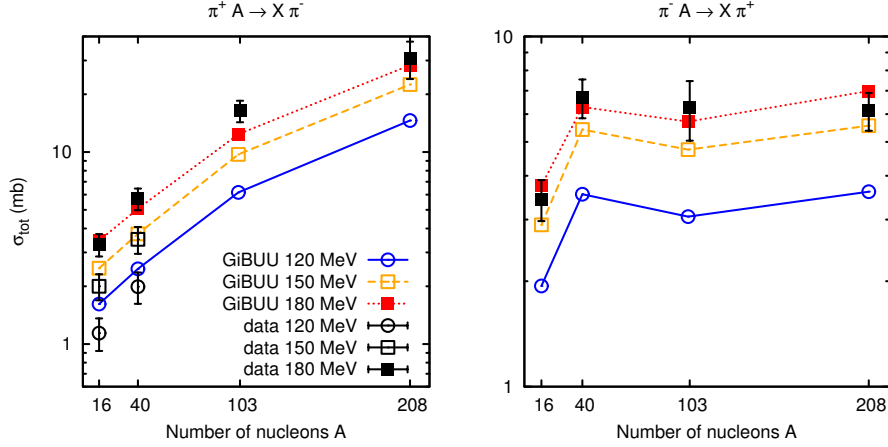
Figure 11: (Color online) The inclusive double charge exchange total cross section as a function of the nuclear-target mass at $E_{kin} = 120, 150$ and $180\,\text{MeV}$. The lines connecting our results are meant to guide the eye; the data are taken from [162] (left panel: $E_{kin} = 120\,\text{MeV}$ (open circles), $150\,\text{MeV}$ (open squares) and $180\,\text{MeV}$ (full squares), right panel: only $180\,\text{MeV}$ (full squares)). Source: Taken from [55].

backwards angles.

The DCX is, due to the small pion-mean-free path in nuclear matter, very sensitive to the surface properties of the nuclei. In particular, neutron skins are very interesting because in these skins only π^+ mesons can undergo charge-exchange reactions. For the positive pions this causes an enhancement of DCX processes at the surface, so the pions do not need to penetrate deeply for this reaction. In [138] also the effects of a neutron skin on the DCX cross sections were explored by comparing results with and without a neutron skin for the density distribution in ^{208}Pb. A significant increase of about 35 % was found for the reaction π^+Pb $\rightarrow \pi^-$Pb for the density distribution with a neutron skin.

To compare with the data measured at LAMPF by Wood *et al.* [162], we first discuss the total cross section. Hereafter, we explore angular distributions and, finally, the double-differential cross section is addressed as a function of both angles and energies of the outgoing pions.

In fig. 11 the good quantitative agreement to the total cross section data at 120, 150 and $180\,\text{MeV}$ for the ^{16}O, ^{40}Ca, ^{103}Rh and ^{208}Pb nuclei is demonstrated. Only for the ^{16}O nucleus and the low energy of $120\,\text{MeV}$ we find statistically significant discrepancies. The difference of full- and parallel-ensemble runs is rather small. Note that GiBUU reproduces the different A dependences of both (π^+, π^-) and (π^-, π^+) reactions. The different A dependences originate from the fact that, when A increases, the number of neutrons increases with respect to the number of protons, and this favors the π^+ induced reaction over the π^- one.

In fig. 12 we show $d\sigma/d\Omega$ for DCX at $E_{kin} = 120\,\text{MeV}$, $150\,\text{MeV}$ and $180\,\text{MeV}$ on ^{16}O, ^{40}Ca and ^{208}Pb as functions of the scattering angle, θ, in the laboratory frame for both the full- and parallel-ensemble schemes. The uncertainties are well under control except at very small and very large angles, where statistics is very scarce. Again, there is a very good quantitative agreement for both ^{40}Ca and ^{208}Pb nuclei. For ^{16}O, the data is somewhat overestimated for low kinetic energies of the pion.

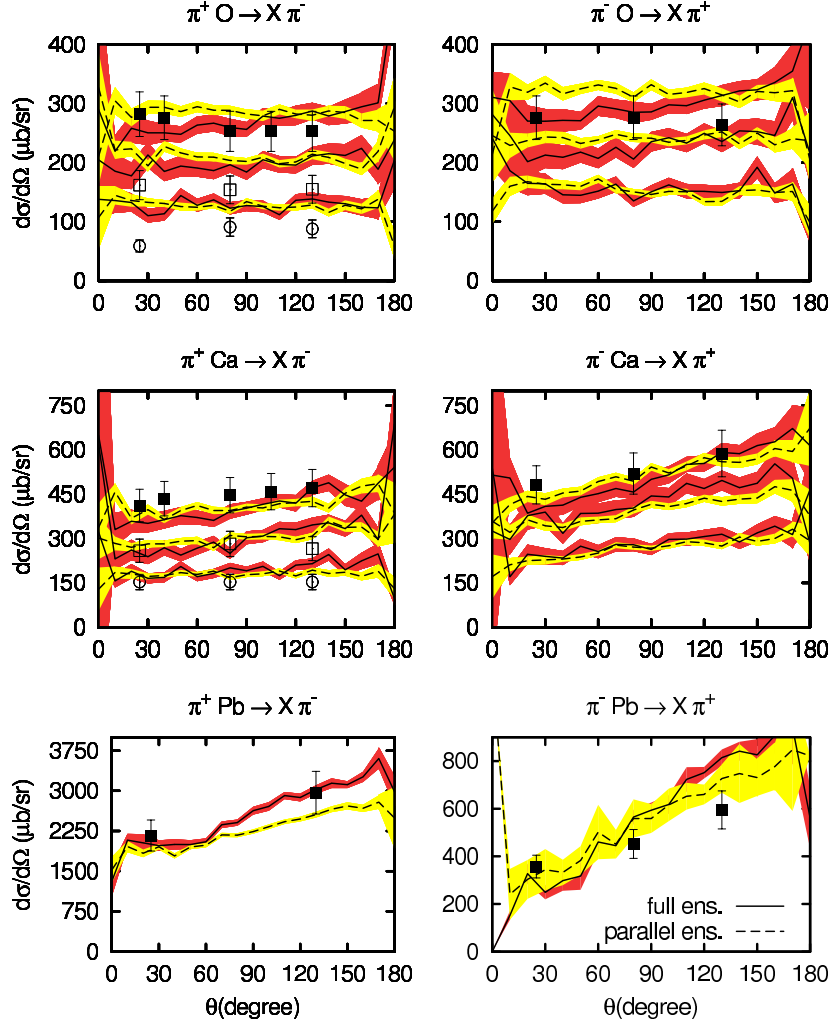Further comparisons of GiBUU results with DCX data can be found in [55, 138].

Figure 12: (Color online) Angular distributions for the DCX process $\pi^{\pm}A \to \pi^{\mp}X$ for the incoming pion kinetic energy $E_{\text{kin}} = 120, 150$ and $180 \,\text{MeV}$. The data points are taken from [162]; only systematical errors are shown. The solid lines represent the GiBUU results obtained using the full-ensemble scheme, the dashed ones the result of the parallel-ensemble scheme. For ^{208}Pb (lower panels) we only show the result and the corresponding experimental data for 180 MeV kinetic energy of the pion. For ^{16}O (upper panels) and ^{40}Ca (middle panels) we show the results for all three energies 120 MeV (experimental data: open circles), 150 MeV (open squares) and 180 MeV (full squares). The lowest curves of our results correspond to 120 MeV, the highest ones to 180 MeV. The yellow and red error bands denote the 1σ confidence level based upon our statistics. Source: Taken from [55].

4.1.2. High-energy pion- and proton-induced reactions

As already mentioned in section 4.1.1, pion- and proton-induced reactions are a crucial test for every transport model.

Recently the HARP experiment has published data for $\pi^\pm$ production by proton or pion beams in the momentum range 3-13 GeV/c impinging on different nuclear targets [172, 173, 174]. Here the main goal is to contribute to the understanding of the neutrino fluxes of accelerator-neutrino experiments such as K2K, MiniBooNE and SciBooNE or for a precise calculation of the atmospheric-neutrino fluxes. Some of the experimental data were also compared to several generator models used in GEANT4- and MARS-simulation packages [173]. The overall agreement is reasonable, while for some models discrepancies up to factors of three are found. Unfortunately, none of these models is applicable for all energies considered in the experiment: in the energy region of 5-10 GeV a distinction between low energies and high energies has to be considered, limiting the range of validity of these models. The lack of high-quality and systematic data concerning hadron-nucleus collisions in this energy regime has for long been an obstacle for a serious test of the models. The advent of the HARP experiment has changed the situation, since it offers charged-pion double-differential cross sections with a good systematics in angle, pion momentum, incident energy and target mass. Contrary to other theoretical frameworks we are able to cover the full energy range of the HARP experiment.

In [111] we have shown, that the current implementation of the proton- and pion-induced collisions in this energy regime, including all the final-state prescriptions, leads to a very satisfactory description of the experimental data. In order to illustrate this excellent agreement with experimental data, we show in fig. 13 the results for 12 GeV proton-beam energy and the large-angle analysis and in fig. 14 the results for 12 GeV pion-beam energy and the small angle analysis.

In Ref. [111] we have shown, that the overall agreement with data is good for all the beam energies 3-12 GeV for pion and proton beams.[16] The best description is achieved for the data with pion beams. The agreement obtained for proton beams is good over the whole energy-range, except for very forward and very backward directions. These deficiencies seem to be due to final-state interactions (FSI), as a comparison with the corresponding data for elementary $p + p$ collisions shows. This underlines the need for an understanding of results on elementary collisions before drawing conclusions on data taken on nuclei as targets.

In Ref. [111], we have also presented first theoretical results for the 30 GeV-proton beam in the NA61/SHINE experiment which aims for a precise determination of the neutrino flux in the T2K experiment.

4.1.3. Antiproton-induced reactions

Antiproton-nucleus interactions have been one of the most interesting fields in hadron-nucleus physics during the last three decades. The $\bar{p}$ scattering and absorption on nuclei is a direct way to access the $\bar{p}$-nucleus optical potential. Such experiments have been performed at LEAR [175, 176] and KEK [177] in the early 80's. Their optical model analysis has led to the conclusion that the antiproton-nucleus optical potential is moderately attractive ($\mathrm{Re}(V_{\mathrm{opt}}) = -(0\text{-}70)\,\mathrm{MeV}$) and strongly absorptive ($\mathrm{Im}(V_{\mathrm{opt}}) = (2\text{-}3)\mathrm{Re}(V_{\mathrm{opt}})$).

The low-energy antiprotons colliding with nuclei can be captured in a Coulomb atomic orbital. The shifts and widths of the $\bar{p}$-atomic levels caused by strong interactions deliver important

---

[16]We note, that after our analysis [111], more systematic data for the large-angles analysis have been published.
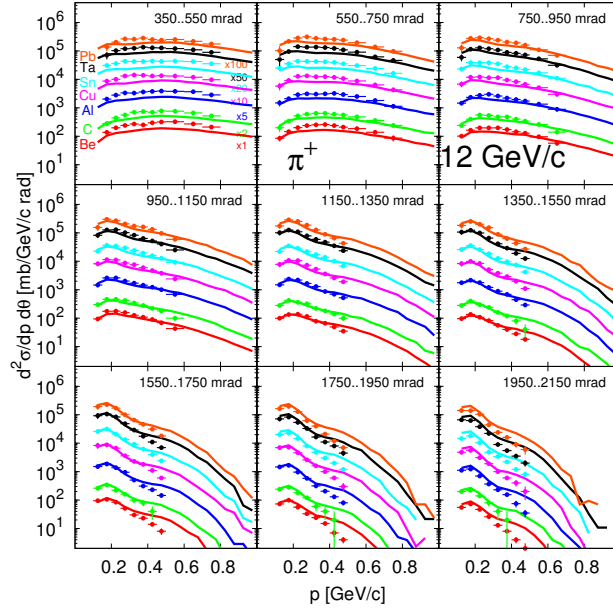
Figure 13: (Color online) Cross section $\mathrm{d}^2\sigma/\mathrm{d}p\,\mathrm{d}\theta$ for $p + A \to \pi^+ + X$ with $12\,\mathrm{GeV}/c$ beam momentum. Experimental data are from [173] (HARP large angle analysis), curves and data are scaled as indicated. The targets are indicated in the top-left frame. Source: Taken from [111].

information on the in-medium modifications of the $\overline{p}$-nucleon scattering amplitude at threshold [178, 77]. The possible formation of deeply bound $\overline{p}$-nuclei predicted by RMF models [179, 180] is expected for the energetic $\overline{p}$-nucleus collisions.

The antiproton annihilation in a nucleus leads to a large energy deposition [181, 182, 183, 184]. As a consequence, strongly excited residual nuclei are formed, which can undergo an explosive breakup to multiply charged fragments [185]. Another exotic scenario is that the propagating annihilation fireball absorbing the nucleons on its way may be transformed into a large quark bag with baryon numbers, $B \geq 1$ [181]. In principle, this can enhance strangeness production [186]. However, the statistical hadronic description can also provide an enhanced strangeness production for the $B \geq 1$-annihilation channels [187]. The strangeness enhancement in $\overline{p}$-annihilations at rest on several nucleons, i.e., for $B \geq 1$-annihilation channels, has been recently found experimentally in [188] which is currently a challenge for theoretical interpretations.

The ongoing plans for the FAIR project include the antiproton-nucleus collisions as one of its important research topics. The experiment PANDA at FAIR [189] will study, in-particular, the formation of (double) hypernuclei and J/Ψ production in $\overline{p}$-nucleus collisions.

In this subsection, we discuss the results of GiBUU calculations of $\overline{p}$ absorption and of pion production in $\overline{p}$ annihilation on nuclei. The elementary antibaryon-baryon cross sections are described in Appendix B.2.

An important ingredient of the transport simulations of $\overline{p}$-induced reactions is the antibaryon-mean-field potential. We describe it on the basis of the RMF model (see section 3.1.3). However, since the original non-linear Walecka model gives a too deep antiproton potential, $\mathrm{Re}(V_{\mathrm{opt}}) \simeq -660\,\mathrm{MeV}$ at normal nuclear density, some modifications are needed. In the most simple way,
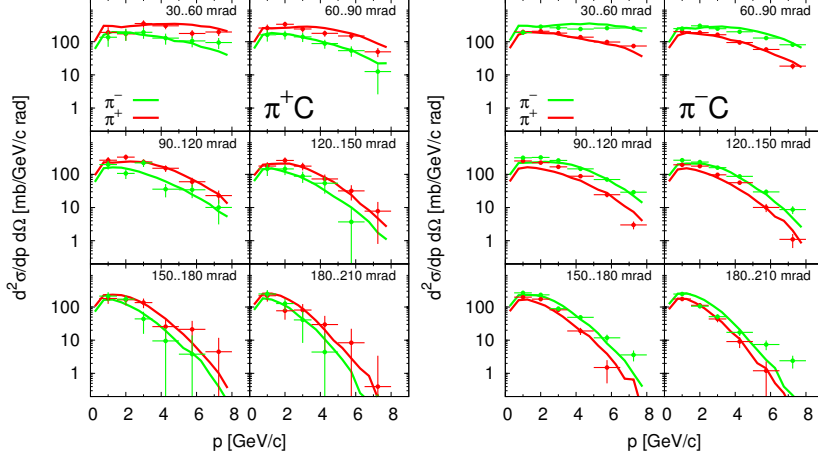
64

Figure 14: (Color online) Cross section $d^2\sigma/dp\,d\Omega$ for $\pi^{\pm} + C \rightarrow \pi^{\pm} + X$ with $12\,\mathrm{GeV}/c$ beam momentum. Experimental data are from [172] (HARP small-angle analysis). Source: Taken from [111].

this can be performed by rescaling the antibaryon-meson coupling constants by a common factor $0 < \xi \leq 1$, as suggested in Ref. [180]. Thus, we set $g_{\omega\bar{B}} = -\xi g_{\omega}$, $g_{\rho\bar{B}} = \xi g_{\rho}$, $g_{\sigma\bar{B}} = \xi g_{\sigma}$, where g_{σ}, g_{ω} and g_{ρ} are the nucleon-meson coupling constants from the non-linear Walecka model. The case of $\xi = 1$ corresponds to the G-parity transformed nucleon fields or, equivalently, to the antibaryon single-particle energies derived from the original non-linear Walecka model Lagrangian density (see eqs. (118) and (132)). The vector and scalar potentials acting on an antibaryon are now redefined as compared to eqs. (129) and (130) by

$$V_{\bar{B}} = g_{\omega\bar{B}}\omega + g_{\rho\bar{B}}\tau^3\rho^3 + \frac{e}{2}(-1 + \tau^3)A \,, \tag{212}$$

$$S_{\bar{B}} = g_{\sigma\bar{B}}\sigma \,. \tag{213}$$

The antibaryon-single-particle energy reads

$$p^0 = \sqrt{(m_{\bar{B}}^{\star})^2 + (\boldsymbol{p} - \boldsymbol{V}_{\bar{B}})^2} + V_{\bar{B}}^0 \,, \tag{214}$$

where $m_{\bar{B}}^{\star} = m_{\bar{B}} + S_{\bar{B}}$. Thus, now the antibaryon single-particle energy has the same form as the nucleon single-particle energy (eq. (131) with "+" sign) with the nucleon-vector and -scalar potentials eqs. (129) and (130) replaced by the antibaryon-vector and -scalar potentials eqs. (212) and (213), respectively. The antibaryons of the species, $\bar{B}$, propagate according to the transport equation (140) with the kinetic momentum, $p^{\star} \equiv p_j - V_{\bar{B}}$, field-strength tensor, $\mathcal{F}^{\mu\nu} \equiv \partial^{\mu}V_{\bar{B}}^{\nu} - \partial^{\nu}V_{\bar{B}}^{\mu}$, and effective mass, $m^{\star} \equiv m_{\bar{B}}^{\star}$.

In order to conserve energy and momentum, the antibaryon contributions to the source terms of the field equations for the σ, ω and ρ mesons eqs. (124)–(126) have also been modified in the case of $\xi \neq 1$. This is especially important for studying the collective response of a nucleus on an antiproton in its interior [179, 180, 84, 190]. For the full Lagrangian formulation in the case of modified antibaryon-meson coupling constants we refer the interested reader to [180, 84, 190]. Below, we will compare our calculations with experimental data on inclusive observables, such as the $\overline{p}$ absorption cross section, pion and proton kinetic energy spectra. Thus, the collective dynamics of the residual nucleus is not considered here.
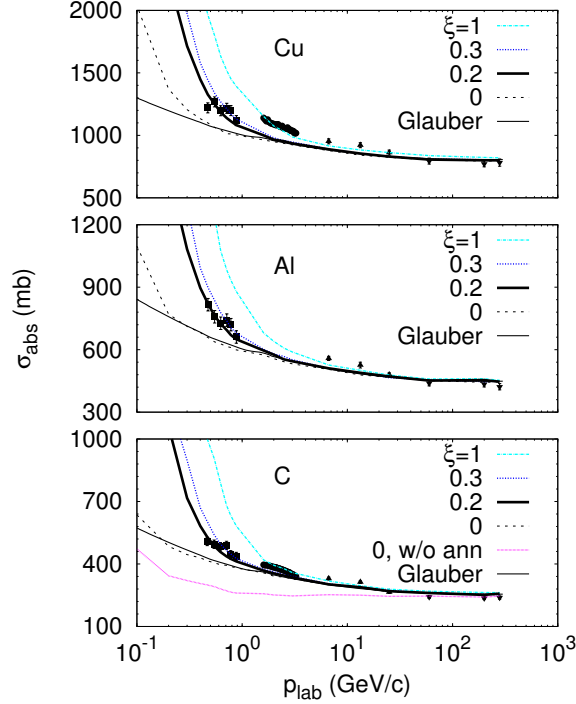
65

Figure 15: (Color online) $\overline{p}$-absorption cross section on various nuclei vs the beam momentum. The lines marked with the value of a scaling factor ξ show the GiBUU results. Thin solid lines represent a simple Glauber-model calculation [191, 192]. For the $\overline{p} + {}^{12}C$ system, a calculation with $\xi = 0$ without annihilation is additionally shown by the dotted line. Data are from Ref. [177] (filled boxes), Ref. [192] (filled circles), Ref. [193] (filled triangles), and Ref. [194] (filled upside-down triangles). The figure is taken from [195].

The calculations, presented in this subsection, have been performed in the full-ensemble technique (see Appendix D.4.1). This is especially important for the low-energy antiprotons, which have a big annihilation cross section on nucleons. The full-ensemble technique helps to better maintain the local structure of the collision term in this case. In order to get rid of the spurious effect of the beam particles' interactions with the secondary produced particles, which unavoidably appears in the full-ensemble simulations of the Boltzmann equation, we have turned off the interactions of the secondaries in the calculations of the absorption cross section. For other calculations, this correction has not been done, however. The parameters of the non-linear Walecka model have been adopted from the NL3 set [78], which is well suited to the nuclear ground state calculations.

Figure 15 shows the $\overline{p}$ absorption cross section on ${}^{12}C$, ${}^{27}Al$ and ${}^{64}Cu$ as a function of the beam momentum. As expected, the calculation without nuclear field acting on the antiproton ($\xi = 0$) is in a good agreement with the Glauber-model calculations[17], except for very low beam momenta, where the Coulomb potential causes the difference. Both, the Glauber-model and

---

[17]It is clear from simple classical considerations, that the calculation of the absorption cross section based on the
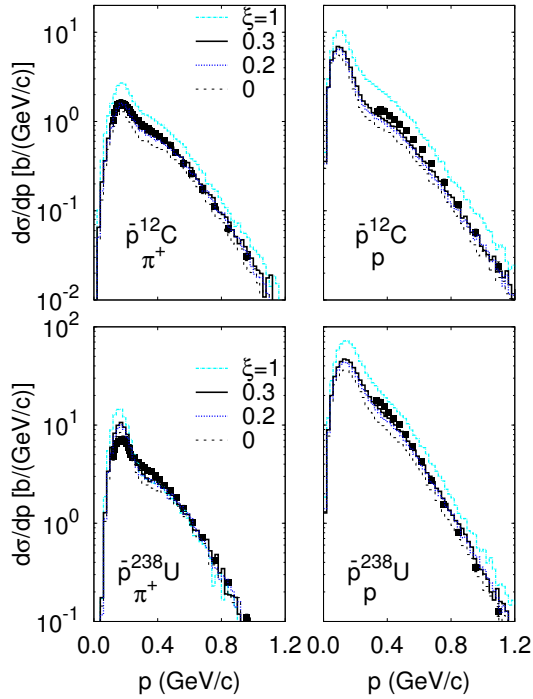
Figure 16: (Color online) The angle-integrated π^+- and proton-laboratory momentum inclusive spectra from $\overline{p}$ interactions with ^{12}C and ^{238}U at 608 MeV/c. The calculated histograms are labeled with the value of the scaling factor, ξ. Data are from [196]. The figure is taken from [195].

GiBUU-($\xi = 0$) calculations describe $\overline{p}$ absorption at high beam momenta $p_{\text{lab}} > 20\,\text{GeV}/c$ quite well.

However, the experimental data on σ_{abs} at low beam momenta require the introduction of an attractive mean-field potential for the antiproton in the GiBUU calculations. Indeed, the antiproton test particles with impact parameters larger than the radius of a nucleus are subject to two-body scatterings, since their trajectories are bent by the attractive potential towards the nucleus. Otherwise, without potential, these particles would propagate along straight-line trajectories avoiding collisions with nucleons[18].

The sensitivity of $\overline{p}$-absorption at low beam momenta to the strength of the attractive potential can be used to determine the scaling factor, ξ, for the antibaryon-meson-coupling constants. This is illustrated in fig. 15 for several values of ξ. As one can see, $\xi = 0.2$-0.3 leads to good agreement with KEK data [177] at $p_{\text{lab}} = 470$-$880\,\text{MeV}/c$. If one defines the real part of the

_____

Boltzmann equation neglecting the interactions of secondaries, exactly reproduces the well known Glauber formula (cf. Eqs. (6),(7) in Ref. [192]). In numerical simulations, small differences appear due to finite statistics.

[18]We have observed a similar effect of the attractive mean-field potential in pion absorption on nuclei, see fig. 10.
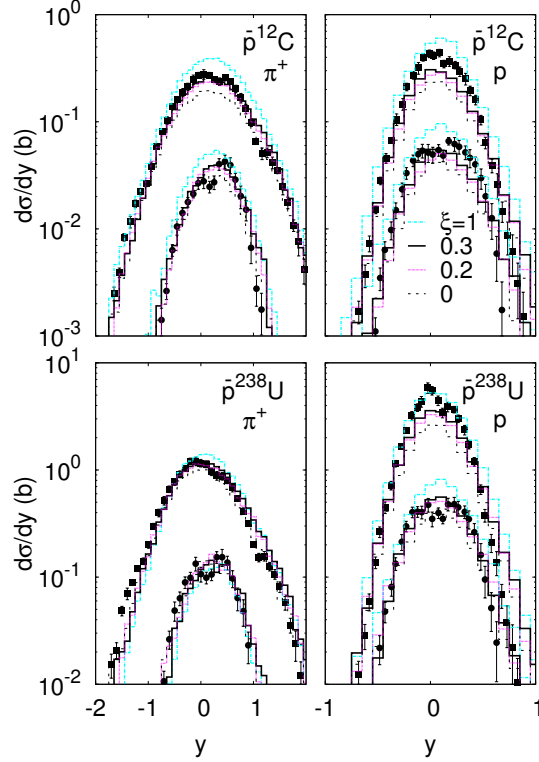
Figure 17: (Color online) π^+- and proton-laboratory rapidity spectra from antiproton interaction with ^{12}C and ^{238}U at 608 MeV/c. The calculated histograms are labeled with the value of the scaling factor, ξ. For the π^+ (proton) spectra, the upper lines and data points correspond to the transverse momenta, $p_T \geq 120$ (330) MeV/c, while lower lines and data points are computed for $p_T \geq 500(600)$ MeV/c. Experimental data are from [196].

antiproton-nucleus optical potential as a Schrödinger-equivalent potential at $E_{\text{lab}} = 0$ GeV [178],

$$\text{Re}(V_{\text{opt}}) = S_{\bar{p}} + V_{\bar{p}}^0 + \frac{S_{\bar{p}}^2 - (V_{\bar{p}}^0)^2}{2m_N} , \tag{215}$$

the range of $\xi = 0.2$-0.3 corresponds to $\text{Re}(V_{\text{opt}}) = -220$ to -150 MeV at normal nuclear density.

In figs. 16 and 17, we show the π^+- and proton-momentum and -rapidity spectra from $\bar{p}$ annihilation on carbon and uranium nuclei at $p_{\text{lab}} = 608$ MeV/c. One observes a quite good agreement of the spectral shapes with experimental data, independent on the choice of the antiproton-mean field. The absolute yields are best described with $\xi = 0.3$, which corresponds to a strongly attractive antiproton potential, $\text{Re}(V_{\text{opt}}) \simeq -200$ MeV in the nuclear center. Such a deep antiproton potential would, in-principle, allow the formation of a strongly bound compact antiproton-nucleus configurations [179, 180, 84, 190].

One observes a peculiar two-slope structure of the pion-momentum spectra. The slope change at $p \simeq 0.3$ GeV/c is caused by pion-nucleon rescattering mediated by the $\Delta(1232)$ resonance. Higher-momentum pions leave the nucleus practically without interacting with nucleons.
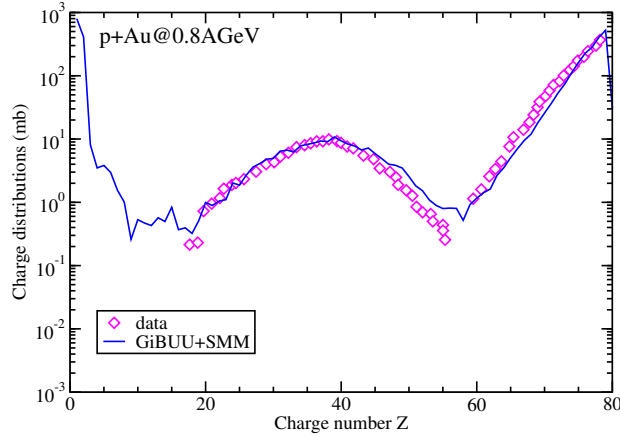
Figure 18: (Color online) Charge distributions for $p + {}^{197}$Au reactions at $E_{\text{beam}} = 0.8$ GeV incident energy. Theoretical calculations (solid line) within the hybrid GiBUU + SMM model are compared with data from [199, 200] (open diamonds). Source: Taken from [80].

Lower-momentum pions are either absorbed via $\Delta(1232)$ resonances, $\Delta N \rightarrow NN$, or get decelerated in collisions with nucleons.

The proton-momentum spectrum shows also two slopes. The fast protons with momenta larger than the Fermi momentum are knocked out from the nucleus by collisions with energetic pions. The lower-momentum protons are slowly evaporated from the nucleus after the fast cascading stage of the reaction.

More discussions on the extraction of the antiproton-nucleus optical potential from GiBUU calculations and comparisons with other analyses can be found in Ref. [195]. Here, we only mention, that in an earlier attempt to extract the $\overline{p}$-optical potential from transport calculations of $\overline{p}$ production from proton-nucleus and nucleus-nucleus collisions, the authors of [197] have found a real part of -200 to -100 MeV consistent with our present analysis.

4.1.4. Reactions induced by protons and heavy ions at SIS energies

The theoretical description of proton-induced reactions at low to intermediate beam energies is a powerful tool to test the GiBUU approach in terms of multifragmentation. A reliable description of the fragmentation process in low-energy reactions is an important step before applying the transport model in reactions at higher energies for the formation of hypernuclei, which is one of the major research topics at the FAIR facility.

However, the description of fragment formation is a non-trivial task within BUU in general. This is so because transport models describe the propagation of one-particle phase-space distributions only and do not account for the evolution of physical phase-space fluctuations. The major difficulty here is the implementation of the real fluctuating part of the collision integral and the reduction of numerical fluctuations using many test particles per physical nucleon, which however would require a large amount of computing resources. Attempts to resolve this issue is still an open problem [198].

The standard approach of phenomenological coalescence models for fragment formation has been found to work surprisingly well in heavy-ion collisions, as long as one considers only one-body dynamical observables (see [201]). In particular, coalescence models are usually applied
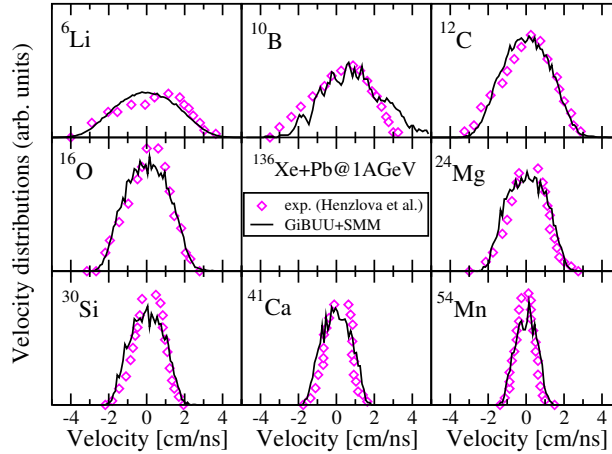
Figure 19: (Color online) Longitudinal velocity distributions in the projectile frame for ^{136}Xe + ^{207}Pb collisions in 1 AGeV collisions. Theoretical calculations (solid curves) are compared with experimental data (open diamonds) from [206]. Source: Taken from [207].

to the description of central heavy-ion collisions, in which a prompt dynamical explosion of a fireball-like system is expected, with the formation of light clusters through nucleon coalescence. In this dilute matter secondary effects are negligible.

However, in hadron-induced reactions and in spectators in non-central heavy-ion collisions the dynamical situation is different. In this cases compression-expansion effects are only moderate (except in reactions with antiprotons, see section 4.1.3), and the fragmentation process happens over a long time scale (compared to the short-lived explosive dynamics of fireballs), which is compatible with a statistical description of the process.

The whole dynamical picture in proton-induced reactions and in spectators in heavy-ion collisions is therefore modeled by a combination of dynamical and statistical models. Usually two types of microscopic approaches have been applied in proton-induced reactions: the intranuclear-cascade (INC) model [202] and the quantum molecular dynamics (QMD) prescription [203], in combination with a statistical multifragmentation model (SMM) [204]. The SMM model is based on the assumption of an equilibrated source and treats its decay statistically. It includes all necessary models of fragment formation, such as sequential evaporation and fission. The transition from the dynamical (BUU) to the statistical (SMM) picture is controlled by the onset of local equilibration, for details see [80]. More information on this field of research can be found in studies of spallation reaction models where very detailed experimental data are available [205].

As an example for the fragmentation of an excited residual source in proton-induced reactions within this approach we compare in fig. 18 our theoretical results for the final charge distribution to experimental data [199, 200] for $p + {}^{197}$Au reactions. The theoretical results are in reasonable agreement both with the *absolute* yields and the shape of the experimental data.

In particular, the fragmentation of the residual source is a complex process involving different mechanisms of dissociation. According to the SMM model, heavy nuclei at low excitation energy mainly undergo evaporation and fission producing the sharp peaks at the very high and low mass numbers. As the excitation energy (or temperature) approaches $T \approx 5$ MeV the sharp structure degrades due to the onset of multifragmentation, and at higher excitations, $T = 5$-17 MeV, one
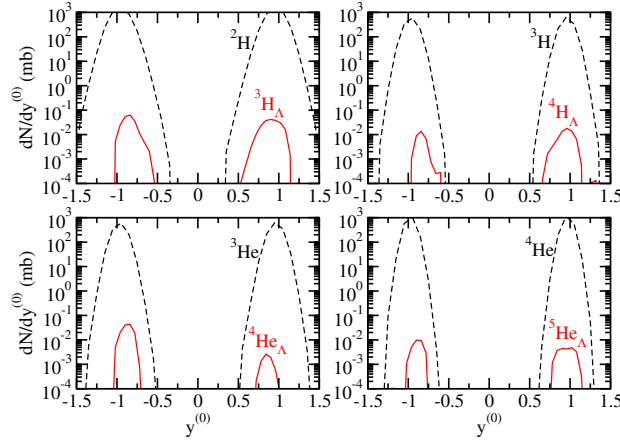
Figure 20: (Color online) Rapidity distributions as function of rapidity, $y^{(0)}$ (normalized to the projectile rapidity in the c.m. frame) of different particle types (as indicated) for ^{12}C+^{12}C at 2 AGeV. Taken from [207].

expects exponentially decreasing yields with decreasing mass/charge number. These different mechanisms of dissociation of an excited source finally lead to a wide distribution in Z as shown in fig. 18. Similar results are obtained for the mass distributions, for the production yields of different isotopes, and also for the energy spectra of emitted neutrons [80].

We have also applied the combined GiBUU+SMM approach to spectator fragmentation in intermediate-energy heavy-ion collisions. A correct description of velocity distributions of statistically produced fragments is crucial for their subsequent coalescence with hyperons. Figure 19 shows fragment-velocity distributions in the projectile frame in comparison with experimental data taken from [206]. The velocity distributions are described rather well on a quantitative level, in particular the width of the Gaussian-like fragment-velocity distributions is well reproduced.

In general, it turns out that the hybrid model leads to a quite satisfactory description for the fragmentation of residual nuclei in proton-induced reactions and for spectator fragmentation in heavy-ion collisions, which is a non-trivial task in transport-dynamical approaches. We note again, that the nonequilibrium dynamics has been treated in a microscopic way using the relativistic coupled-channel transport approach, which is an important step in extracting the properties of the excited configuration. Afterwards the excited fireball-like systems decay statistically according to the SMM model.

An important application of the combined GiBUU+SMM model is the study of hypernuclei in spectator fragmentation. The production of hypernuclei in energetic collisions between light nuclei is one of the major research topics investigated by the HypHI-collaboration at GSI. The reason for selecting very light systems is the easier identification of hypernuclei via the weak decay of a Λ hyperon into a proton and a negative pion. In earlier theoretical studies, see, e.g., [208], cross sections of the order of only few microbarn (μb) were predicted, which can be easily understood: in collisions between very light systems, such as ^{12}C+^{12}C at 2 AGeV, secondary re-scattering events inside the spectator matter, which are important for producing low energetic hyperons, are rare processes due to the small interaction volume. The situation is different in collisions between heavy nuclei due to the high production rate of strangeness and many secondary scattering events. The formation of hypernuclei in spectator fragmentation is performed with a phase-space coalescence prescription between the hyperons produced dynamically from GiBUU

and the fragments generated from the SMM model.

We have studied the formation of hypernuclei in spectator fragmentation in $2\,A$GeV ^{12}C$+^{12}$C collisions. Inclusive rapidity spectra for different light fragments and hyperfragments from spectator matter are shown in fig. 20. The estimated hyperfragment-production rate is approximately 5 to 6 orders of magnitude lower than that of fragment production in general. This is obvious, since the strangeness-production cross sections from exclusive primary channels, i.e., primary $BB \to BYK$, $BB \to BBK\overline{K}$, and secondary ones ($B\pi \to YK$ and $B\overline{K} \to \pi Y$, where B stands for a baryon and Y for a hyperon) are very small (orders of few μb) [123]. Among the different processes contributing to the formation of hypernuclei, $BB \to BYK$ and $\Lambda B \to \Lambda B$ and the secondary one $B\pi \to YK$ give the major contribution to the formation of hypernuclei. Strangeness production channels with three- and four-body final states are important for the production of low-energy hyperons that can be captured by spectator matter. The same argument also holds for secondary re-scattering via elastic hyperon-nucleon and pion-nucleon processes.

4.1.5. Dilepton spectra from proton-induced reactions

While the vacuum properties of most hadrons are known to reasonable accuracy nowadays, modifications of hadron properties in a strongly interacting environment have attracted a lot of attention and have been intensively studied both theoretically and experimentally. These studies were motivated by the expectation that chiral symmetry may be restored in a nuclear medium at high temperatures or densities [209, 210] and that, as a consequence, the masses of the light vector mesons should be shifted downwards. In the vacuum this approximate symmetry is spontaneously broken as visible in the low-mass part of the hadronic spectrum: chiral partners – hadronic states with the same spin but opposite parity – like the ρ and a_1 meson are different in mass while they should be mass degenerate if chiral symmetry were not spontaneously broken. It turns out, however, that a connection between chiral-symmetry restoration and hadronic in-medium spectral functions is much more involved. QCD sum rules provide a link between the quark-gluon sector and hadronic descriptions but do not determine the properties of hadrons in the strongly interacting medium uniquely. They only provide constraints for hadronic models, which are still needed for calculating the in-medium self-energies of hadrons and their spectral functions. Most of these models predict a sizeable in-medium broadening of the vector mesons, but only very small mass shifts [68]. Experiments looking for such effects have used various probes (for details see [68, 211]).

For studying in-medium effects, the more prominent hadronic decay modes of the vector mesons are unfavorable, since they are affected by strong final-state interactions with the hadronic medium – in contrast to the rare dilepton decay modes, which only feel the electromagnetic force. Therefore the latter are ideally suited to carry the in-medium information outside to the detector, undisturbed by the hadronic medium.

Light vector mesons are particularly suited for these investigations since – after production in a nuclear reaction – they decay in the nuclear medium with sizable probability because of their short lifetimes (this is particularly valid for the ρ meson, and to a lesser extent for the ω and ϕ). Experimentally this field has been addressed in reactions with hadronic and with photon beams (for the latter see discussion in section 4.3.4). Experimental results are summarized and critically evaluated in recent reviews [68, 211, 212, 213]. Almost all experiments report a softening of the spectral functions of the light vector mesons ρ, ω, and ϕ. Increases in width are observed depending on the density and temperature of the hadronic environment. Mass shifts are only reported by the KEK group [214, 215], which studied ρ, ω, and ϕ production in proton-nucleus
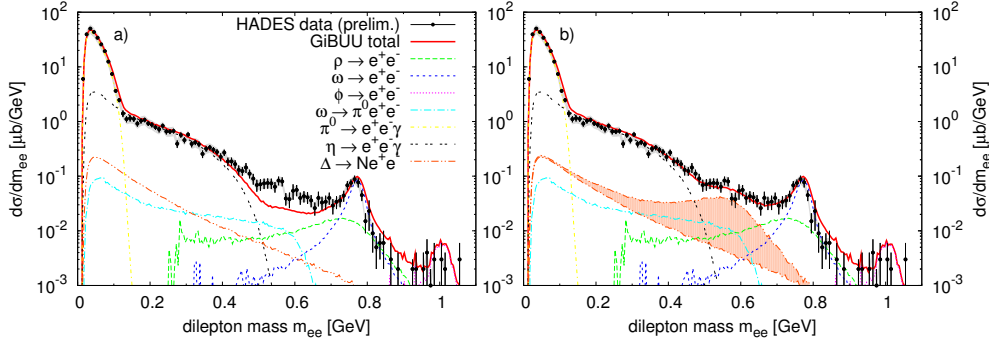
Figure 21: (Color online) Dilepton spectra for $p + p$ collisions at $E_{\text{kin}} = 3.5$ GeV. a) Mass spectrum without Δ form factor, b) mass spectrum with Δ form factor. Figure taken from [219].

reactions at 12 GeV. Also, the HADES detector at GSI has started an ambitious program for measuring dilepton spectra from $p + p$, $p + A$ and $A + A$ reactions [216].

First transport-theoretical calculations for dilepton production in heavy-ion reactions were done quite early (see, e.g., the work by Ko *et al.* [217] and by the Giessen group using a predecessor code to GiBUU [218]). Here we apply the GiBUU transport model to the $p + p$ and $p + \text{Nb}$ reactions studied by the HADES collaboration. We use GiBUU to generate dilepton events and pass them through the HADES acceptance filter, in order to compare our calculations directly to the experimental data measured by HADES.

It is very important to make sure that one understands the elementary reactions before moving on to heavier systems, which involve effects of the nuclear medium. Fortunately, HADES has also measured dilepton spectra from elementary $p + p$ reactions. These provide a base line for exploring the heavier nuclear systems.

Figure 21 shows a comparison plot of a GiBUU simulation to HADES data [220] for a proton beam of 3.5 GeV kinetic energy impinging on a fixed proton target. This setup corresponds to a center-of-mass energy of $\sqrt{s} = 3.18$ GeV. The theoretical results have been corrected for the HADES acceptance and reasonably reproduce the shape of the data over most of the mass spectrum. In the intermediate mass region around 500-600 MeV the inclusion of a proper transition form factor for the Δ-Dalitz decay [221] (shaded area) is crucial for describing the data. Without such a form factor, the calculation strongly underestimates the experimental data in this region (by at least a factor of two). The electromagnetic N-Δ transition form factor is well-constrained by electron-scattering data in the space-like region. In the time-like regime of the Δ-Dalitz decay, however, there is no reliable data available so far. This missing experimental information on the Δ form factor represents one of the largest uncertainties in the dilepton spectra presented here. Eventually the HADES data might help to shed more light on this open issue and to provide constraints for form factor-models like the one of [221].

Another channel which could possibly contribute in the intermediate-mass region is $\eta \rightarrow e^+e^-$. The current upper limit for the branching ratio of this decay would overshoot the HADES data by at least a factor of four. However, there is no η peak visible in the data, and also the theoretical expectations from helicity suppression are still orders of magnitude below the current experimental limit. Therefore, the observed HADES dilepton spectrum at 3.5 GeV constrains this partial decay width even further.

Within the level of agreement in the elementary $p + p$ collisions shown in fig. 21, we have a

good baseline for studying in-medium effects in p + Nb, although the issue of the Δ-Dalitz form factor is not completely settled.

In p + Nb reactions one has to consider some additional effects, compared to the elementary $p + p$ reactions. First of all, the primary $p + N$ collisions will be nearly identical, apart from binding effects and some Fermi smearing, but besides $p + p$ also $p + n$ collisions will play a role. Furthermore, the produced particles will undergo final-state interactions within the Nb nucleus, and processes like meson absorption and regeneration may become important. On average, the secondary collisions will have lower energies than the primary $N+N$ collisions, therefore also the low-energy resonance part of the collision term will be involved. Finally, also the vector-meson spectral functions may be modified in the nuclear medium.

Figure 22 shows simulated dilepton spectra for p + Nb collisions at 3.5 GeV in various scenarios, compared to the data from [222]. The overall agreement is not quite as good as in the $p + p$ case. Already in the pion channel we slightly overestimate the data. This might have various reasons: too little absorption, too much secondary-pion production in GiBUU or even a normalization problem in the data.

According to [223], the data have been normalized by comparing charged-pion spectra measured by HADES in p + Nb to those measured by the HARP collaboration. However, the cross sections obtained by HARP had to be extrapolated to the slightly different beam energy and nuclear target of HADES. This procedure is responsible for most of the systematic error of the data (roughly 28 %), which is shown as a gray band in the figures.

Another striking feature of the $p+$Nb system is that the simulation gets close to the data in the intermediate mass range, even without any Δ form factor. Including the form factor will slightly overshoot the data. Most of the intermediate-mass gap observed in $p + p$ is now filled up by low-mass ρ mesons, which are produced in secondary collisions. Even in $p + p$ collisions, one might already find a similar effect by describing ρ-meson production via resonance excitation, which could give stronger contributions in the low-mass part of the ρ spectral function than Pythia's string-fragmentation model.

The mass spectrum above 500 MeV can receive further modifications from the inclusion of in-medium effects in the vector-meson spectral functions. Figure 22 shows a few typical in-medium scenarios: The first one includes a collisionally broadened in-medium width (cf. section 2.4.2), while the second one assumes a pole-mass shift according to

$$m^*(\rho) = m_0 \left(1 - \alpha \frac{\rho}{\rho_0} \right) \tag{216}$$

with a scaling parameter, $\alpha = 16\%$. The third scenario combines both of these effects. The modifications introduced by these scenarios are roughly as large as the systematic errors of the data. This fact, together with the discrepancy in the π^0 channel and the uncertainty of the Δ form factor, presently makes it impossible to draw any hard conclusions on vector-meson properties in cold nuclear matter from the HADES data.

In summary, the HADES data from elementary $p + p$ collisions at 3.5 GeV kinetic beam energy can be described very well by the Pythia event generator with a few adjusted parameters, as employed in the GiBUU model. It has been found that the intermediate mass region is sensitive to a VMD-like transition form factor for the Δ Dalitz decay. Building on this agreement for the elementary reaction, the p + Nb reaction at the same beam energy is reasonably well described by the GiBUU transport model.

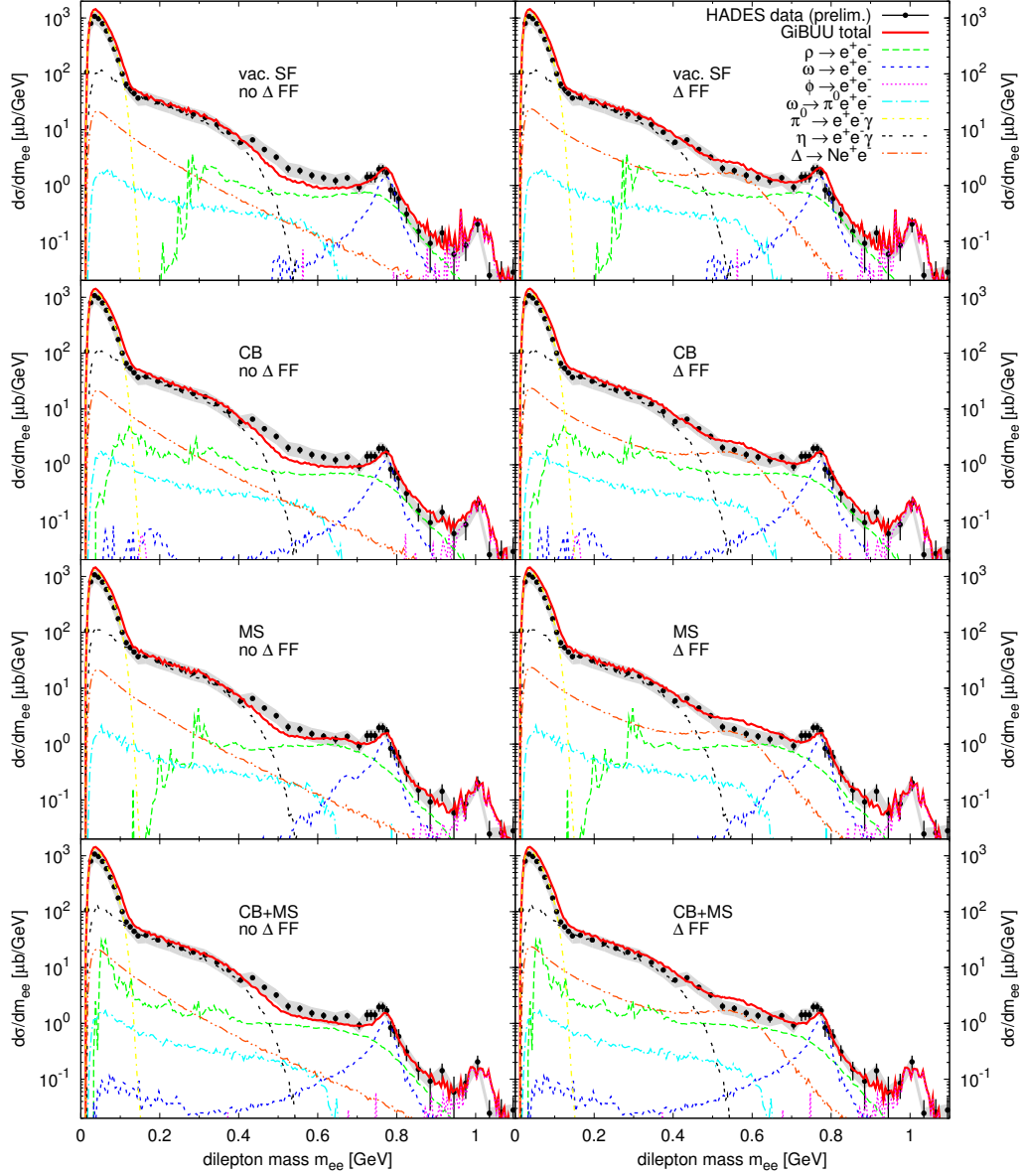Figure 22: (Color online) Dilepton mass spectra for p + Nb collisions at E_{kin} = 3.5 GeV. Left column: without Δ form factor. Right column: with Δ form factor. From top to bottom: vacuum spectral functions for the vector mesons, collisional broadening, 16 % mass shift, collisional broadening plus mass shift. Figure taken from [219].
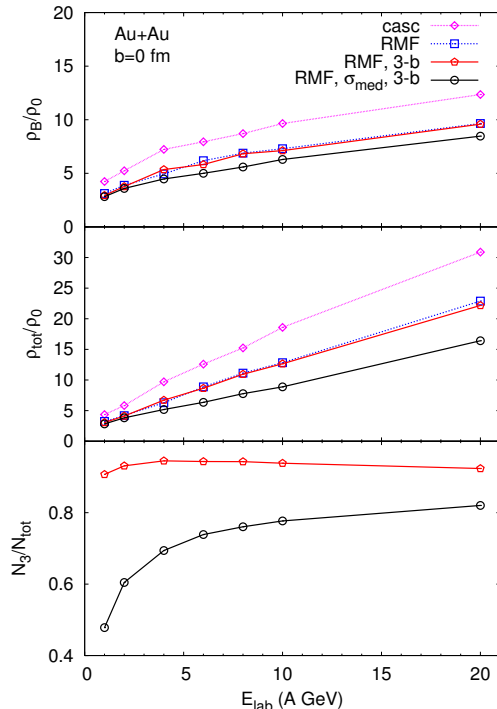
Figure 23: (Color online) Top, middle and bottom panels, respectively: the maximum central baryon density, the maximum central total (i.e. baryon plus meson) density, and the maximum ratio of the three-body collision frequency to the total (two- plus three-body) collision frequency reached in central Au+Au collisions vs. the beam energy. The binary-cascade calculation (i) is shown by lines with open diamonds. The calculation with RMF and vacuum cross sections (ii) is presented by lines with open boxes. The results with RMF and three-body collisions computed with vacuum cross sections (iii) are plotted with lines with open pentagons. Finally, calculations with RMF, three-body collisions and in-medium cross sections (iv) are shown by lines with open circles. Figure taken from [79].

4.1.6. Heavy-ion collisions at AGS/SPS energies

At higher incident energies the meson production starts to dominate the reaction dynamics. Heavy-ion collisions (HICs) are very complicated processes, where all possible hadron-hadron collision channels can potentially contribute, particularly in the AGS/SPS energy regime relevant for CBM@FAIR physics. The microscopic transport description of HICs at these high energies is not only an interesting physical problem, but also a quality test of practically all parts of the GiBUU code.

Here we will consider the central Au(2-20 AGeV) + Au and Pb(30 and 40 AGeV) + Pb collisions. The formation of a highly-compressed baryonic matter ($\rho \sim 10\rho_0$) is expected in these reactions with a possible transition to the partonic phase [224, 225, 226, 127, 227, 79]. By observing the deviations of the microscopic transport predictions with experiment one can, in principle, speculate on the signals of a deconfinement.

The RMF mode of calculations (see sections 3.1.3 and 3.1.5) is used in the description of HICs. The relativistic description of a nuclear mean field is important since even in the ground state nuclear matter at high densities the motion of nucleons is relativistic. The NL2 set of parameters of the RMF model from Ref. [228] has been applied, see table 2 in section 3.1.3.
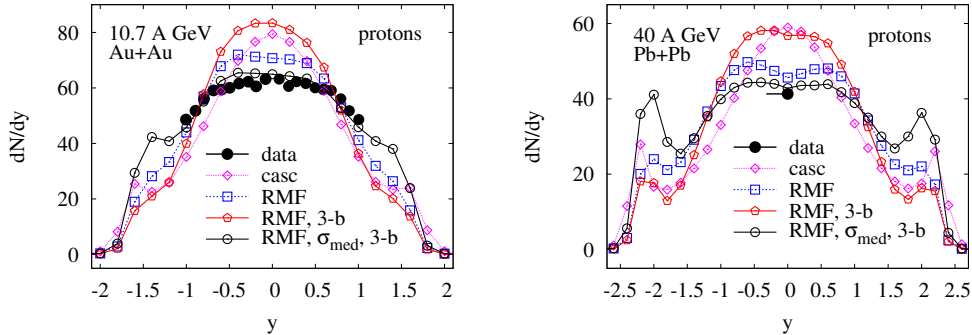
Figure 24: (Color online) Proton rapidity distributions for central ($b \leq 3.5$ fm) Au+Au collisions at 10.7 AGeV (left panel), and central ($b \leq 4$ fm) Pb+Pb collisions at 40 AGeV (right panel). The experimental data for the Au+Au system are taken from Ref. [230] and correspond to the 5 % most central events. The data for Pb+Pb are from Ref. [231] (7 % centrality). Notations are the same as in fig. 23. Source: Figure taken from [79].

An important feature of relativistic HICs is the Lorentz contraction of colliding nuclei in the c.m. frame. In order to resolve Lorentz-contracted density profiles, in calculating the σ-field and the baryon four-current we have used a grid with cell sizes of $\simeq (1 \times 1 \times 1/\gamma)$ fm. Here, the z-axis is the beam axis, and the γ-factor is taken in the c.m. frame of the colliding nuclei (cf. Appendix D.1). We have used the parallel-ensemble technique (cf. Appendix D.4.1) with $N = 200$ test particles per nucleon. For more details concerning the numerical treatment of the mean-field propagation and high-energy baryon-baryon and meson-baryon collisions see Ref. [79, 67].

The cross sections entering the collision integral are taken from a fit to data or from simple model calculations tuned to reproduce some selected data sets on elementary hadron-nucleon collisions. Such a procedure can only describe vacuum cross sections. In the nuclear medium, the cross sections are modified, e.g., due to the change of the energy threshold for particle production by the mean fields. There is no well established theoretical method to determine the in-medium cross sections yet. Only for relatively simple processes, like, e.g., elastic scattering, $NN \rightarrow NN$, [53] or $\Delta(1232)$ resonance excitation, $NN \rightarrow N\Delta$, [119, 229] the theoretical model calculations of in-medium cross sections are available. These calculations point toward an in-medium reduction of the baryon-baryon cross sections at high baryon densities. The same effect is expected also from a simple screening picture [96], since the geometrical radius of the cross section should not exceed the inter-particle distance.

We have applied two simple models for the in-medium cross sections described in section 3.3.4. In the first scheme, the "free" invariant energy $\sqrt{s_{\text{free}}}$ of the colliding particles is determined from eq. (191) and used for all reaction cross sections, $\sigma_{12 \rightarrow X}(\sqrt{s_{\text{free}}})$. In the second scheme, we apply the in-medium-modified cross sections of eq. (194) to baryon-baryon collisions. We recall, that these reduced cross sections are obtained assuming that the matrix elements of the processes $B_1 B_2 \rightarrow B_{1'} B_{2'} M_{3'} M_{4'} ... M_{N'}$ and $B_1 B_2 \rightarrow B_{1'} B_{2'}$ are not changed in nuclear medium. The baryon-meson and meson-meson cross sections are always calculated in the vacuum. We expect that these cross sections are less subject to in-medium modifications due to the smaller number of participating fermions providing the main in-medium reduction effect by powers of m^*/m in the modification factor (195). For brevity, the first scheme will be referred to as the calculation with vacuum cross sections below. The second scheme will be called the
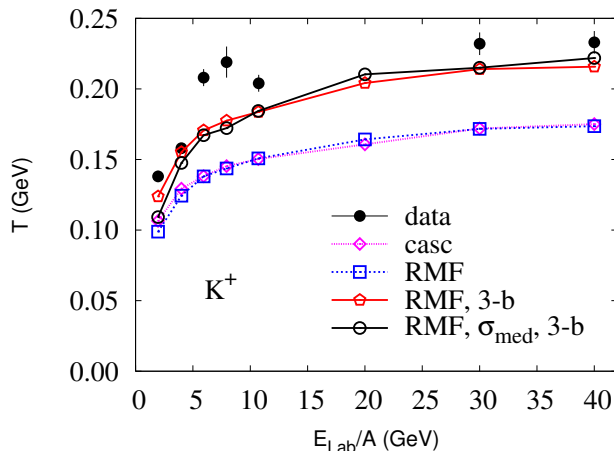
77

Figure 25: (Color online) Inverse-slope parameter of the K^+ transverse mass spectrum at mid rapidity for central Au+Au and Pb+Pb collisions as a function of the beam energy. The data are taken from [236, 237, 238]. Notations are the same as in fig. 23. Source: Figure taken from [79].

calculation with in-medium cross sections.

As we will see below, baryon densities 5-10ρ_0 are reached in central HIC at $E_{\text{lab}} = 5$-20 AGeV (see also [227] for a comparison of the different transport models in this energy region). At such high densities, the transition to a partonic phase is possible, which is under extensive discussion in the literature (cf. [224, 225, 226, 232, 227, 233, 234, 235]). In our calculations we follow a more conservative approach based on (pre)hadronic and string degrees of freedom. However, a consistent description of the dynamics of the high baryon density system requires some modification of the standard kinetic approach based on two-body collisions. Indeed, the gas parameter [30] defined as the number of particles in the two-body interaction radius can be larger than unity, $\gamma_{\text{gas}} = (\sigma/\pi)^{3/2}\rho_B \simeq 2$. Here we have taken $\sigma \simeq 40$ mb as the asymptotic high-energy value of the total pp-vacuum cross section and $\rho_B = 10\rho_0$ as the maximum density reached in central Au+Au collision at 20 AGeV. The Boltzmann equation has a firm theoretical ground only if $\gamma_{\text{gas}} \ll 1$. Therefore, many-body collisions should be taken into account at high densities. We have included only the three-body collisions [79], following a simple geometrical approach of Ref. [106].

In order to demonstrate the influence of the various physical ingredients to our model, four types of calculations have been done: (i) pure binary-cascade calculation without mean field using vacuum cross sections; (ii) calculation including the RMF, with only binary collisions using vacuum cross sections; (iii) the same as (ii) but including three-body collisions; (iv) the same as (iii), but using the in-medium baryon-baryon cross sections.

Figure 23 shows the beam-energy dependence of the maximum central baryon and total densities and of the maximum ratio of the three-body and the total collision frequency N_3/N_{tot} reached in central Au+Au collisions. The various schemes lead to an uncertainty in the maximum-baryon density of about 30 % and in the maximum total density of about 50%. The RMF strongly reduces the reached maximum-baryon and total densities. This can be understood as a consequence of the formation of a repulsive vector field. The three-body collisions do not influence these two observables. The in-medium cross sections reduce the maximum densities
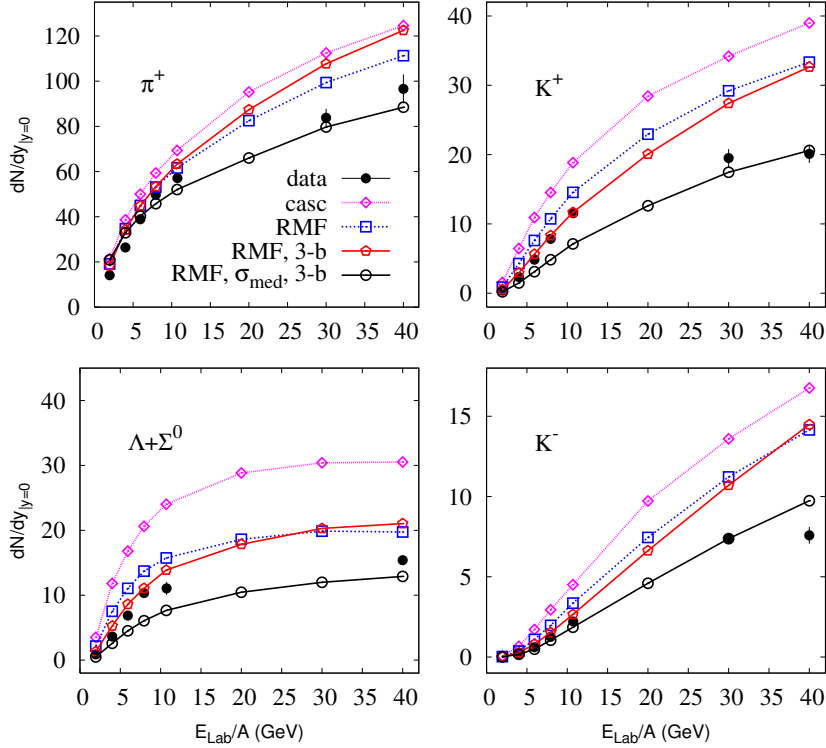
Figure 26: (Color online) The yield of π^+ (upper left panel), K^+ (upper right panel), $\Lambda + \Sigma^0$ (lower left panel) and K^- (lower right panel) at mid rapidity as function of the beam energy for central Au+Au collisions at $E_{lab} \leq 20\,A$GeV and Pb+Pb at $E_{lab} = 30$ and $40\,A$GeV. The data are taken from [239, 236, 237, 238, 240, 241, 242, 243, 244]. Notations are the same as in fig. 23. Figure taken from [79].

further. In particular, the total density decreases strongly due to less pion production. The fraction of three-body collisions is quite high, about 80-90 % of all particle-collision events in a HIC at $E_{lab} = 10$-$20\,A$GeV. At high beam energies, the meson-baryon collisions dominate, which are always computed with vacuum cross sections. Therefore, the sensitivity of the ratio N_3/N_{tot} to the in-medium baryon-baryon cross sections becomes weaker with increasing beam energy.

For comparison with experiments we first address the stopping power of nuclear matter. Figure 24 shows the proton-rapidity distributions in central Au+Au collisions at 10.7 AGeV and for the central Pb+Pb collisions at 40 AGeV. The cascade calculation produces too much stopping. Including the RMF reduces the stopping power, leading to closer agreement with the experimental rapidity spectra. Taking into account three-body collisions increases the stopping power strongly, which again results in an overestimation of the mid-rapidity-proton yields. Using in-medium cross sections reduces the stopping power, leading again to good agreement with the data. Therefore, a stronger deviation from thermal equilibrium caused by in-medium reduced cross sections is compensated by the additional thermalization efficiency due to three-body collisions.

In fig. 25 we present the inverse-slope parameter, T [236, 237, 238] of the K^+-transverse mass spectrum at mid rapidity vs. the beam energy. Neglecting three-body collisions, we under-
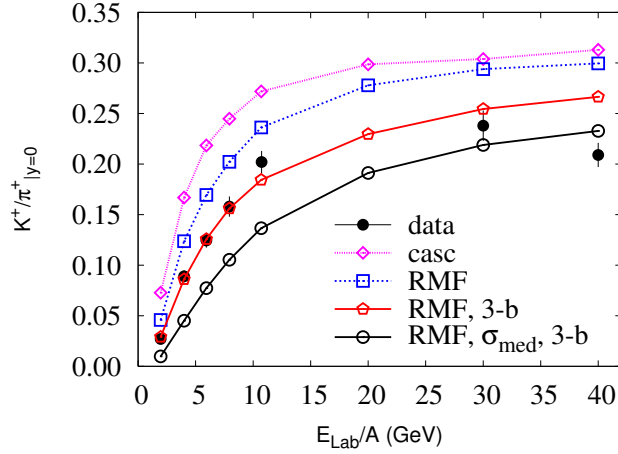
Figure 27: (Color online) The yield ratio K^+/π^+ at mid rapidity in central Au+Au and Pb+Pb collisions. The data are taken from [239, 237, 238]. Notations are the same as in fig. 23. Figure taken from [79].

estimate the inverse-slope parameter, T, by about 30 %. Including three-body collisions leads to a fair agreement with the data, except for the points at 5.93 and 7.94 AGeV, where we still underestimate the experimental inverse slope parameter by about 20 %.

Figure 26 shows the midrapidity yields of π^+, K^+, $(\Lambda + \Sigma^0)$, and K^- vs. the beam energy for central Au+Au collisions at 1.96, 4.00, 5.93, 7.94, 10.7 AGeV, and 20 AGeV and for central Pb+Pb collisions at 30 and 40 AGeV. The calculations for the Au+Au system were done in the impact parameter range $b \leq 3.5$ fm (5 % of the geometrical cross section, cf. [239]). For the Pb+Pb system, we have chosen a slightly larger impact parameter range of $b \leq 4$ fm (7 % of the geometrical cross section, cf. [237]).

We observe that the pure cascade calculation overestimates the meson and hyperon production. Using the RMF reduces the mid-rapidity-meson yields by about 15 %. The mid-rapidity-hyperon yield is reduced even more, by about 30 %. This reflects the behavior of the proton-mid-rapidity yield shown in fig. 24, since the mean field acts on the hyperons too. The inclusion of three-body collisions affects the mid-rapidity yields of the produced particles rather weakly. Finally, using the in-medium cross sections reduces the particle production quite strongly: for mesons by about 30 % and for hyperons by about 50 %. The calculation with the in-medium cross sections turns out to be in good agreement with the data on pion and K^- production, while it underestimates the K^+ and hyperon yields below 40 AGeV.

Figure 27 shows the K^+/π^+ ratio at midrapidity vs. the beam energy. It is interesting, that the three-body collisions reduce the ratio quite strongly. This is due to a combination of two small effects visible in fig. 26: increase of the pion yield and decrease of the kaon yield by the three-body collisions. The calculation in the RMF mode with vacuum cross sections and three-body collisions is in the best agreement with the experimental data below 30 AGeV. However, we fail to describe the reduction of the K^+/π^+ ratio above 30 AGeV.

To summarize this subsection, the model works quite well for HICs in the energy region between 2 and 40 AGeV. HICs at lower beam energies remain to be studied in detail within the present implementation of the model. At higher energies explicit consideration of partonic degrees of freedom may become important.

4.2. Electron-induced reactions

In photonuclear reactions, either with electrons or with real photons in the incoming channel, nearly the entire nucleus is 'illuminated' during the first interaction[19] This is not so in hadron-induced reactions, where already a sizeable initial-state interaction occurs. The photonuclear reactions are, therefore, an ideal testing ground for theories of in-medium changes of hadronic properties. They also present an opportunity for a sensitive test of theories and methods to describe neutrino-nucleus interactions, essential for an understanding of neutrino long-baseline experiments, that today exclusively work with nuclear targets (see discussions later in section 4.4) because photonuclear reactions contain the very same vector part of the interaction as in the neutrino-induced reactions.

Electron scattering off nuclei in the regime of energy transfer between 0.1 and $1\,\mathrm{GeV}^2$ has been addressed by several experiments within the last two decades; for a recent review of quasi-elastic scattering off nuclei cf. Ref. [248]. Comparing the measured nuclear cross sections to the nucleon cross sections, several modifications have been observed. First of all, nuclear Fermi motion leads to a smearing of the peak structures such as in the quasi-elastic and Δ regions. Furthermore, one observes a quenching of the spectral strength around the quasi-elastic peak. In contrast to the quenching in the peak region, one observes an enhancement in the so-called dip-region between the quasi-elastic and the Δ peak. The peak position of the Δ resonance is found to be both A and Q^2 dependent: it exhibits a shift towards lower invariant masses for $Q^2 \leq 0.1\,\mathrm{GeV}^2$ and a shift towards higher invariant masses for higher Q^2 (for more details see the discussions in Ref. [58]).

The basis of nearly all theoretical studies of photonuclear reactions with nuclei has been the so-called impulse approximation. In this approximation one assumes that the incoming photon interacts only with one nucleon at a time; simultaneous interactions with two or more nucleons are neglected. This approximation should hold for momentum transfers large enough that a single nucleon is resolved (i.e. roughly for $|q| > 300\,\mathrm{MeV}$). Only very few studies have been undertaken to investigate the influence of 2-nucleon primary interaction processes (see, e.g., [249, 250, 251, 252], for a broader discussion of 2N processes see [253]).

The influence of nuclear effects on both elastic electron- and neutrino-scattering cross sections has been investigated by Benhar *et al.* using an impulse approximation model with realistic spectral functions obtained from nuclear many-body-theory calculations [254, 255]. In particular, they achieve good agreement with inclusive electron-scattering data in the quasi-elastic-peak region. Nuclear effects in the quasi-elastic (QE) region have also been investigated in detail by Nieves *et al.* for electrons [251] and neutrinos [256] where, among other nuclear corrections, long range nuclear correlations have been included. Also this approach describes inclusive electron scattering data with impressive agreement. A relativistic Green's-function approach has been applied by Meucci *et al.* to inclusive electron [257] as well as to inclusive neutrino nucleus reactions [258]. Butkevich *et al.* [259] addresses both neutrino and electron scattering with special emphasis on the impact of different impulse approximation (IA) schemes: plane wave IA (PWIA) and relativistic distorted wave IA (RDWIA). Also the Ghent group applies RPWIA and RDWIA models to neutrino and electron scattering in the QE region [260]; lately they have extended their framework to pion production [261].

---

[19]Here, we disregard the phenomenon of shadowing, which may become important for low Q^2 processes at higher energies [245]. In Ref. [246, 247] we have developed a method to take the shadowing effect into account in BUU calculations by using a properly derived profile function for the nucleus.

In this subsection we will, therefore, compare results of some of these studies with those obtained within the GiBUU model for electron-induced reactions on nuclei, starting from low-energy quasi-elastic scattering over resonance excitations up to the highest energies available, where one tries to learn something about hadron formation and attenuation in the medium. We start with a discussion of electron- and photon-induced processes and then turn to neutrino-induced reactions. Within our GiBUU framework, we aim at a consistent treatment of the initial vertex and the final state processes and we emphasize that these should not be treated separately.

The relevant elementary cross sections are all given in Appendix C.

4.2.1. Inclusive cross sections

Within the GiBUU model, which employs a local Thomas-Fermi distribution for the momentum distribution of nucleons, the inclusive cross section for scattering off a nucleus is given by (cf. eq. (144))

$$d\sigma_{\text{tot}}^{\ell A \to \ell' A} = g \int_{\text{nucleus}} d^3r \int \frac{d^3p}{(2\pi)^3} \Theta\left(p_F(\boldsymbol{r}) - |\boldsymbol{p}|\right) d\sigma_{\text{tot}}^{\text{med}}. \tag{217}$$

Here, g is the spin-degeneracy factor. The medium-corrected cross section, $d\sigma_{\text{tot}}^{\text{med}}$, contains medium-dependent changes of the elementary cross section such as the spectral function of the outgoing nucleons, the effects of Pauli-blocking of the final state and a flux correction factor.

This expression for the total cross section can be rewritten such that the hole spectral function appears in it. With that aim in mind we define the hole spectral function by

$$P(\boldsymbol{p}, E) = \int_{\text{nucleus}} d^3r \, \Theta\left[p_F(\boldsymbol{r}) - |\boldsymbol{p}|\right] \Theta(E)\delta\left(E - m^* + \sqrt{\boldsymbol{p}^2 + m^{*2}(\boldsymbol{r}, \boldsymbol{p})}\right). \tag{218}$$

In eq. (218), m^* is the effective mass of the bound nucleon, which contains the coordinate- and momentum-dependent potential and E is, as usual, the nuclear separation energy. Equation (217) can now be rewritten as

$$d\sigma_{\text{tot}}^{\ell A \to \ell' A} = g \int dE \int \frac{d^3p}{(2\pi)^3} P(\boldsymbol{p}, E) \, d\sigma_{\text{tot}}^{\text{med}}. \tag{219}$$

Written in this form the cross section has the same appearance as that in [248] or [262].

The spectral function in eq. (218) contains the real part of the self-energy through the potential in m^*, but it does not account for the imaginary part. The latter can be implemented by using first

$$\delta\left(E - m^* + \sqrt{\boldsymbol{p}^2 + m^{*2}(\boldsymbol{r}, \boldsymbol{p})}\right) = 2p^{*0}\delta\left(p^2 - m^{*2}\right) \tag{220}$$

with the four-vector $p = (p^{*0}, \boldsymbol{p})$ and $p^{*0} = m^* - E$. One can then replace the δ-function in eq. (220) by a Breit-Wigner distribution of the form (cf. eqs. (76) and (81))

$$\mathcal{A}(p) = -\frac{1}{\pi} \frac{\text{Im}\,\Pi(p)}{(p^2 - m^2 - \text{Re}\Pi(p))^2 + (\text{Im}\,\Pi(p))^2}, \tag{221}$$

where $\Pi(p)$ denotes the self-energy of the nucleon. The real part of Π contains the effects of the mean field potential (and possible dispersive corrections)
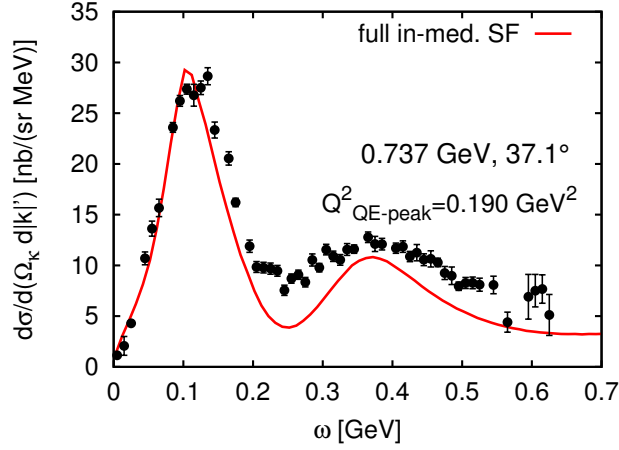
$$m^{*2} = (m + U_s)^2 = m^2 - \text{Re}\,\Pi, \tag{222}$$

Figure 28: (Color online) Inclusive electron cross section $\mathrm{d}^2\sigma/\mathrm{d}\omega\mathrm{d}\Omega_{k'}$ on ^{16}O as a function of the energy transfer ω for a beam energy of 0.737 GeV and a scattering angle, $\theta_{k'} = 37.1\,^\circ$, in comparison with the data measured by O'Connell *et al.* [263]. The parameter Q^2 denotes the four-momentum-squared at the quasi-elastic-peak position (from [58]).

the imaginary part, $\mathrm{Im}\,\Pi$, contains the width of the nucleon's spectral function in medium (see eq. (80)). In a low-density approximation the latter is given by

$$\Gamma = -\frac{1}{\sqrt{p^2}}\,\mathrm{Im}\,\Pi(p) = \rho v \sigma_{\mathrm{NN}}\,. \tag{223}$$

In [264, 265, 266] we have shown that transport theory can be used to calculate selfconsistently spectral functions of nucleons in nuclei which agree very well with those obtained in state-of-the-art nuclear many-body calculations.

The spectral function in eq. (218) differs in two essential aspects from that of the global Fermi-gas model often used in theoretical treatments of quasi-elastic scattering off nuclei. While the momentum distribution of a global Fermi-gas model is constant up to the Fermi momentum and then drops abruptly to zero, here – because of the smooth density distribution – the momentum distribution has more strength at lower momenta and drops smoothly to zero for large p (see Fig. 6 in [58]). In addition, the presence of the *r*-dependent potential, V (implicit in m^*), in eq. (218) leads to a smoothing of the distribution in E, which in the global Fermi-gas model exhibits sharp ridges at the on-shell values of this variable. This E smearing appears even without using a width (related to the imaginary part of the self-energy) in the spectral function eq. (221). The spectral function eq. (218) is thus much closer to that in realistic models [254] than that of the global Fermi gas.

It is, therefore, not surprising that the spectral function eq. (218), when used in calculations of the total inclusive electron cross section on nuclei, leads to very reasonable results. This is illustrated in fig. 28, where the peak at the lower energy transfer, $\omega \approx 0.1$ GeV, is the quasi-elastic peak. In general, the agreement with the data at the quasi-elastic peak is nearly as good as that of Benhar *et al.* [267]. The latter is based on a state-of-the-art nuclear many-body calculation, but does not contain the Δ resonance excitation.

In fig. 29 we compare the results of the GiBUU model over a wider range of electron energies with the results of other theoretical approaches. At the lowest energy, the QE peak in GiBUU occurs at too low energy transfer with too much strength, similar to the result obtained by Butkevich
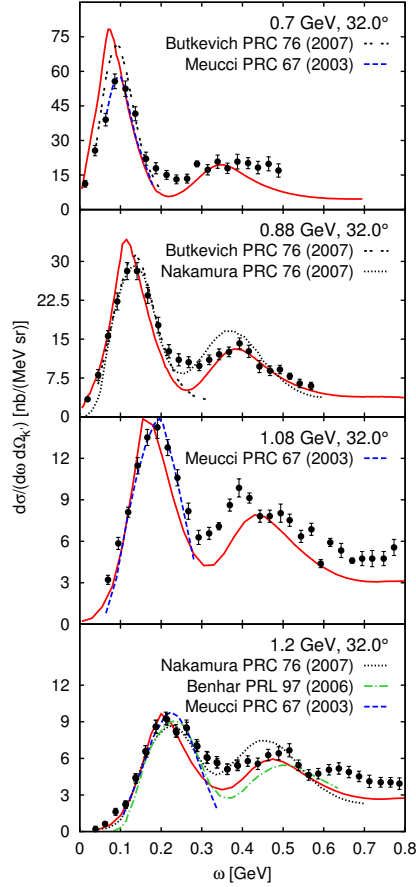
Figure 29: Inclusive electron cross section $\mathrm{d}^2\sigma/\mathrm{d}\omega\mathrm{d}\Omega_{k'}$ on $^{16}\mathrm{O}$ as a function of the energy transfer, ω, for four beam energies indicated in the figure and a scattering angle $\theta_{k'} = 32^\circ$. The solid lines give the results of the GiBUU calculation, the dashed lines are taken from Meucci *et al.* [258], the double-dashed lines give the results of Butkevich *et al.* [259], the dotted lines those of Nakamura *et al.* [255], and the dash-dotted line shows the result of Benhar *et al.* [268]. The data are from Anghinolfi *et al.* [269, 270]. Taken from [58].

et al. [259]. These deficiencies may be due to the invalidity of the impulse approximation for the very small momentum transfer at the quasi-elastic peak. For higher energies the peak positions and strengths are described quite well by GiBUU. Similar to fig. 28, a consistent discrepancy shows up at the high-energy side of the QE peak, where the data are systematically slightly underestimated. This may be due to either an underestimate of the Δ strength at this higher energy, possibly due to coherent excitation, or to some contribution from more complicated particle-hole configurations than those contained in the Local Fermi-gas model. The former possibility indicates that it is indeed essential to describe quasi-elastic scattering and resonance excitation simultaneously since both processes overlap in the total inelastic cross section for intermediate energy transfer.
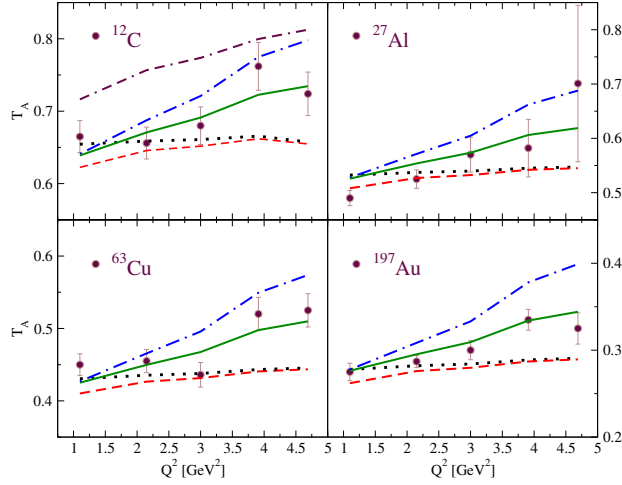
Figure 30: (Color online) Transparency, T_A, vs. Q^2 for ^{12}C (left, top panel), ^{27}Al (right, top), ^{63}Cu (left, bottom) and ^{197}Au (right, bottom). The dotted curves correspond to FSI with the full hadronic cross section, and the dashed curves include the shadowing corrections. The dash-dotted curves correspond to the in-medium cross sections defined according to the Lund-model-formation-time concept, which includes the Q^2-dependent (pre)hadronic interactions, eq. (227), for the transverse contribution. The solid curves describe the effect of only time dilatation with a Q^2-independent pedestal value in the effective cross section. The dash-dash-dotted curve in the top-left panel realizes the CT effect both in the longitudinal and transverse channels. The experimental data are from Ref. [271]. Taken from [273].

4.2.2. Exclusive pion production

The interactions of high-energy virtual photons with nuclei provide an important tool to study the early stage of hadronization and (pre)hadronic FSI at small distances $d \sim 1/\sqrt{Q^2}$. A further advantage of lepton-induced reactions is that one may vary the energy ν and virtuality Q^2 of the incident photon independently of each other. This allows us to study the phenomenon of Color Transparency (CT), i.e. the reduced interaction cross section of a small sized color singlet object produced in processes at high momentum transfer.

The early onset of CT has been observed at JLAB in semi-exclusive charged pion electro-production off nuclei. Particularly for a theoretical understanding of this kind of experiments the use of BUU is mandatory since the analysis involves different kinematic and acceptance cuts. Transport theory can give all particles in the final state such that the same cuts can be applied also in the calculations.

The nuclear transparencies of pions in the reaction $A(e, e'\pi^+)A^*$ off nuclei are presented in fig. 30. The experimental data are from Ref. [271]. The microscopic input for the primary interaction of the virtual photon with the nucleon follows the GiBUU model which describes both the transverse and the longitudinal cross sections [272]. The coupled–channel GiBUU transport model has been used to describe the FSI of hadrons in the nuclear medium. The formation times of (pre)hadrons follow the time–dependent hadronization pattern as shown in section 3.4.

Our results are consistent with the JLAB data. The data are well reproduced if one assumes that point-like configurations are produced in the regime of hard deep-inelastic scattering (DIS) off partons and dominate the transverse channel.
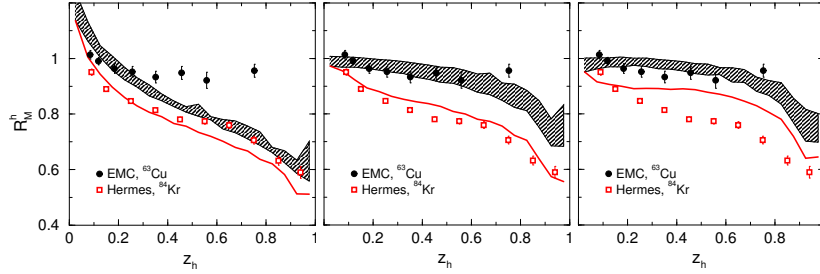
85

Figure 31: (Color online) Nuclear modification factor for charged hadrons. Experimental data are from HERMES at 27 GeV [274, 275, 276] and EMC at 100 and 280 GeV [277]. The predictions for the two EMC energies are given by the lower and upper bounds of the shaded band. he cross-section-evolution scenarios in the calculations are: constant, linear, quadratic (from left to right). Taken from [133].

4.2.3. Hadron attenuation

In the following discussions we will express the medium modification of the spectra via the usual nuclear-modification ratio,

$$R_M^h(\nu, Q^2, z_h, p_T^2, \dots) = \frac{\left[N_h(\nu, Q^2, z_h, p_T^2, \dots)/N_e(\nu, Q^2)\right]_A}{\left[N_h(\nu, Q^2, z_h, p_T^2, \dots)/N_e(\nu, Q^2)\right]_d}, \tag{224}$$

where the hadronic spectra on the nucleus ("A") and on deuterium ("d") are normalized to the corresponding number of scattered electrons. As indicated, the nuclear-modification ratio can be displayed as function of many variables as, e.g., ν, z_h, p_T^2, etc. More detailed information would be provided by multidimensional distributions, which are, however, not yet available experimentally.

The "photonic" parameters of the collisions are given by ν as photon energy and by Q^2 as the transferred squared four momentum. The third parameter to fix the lepton/photon kinematics complete is given by the lepton-beam energy.

The "hadronic" variables we focus on are z_h or p_T^2. Here $z_h = E_h/\nu$ stands for the ratio of the energy of the hadron divided by the energy of the photon, while the squared transverse momentum in respect to the photon direction is indicated by p_T^2.

In fig. 31 we show the results of our calculations compared to experimental data [274, 275, 276, 277] for some different scenarios. In all scenarios the (pre-)hadronic cross section is zero before t_P and equals the full hadronic cross section after t_F. The most essential feature of color transparency – larger hadrons (smaller Q^2) get attenuated more than smaller ones – is thus included in all four scenarios.

In the first scenario we assume no time dependence, i.e., the pre-hadronic cross section is assumed constant,

$$\sigma^*/\sigma = \text{const} = 0.5, \tag{225}$$

where σ is the total hadronic cross section. Here, the value 0.5 for the constant cross section ratio is chosen, because it leads to a reasonable description of the HERMES data [67]. The following two scenarios are the "quantum-mechanically inspired" and the "naive" assumptions of linear or quadratic increase, respectively [278]

$$\sigma^*(t)/\sigma = \left(\frac{t - t_P}{t_F - t_P}\right)^n, \quad n \in [1, 2]. \tag{226}$$
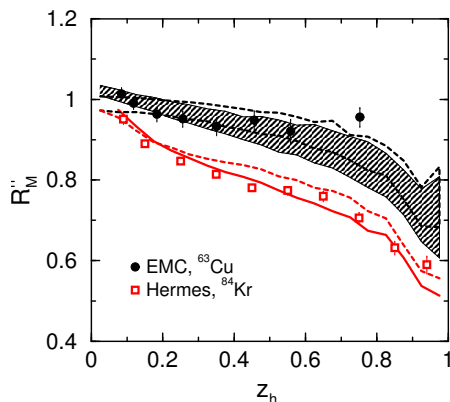
Figure 32: (Color online) Nuclear modification factor for charged hadrons as in fig. 31. The cross-section-evolution scenario in the calculations is according to eq. (227). Dashed lines repeat curves from fig. 31 (middle panel). Taken from [133].

All three scenarios for the pre-hadronic interaction mimic color transparency to some extent, because the interaction rates are reduced until the formation of the final hadron. The times t_P, t_F are as defined in section 3.4.

Finally, we implement the 'quantum diffusion' picture of Farrar *et al.* [279] proposed by these authors to describe the time development of the interactions of a point-like configuration produced in a hard initial reaction (see also [280]). This picture combines the linear increase with the assumption that the cross section for the *leading* particles does not start at zero, but at a finite value connected with Q^2 of the initial interaction,

$$\sigma^*(t)/\sigma = X_0 + (1 - X_0) \cdot \left(\frac{t - t_P}{t_F - t_P} \right), \qquad X_0 = r_{\text{lead}} \frac{\text{const}}{Q^2}, \tag{227}$$

with r_{lead} denoting the ratios of leading partons over the total number of partons (2 for mesons, 3 for baryons).

The baseline value, X_0, is inspired by the coefficient $\langle n^2 k_T^2 \rangle / Q^2$ in Ref. [279]. Our scaling with r_{lead} guarantees that summing over all particles in an event, on average the prefactor becomes unity. The numerical value of the constant in the numerator of X_0 is chosen to be $1\,\text{GeV}^2$ for simplicity, close to the value used in [279]. This value is also constrained by the considered Q^2 range such that the pedestal value $X_0 \leq 1$ is fulfilled.

Because it remains unclear, how the (very) different lepton energies have been considered in the experimental results given in [277] we have performed calculations for the two most prominent energies of that experiment, i.e., for beam energies of $100\,\text{GeV}$ and $280\,\text{GeV}$. We illustrate the results of our calculations by a shaded band in fig. 31 and fig. 32 that reflects the energy range just mentioned.

Assuming a constant cross section (cf. fig. 31), we obtain a good description of the HERMES results, while the attenuation for the EMC experiment is severely overestimated (cf. [67]). Assuming a linear time dependence, both the HERMES and EMC attenuation are well described. Going even further and assuming a quadratic time dependence, leads to a too small attenuation for both the HERMES and the EMC experiment, with the discrepancy between theoretical and experimental results being significant for the HERMES experiment. Only the theoretical sce-
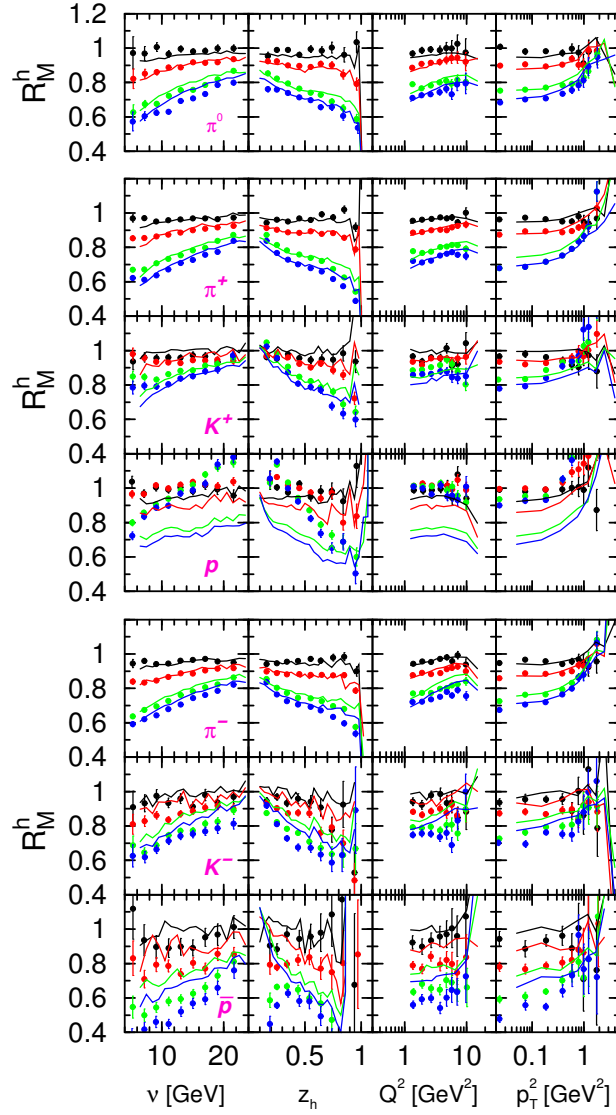
Figure 33: (Color online) Nuclear modification factor for identified hadrons for HERMES at 27 GeV with ^{4}He, ^{20}Ne, ^{84}Kr, and ^{131}Xe-target nuclei (top to bottom). Points indicate experimental data [274, 275, 276] while the curves represent our calculations with the time-dependence scenario cf. eq. (227) with diffractive events excluded. Taken from [133].
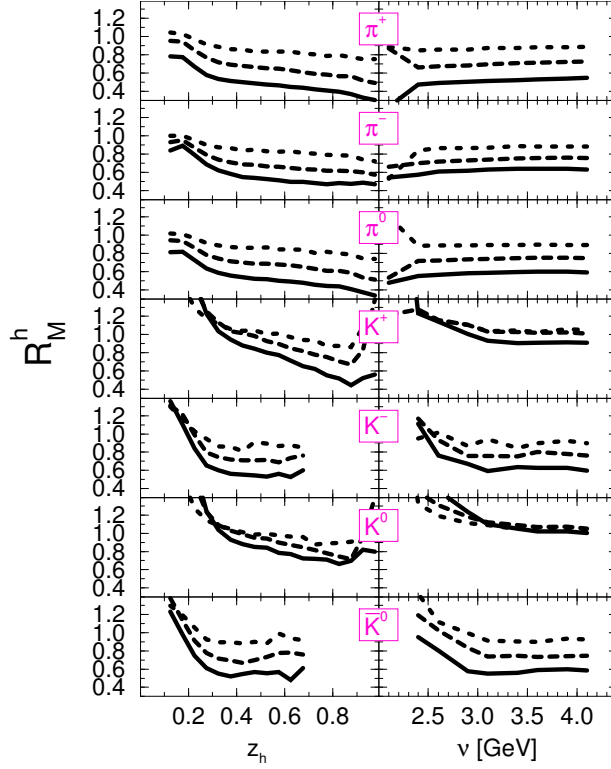
Figure 34: (Color online) Nuclear modification factor of identified mesons $\pi^{\pm,0}$ and $K^{\pm,0}, \bar{K}^0$ for JLAB(CLAS) at 5 GeV with different targets: ^{12}C (dotted), ^{56}Fe (dashed), and ^{208}Pb (solid lines). Taken from [133].

nario with a cross section evolving linearly in time is able to describe both data sets at the same time.

Figure 32 shows results of our calculations employing the scenario as given by eq. (227). Although not very pronounced, the effect of the non-vanishing, Q^2-dependent initial cross section of the leading particles is visible when comparing fig. 32 with the middle panel in fig. 31; a slight improvement in the description can be seen. The observed weak Q^2 dependence is in line with experimental observations of both the HERMES and the EMC experiments [274, 275, 276, 277]. This scenario (eq. (227)) will therefore be used in the following considerations.

Figure 33 shows a comparison of our calculations with the latest experimental data of the HERMES collaboration with 27 GeV beam energy for identified hadrons for the four targets ^{4}He, ^{20}Ne, ^{84}Kr, and ^{131}Xe.

As expected from fig. 32, for the total hadron yield, the data for pions, which are the most frequently produced hadrons, are described well by our model. In the large-z_h region charged pions originate mostly from decays of diffractive ρ mesons. Since these pions are taken out from the experimental data, we also switch off diffractive production of ρ mesons in the calculations. While the description of the data in the strange and anti-baryonic sectors is also quite good, one still finds the well known discrepancy of data and calculations for protons: the regions with "low z_h"/"high ν" are clearly underestimated in our model. We recall that this is
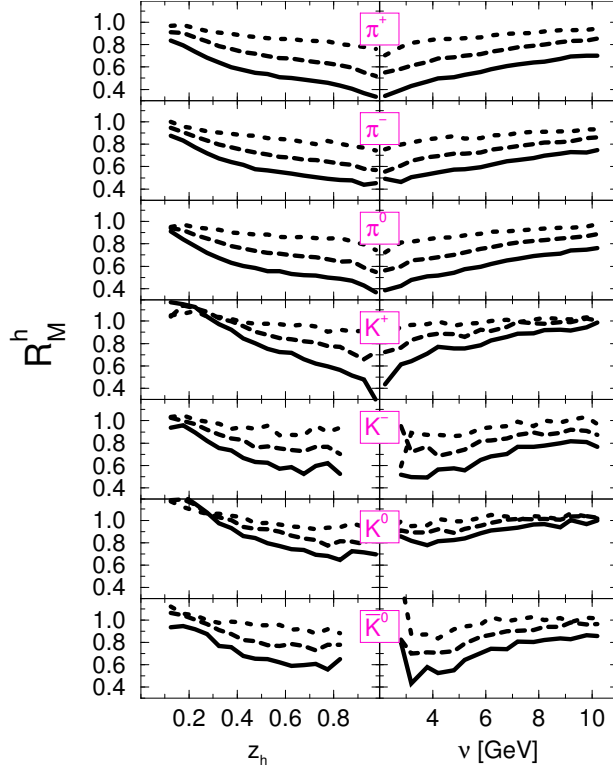
Figure 35: (Color online) The same as fig. 34, but for JLAB (CLAS) at 12 GeV lepton-beam energy. Taken from [133].

not a new finding but already known from our previous work [67]. The observed discrepancy may reflect a deficiency in our treatment of final-state interactions at high proton energies since the (strongly non-perturbative) low-z_h protons arise mainly from energy-degrading rescattering events. The discrepancy may, however, also reflect some problems with the treatment of experimental geometrical acceptance limitations, which affect the data (and are taken into account in the calculations).

Based on our successful description of the experimental data of the HERMES collaboration for 27 GeV and 12 GeV beam energies, we now make predictions for the meson spectra at the presently available 5 GeV lepton-beam energy and at the future JLAB facility with 12 GeV.

We start with a discussion of our results for a 5 GeV beam energy in fig. 34.

A comparison of our results fig. 34 with preliminary experimental data on the z_h dependence of the π^+ attenuation for the three nuclear targets [281] is satisfactory, both in its magnitude and its target-mass-number dependence.

Contrary to the situation at higher beam energies, feeding effects leading to attenuation ratios larger than unity at small z_h are more pronounced and turn out to be an essential feature in this energy range. For the rarer kaons we stop showing the attenuation at $z_h = 0.7$ because the spectra for K^- drop rapidly at $z_h \simeq 0.7$-0.8. On the contrary, the spectra for K^+ reach significantly farther out. This is a direct consequence of the fact that contrary to K^+ mesons the K^- mesons can only be produced in the associated strangeness-production mechanism and thus have a higher

threshold than the former. The same holds for K^0 and $\overline{K}^0$, respectively.

At this low energy (and corresponding momentum transfer) the invariant masses populated in the first interaction are rather small ($\langle W \rangle = 2.2\,\text{GeV}$) and thus just above the resonance region. We have also already noted that at this low energy we have formation times of only $\simeq 4\,\text{fm}/c$ at large z_h. Therefore, the interactions of the formed hadrons are strongly affected by hadronic interactions while pre-hadronic interactions play only a minor role (at least for the heavier targets). This can be seen in fig. 34 in the different attenuation for K^+ and K^-, the latter being more strongly attenuated due to hadronic FSI. We also recall our earlier finding [67] that at this low energy also the effects of Fermi motion are essential and have to be taken into account. The dynamics in this energy regime is thus more determined by 'classical' meson-nucleon dynamics than by perturbative QCD, which underlies many of the other theoretical descriptions of the attenuation experiments [282, 283, 284].

Figure 35 shows the calculated results for the multiplicity ratio of the three pion and four kaon species for the exemplary nuclei ^{12}C, ^{56}Fe, and ^{208}Pb with 12 GeV lepton-beam energy as in the future JLAB upgrade.

For all particle species, a strong dependence of the attenuation ratios on the size of the nucleus is obtained. It is interesting to observe that at this higher energy the attenuation of K^+ and K^- becomes similar at $z_h \approx 0.7$, contrary to the behavior at 5 GeV. This reflects the longer formation times at higher energies and the corresponding predominance of pre-hadronic interactions, which affect the non-leading K^- only weakly.

4.3. Photon-induced reactions

Photon-induced reactions share with the electron-induced ones the advantage that there are no initial state interactions, i.e. photons illuminate the whole nucleus (again disregarding shadowing, cf. footnote at the start of section 4.2). GiBUU and its predecessors have been used to investigate scalar-, pseudoscalar-, and vector-meson production off nuclei (see [285, 286, 287, 288, 289, 290, 291, 292, 293] and refs. therein). Here we discuss as examples the total photoabsorption cross sections as well as single- and double-pion production and omega production.

4.3.1. Total photoabsorption cross section

In the total photoabsorption cross section on nucleons, one observes three major peaks (see fig. C.62 in Appendix C.5) generated by several overlapping resonances. The most important ones are the $P_{33}(1232)$, $S_{11}(1535)$, $D_{13}(1520)$ and $F_{15}(1680)$ resonance states. To study the properties of these resonance states embedded in nuclear matter, one has investigated their photon-induced excitation in nuclei. First experiments using a tagged high-energy photon beam ($E_\gamma = 0.3$-$2.6\,\text{GeV}$), which offered sufficient energy to excite the second resonance region, have been performed by the Yerevan group [294, 295]. Following up this pioneering work, photon absorption on nuclei has been measured at the Mainz Microton (MAMI) facility [296, 297] with a beam energy of $E_\gamma = 0.05$-$0.8\,\text{GeV}$, with higher energies of $E_\gamma = 0.2$-$1.2\,\text{GeV}$ at the Adone storage ring facility (Frascati, Italy) [298, 299, 300, 301, 302], using the SAPHIR tagged photon beam of $E_\gamma = 0.5$-$2.67\,\text{GeV}$ at ELSA (Bonn, Germany) [303] and at Hall B of the Jefferson Laboratory (Newport News, USA) [304, 305] with a beam energy of $E_\gamma = 0.17$-$3.84\,\text{GeV}$. In fact, some of the above experiments have not measured directly the photoabsorption cross section but only the photofission cross section [296, 297, 300, 298, 304, 305]. Contrary to earlier assumptions, it has been shown by Cetina *et al.* [304, 305] that these two cross sections need not be identical. Thus, for our analysis we focus on a comparison with the direct measurements of photon absorption as presented by Bianchi *et al.* [301, 302] and Muccifora *et al.* [303].
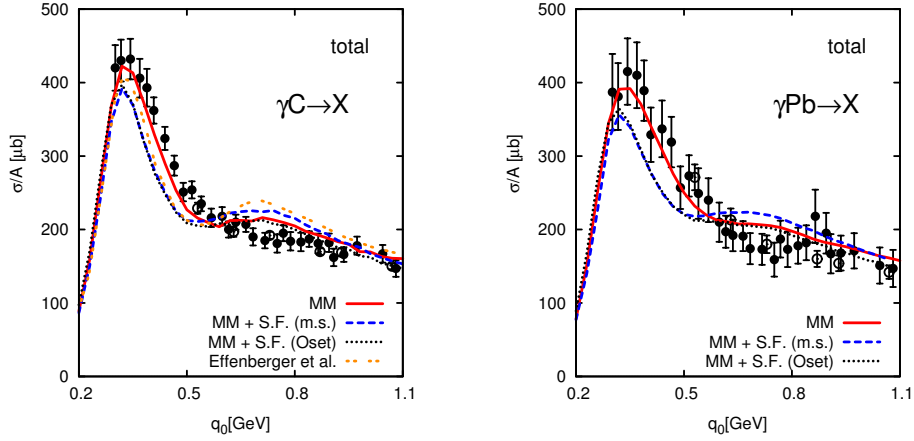
Figure 36: (Color online) The photoabsorption cross section for ^{12}C and ^{207}Pb. The (red) solid line denotes the result with a momentum-dependent potential (see label "MM" in table 1). In addition we show two different modifications of the in-medium self-energy: mass shift (m.s.) option (blue, dashed), and the result using the Oset option for the Δ (black, dotted). The data are taken from Bianchi *et al.* [302] (full circles) and Muccifora *et al.* [303] (open circles), the error bars denote the sum of statistical and systematical errors. Source: Taken from [55].

Experimentally, the Δ-resonance region within the nucleus still exhibits a peak-like structure. However, a slight shift to higher energies and a broadening is observed, as compared to the vacuum structure. Carrasco *et al.* [306] have shown in a microscopic model approach, that it is possible to describe the data in the Δ resonance region in a very satisfactory manner when including the Δ self-energy. This work emphasizes the importance of many-body absorption channels not included in the commonly used impulse approximation.

At higher energies the experimental results show no structures in the second and third resonance region. This is often referred to as the disappearance of the resonances in the medium and presents a direct observation of an in-medium effect [68].

After the publication of this surprising result in the second resonance region, various theoretical explanations and analyses have been put forward. Kondratyuk *et al.* [307] investigated a baryon-resonance model including the collisional widths of the resonances as free parameters. The extracted widths turned out to be extraordinary large (ca. 320 MeV for the $S_{11}(1535)$, $D_{13}(1520)$ and $F_{15}(1680)$ resonance), and the whole analysis has drawn some criticism (cf. pages 368-369 in [308]). Rapp *et al.* [309, 310] have applied a vector-meson dominance (VMD) model to the problem. An energy-independent collisional broadening of the baryon resonances of 15 MeV for the Δ, 250 MeV for the D_{13} and 50 MeV for all other contributing resonances has been included by hand. The model reproduces the elementary data on the proton in the region between the Δ- and the second-resonance region at the expense of having to use a very soft π-NN form factor; it describes the nuclear data in a satisfactory manner. According to Hirata *et al.* [311], the interference patterns among the resonances and the background change from vacuum to medium, which is the driving force for the disappearance of the resonances. Iljinov *et al.* [312] have extended the Dubna/Moscow INC model, a hadronic transport model, such that it can be used for high photon energies up to 10 GeV. They achieve a good correspondence with exclusive channels such as single-pion production. Based on the Dubna/Moscow INC model, the RELDIS code [313] has achieved good results for photoabsorption on large nuclei. Both the INC

92

and RELDIS models include a phenomenological two-body absorption channel on top of single-particle absorption. Also the LAQGSM model [314] is based on the Dubna/Moscow INC model and gives good results for nuclear fissilities. Deppman *et al.* [315] have successfully applied the so-called MCMC/MCEF cascade model to evaluate photon-fission cross sections using the photoabsorption cross section as given input. Complementary to this first work, Deppman achieved with the CRISP code [316, 317], where the photon absorption is modeled via a microscopic resonance model, also satisfactory results for photon absorption.

In view of these numerous attempts to describe the disappearance of nucleon resonances inside the nuclear medium, Effenberger *et al.* [308] have attempted to explain this observation within a precursor of the GiBUU model. Quite a good description of the Δ peak has been achieved, although some strength on the high energy side of the Delta peak is missing. Furthermore, the model failed to describe the data at higher energies; the results still showed a prominent structure in the second and third resonance region.

The present implementation of GiBUU has improved various theoretical aspects of the calculation (for a detailed discussion see Ref. [55]). Figure 36 shows the results of these new calculations with a momentum-dependent mean field, as well as calculations for which the in-medium width and the dispersive contributions to the real parts have been taken into account (for details see Ref. [55]). There is an excellent agreement with the data when only the momentum dependent potential is switched on. However, when the improvements to the resonance spectral function are turned on the agreement gets worse, in particular on the high-energy side of the Δ resonance. This is partly due to the lowering of the peak due to the larger width, but also to an inconsistency; the increased in-medium width obtained by Oset *et al.* [56] contains contributions from 2-body absorption while the calculation relies on an impulse approximation without such a process.

The results shown in fig. 36 contain the sum of resonance and background contributions. Note that the background contributions differ for all calculations, which is caused by the inclusion of the dispersive parts. These dispersive parts basically shift strength from the resonances to the background. The figure shows that the Δ region is underestimated for both options for the in-medium width. The situation also does not improve in the second resonance region, where a strong in-medium broadening, as in the mass-shift scenario, even leads to an enhancement of the peak structure due to a shift of Δ spectral strength towards higher masses.

For completeness, we show in fig. 36 also the photon absorption in lead. Compared to the carbon case we do not see a qualitative change of the picture. We observe the same level of correspondence with the experimental data as for the carbon case.

4.3.2. Single π^0 photoproduction

By taking into account rescattering effects leading to a change in the final-state-particle multiplicities and distributions, the GiBUU transport model is very well suited for the study of semi-exclusive reactions. To give a flavor of the GiBUU capabilities, in the next sections we address π, $\pi\pi$ and ω photoproduction. Based upon a precursor version of GiBUU, there also ρ [318], ϕ [288, 319], and η [320] production in photon-induced reactions have been analyzed.

High quality data on π^0-meson production have been taken by Krusche *et al.* [321, 290] using the TAPS spectrometer installed at the MAMI facility in Mainz, and on π^+-meson production by Fissum *et al.* [322] at the Saskatchewan Accelerator Laboratory. The Fissum data are taken in the very threshold region, where most of the produced pions have energies below $40\,\mathrm{MeV}$ and our FSI model becomes unreliable.
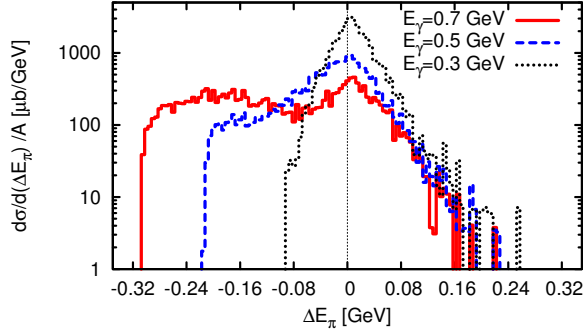
Figure 37: (Color online) A typical plot for $d\sigma_{\pi^0,\text{total}}/d(\Delta E)$ for a $\gamma^{40}\text{Ca} \to \pi^0 X$ reaction at 0.5 GeV and 0.7 GeV right after production (*i.e., FSI effects are not included*). This result is obtained with a momentum-dependent potential (label "MM" in table 1) and the Oset choice according to [55] for the self-energies. Source: Taken from [55].

For the π^0-production experiment performed by Krusche *et al.* [321, 290], the MAMI facility delivered a photon beam of 200-800 MeV energy on deuterium, carbon and lead targets. In this each produced neutral pion has been counted as a single event. Therefore, events with $2\pi^0$ in the final state are doubly counted. So the total cross section for neutral pion production is experimentally defined as

$$\sigma_{\pi^0,\text{ total}} = \sigma_{\pi^0} + 2\sigma_{\pi^0\pi^0} + \sigma_{\pi^0\pi^+} + \sigma_{\pi^0\pi^-} + \beta\sigma_\eta \tag{228}$$

where $\beta \approx 1.2$ is the expected average number of π^0's in the final state of an η decay.

In the experimental analysis one tries to differentiate between quasi-free pion production and in-medium pion production. For the production of quasi-free pions one assumes that the energy of those is similar to the energy of a pion produced on a nucleon at rest. This energy in the πN CM frame is given by

$$E_\pi^{\text{free}} = \sqrt{|\boldsymbol{p}_{\text{CM}}|^2 + m_\pi^2} \tag{229}$$

with

$$|\boldsymbol{p}_{\text{CM}}| = \sqrt{(s + m_\pi^2 - m_N^2)^2/(4s) - m_\pi^2} \, , \tag{230}$$

where $s = (E_\gamma + m_N)^2 - E_\gamma^2 = m_N^2 + 2m_N E_\gamma$. The difference of the reconstructed energy in the πN CM frame to that *quasi-free* energy is defined as ΔE_π (cf. also [290]),

$$\Delta E_\pi = E_\pi^{\pi N-\text{CM}} - E_\pi^{\text{free}}(E_\gamma) \, . \tag{231}$$

A typical plot of such a distribution without final-state interactions is shown in fig. 37. Indeed, one observes a peak at $\Delta E_\pi \approx 0$, but the peak is not sharp but rather smeared out due to the potentials and Fermi motion. Additionally, one observes a broad background at lower $\Delta E_\pi < 0$, which originates from $\pi\pi$ production. Since this background leaks into the single-π peak, it may affect the actual signal.

In the experimental analysis the spectrum has, therefore, been approximated by a symmetric one, i.e., the left-hand side of the quasi-free peak is assumed to equal the right-hand side so
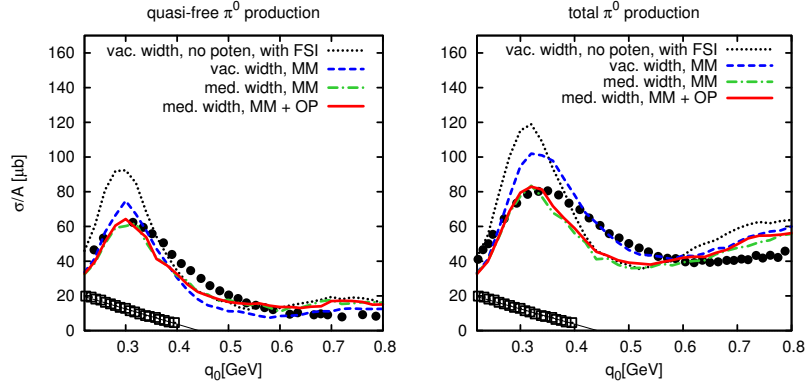
Figure 38: (Color online) Quasi-free and total cross sections for the $\gamma^{40}\text{Ca} \to \pi^0 X$ reaction: the left panel shows the *quasi-free* yield, whereas the right one depicts the total yield of π^0's. The statistical error bars of the data are negligible and have been omitted. The squares show the data for the coherent π^0-production cross section [323], and the circles depict the data for the quasi-free, respectively total, cross section [290]. The dotted line represents the calculation without in-medium modification of widths (i.e., vacuum widths) and without potential; the dashed one also uses vacuum widths but an in-medium momentum-dependent potential (label "MM" in table 1); both the dashed-dotted and the dotted curves have been obtained by calculations, which include in-medium widths and an "MM" potential. In the solid curve, the off-shell potential (OP) has been additionally included as described in section 2.4.3 (while all other results do not include any OP). The thin solid line connecting the coherent data points (squares) shows our fit of these data. Source: Taken from [55].

that effectively only events with $\Delta E_\pi > 0$ were counted. The so-called quasi-free cross section, reported by the experiment, is thus defined as

$$\sigma_{\pi^0, \text{quasi-free}} = \frac{2 \times \text{ rate of events with } \Delta E_\pi > 0}{\text{photon flux} \times \text{density of targets}} \ . \tag{232}$$

To compare to data, we apply the same counting and cutting scheme also in our analysis. Note that the sizable coherent contribution [323] also contributes to $\sigma_{\pi^0, \text{quasi-free}}$ and $\sigma_{\pi^0, \text{total}}$. Since GiBUU only gives the incoherent contribution we have fitted the data for the coherent process [323] as shown in fig. 38.

This fit of the coherent data has then been added to our incoherent result. The resulting curves are shown in fig. 38, both for the quasi-free cross section, $\sigma_{\pi^0, \text{quasi-free}}$, and for the total one, $\sigma_{\pi^0, \text{total}}$. When including in-medium width and momentum-dependent potentials, one retrieves a quite good description of the quasi-free cross section. The influence of the off-shell potential is rather minor. Considering the large slowdown of our simulations due to this off-shell potential, it is favorable, that neglecting this potential does not change our results in a significant manner.

For the total cross section the quality of the description data is similar to that obtained earlier by Lehr *et al.* [61]. One may speculate whether there is a problem with the 2π contribution, which rises continuously from almost 0 % at $q_0 = 0.45$ GeV to roughly 30 % of the π^0 yield at $q_0 = 0.8$ GeV. An additional in-medium modification of the $\pi\pi$ background could, therefore, have a major impact on the spectra. One should also note, that interference effects play a major role in single-π^0 production at the energy region of discrepancy (see also fig. C.62). In addition, there is the possibility that primary 2N absorption processes play a role, such as $\gamma NN \to N\Delta$.

In any case, there is major impact of FSI on the spectra. This is illustrated in fig. 39, which shows that for a calculation that does not include any medium modifications of self-energies, i.e.,
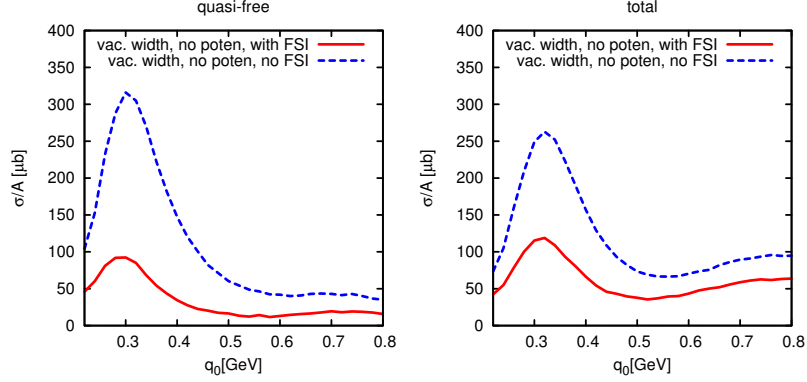
95

Figure 39: (Color online) Quasi-free and total cross sections for the $\gamma^{40}Ca \rightarrow \pi^0 X$ reaction with and without final-state interactions: the left panel shows the *quasi-free* yield, whereas the right one depicts the total yield of π^0's. The lines represent calculations, which have been performed neglecting the in-medium width and potentials. The dashed line does not include any FSI, whereas the solid line includes them. Source: Taken from [55].

no potentials or collisional broadening, FSI lead to an overall reduction of the pion yield[20] by approximately a factor of 3. Thus, to achieve a proper agreement with the data, the accuracy of the FSI must be very high.

4.3.3. Double pion photoproduction

Possible changes of the properties of hadrons when they are embedded inside the nuclear medium have recently attracted considerable interest (for two recent reviews see Ref. [211, 68]). While many studies have concentrated on the investigation of in-medium properties of vector mesons (cf. section 4.3.4), there has also been an interesting prediction of a change of scalar mesons inside nuclei.

In the limit of vanishing quark masses QCD incorporates chiral symmetry, which is spontaneously broken in vacuum. The order parameter, the quark condensate, $\langle \bar{q}q \rangle$, of this symmetry breaking is expected to decrease by about 30 % already at normal nuclear-matter density [324, 325, 326]. Therefore, signals for partial chiral-symmetry restoration should be observable in nuclear-reaction experiments and, in particular, also in photon-induced processes where initial state interactions are absent.

The modification of the σ or $f_0(600)$ meson in the nuclear medium has been proposed as a signal for partial symmetry restoration. Theoretical models predict a shift of its spectral strength to lower masses and narrower widths due to the onset of the chiral-symmetry restoration [327, 328]. The σ-meson is a short-lived state with a width of roughly 600-1000 MeV [129], decaying predominantly into an S-wave $\pi\pi$-final state. Owing to its short life time, this decay occurs very close to its production place, i.e., in the medium. If there were no final-state interactions acting on the pionic decay products, then the mass of the σ-meson could be directly determined

---

[20]In fig. 39, the quasi-free yield at low photon energies is higher than the total yield if FSI are not included. This is not an inconsistency, but a feature, which in implied by the definition of $\sigma_{quasi-free}$ in the analysis procedure: since the quasi-free peak without FSI treatment is slightly shifted towards positive ΔE_π (see fig. 37), we obtain $\sigma_{quasi-free} = 2\int_0^\infty d\sigma(\Delta E_\pi) > \int_{-\infty}^\infty d\sigma(\Delta E_\pi) = \sigma_{tot}$.
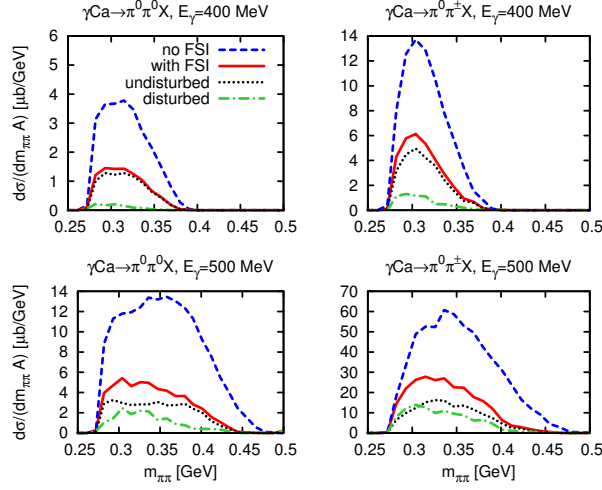
Figure 40: (Color online) The upper figure visualizes the impact of final-state rescattering on the mass-differential cross section for $\pi\pi$ production in ^{40}Ca. The dashed curve has been obtained neglecting FSI, while for the calculations, represented by the solid, dotted and dashed-dotted curves, the FSI have been included. The solid curve shows the total result including FSI; the dotted one represents the "undisturbed" contribution of pions which left the medium without rescattering; one of the pions out of each pair contributing to the dashed-dotted "disturbed" contribution underwent at least one scattering event. Source: Taken from [55].

measuring the four-momenta of the pions. Thus experiments have studied the $\pi\pi$ production rate as a function of the total mass of the $\pi\pi$ pair. The major aim is to observe a modification of this signal when comparing the nuclear production rate to the vacuum rate. Using different nuclear targets, one probes different effective densities, which allows for a detailed study of the density dependence of this production rate. Experiments on $\pi\pi$ production in nuclear matter have been performed with incident pions by the CHAOS collaboration [329, 330] and with photons by the TAPS collaboration [134, 135, 331]. Both experiments have shown an accumulation of strength near the $\pi\pi$ threshold in the decay channel of the σ in large nuclei. A possible interpretation of this effect is the in-medium modification of the σ resonance due to partial symmetry restoration.

Roca *et al.* [332] have indeed obtained a good description of these data by assuming pion-pion correlations and using a straight-line Glauber-like damping factor for pion absorption.

However, the authors of [333] have pointed out the importance of conventional final-state effects in the analysis of the TAPS experiment. In this section we improve on our early calculations using up-to-date input for the elementary rates and using an improved final-state model. In order to compare to the work by Roca *et al.* [332] the absorption probability for pions is assumed to be the same as in their paper.

As was already shown in section 4.1.1, the GiBUU transport model successfully describes pion absorption and rescattering off complex nuclei. It is, therefore, tempting to apply this model also to this reaction. The results presented in this Section have been published in [333, 334, 335, 139, 140]. The calculations contain all the effects of pion-nucleon-Delta interactions inside the nucleus, but they do not contain any pion-pion interaction.

As already discussed in [333], we observe that absorption, elastic scattering and charge exchange processes cause a considerable change of the spectra with the peak of the mass distribu-
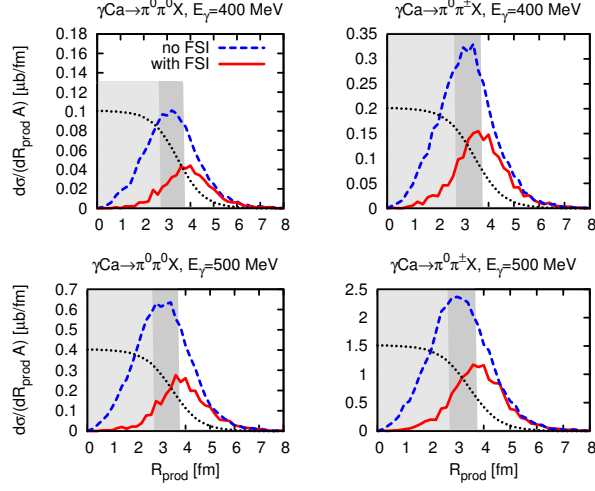
97

Figure 41: (Color online) Cross section for $\pi\pi$ production in ^{40}Ca as a function of the production radius, $R_{prod} = (x_{prod}^2 + y_{prod}^2 + z_{prod}^2)^{1/2}$: the solid curve depicts the result with FSI, the dashed one does not include FSI. Additionally, the dotted line depicts the density profile of the ^{40}Ca nucleus; the light-gray areas show the R_{prod} region with $\rho \geq 0.15 \, \text{fm}^{-3}$, the dark shaded areas show the region with $0.15 \, \text{fm}^{-3} \geq \rho \geq 0.075 \, \text{fm}^{-3}$. Source: Taken from [55].

tion moving to lower masses due to rescattering. This effect is visualized in fig. 40, where we show our results for $\pi\pi$ production of ^{40}Ca assuming no FSI and by including FSI. One observes a reduction of the cross section by a factor of roughly 2-3 and a shift of the peaks towards lower masses due to FSI. There are two major effects, which lead to the modifications: absorption and rescattering. To point out the role of rescattering, fig. 40 shows so-called *disturbed* and *undisturbed* contributions to the cross section. The undisturbed contribution includes all pion pairs which do not undergo rescatterings and reach the detector almost undisturbed; the *disturbed* contribution represents pairs, where at least one of the two pions scatters with the medium but is not absorbed. The total cross section is the sum of the disturbed and the undisturbed contributions. Obviously, the disturbed contribution is shifted towards lower masses more than the undisturbed one since the pions (on average) loose energy in a scattering event. At low photon energies the disturbed contribution is small compared to the undisturbed one. Here, the energies of the produced pions is small, such that FSI are dominated by the $NN\pi \rightarrow NN$ process and the effect of $N\pi \rightarrow N\pi$ scattering is small. At higher photon energy (500 MeV) also the average pion energy is higher and, therefore, elastic and charge-exchange scatterings become more important. Thus the disturbed and undisturbed contributions are of the same magnitude for $E_\gamma = 500$ MeV.

To analyze the possible impact of additional in-medium modifications, such as e.g. chiral symmetry restoration, the production points of those pion pairs which are not absorbed and which are, finally, observed were studied. Figure 41 shows the cross section for $\pi\pi$ production off ^{40}Ca at 400 MeV and 500 MeV as function of those production points R_{prod}. Without FSI the distribution $d\sigma_{\pi^0\pi^0}/dR_{prod}$ is proportional to $\rho(R_{prod})R_{prod}^2$; including FSI the distribution is shifted towards higher radius and centered around 3.6 fm which corresponds to roughly $\rho = 0.075 \, \text{fm}^{-3}$. Most of the observed signal originates from low-density regions, which implies that possible in-medium signals are expected to be rather weak. Also calculations including a pion potential
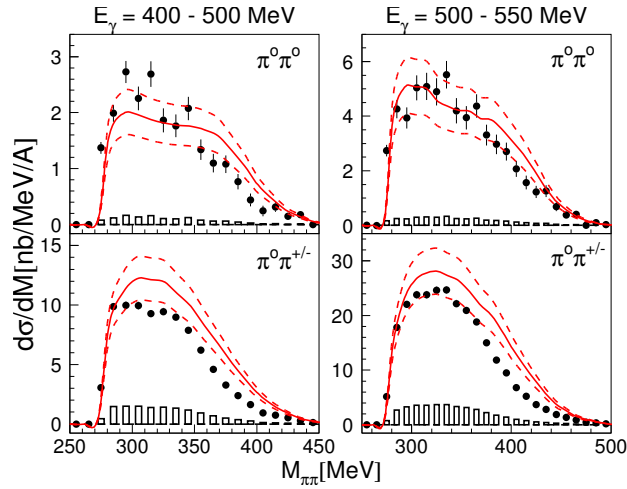
98

Figure 42: (Color online)Pion-pion invariant mass distributions for ^{40}Ca for the two energy ranges indicated compared to results of the GiBUU model in Ref. [135]. The bars at the bottom represent the systematic uncertainty of the data, the dashed lines represent the error band for the GiBUU calculation. Source: Taken from [135].

have been performed; only a minor effect on the observed pions is found due to the low density at the initial production point.

The previous discussions showed the strength of a transport model description of nuclear reactions in that it gives some physical insight into the 'inner workings' of dynamic many-body processes. The direct comparison with experimental results then shows how far a model that contains no $\pi - \pi$ interactions can go. While earlier results [333] gave a reasonable description of the TAPS data [134], a later measurement by the same group has resulted in data that are very well described by the GiBUU model (see fig. 42). The agreement now is excellent.

In summary, final-state interactions of the pions are strong and tend to shift the maximum of the $\pi\pi$ mass distribution in all channels towards lower masses. This effect considerably complicates drawing a link between the experimental data and a possible softening of the in-medium $I = 0$ channel. Any theory aiming to describe the observed effect on the basis of a partial chiral-symmetry restoration or an in-medium modification of the $\pi\pi$-production process must include a state-of-the-art treatment of the final-state effects.

4.3.4. Photoproduction of vector mesons

As already discussed in sections 4.1.5 and 4.3.3, modifications of hadron properties in a strongly interacting environment have attracted a lot of attention and have been intensively studied both theoretically and experimentally. The dilepton channel is particularly suitable for such studies since the final state is not affected by FSI. The experiments with hadronic beams discussed in section 4.1.5 do suffer from initial state interactions which may hinder the population of the higher-density zones in the target. On the contrary, experiments using photons as incoming particles are nearly ideal for these studies since they do not involve any initial state interactions. Such an experiment was first studied with an early version of GiBUU [336] and has by now been performed with the CLAS detector at JLAB, where photons with energies of a few GeV interacted with nuclei [318, 293]. The results of this experiment have been analyzed with GiBUU; a broadening of the ρ meson in line with theoretical expectations but no mass shift has been ob-
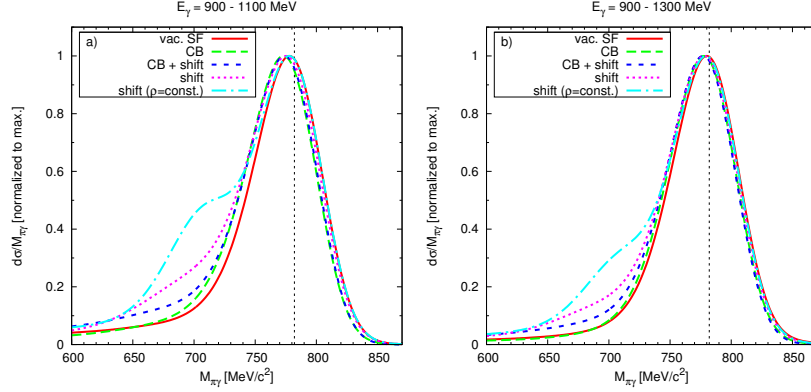
Figure 43: (Color online) ω-meson line shape predicted for a Nb target in GiBUU transport-model calculations for different in-medium modification scenarios: vacuum spectral function (solid), collisional broadening of $\Gamma_{\text{coll}} = 140\,\text{MeV}$ (long dashed), collisional broadening and an attractive mass shift of $-16\,\%$ at nuclear matter density (short dashed), and a mass shift without broadening (dotted). The dash-dotted curve shows the results for a constant nuclear density of $\rho = 0.6\rho_0$. The signals are folded with the detector response and take into account the $1/E_\gamma$ weighting of the bremsstrahlung spectrum. a) incident photon energies of 900-1100 MeV; b) incident photon energies of 900-1300 MeV. Source: Taken from [339].

served. A recent study on in-medium modifications of the ρ meson in connection with the CLAS data comes to a similar conclusion [337, 338].

Another experiment also using photons as incoming particles looks at the semi-hadronic decay of vector mesons thus suffering from some FSI. Here the decay $\omega \rightarrow \pi^0\gamma$ is investigated by the CB/TAPS group in photon-induced reactions at the ELSA accelerator [339]. This experiment has again given a significant in-medium broadening of the ω meson [340] but no mass shift; the earlier claim of a mass shift of the ω meson in photoproduction on Nb [341] has not been confirmed in a reanalysis of the data [342].

In this experiment, incident photon energies covered the range from 900-2200 MeV. Because of the increase of the production cross section with photon energy most of the observed ω mesons are produced with photons of energies larger than 1500 MeV. For the energy range of 1500-2200 MeV, early transport calculations [343, 62] have shown that the ω line shape is rather insensitive to different in-medium modification scenarios like collisional broadening or mass shifts, since most of the ω decays occur outside of the nuclear medium, even despite of a cut on the ω momentum ($p_\omega \leq 500\,\text{MeV}/c$). Furthermore, due to the experimentally observed strong absorption of ω mesons in the nuclear medium [340], ω mesons produced in the interior of the nucleus are largely removed by inelastic reactions and do not reach the detector; information on possible in-medium modifications thereby is lost. The limited sensitivity of the ω line shape to in-medium effects has been confirmed experimentally in [342].

It has been argued in [343] that a search for medium modifications is much more promising for incident photon energies below or near the photoproduction threshold (which is at $E_\gamma^{\text{lab}} = 1109\,\text{MeV}$ on a free nucleon). New calculations along these lines illustrate in fig. 43 the expected sensitivity of the ω signal to various in-medium changes, such as a mass shift with and without collisional broadening for two different energy ranges. It is seen that the lower-energy window indeed leads to a more pronounced – though not dramatic – sensitivity than the higher-energy one. This relatively weak sensitivity is to a large extent a consequence of the density profile of

the nucleus that spans all densities from 0 to ρ_0 and thus smears any density-dependent signal. Assuming for the sake of the argument a density profile with a constant density of $0.6\rho_0$ – roughly corresponding to the average density in nuclei – and a sharp fall off at the surface the dash-dotted line in fig. 43 is obtained; here, the in-medium signal is significantly stronger. For a realistic Woods-Saxon nuclear density profile, contributions to the spectral function from the surface dominate, suppressing contributions from higher density regions [344].

In both energy windows, a tail towards lower masses is predicted for the scenario of a dropping ω mass. This tail is due to ω mesons which are produced off-shell within the nucleus. In [343, 62] an even stronger enhancement in the low-mass-tail region has been obtained. This calculation used a phenomenological method for the off-shell propagation, while the present results are based on the theoretical framework by Leupold [41] and Juchem and Cassing [34]. For details see section 2.4.3.

Recently, the ω-line shape has also been measured in the near-threshold range of incident photon energies, i.e., 900-1300 MeV [339]. A tagged bremsstrahlung photon beam has been impinged on LH_2, C and Nb targets, and photon triples from $\omega \rightarrow \pi^0\gamma$ decays are measured by the CBELSA/TAPS detector setup at Bonn. After subtraction of the background from the $\pi^0\gamma$ spectrum, the ω-line shape shown in fig. 44 (a) is obtained for the Nb target. The experimental distribution has been fitted using the Novosibirsk function [345], in order to model the detector response and the resulting mass resolution. The resulting fit is compared with the ω signal measured on the LH_2 target and with a MC detector simulation in fig. 44 (a). The agreement between the ω signal on the LH_2 target with the MC simulation demonstrates that the detector response is under control. Nevertheless, in view of the systematic and statistical uncertainties, no significant deviation from the reference signals is claimed. Higher statistics will be needed to draw any conclusion. Corresponding data have been taken at MAMI-C using the Crystal Ball/TAPS set up. The analysis is ongoing.

In fig. 44 (b) the measured ω signal is compared to predictions of transport calculations using the GiBUU model for the same scenarios as in fig. 43. Due to the rather large statistical errors, the experimental data obviously do not allow to distinguish between the various theoretical scenarios, in contrast to initial expectations.

Access to the in-medium spectral function of vector mesons is thus very limited, mainly due to the dependence of the in-medium properties such as mass and width on the nuclear density [344, 346] and the inherent smearing caused by the density profile of nuclei. From the analyses just discussed it is clear that any extraction of an in-medium effect on spectral functions of hadrons requires a state-of-the-art treatment of final state interactions. On the other hand, transparency measurements [347, 291] can give at least access to the imaginary part of the in-medium self-energy of the hadron. Another promising tool could be the measurement of excitation functions [289]. Such experiments are presently being analyzed.

4.4. Neutrino-induced reactions

The discovery of neutrino oscillations has renewed the interest in and the need for a better determination of the neutrino-nucleus cross sections since nuclear effects are known to be the largest source of systematic uncertainties in long-baseline neutrino experiments [348]. To increase the neutrino cross section, experiments use targets with a large atomic mass number, A, e.g., carbon, oxygen, iron, and lead. This causes a major difficulty: particles produced in neutrino interactions can reinteract before leaving the nucleus and can be absorbed, change their kinematics or even charge before being detected. Nuclear reinteractions limit our ability to identify the reaction channel, and they change the topology of the measured hadronic final state.
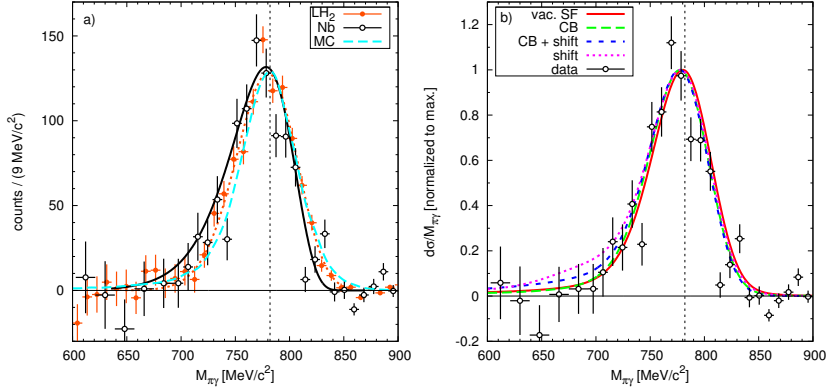
Figure 44: (Color online) (a) ω signal (solid points) for the Nb target and incident photon energies from 900-1300 MeV. The errors are purely statistical. Systematic errors introduced by the background subtraction are of the order of 5 %. A fit to the data points is shown in comparison to the ω-line shape measured on a LH$_2$ target and a Monte Carlo simulation; (b) ω signal for the Nb target in comparison to recent GiBUU simulations for the following scenarios: no medium modification (solid), in-medium broadening of $\Gamma_{\text{coll}} = 140$ MeV at nuclear saturation density (long dashed), an additional mass shift by -16 % (short dashed), mass shift without broadening (dotted) and mass shift without broadening assuming a constant nuclear density of $\rho = 0.6\rho_0$ (dash-dotted). The signals are folded with the detector response and take into account a $1/E_\gamma$ weighting of the bremsstrahlung spectrum. Source: Taken from [339].

Consequently, the detected rates on nuclei are changed significantly compared to the ones on free nucleons.

The oscillation probability depends directly on the neutrino energy: ν_μ-disappearance experiments for example search for a distortion in the neutrino flux in the detector positioned far away from the source. By comparing the un-oscillated with the oscillated flux, one gains information about the oscillation probability and with that about mixing angles and squared-mass differences. However, the neutrino energy cannot be measured directly but has to be reconstructed from the final-state particles that are detected. But, as we have pointed out before, these are affected by in-medium effects and final-state interactions in the nucleus. Appearance experiments, on the other hand, search for a specific neutrino flavor in a neutrino beam of different flavor. The flavor of the neutrino can only be determined from the charged lepton produced in the interaction. π^0-production events in neutral-current reactions are a source of background in ν_e-appearance searches in a ν_μ beam, because they might be misidentified as charged-current (ν_e, e^-) interactions.

To extract the oscillation parameters from the measured particle yields, the experimental analyses thus have to rely on models for the neutrino-nucleus interaction that describe many different effects quite reliably. This is even more important because the neutrino long-baseline experiments do not work with a fixed neutrino energy, but instead a broad neutrino spectrum, and thus implicitly sum over very different reaction types: quasi-elastic (QE), pion production and DIS. Quasi-elastic scattering alone as well as nucleon knockout is studied in many different models; only a few study pion production. The particular strength of GiBUU is that it describes all these different initial processes and the interactions in their final particles equally well. In the following we illustrate these points by discussing some results for neutrino-nucleus cross sections obtained with the GiBUU model. More detailed discussions can be found in [349, 350, 351]. All the results shown here rely on the impulse approximation. For true quasi-elastic scattering this
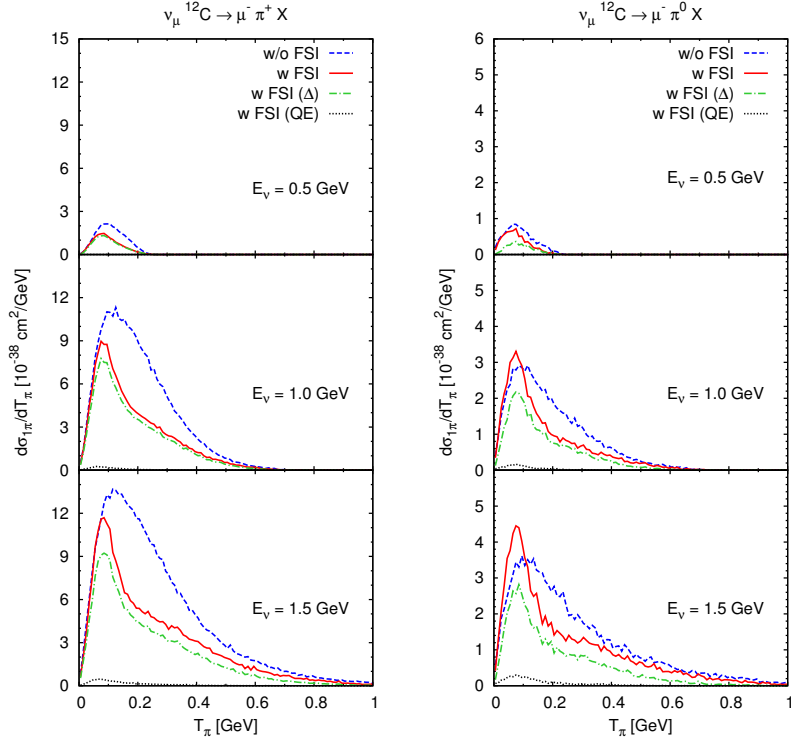
Figure 45: (Color online) Kinetic-energy differential cross section for CC $1\pi^+$ (left) and $1\pi^0$ (right panels) production on ^{12}C versus the pion kinetic energy T_π at different values of E_ν. The dashed lines show the results without FSI interactions (only the decay of resonances is possible), the results denoted by the solid lines include FSI. Furthermore, the origin of the pions is indicated (QE or Δ excitation). Source: Taken from from [351].

should be an excellent approximation, but for pion production and total cross sections this may not be sufficient. For a discussion of the influence of 2N correlations on nuclear neutrino-induced reactions see Refs. [352, 353, 354, 355].

4.4.1. Pion production

Neutrino-induced pion production on nucleons up to neutrino energies of about 1.5 GeV is dominated by the excitation and subsequent decay of the Δ resonance, but, depending on the channel, non-resonant pion production is not negligible. At higher energies, higher-mass resonances become increasingly important.

A realistic treatment of the FSI is an essential ingredient for modeling pion production off nuclei in a realistic manner. FSI may lead, e.g., to pionic final-state particles, even though the initial event is quasi-elastic scattering. As an example, we present the single-pion (1π) kinetic-energy distributions. They are shown in fig. 45 for ν_μ charged current (CC) π^+ and π^0 production (CC 1π) on ^{12}C target at different values of E_ν.

The maximum of the calculation with final-state interactions peaks at 0.05-0.1 GeV in all cases shown in fig. 45. This is due to the energy dependence of the pion absorption. The absorption is higher in the resonance region, where the pions are mainly absorbed through the reaction
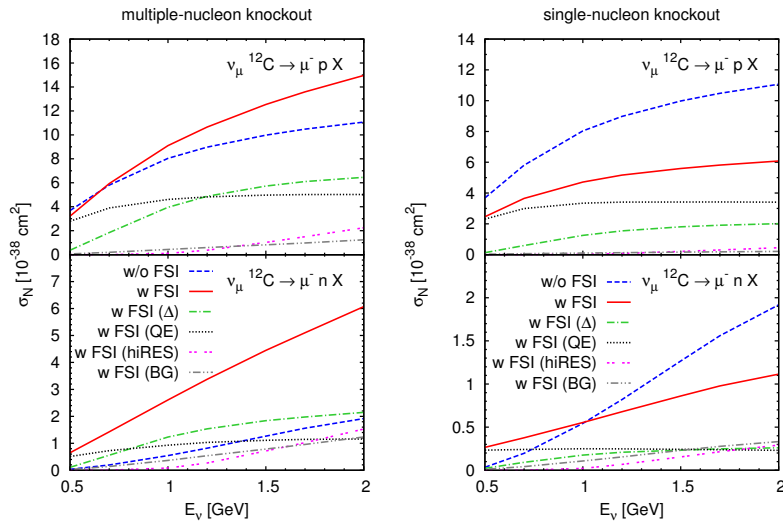
Figure 46: (Color online) Total cross section for CC multiple-p (top left), n (bottom left) knockout and CC single-p (top right) and n (bottom right) knockout on ^{12}C. Multiple-nucleon knockout means that the final state may contain any number of knocked-out nucleons. Single-nucleon knockout means that the final state does not contain any other knocked-out nucleons. The dashed lines show the results without FSI (only the decay of resonances is possible); the results denoted by the solid lines include FSI. Furthermore, the origin of the pions is indicated (QE, Δ excitation, excitation of higher resonances, single-pion background). Source: Taken from from [351].

$\pi N \rightarrow \Delta$, followed by $\Delta N \rightarrow NN$. This strong reduction for high-energy pions and the corresponding shift of the maximum to lower energies can be seen by comparing the dashed and the solid lines. These absorption processes equally affect π^+ and π^0 yields. But pions do not only undergo absorption when propagating through the nucleus. Of particular importance for pions of all energies is elastic scattering, $\pi N \rightarrow \pi N$, which redistributes the kinetic energy, again shifting the maximum to lower energies.

The contributions from initial Δ excitation and from initial QE events are also plotted. π^0 and π^+ production through FSI of QE scattering contributes mostly to the low-energy region of the pion spectra because of the energy redistribution in the collisions.

The different scale of CC π^+ and π^0 is a consequence of their different production rates in the neutrino-nucleon reaction. This leads to side feeding from the dominant π^+ channel to the π^0 channel. Pions produced from initial QE events contribute relatively more to the π^0 channel. This together with the side feeding produces the enhancement in the π^0 cross section at low kinetic energies compared to the calculation without final-state interactions for $E_\nu \gtrsim 1\,\text{GeV}$.

4.4.2. Nucleon knockout

The total cross sections for proton and neutron knockout are shown in fig. 46 for multiple-nucleon emission and for single-nucleon emission for ^{12}C. In the case of multiple-nucleon knockout, we find, that the result with all final-state interactions included lies well above the one without FSI already for the protons, but even more so for the neutrons. This enhancement is entirely caused by secondary interactions and cannot be obtained in a Glauber treatment or in any other quantum-mechanical approach such as the often used relativistic impulse approximation.
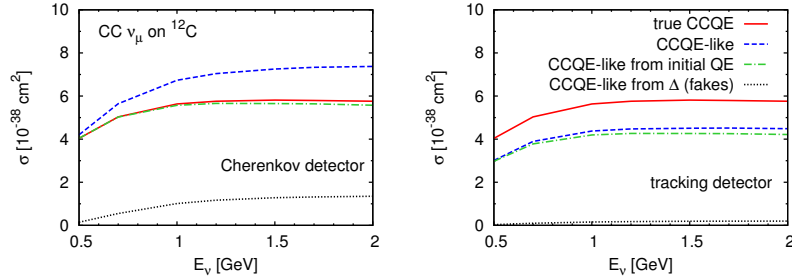
Figure 47: (Color online) Total QE cross section on ^{12}C (solid lines) compared to different methods on how to identify CCQE-like events in experiments (dashed lines). The top panel shows the method commonly applied in Cherenkov detectors, the lower panel the tracking-detector method as described in the text. The contributions to the CCQE-like events are also classified (CCQE-like from initial QE (dash-dotted), from initial Δ (dotted lines)). Experimental detection thresholds are not taken into account. Source: Taken from [356].

Furthermore, it is indicated in fig. 46, whether the knocked-out nucleon stems from initial QE scattering or Δ excitation (the contributions from higher resonances and from the non-resonant background are also shown). In contrast to the pion case, both contribute to the total cross section, even though with different weights depending on the neutrino energy. The phase space for Δ excitations opens later than for QE; this explains the small contribution of the Δ at $E_\nu = 0.5$ GeV, which increases with energy.

Events with multiple nucleons in the final state are disregarded in the right panels of fig. 46. This leads to a very different behavior, in particular, the cross section without FSI is in general above the one with FSI included. Comparing both scenarios shows, that for single-nucleon knockout the Δ contribution is smaller than the QE one while it can be larger for the multiple-nucleon knockout. Through processes like $\Delta N \to NN$ and $\Delta \to \pi N$ followed by $\pi N \to \pi N$, the Δ contributes in large parts to the multiple-nucleon knockout.

One important result of our approach is the finding that already at $E_\nu \approx 1$ GeV a large part of the ejected nucleons stems from Δ excitation and/or other processes different from QE, or, in other words, QE and non-QE processes are "mixed" due to FSI. This is a unique feature of a coupled-channel approach, such as the GiBUU model, not present in other models. Except for empirical event generators, we do not know of any other model for neutrino-induced nucleon knockout which accounts for QE and non-QE scattering simultaneously. This mixing, however, has major implications for neutrino-oscillation experiments since it can lead to misidentification of events as we shall see in the following.

4.4.3. Charged-current quasi-elastic identification and energy reconstruction

The charged-current quasi-elastic (CCQE) reaction, $\nu_\ell n \to \ell^- p$, being the dominant cross section at low energies, is commonly used to reconstruct the neutrino energy. In other words, CCQE is the signal event in present oscillation experiments.

The experimental challenge is to identify *true* CCQE events in the detector, i.e., muons originating from an initial QE process. To be more precise: true CCQE corresponds to the inclusive cross section including all medium effects, or, in other words, the CCQE cross section before FSI. The difficulty is that the true CCQE events are masked by FSI in a detector built out of nuclei. The FSI lead to misidentification of events, e.g., an initial Δ whose decay pion is absorbed or which undergoes "pion-less decay" contributes to knock-out nucleons and can thus be counted

as CCQE event – we call this type of background events "fake CCQE" events. We denote every event which looks like a CCQE event by "CCQE-like".

At Cherenkov detectors CCQE-like events are all those, where no pion is detected, while in tracking detectors CCQE-like events are those, where a single-proton track is visible and at the same time no pions are detected. The two methods are compared in fig. 47. The "true CCQE" events are denoted with the solid lines, the CCQE-like events by the dashed ones. The Cherenkov detector is able to detect almost all true CCQE (left panel, solid vs. dash-dotted lines agree approximately) but sees also a considerable amount of "fake CCQE" (or "CC non-QE") events (left panel, the dashed line is roughly 20 % higher than the solid line). They are caused mainly by initial Δ excitation as described in the previous paragraph (absorption of the decay pion or "pion-less decay"); their contribution to the cross section is given by the dotted lines. These additional (fake) events have to be removed from the measured event rates by means of event generators, if one is interested only in the true QE events. It is obvious that this removal is the better the more realistic the generator is in handling the in-medium π-N-Δ dynamics.

On the contrary, less CCQE-like than true CCQE events are detected using the method applied in tracking detectors, which trigger both on pions and protons (right panel, difference between dashed and solid lines). The final-state interactions of the initial proton lead to secondary protons, or, via charge exchange, to neutrons which are then not detected as CCQE-like any more (*single*-proton track). We find, that at tracking detectors the amount of fake events in the CCQE-like sample is less than at Cherenkov detectors (dashed and dash-dotted lines almost agree with each other in the right panel but not in the left panel). We conclude, that even if the additional cut on the proton helps to restrict the background, an error of about 20 % remains, since the measured CCQE cross section underestimates the true one by that amount. Thus about 20 % of the total cross section has to be reconstructed by using event generators. In this case these generators have to be very realistic in describing the in-medium nucleon-nucleon interactions. Note that for both detector types experimental detection thresholds are not yet taken into account. Their effect will make the errors even larger [356, 357].

The neutrino energy is commonly reconstructed from QE events using a relation for quasifree scattering on a nucleon at rest,

$$E_\nu^{\text{rec}} = \frac{2(M_N - E_B)E_\mu - (E_B^2 - 2M_N E_B + m_\mu^2)}{2\left[(M_N - E_B) - E_\mu + |\mathbf{k}'|\cos\theta_\mu\right]}, \tag{233}$$

with a binding-energy correction of $E_B = 34$ MeV [358], and the measured muon energy, E_μ, and scattering angle, θ_μ.

In fig. 48 we plot the distribution of the reconstructed neutrino energy obtained using eq. (233) with $E_B = 34$ MeV for four fixed E_ν^{real} (0.5, 0.7, 1.0, and 1.5 GeV). The dashed lines show the true CCQE events only, the solid lines all CCQE-like events (using the Cherenkov definition but without any threshold cuts). Both curves show a prominent peak around the real energy, which is slightly shifted to higher E_ν^{rec}. This shift is caused by the difference between our potential and the specific choice of E_B. The peak has a width of around 100 MeV. This broadening is entirely caused by the Fermi motion of the nucleons – eq. (233) assumes nucleons at rest.

While the distribution of the reconstructed energy for the true CCQE events is symmetric around the peak, this is not the case for the CCQE-like distribution. The reconstruction procedure now includes also CC non-QE events. However, eq. (233) is entirely based on the muon kinematics and, in the case of Δ-induced CC non-QE events, more transferred energy is needed
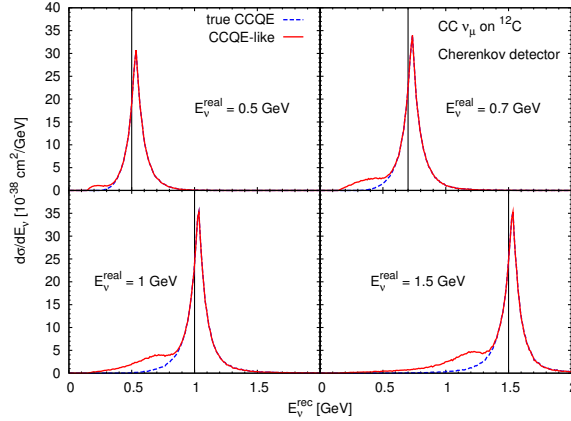
106

Figure 48: (Color online) Distribution of the reconstructed neutrino energy according to eq. (233) for E_ν^{real} = 0.5, 0.7, 1.0, and 1.5 GeV. The reconstructed energy denoted by the dashed lines includes only true CCQE events, while the solid lines are obtained by reconstructing the energy with CCQE-like events under Cherenkov assumptions. Source: Taken from [356].

than for true CCQE, thus, the muon energy is smaller. This lower muon energy then leads to the second smaller bump at lower reconstructed energies. Thus, the asymmetry is caused by the CC non-QE events identified as CCQE-like.

We have seen in the previous subsection, that the tracking detector allows to extract a much cleaner CCQE-like sample than the Cherenkov detector – almost no fake, i.e., CC non-QE events spoil the CCQE-like sample. Consequently, the reconstructed distribution is again symmetric but at the cost of a lower detection rate (see Fig. 8 in [356]).

The energy reconstruction influences directly the flux reconstruction needed for the extraction of neutrino oscillation parameters from long-baseline experiments which relies on flux comparisons at the near-side and the far-side detectors. The uncertainties in the flux related to the energy reconstruction are illustrated in fig. 49. The figure shows clearly that in particular the Cherenkov-type detectors lead to a downward shift of the energy distribution which has to be removed by event generators before a flux comparison can be done.

To conclude, we have shown that a correct identification of CCQE events is relevant for the neutrino energy reconstruction and thus for the oscillation result. A significant part of CC $1\pi^+$ events is detected as CCQE-like, which is mainly caused by the pion absorption in the nucleus. This has to be corrected by means of event generators, which is why the final experimental cross sections contain a significant model dependence. Thus, because of the close entanglement of CCQE and CC $1\pi^+$ on nuclei, both these channels have to be accounted for equally precise by any model aiming at describing the experimental measurements, in particular the directly observable rates for nucleon knockout and $1\pi^+$ production.

In this regard, the GiBUU is a flexible model of nuclear effects and is thus uniquely suited for a description of broad-band neutrino experiments. The requirements formulated by Benhar *et al.* [267] for a new paradigm in neutrino-nucleus scattering are all met. The GiBUU model can also accommodate the recently much discussed effects of $2p2h$ initial excitations that are not contained in the impulse approximation (see [355] and refs. therein). Following the method discussed in section 3.3.3 for the case of pion-induced reactions such excitations could easily be
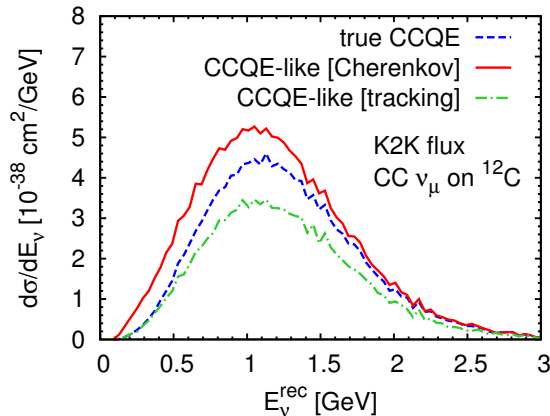
107

Figure 49: (Color online) Reconstructed energy distribution for the K2K flux under different detector assumptions. Equation (233) is used for the reconstruction, but with $E_B = 0$ (from [356]).

implemented.

5. Summary

In this article we have given a comprehensive, detailed discussion of transport theory and its practical implementation in the GiBUU transport model. It has been our aim to give all the essential ingredients of this model so that GiBUU is not a black box to other theorists or experimenters using it for planning or analyzing an experiment.

GiBUU is unique in the sense that it uses the same physics input for very different nuclear reactions and is not a model of many-body physics optimized for one particular reaction or energy range. For example, the very same theory and numerical implementation of $\Delta N\pi$ dynamics is used both for heavy-ion collisions and for neutrino-induced reactions on nuclei. As another example, it is able to give a reasonable description of quasi-elastic scattering off nuclei as well as of pion production through resonance excitations and is thus, for example, an ideal tool for an analysis of broad-energy band neutrino long-baseline experiments that necessarily average over many reaction types. The primary strength of GiBUU lies in the description of final-state interactions and here again it can be used both for heavy-ion and for electroweak reactions. Many important analyses of fundamental physics questions, such as short-range correlation studies from $(e, e'p)$ reactions on nuclei, the search for color transparency in electron- or pion-induced reactions or the investigation of in-medium changes of hadron-spectral properties depend crucially on a precise treatment of final-state interactions. The often used Glauber approximation in its most simple form only describes attenuation of primarily produced particles on straight-line trajectories. However, in reality the final, observed particles outside the nucleus, that reach the detector, may not be the ones that were originally hit by the incoming probe. They can change their identity, and they can also change their energy while traveling through the nucleus. All these effects are not included in the widely used Glauber attenuation treatment, but are contained in a transport theoretical description.

On the other hand, transport theory also has its limitations. Fully exclusive or coherent particle production reactions on nuclei can only be described by quantum-mechanical methods

since here the phase relations between the interaction amplitudes for all the nucleons in the nuclear target are essential so that transport theory must fail. However, for inclusive and semi-inclusive reactions on nuclei, where the phase-coherence between various reaction steps is lost due to multiple scattering, transport theory is the theory of choice. For fully inclusive reactions it gives cross sections that are as good as those obtained from quantum-mechanical methods, such as distorted-wave approximations or optical-model descriptions. For semi-inclusive reactions it is, however, superior to the latter ones since it does not only describe the loss of flux out of a given channel of interest, but also tells where this flux goes.

In the present article we have first considered the general theoretical framework starting from nonequilibrium nuclear many-body dynamics and leading to the off-shell transport equations that are actually being solved. From this discussion it is clear that even after so many years the Kadanoff-Baym equations have not been fully solved, and the back flow term still presents a problem. However, there have been physics-motivated approaches around this problem, that lead to the actual transport equations. We have then given all the details on the mean fields and the collision terms being used in many of the existing codes. One problem that arises in using self-energies defined only in the local rest frame, such as those provided by the Skyrme force, is that of handling the necessary Lorentz-transformations in a 'clean' way. The use of a relativistic mean-field theory with its well-defined Lorentz-transformation properties of all involved potentials avoids this problem, but the presently available relativistic mean-field theory still suffers from the problem of leading to too repulsive nucleon-nucleus potentials at large energies. This is clearly a point that deserves more attention in the future.

We have then presented a broad range of physics illustrations for results obtained with GiBUU covering a wide range of reaction types and energies. Common to all of them is that final-state interactions play a major role. In particular, if one is after physically interesting and challenging questions such as, e.g., color transparency or in-medium properties of hadrons, to name just two, one has to treat the final-state interactions at the same state-of-the-art level as the actual physics process to arrive at the final observables. This is still not so in many theoretical studies of such effects, which employ state-of-the-art QCD-based methods to calculate the primary physics effects in an idealized environment and then use much less sophisticated methods to describe the ever-present final-state interactions. GiBUU provides a method to include the best presently available treatment of final-state interactions into any such calculations. We have illustrated that with a broad range of applications and comparisons to experiment. To name just a few, examples ranged from antiproton reactions on nuclei over nuclear fragmentation in heavy-ion collisions to studies of electroweak interactions with nuclei, including hadronization and the search for color transparency. This, for example, makes GiBUU a tool well suited for investigations of $e + A$ reactions at the electron-ion collider which is now being planned as one of the new machines for the next decade [359]. The GiBUU method and code has been explained in quite some detail in this article. The actual code is publicly available from [23].

Future developments go into the direction of hybrid codes that contain both hadronic and partonic degrees of freedom. For ultrarelativistic heavy-ion reactions this is necessary to pin down observable consequences of the formation of a quark-gluon plasma phase during the collision and thus to verify its production. First attempts in this direction have already been undertaken [233, 360, 361]. For electroweak reactions at high energies the observation of produced hadrons can give valuable information on production, formation and expansion times of pre-hadrons or hadrons formed out of the struck quarks inside the nuclear medium. Thus, both degrees of freedom, hadronic and partonic ones, have to be described and their time-development has to be investigated also in the more microscopic reactions. Such work has only very re-

cently started [273, 133]; transport theory is the only known tool to gain insight into these questions. We foresee future applications for GiBUU in antiproton-induced hypernucleus formation at PANDA@FAIR, in hadronization and color transparency studies at JLAB at 12 GeV and in $e + A$ reactions at the EIC [359]. In addition, the understanding of the detector response in the new class of long-baseline neutrino experiments will be an interesting application.

Acknowledgment

Appendix

In order to make the GiBUU model as transparent as possible and to give the interested reader and/or practitioner sufficient information about the 'inner workings' of the model and code we give in the following extensive paragraphs essential details for the particles implemented in the actual event description and for the decay rates and cross sections entering the collision term. In this way we want to make sure that GiBUU as a method and code is not a 'black box' to the user, but that instead the microscopic input is known. We also give some details about the numerical implementation.

Appendix A. Properties and decay channels of implemented baryons and mesons

Herein, we list all particles considered in the GiBUU model with their masses, widths, quantum numbers and decay modes. Only the strong and, in some cases, electromagnetic decay modes are taken into account. The weak decay modes are neglected and the corresponding widths are set to zero. Also the dilepton decays are usually neglected, but can be treated perturbatively if required (cf. Appendix A.1).

The properties of the thirty-one non-strange/non-charm resonances included in the code are listed in table A.3 together with their decay channels. These properties are taken from the partial wave analysis of πN amplitudes of ref. [64]. We use the common notation which reads l_{ij} with the spin $J = \frac{j}{2}$ and isospin $I = \frac{i}{2}$, while l denotes the relative angular momentum of the πN system. The parity follows from $P = (-1)^{l+1}$. By default, all the baryonic resonances listed in table A.3 except for the $I = \frac{1}{2}$ resonances with one-star (*) rating are allowed to be created in the meson-baryon collisions.

The properties of the baryons with strangeness and charm quantum numbers are collected in tables A.4 and A.5. The masses, widths and quantum numbers are taken from the PDG analysis [54]. The most branching ratios are also adopted from Ref. [54]. The branching ratios not given in [54] (e.g. $\Sigma^*\pi$ for $\Lambda(1520)$, $\Lambda(1690)$, $\Sigma(1775)$ and $\Lambda(2100)$) have been estimated or set to saturate the sum of the branching ratios to 100 %.

The mesons and their properties are listed in table A.6. Their quantum numbers and the most important decay channels with their branching ratios are given explicitly. The meson properties are defined according to the PDG analysis [54].

Appendix A.1. Dilepton decays

In the GiBUU model the following dilepton decay modes are taken into account:

- direct decays, as $V \rightarrow e^+e^-$ with $V = \rho^0, \omega, \phi$, or $\eta \rightarrow e^+e^-$,

- Dalitz decays, as $P \rightarrow e^+e^-\gamma$ with $P = \pi^0, \eta, \omega \rightarrow \pi^0 e^+e^-$, or $\Delta \rightarrow Ne^+e^-$

Most of them are treated similarly as in Ref. [60]. The leptonic decay widths of the vector mesons are calculated under the assumption of strict vector-meson dominance (VMD),

$$\Gamma_{V \rightarrow e^+e^-}(\mu) = C_V \frac{m_V^4}{\mu^3},$$

with the constants, C_V, listed in table A.7.

		M_B [MeV]	Γ_0 [MeV]	branching ratio in %								
				$N\pi$	$N\eta$	$N\omega$	$K\Lambda$	$\Delta\pi$	$N\rho$	$N\sigma$	$N^*\pi$	$\Delta\rho$
N(938)	****	938	0	—	—	—	—	—	—	—	—	—
P$_{33}$(1232)	****	1232	118	100	—	—	—	—	—	—	—	—
P$_{11}$(1440)	****	1462	391	69	—	—	—	22	—	9	—	—
S$_{11}$(1535)	***	1534	151	51	43	—	—	—	3	1	2	—
S$_{11}$(1650)	****	1659	173	89	3	—	—	2	3	2	1	—
S$_{11}$(2090)	*	1928	414	10	—	—	—	6	49	5	30	—
D$_{13}$(1520)	****	1524	124	59	—	—	—	20	21	—	—	—
D$_{13}$(1700)	*	1737	249	1	—	—	—	84	13	2	—	—
D$_{13}$(2080)	*	1804	447	23	—	—	—	24	26	27	—	—
D$_{15}$(1675)	****	1676	159	47	—	—	—	53	—	—	—	—
G$_{17}$(2190)	****	2127	547	22	—	49	—	—	29	—	—	—
P$_{11}$(1710)	*	1717	478	9	—	—	37	49	3	2	—	—
P$_{11}$(2100)	*	1885	113	15	—	—	2	24	27	32	—	—
P$_{13}$(1720)	*	1717	383	13	—	—	—	—	87	—	—	—
P$_{13}$(1900)	***	1879	498	26	—	30	—	—	44	—	—	—
F$_{15}$(1680)	****	1684	139	70	—	—	—	11	7	12	—	—
F$_{15}$(2000)	*	1903	494	8	—	—	—	12	75	5	—	—
F$_{17}$(1990)	**	2086	535	6	94	—	—	—	—	—	—	—
S$_{31}$(1620)	**	1672	154	9	—	—	—	62	29	—	—	—
S$_{31}$(1900)	***	1920	263	4	—	—	—	16	38	—	6	—
D$_{33}$(1700)	*	1762	599	14	—	—	—	78	8	—	—	—
D$_{33}$(1940)	*	2057	460	18	—	—	—	47	35	—	—	—
D$_{35}$(1930)	**	1956	526	18	—	—	—	—	—	—	—	82
D$_{35}$(2350)	**	2171	264	2	—	—	—	—	—	—	—	98
P$_{31}$(1750)	*	1744	299	8	—	—	—	—	—	—	28	64
P$_{31}$(1910)	****	1882	239	23	—	—	—	—	10	—	67	—
P$_{33}$(1600)	***	1706	430	12	—	—	—	68	—	—	20	—
P$_{33}$(1920)	*	2014	152	2	—	—	—	83	—	—	15	—
F$_{35}$(1750)	*	1752	251	2	—	—	—	76	22	—	—	—
F$_{35}$(1905)	***	1881	327	12	—	—	—	1	87	—	—	—
F$_{37}$(1950)	****	1945	300	38	—	—	—	18	—	—	—	44

Table A.3: Properties and decay channels for the non-strange/non-charm baryons. Given are the rating, the Breit-Wigner mass M_B, the width Γ_0 at M_B and the branching ratios into the various decay channels. Adopted from ref. [64].

		M_B [MeV]	Γ_0 [MeV]	J	branching ratio in %						
					$\Lambda\pi$	$N\bar{K}$	$\Sigma\pi$	$\Sigma^*\pi$	$\Lambda\eta$	$N\bar{K}^*$	$\Lambda^*\pi$
$\Lambda(1116)$	****	1116	0	1/2	—	—	—	—	—	—	—
$\Sigma(1189)$	****	1189	0	1/2	—	—	—	—	—	—	—
$\Sigma(1385)$	****	1385	36	3/2	88	—	12	—	—	—	—
$\Lambda(1405)$	****	1405	50	1/2	—	—	100	—	—	—	—
$\Lambda(1520)$	****	1520	16	3/2	—	46	43	11	—	—	—
$\Lambda(1600)$	***	1600	150	1/2	—	35	65	—	—	—	—
$\Sigma(1660)$	***	1660	100	1/2	40	20	40	—	—	—	—
$\Lambda(1670)$	****	1670	35	1/2	—	25	45	—	30	—	—
$\Sigma(1670)$	****	1670	60	3/2	15	15	70	—	—	—	—
$\Lambda(1690)$	****	1690	60	3/2	—	25	30	45	—	—	—
$\Sigma(1750)$	***	1750	90	1/2	10	30	60	—	—	—	—
$\Sigma(1775)$	****	1775	120	5/2	20	45	5	10	—	—	20
$\Lambda(1800)$	***	1800	300	1/2	—	35	35	30	—	—	—
$\Lambda(1810)$	***	1810	150	1/2	—	35	20	—	—	45	—
$\Lambda(1820)$	****	1820	80	5/2	—	60	12	28	—	—	—
$\Lambda(1830)$	****	1830	95	5/2	—	5	60	35	—	—	—
$\Lambda(1890)$	****	1890	100	3/2	—	30	10	30	—	30	—
$\Sigma(1915)$	****	1915	120	5/2	45	10	45	—	—	—	—
$\Sigma(2030)$	****	2030	180	7/2	25	25	10	15	—	5	20
$\Lambda(2100)$	****	2100	200	7/2	—	30	5	45	—	20	—
$\Lambda(2110)$	***	2110	200	5/2	—	15	30	—	—	55	—

Table A.4: Properties and decay channels for the baryons with strangeness $S = -1$. Given are the rating, the Breit-Wigner mass M_B, the width Γ_0 at M_B, the spin J and the branching ratios into the various decay channels. Based on the PDG review [54].

		M_B [MeV]	Γ_0 [MeV]	$I(J^P)$	S	C	decay mode
Ξ	****	1315	0	$\frac{1}{2}(\frac{1}{2}^+)$	-2	0	—
$\Xi^\star$	****	1530	9.5	$\frac{1}{2}(\frac{3}{2}^+)$	-2	0	$\Xi\pi$
Ω	****	1672	0	$0(\frac{3}{2}^+)$	-3	0	—
Λ_c	****	2285	0	$0(\frac{1}{2}^+)$	0	1	—
Σ_c	****	2452	0	$1(\frac{1}{2}^+)$	0	1	—
Σ_c^*	****	2520	15	$1(\frac{3}{2}^+)$	0	1	$\Lambda_c\pi$
Ξ_c	***	2466	0	$\frac{1}{2}(\frac{1}{2}^+)$	-1	1	—
Ξ_c^*	***	2645	4	$\frac{1}{2}(\frac{3}{2}^+)$	-1	1	$\Xi_c\pi$
Ω_c	***	2698	0	$0(\frac{1}{2}^+)$	-2	1	—

Table A.5: Properties and decay channels for the baryons with strangeness $S < -1$ and charm $C = 1$. Given are the rating, the Breit-Wigner mass, M_B, the width Γ_0 at M_B, the quantum numbers and decay channels. Taken from the PDG review [54].

	m_m[MeV]	Γ_0 [MeV]	J	I	S	C	decay channels
π	138	0	0	1	0	0	
η	547	$1.2 \cdot 10^{-3}$	0	0	0	0	$\gamma\gamma$ (40%), $\pi^+\pi^-\pi^0$ (28%), $3\pi^0$ (32%)
ρ	770	151	1	1	0	0	$\pi\pi$
σ	800	800	0	0	0	0	$\pi\pi$
ω	782	8.4	1	0	0	0	$\pi\pi$ (2%), $\pi^0\gamma$ (9%), $\pi^+\pi^-\pi^0$ (89%)
η'	958	0.2	0	0	0	0	$\rho^0\gamma$ (31%), $\pi\pi\eta$ (69%)
ϕ	1020	4.4	1	0	0	0	$\rho\pi$ (13%), $K\bar{K}$ (84%), $\pi^+\pi^-\pi^0$ (3%)
K	496	0	0	1/2	1	0	
$\bar{K}$	496	0	0	1/2	-1	0	
K^*	892	50	1	1/2	1	0	$K\pi$
$\bar{K}^*$	892	50	1	1/2	-1	0	$\bar{K}\pi$
η_c	2980	0	0	0	0	0	
J/Ψ	3097	0	1	0	0	0	
D	1867	0	0	1/2	0	1	
$\bar{D}$	1867	0	0	1/2	0	-1	
$(D^*)^0$	2007	2	1	1/2	0	1	$D\gamma$ (38%), $D\pi$ (62%)
$(D^*)^+$	2007	96×10^{-3}	1	1/2	0	1	$D\gamma$ (2%), $D\pi$ (98%)
$(\bar{D}^*)^0$	2007	2	1	1/2	0	-1	$\bar{D}\gamma$ (38%), $\bar{D}\pi$ (62%)
$(\bar{D}^*)^-$	2007	96×10^{-3}	1	1/2	0	-1	$\bar{D}\gamma$ (2%), $\bar{D}\pi$ (98%)
D_s	1969	0	0	0	1	1	
$\bar{D}_s$	1969	0	0	0	-1	-1	
D_s^*	2112	1	0	0	1	1	$D_s\gamma$ (95%), $D_s\pi$ (5%)
$\bar{D}_s^*$	2112	1	0	0	-1	-1	$\bar{D}_s\gamma$ (95%), $\bar{D}_s\pi$ (5%)

Table A.6: Properties and decay channels for the light mesons. Given are the pole mass m_m, the width Γ_0 at m_m, spin J, isospin I, strangeness S, and the branching ratios into the various decay channels. Based on the PDG review [54].

V	$m_V(\text{MeV})$	$\Gamma_{ee}(\text{keV})$	$C_V = \Gamma_{ee}/m_V$
ρ	775.49	7.04	$9.078 \cdot 10^{-6}$
ω	782.65	0.60	$7.666 \cdot 10^{-7}$
ϕ	1019.455	1.27	$1.246 \cdot 10^{-6}$

Table A.7: Dilepton-decay constants for $V \to e^+e^-$.

While the direct decay of the η meson into a $\mu^+\mu^-$ pair has been observed, for the corresponding e^+e^- decay only an upper limit of $\text{BR}(\eta \to e^+e^-) < 2.7 \cdot 10^{-5}$ is known [362]. However, the theoretical expectation from helicity suppression is still four orders of magnitude lower [363]. The Dalitz decays of the pseudoscalar mesons, $P = \pi^0, \eta, \eta'$, are treated via the parametrization [364],

$$\frac{\mathrm{d}\Gamma_{P \to \gamma e^+e^-}}{\mathrm{d}\mu} = \frac{4\alpha}{3\pi} \frac{\Gamma_{P \to \gamma\gamma}}{\mu} \left(1 - \frac{\mu^2}{m_P^2}\right)^3 |F_P(\mu)|^2, \tag{A.1}$$

with $\Gamma_{\pi^0 \to \gamma\gamma} = 7.8 \cdot 10^{-6}\,\text{MeV}$ and $\Gamma_{\eta \to \gamma\gamma} = 4.6 \cdot 10^{-4}\,\text{MeV}$ and the form factors,

$$F_{\pi^0}(\mu) = 1 + b_{\pi^0}\mu^2, \qquad b_{\pi^0} = 5.5\,\text{GeV}^{-2}, \tag{A.2}$$

$$F_\eta(\mu) = \left(1 - \frac{\mu^2}{\Lambda_\eta^2}\right)^{-1}, \quad \Lambda_\eta = 0.676\,\text{GeV}. \tag{A.3}$$

The above value of Λ_η has been recently determined from HADES data [365]. It should be noted that the form factors of the π^0 and η Dalitz decays are sufficiently constrained by data, while the experimental constraints of the η' form factor are much weaker [364]. A VMD form factor for the η' Dalitz decay can be found for example in [366]. The parametrization of the ω Dalitz decay,

$$\frac{\mathrm{d}\Gamma_{\omega \to \pi^0 e^+e^-}}{\mathrm{d}\mu} = \frac{2\alpha}{3\pi} \frac{\Gamma_{\omega \to \pi^0\gamma}}{\mu} \left[\left(1 + \frac{\mu^2}{\mu_\omega^2 - m_\pi^2}\right)^2 - \frac{4\mu_\omega^2\mu^2}{(\mu_\omega^2 - m_\pi^2)^2}\right]^{3/2} |F_\omega(\mu)|^2,$$

$$|F_\omega(\mu)|^2 = \frac{\Lambda_\omega^4}{(\Lambda_\omega^2 - \mu^2)^2 + \Lambda_\omega^2\Gamma_\omega^2}, \tag{A.4}$$

is adopted from [367] with $\Gamma_{\omega \to \pi^0\gamma} = 0.703\,\text{MeV}$, $\Lambda_\omega = 0.65\,\text{GeV}$ and $\Gamma_\omega = 75\,\text{MeV}$. We note here that the form factor of the ω Dalitz decay is also well-constrained by data [368]. For the Δ-Dalitz decay we use the parametrization from Ref. [369],

$$\frac{\mathrm{d}\Gamma_{\Delta \to Ne^+e^-}}{\mathrm{d}\mu} = \frac{2\alpha}{3\pi\mu}\Gamma_{\Delta \to N\gamma^*},$$

$$\Gamma_{\Delta \to N\gamma^*} = \frac{\alpha}{16} \frac{(m_\Delta + m_N)^2}{m_\Delta^3 m_N^2} \left[(m_\Delta + m_N)^2 - \mu^2\right]^{1/2} \left[(m_\Delta - m_N)^2 - \mu^2\right]^{3/2} |F_\Delta(\mu)|^2, \tag{A.5}$$

where we neglect the electron mass. The electromagnetic N-Δ transition form factor $F_\Delta(\mu)$ is an issue of ongoing debate. Unlike the other semileptonic Dalitz decays, it is poorly constrained by data. At least at the real-photon point ($\mu = 0$) it is fixed by the decay $\Delta \to N\gamma$ to $|F_\Delta(0)| = 3.029$, and also in the space-like region this form factor is well-constrained by electron scattering data

on the nucleon. However, this form factor is basically unknown in the time-like regime, which is being probed by the Δ Dalitz decay.

From the theoretical side, many parametrizations are available for the space-like part, but most of them are not applicable in the time-like region. One of the few models which take care of the continuation to the time-like region is the two-component quark model given in [221].

Appendix B. Cross sections

The cross sections are mostly given by some suitable fits to the experimental data. In some cases, e.g., for the $NN \rightarrow N\Delta$ process, a simple one-boson exchange model is applied. The meson-baryon collisions are dominated by the intermediate resonance excitation. At high invariant energies, we rely mostly on the PYTHIA [110] and FRITIOF [370] event generators. In the following, we describe in detail the cross sections used in the GiBUU collision term.

Appendix B.1. Baryon-baryon cross sections

At $\sqrt{s} > 2.6$ GeV, a baryon-baryon collision is considered as a highly-energetic one in our model[21]. In this case, the simulation of elastic collision events is done according to the cross section parametrization of Ref. [371] fitted to the pp data,

$$\sigma_{\text{el}} = 11.9 + 26.9 p_{\text{lab}}^{-1.21} + 0.169 \ln^2(p_{\text{lab}}) - 1.85 \ln(p_{\text{lab}}) , \tag{B.1}$$

where the beam momentum p_{lab} is given in GeV/c, and the cross section in mb. The angular distribution for the elastic scattering events is chosen as

$$\frac{\mathrm{d}\sigma_{\text{el}}}{\mathrm{d}t} \propto \exp(bt) \tag{B.2}$$

with the energy dependent slope parameter $b = 5.0 + 4s^{0.0808}$ taken from the PYTHIA model (see also Ref. [67]), where s is given in GeV^2 and b in GeV^{-2}. The inelastic collision events are simulated with the help of a PYTHIA event generator. The cross section for the inelastic events is given as the difference $\sigma_{\text{tot}} - \sigma_{\text{el}}$ with the total cross section parametrized in Ref. [371] to the pp data,

$$\sigma_{\text{tot}} = 48.0 + 0.522 \ln^2(p_{\text{lab}}) - 4.51 \ln(p_{\text{lab}}) , \tag{B.3}$$

where p_{lab} is in GeV/c, and σ_{tot} in mb.

At the lower invariant energies $\sqrt{s}$, we take into account the baryon-baryon (BB) elastic scattering or charge exchange (CEX) $BB \rightarrow BB$, resonance (R), and double-Δ production and absorption in nucleon-nucleon (NN) collisions $NN \leftrightarrow NR$, $NN \leftrightarrow \Delta\Delta$, as well as the (direct) pion production and absorption $NN \leftrightarrow NN\pi$. Also the strangeness production in the processes $BB \rightarrow KYB$ and $BB \rightarrow NNK\bar{K}$ is included in the model. The explicit low-energy BB collision channels are listed below.

---

[21]See section 3.3.2 for more precise definition of the low- and high-energy two-body collisions.

NN ↔ NN

The cross sections for elastic pp and np scattering at low energies are based on the parametrizations of Cugnon *et al.* [372]. The only difference of our cross sections compared to those of Ref. [372] is that at the beam momenta below 0.4-0.5 GeV/c we adopt different functional form [373] with numerical parameters refitted to the world data on pp and np total cross sections [374]. This results in the following expressions in various beam momentum ranges,

$$
\sigma_{\text{el}}^{pp} = \begin{cases} 5.12 m_N/(s - 4m_N^2) + 1.67 & \text{for} & p_{\text{lab}} < 0.435 \\ 23.5 + 1000(p_{\text{lab}} - 0.7)^4 & \text{for} & 0.435 < p_{\text{lab}} < 0.8 \\ 1250/(p_{\text{lab}} + 50) - 4(p_{\text{lab}} - 1.3)^2 & \text{for} & 0.8 < p_{\text{lab}} < 2 \\ 77/(p_{\text{lab}} + 1.5) & \text{for} & 2 < p_{\text{lab}} < 6 \end{cases}
\tag{B.4}
$$

and

$$
\sigma_{\text{el}}^{np} = \begin{cases} 17.05 m_N/(s - 4m_N^2) - 6.83 & \text{for} & p_{\text{lab}} < 0.525 \\ 33 + 196|p_{\text{lab}} - 0.95|^{2.5} & \text{for} & 0.525 < p_{\text{lab}} < 0.8 \\ 31/\sqrt{p_{\text{lab}}} & \text{for} & 0.8 < p_{\text{lab}} < 2 \\ 77/(p_{\text{lab}} + 1.5) & \text{for} & 2 < p_{\text{lab}} < 6 \end{cases} ,
\tag{B.5}
$$

where the beam momentum p_{lab} is given in GeV/c, the nucleon mass m_N and the invariant energy $\sqrt{s} = \sqrt{2m_N^2 + 2m_N E_{lab}}$ (with $E_{lab} = \sqrt{m_N^2 + p_{\text{lab}}^2}$) in GeV , and the cross sections in mb. The neutron-neutron elastic-scattering cross section is obtained from the proton-proton one by isospin symmetry, $\sigma_{\text{el}}^{nn} = \sigma_{\text{el}}^{pp}$. The angular dependence of the NN-elastic scattering is chosen according to Ref. [372], where accurate and compact parametrizations of the experimental pp and np angular differential cross sections are developed.

NN ↔ NΔ

The differential cross section for Δ-resonance production in an NN collision is calculated as a special case of eq. (D.28) as

$$
\frac{d\sigma_{NN \to N\Delta}}{d\mu_\Delta^2 d\Omega} = \frac{\overline{|\mathcal{M}_{NN \to N\Delta}|^2}}{64\pi^2 s} \frac{p_{N\Delta}}{p_{NN}} \mathcal{A}_\Delta(\mu_\Delta^2) ,
\tag{B.6}
$$

where p_{NN} and $p_{N\Delta}$ are the initial and final center-mass (CM) momenta, respectively, and $\mathcal{A}_\Delta(\mu_\Delta^2)$ denotes the spectral function of the Δ resonance (see eq. (76)). $\overline{|\mathcal{M}_{NN \to N\Delta}|^2}$ is the matrix element squared, averaged over spins of particles in the initial and summed over spins of particles in the final state. It has been calculated for the channel $pp \to n\Delta^{++}$ by Dmitriev *et al.* [120] within the one-pion exchange model. This model describes the differential $pp \to n\Delta^{++}$ cross sections at beam momenta 1-6 GeV/c very accurately [120]. For other isospin channels, the cross sections are related to the $pp \to n\Delta^{++}$ cross section by Clebsch-Gordan coefficients, which gives

$$
\sigma_{pp \to p\Delta^+} = \sigma_{pn \to p\Delta^0} = \sigma_{pn \to n\Delta^+} = \sigma_{nn \to n\Delta^0} = \frac{1}{3}\sigma_{pp \to n\Delta^{++}} ,
\tag{B.7}
$$

$$
\sigma_{nn \to p\Delta^-} = \sigma_{pp \to n\Delta^{++}} .
\tag{B.8}
$$

			$\mathcal{I}$
$p\Delta^{++}$	$\rightarrow$	$p\Delta^{++}$	9/4
$p\Delta^{+}$	$\rightarrow$	$n\Delta^{++}$	3
$p\Delta^{+}$	$\rightarrow$	$p\Delta^{+}$	1/4
$p\Delta^{0}$	$\rightarrow$	$p\Delta^{0}$	1/4
$p\Delta^{0}$	$\rightarrow$	$n\Delta^{+}$	4
$p\Delta^{-}$	$\rightarrow$	$p\Delta^{-}$	9/4
$p\Delta^{-}$	$\rightarrow$	$n\Delta^{0}$	3

Table B.8: Isospin factors for the $N\Delta \rightarrow N\Delta$ process. For the neutron channels, the isospin factors follow by isospin symmetry.

Using the detailed balance relation eq. (181), the inverse reaction cross sections are obtained as

$$\frac{\mathrm{d}\sigma_{N\Delta\rightarrow NN}}{\mathrm{d}\Omega} = \frac{\overline{|\mathcal{M}_{NN\rightarrow N\Delta}|^2}}{128\pi^2 s} \frac{p_{NN}}{p_{N\Delta}} S_{NN} \,, \tag{B.9}$$

where $S_{pp} = S_{nn} = 1/2$, $S_{pn} = 1$ is the symmetry factor for the final-state nucleons.

$N\Delta \rightarrow N\Delta$

The differential cross section of this process can be expressed in a similar way as for the process, $NN \rightarrow N\Delta$, see eq. (B.6),

$$\frac{\mathrm{d}\sigma_{N\Delta_i\rightarrow N\Delta_f}}{\mathrm{d}\mu_f^2 \mathrm{d}\Omega} = \frac{\overline{|\mathcal{M}_{N\Delta_i\rightarrow N\Delta_f}|^2}}{64\pi^2 s} \frac{p_{N\Delta_f}}{p_{N\Delta_i}} \mathcal{A}_\Delta(\mu_f^2) \,, \tag{B.10}$$

where $p_{N\Delta_i}$ and $p_{N\Delta_f}$ are the initial and final c.m. momenta, respectively. For the matrix element $\overline{|\mathcal{M}_{N\Delta_i\rightarrow N\Delta_f}|^2}$, we apply the one-pion exchange model, based on the $NN\pi$ and $\Delta\Delta\pi$ interactions, which results in the following expression (see e.g. [375, 55] for the details of the derivation),

$$\overline{|\mathcal{M}_{N\Delta_i\rightarrow N\Delta_f}|^2} = \mathcal{I}\frac{1}{8}\left(\frac{f_{NN\pi}f_{\Delta\Delta\pi}}{m_\pi^2}\right)^2 \frac{F^4(t)}{(t-m_\pi^2)^2} \frac{16(\mu_i+\mu_f)^2 m_N^2 t}{9\mu_i^2\mu_f^2} \times$$
$$\times (-\mu_i^2 + 2\mu_i\mu_f - \mu_f^2 + t)(\mu_i^4 - 2\mu_i^3\mu_f + 12\mu_i^2\mu_f^2 - 2\mu_i\mu_f^3 + \mu_f^4 - 2\mu_i^2 t \tag{B.11}$$
$$+ 2\mu_i\mu_f t - 2\mu_f^2 t + t^2).$$

Here $F(t)$ is a usual monopole form factor [120]. The masses of the initial and final state Δ resonance are denoted as μ_i and μ_f, respectively. The isospin factors, $\mathcal{I}$, are given in table B.8. The $NN\pi$ coupling constant, $f_{NN\pi} = m_\pi g_A/(2f_\pi) = 0.946$, is used by default in our numerical evaluations of eq. (B.11). Here, $g_A = 1.267$ is the axial coupling of the nucleon, and $f_\pi = 92.4$ MeV is the pion-decay constant (cf. Ref. [376]). We choose the $\Delta\Delta\pi$ coupling constant, $f_{\Delta\Delta\pi} = 9/5 f_{NN\pi}$, motivated by the large-N_c limit [376]. The cutoff parameter, $\Lambda = 0.6$ GeV, is chosen according to Ref. [120].

In–medium Δ width based on the NN^{-1} and ΔN^{-1} model

In our default-model setup, the collisional (or spreading) width of the Δ resonance is given by eq. (84) with in-medium total Δ-nucleon cross sections given by the sum of the Pauli-blocked

vacuum partial $\Delta N \rightarrow \Delta N$ and $\Delta N \rightarrow NN$ cross sections calculated within the pion-exchange model as described above. The only in-medium effect appears in eq. (84) due to inclusion of Pauli blocking for the outgoing nucleon(s). Such a simple semiclassical approximation, however, completely neglects the in-medium modifications of the exchange pions and vertex corrections due to the short-range spin-isospin interactions. It also neglects the contribution of the Δ absorption by two nucleons, $\Delta NN \rightarrow NNN$. All these effects are quite important for a more realistic description of the processes mediated by Δ-resonance excitation in nuclear matter as shown within the NN^{-1} and ΔN^{-1} model by Oset and Salcedo [56]. Thus, we have optionally included the description of the collisional width of the Δ resonance using the parametrization from Ref. [56] in our model.

In Ref. [56], a special kinematic situation is considered when the Δ is created by a $N\pi$ collision. According to Eq. (4.4) of Ref. [56], the imaginary part of the collisional contribution to the Δ self-energy is parametrized as the sum of the higher order quasi-elastic (Q), two-body (A2), and three-body (A3) absorption components,

$$- \operatorname{Im} \Sigma_\Delta = C_Q (\rho/\rho_0)^\alpha + C_{A2} (\rho/\rho_0)^\beta + C_{A3} (\rho/\rho_0)^\gamma \, , \qquad (B.12)$$

where the coefficients, C_Q, C_{A2} and C_{A3}, and exponents, α, β, and γ are functions of the incoming pion-kinetic energy, T_π. Here, the sorting of the processes is done with respect to the pion interaction with nucleons. In the quasi-elastic case, the pion reappears in the final state, which is mainly mediated by the process $\Delta N \rightarrow \Delta N$[22]. The pion absorption by two and three nucleons is mediated by the processes, $\Delta N \rightarrow NN$ and $\Delta NN \rightarrow NNN$, respectively.

The collisional width of the Δ resonance can also be decomposed into the quasi-elastic, two- and three-body absorption-partial widths as readily follows from eq. (B.12),

$$\Gamma_{\mathrm{coll}} = -2 \operatorname{Im} \Sigma_\Delta = \Gamma_Q + \Gamma_{A2} + \Gamma_{A3} \, . \qquad (B.13)$$

In this expression, all partial widths are given in the Δ-rest frame and depend on the nucleon density, ρ, and on the mass, $\mu_\Delta = \sqrt{m_\pi^2 + m_N^2 + 2(T_\pi + m_\pi)(\frac{3}{5}E_F + m_N)}$, of the Δ resonance produced in the collision of the incoming pion with kinetic energy, T_π, with a nucleon in the Fermi sea. The energy and momentum of the Δ are correlated since they both are unique functions of the pion-kinetic energy, T_π. Thus, the above formula eq. (B.13) is, strictly speaking, applicable only to the Δ's created in πN collisions. However, this is the most important Δ-excitation channel for the pion-induced reactions on nuclei.

In earlier versions of the GiBUU model (cf. [60, 61]), the absorptional component $\Gamma_{A2} + \Gamma_{A3}$ of Γ_{coll} has been treated by converting the Δ to the nucleon or, for the case of perturbative treatment, by just deleting it with probability, $1 - \exp[-\Delta t (\Gamma_{A2} + \Gamma_{A3})/\gamma]$, during the time interval $[t; t + \Delta t]$. Here, $\gamma = p_\Delta^0 / \mu_\Delta$ is the Lorentz factor for the transformation of the widths from the Δ-rest frame to the laboratory frame, where the nucleus is at rest. To go beyond this relatively simple modeling, we now explicitly treat all three processes, $\Delta N \rightarrow \Delta N$, $\Delta N \rightarrow NN$, and $\Delta NN \rightarrow NNN$. This is important, if one is interested, e.g., in the spectra of outgoing nucleons or nuclear fragments from pion-induced reactions.

The (effective) cross sections of the former two processes are expressed in terms of the cor-

---

[22]In lowest order, the quasi-elastic pion scattering proceeds simply via the decay of the intermediate Δ resonance without any interactions of the latter with the nuclear medium. This process is, however, neglected in eq. (B.12).

responding partial widths by formally using the low-density approximation eq. (84) as follows

$$\sigma_{\Delta N \to \Delta N} = \Gamma_Q(\rho, \mu_\Delta)/\bar{v}_{\mathrm{rel}}(p_\Delta)\rho, \tag{B.14}$$

$$\sigma_{\Delta N \to NN} = \Gamma_{A2}(\rho, \mu_\Delta)/\bar{v}_{\mathrm{rel}}(p_\Delta)\rho, \tag{B.15}$$

where $\bar{v}_{\mathrm{rel}}(p_\Delta)$ denotes the average relative velocity of the Δ and a nucleon from the Fermi sea,

$$\bar{v}_{\mathrm{rel}}(p_\Delta) = \frac{4}{\rho} \int\limits_{p<p_F} \frac{\mathrm{d}^3 \boldsymbol{p}}{(2\pi)^3} \left| \boldsymbol{p}_\Delta/p_\Delta^0 - \boldsymbol{p}/p^0 \right| . \tag{B.16}$$

For the derivation of eqs. (B.14) and (B.15) it is assumed for simplicity that the cross sections, $\sigma_{\Delta N \to \Delta N}, \sigma_{\Delta N \to NN}$, do not depend on the Fermi-momentum $\boldsymbol{p}$.

The partial width, Γ_{A3}, can be approximately regarded as a three-body reaction rate, $\Delta NN \to NNN$ [56]. For the Δ mass in the pole region, all partial widths in eq. (B.13) are of equal importance: $\Gamma_Q \simeq \Gamma_{A2} \simeq \Gamma_{A3} \simeq 25\,\mathrm{MeV}$ (see Fig. 12 in Ref. [56]). Therefore, inclusion of the Δ absorption by two nucleons is the origin of the main difference between our standard calculations involving vacuum $\Delta N \to NN$ and $\Delta N \to \Delta N$ cross sections only, and the modified scheme based on the collisional width eq. (B.13).

To simulate the process, $\Delta NN \to NNN$, first, it is decided whether a given Δ will be absorbed during the time interval $[t; t + \Delta t]$ according to the probability $1 - \exp(-\Delta t \Gamma_{A3}/\gamma)$. Then, the two nucleons are randomly chosen in the vicinity of this Δ. Finally, the momenta of the outgoing nucleons are sampled according to the invariant three-body phase space.

$NN \leftrightarrow NR$, $NN \leftrightarrow \Delta\Delta$, $NR \leftrightarrow NR'$

We use the same cross sections as detailed in Appendix A1.2 of [60] based on the analysis presented by Teis [70]. Note, that we have chosen the $NN \to NS_{11}(1535)$ matrix element, $20 \cdot 16\pi\,\mathrm{mb\,GeV}^2$ (in Ref. [60], table A.1, three different values were presented).

$NR \leftrightarrow NR$

For all resonances besides the Δ, we assume

$$\sigma_{NR \to NR}(\sqrt{s}) = \sigma_{NN \to NN}(\sqrt{s} - m_R + m_N) . \tag{B.17}$$

$NN \leftrightarrow NN\pi$

For the $NN \leftrightarrow NN\pi$ process, we consider besides resonance processes, as e.g., $NN \to N\Delta \to NN\pi$, also a point-like background cross section. In fig. B.50 we show the relevant cross sections.

$BB \to BYK$

For the kaon-production cross section from baryon-baryon scattering we use the parametrization adopted by Tsushima $et\ al.$ [123]

$$\sigma(BB \to BYK) = a \left(\frac{s}{s_0} - 1 \right)^b \left(\frac{s_0}{s} \right)^c , \tag{B.18}$$

where s and s_0 are the squares of the invariant collision energy and the threshold energy. The parameters, a, b and c have been determined such as to reproduce the calculated energy dependence of the total cross sections. In the parametrization eq. (B.18) B stands for a baryon (p, n, or Δ resonance), Y for a hyperon (Λ or Σ) and K for a kaon (K^+ or K^0). All isospin channels are taken into account.
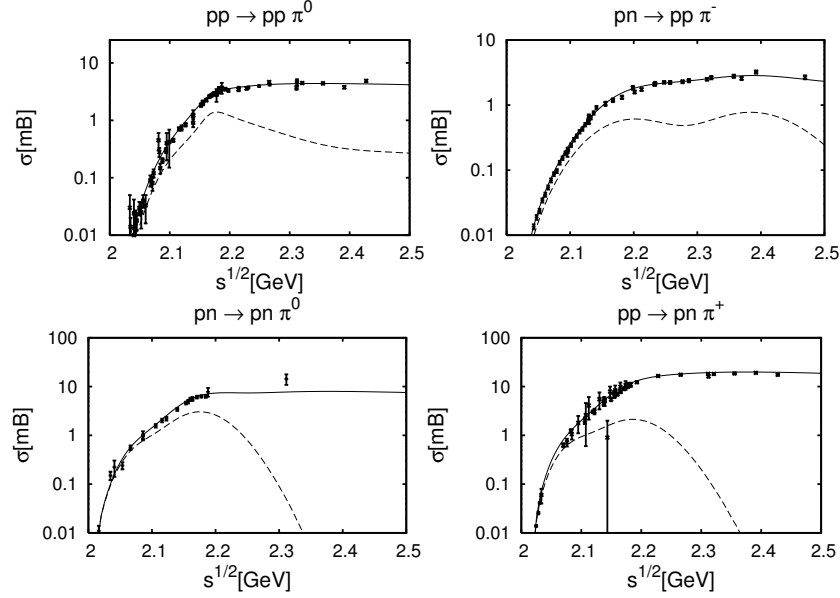
Figure B.50: Elementary cross sections for different $NN \to NN\pi$-isospin channels. The solid lines show the full cross section, whereas the dashed lines represent the non-resonant-background contribution. The data are from [112, 113, 114, 115, 116, 117, 118].

Appendix B.2. Antibaryon-baryon cross sections

In this subsection, the beam momentum p_{lab} is given in GeV/c and the cross sections in mb. For the $\overline{p}p$- ($\overline{n}n$-) annihilation cross section we use the following parametrizations

$$\sigma_{\text{ann}}^{\overline{p}p} = \begin{cases} 51.52 p_{\text{lab}}^{-0.85} + 0.034 p_{\text{lab}}^{-2.94} & \text{for} & p_{\text{lab}} < 0.51 \\ 88.8 p_{\text{lab}}^{-0.4} - 24.2 & \text{for} & 0.51 < p_{\text{lab}} < 6.34 \\ 38 p_{\text{lab}}^{-0.5} + 24 p_{\text{lab}}^{-1.1} & \text{for} & 6.34 < p_{\text{lab}} \end{cases} \tag{B.19}$$

At the highest momenta, the formula from Ref. [377] is applied in eq. (B.19). The $\overline{n}p$ ($\overline{p}n$) annihilation cross section is significantly lower than the $\overline{p}p$ one at low beam momenta [378, 379] and practically coincide with $\sigma_{\text{ann}}^{\overline{p}p}$ at large beam momenta. We take this into account as

$$\sigma_{\text{ann}}^{\overline{n}p} = \begin{cases} 41.4 + 29/p_{\text{lab}} & \text{for} & p_{\text{lab}} < 0.382 \\ \sigma_{\text{ann}}^{\overline{p}p} & \text{for} & 0.382 < p_{\text{lab}} \,, \end{cases} \tag{B.20}$$

where an expression from Ref. [378] is used at the lowest momenta. For the low-energy $\overline{p}p$ collisions (see section 3.3.2 for the definition of the low- and high-energy two-body collisions), the elastic $\overline{p}p$ cross section is similar to that from Ref. [377], but with slightly readjusted parameters,

$$\sigma_{\text{el}}^{\overline{p}p} = 40 p_{\text{lab}}^{-0.56} + 5.8 \exp[-(p_{\text{lab}} - 1.85)^2] \,. \tag{B.21}$$

The charge-exchange cross section, $\sigma_{\text{CEX}}^{\overline{p}p}$, of the processes, $\overline{p}p \leftrightarrow \overline{n}n$, is adopted from [377]. The annihilation and elastic cross sections for all other possible $\overline{B}B$ collisions, as well as the charge-exchange cross sections of the $\overline{\Delta}N$ and $\overline{N}\Delta$ collisions (e.g., $\overline{\Delta}^{--} n \to \overline{\Delta}^{-} p$ and $\overline{p}\Delta^{+} \to \overline{n}\Delta^{0}$)
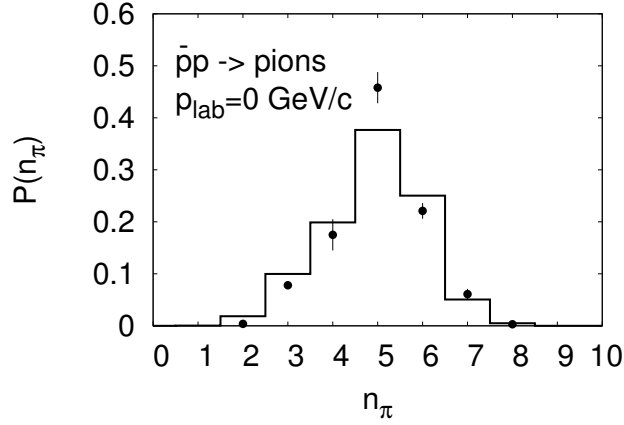
Figure B.51: Total pion multiplicity distribution for $\overline{p}p$ annihilation at rest (see also [187]). Source: The data are from [380].

are taken equal to the corresponding cross sections for the $\overline{p}p$ collisions with the same relative velocity.

For the low-energy $\overline{N}N$, $\overline{\Delta}N$ and $\overline{N}\Delta$ collisions, apart from elastic scattering, charge exchange, and annihilation, we also take into account the processes, $\overline{N}N \leftrightarrow \overline{N}\Delta$ and $\overline{N}N \leftrightarrow \overline{\Delta}N$. The cross sections of the Δ- ($\overline{\Delta}$-) resonance production in $\overline{N}N$ collisions are calculated on the basis of the one-pion exchange model [120]. For the other low-energy $\overline{B}B$ collisions, only annihilation and elastic scattering are considered.

For the high-energy $\overline{B}B$ collisions, the annihilation, elastic scattering, charge exchange (for $\overline{N}N$, $\overline{\Delta}N$ and $\overline{N}\Delta$ collisions), and inelastic production processes, $\overline{B}B \to \overline{B}B$ + mesons, are taken into account. The latter process is simulated via FRITIOF [370]. The partial cross section of the inelastic production is obtained by subtracting the contributions from annihilation, elastic scattering and charge exchange from the total cross section. The total and elastic $B\overline{B}$ scattering cross sections are parametrized according to Ref. [371]:

$$
\begin{aligned}
\sigma_{\text{tot}} &= 38.4 + 77.6 p_{\text{lab}}^{-0.64} + 0.26 \ln^2(p_{\text{lab}}) - 1.2 \ln(p_{\text{lab}}) , \\
\sigma_{\text{elast}} &= 10.2 + 52.7 p_{\text{lab}}^{-1.16} + 0.125 \ln^2(p_{\text{lab}}) - 1.28 \ln(p_{\text{lab}}) ,
\end{aligned}
\tag{B.22}
$$

where only positive values are allowed.

The angular distribution for the elastic and charge-exchange $\overline{p}p$ scattering is given by eq. (B.2) where the slope parameter (in GeV^{-2}) is

$$
b = (A + \hbar B / p_{\overline{p}p})^2 / \hbar^2
\tag{B.23}
$$

for the elastic scattering [381] with $A = 0.67$ fm, $B = 0.35$ and $p_{\overline{p}p}$ being the c.m. momentum, and

$$
b = 11 \exp(-0.23 p_{\text{lab}}) + 8 p_{\text{lab}}^{2.2} / (254 + p_{\text{lab}}^{2.2})
\tag{B.24}
$$

for the charge exchange scattering.

The $\overline{N}N$ annihilation is described with help of a statistical annihilation model [382, 383]. In this model, the probability of a given $\overline{N}N$-annihilation channel is proportional to the invariant phase-space volume. It is also proportional to other factors taking into account, in particular,
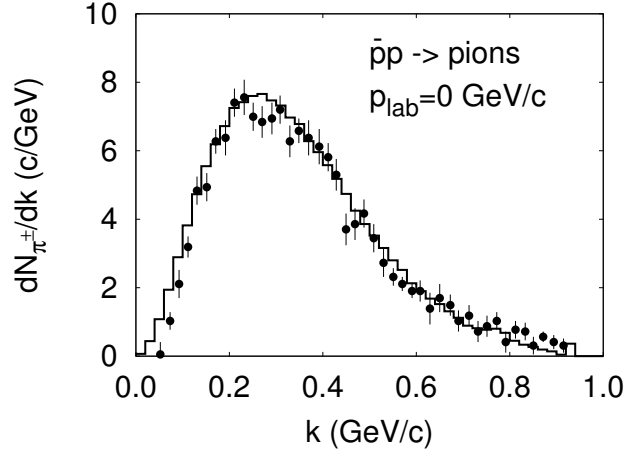
Figure B.52: Charged pion momentum distribution for $\overline{p}p$ annihilation at rest. Calculations are normalized to the number of charged pions per annihilation event. Experimental data (in arbitrary units) are taken from the review [379] and rescaled to agree with calculations at $k = 0.2\,\mathrm{GeV}/c$.

the SU(3) symmetry in terms of particle multiplets (for details see [382, 383] and refs. therein). The third isospin components of the final-state particles are randomly sampled according to the probabilities given by all possible subsequent couplings to the total isospin, I, and its third component, I_3, via Clebsch-Gordan coefficients[23]. Up to six outgoing particles can be produced, which are various combinations of $\pi, \eta, \omega, \rho, K, \bar{K}, K^*$ and $\bar{K}^*$ mesons. The model is proved to well describe the $\overline{p}p$ annihilation observables at $1 < p_{\mathrm{lab}} < 10\,\mathrm{GeV}/c$ [382], while at lower beam momenta it fails to describe the experimental pion-multiplicity distributions. Therefore, the original statistical model has been supplemented by empirical branching ratios for annihilation at rest, which are tabulated in [382, 383]. In our calculations, first we choose randomly whether the empirical branching ratios are used or the statistical model itself. The probability to select the branching ratios at rest drops linearly with the invariant energy of the annihilating pair as

$$P_{\mathrm{at\ rest}} = 1 - \frac{\sqrt{s} - 2m_N}{\sqrt{s_{\mathrm{max}}} - 2m_N} \, , \tag{B.25}$$

where $\sqrt{s_{\mathrm{max}}} = 2.6\,\mathrm{GeV}$ is the maximum invariant energy up to which the annihilation tables at rest still can be selected (respective beam momentum $p_{\mathrm{lab}} = 2.5\,\mathrm{GeV}/c$). (The probability is set to 0, if the above definition becomes negative.) The momenta of the outgoing mesons in $\overline{N}N$ annihilation are sampled microcanonically, i.e., the probability for certain momentum configuration is proportional to the corresponding phase-space-volume element, eq. (D.18).

Figure B.51 shows the pion-multiplicity distribution for $\overline{p}p$ annihilation at rest, calculated taking into account the decays of ω and ρ mesons produced in the annihilation process. The model delivers an excellent description of the experimental data. Also the momentum spectra of the produced pions in $\overline{p}p$ annihilation at rest are in a very good agreement with the data, as as shown in fig. B.52.

---

[23]The total isospin, I, and its projection, I_3, are exactly conserved in this model, in contrast to the string-based description of $\overline{N}N$ annihilation included in the earlier versions of the GiBUU model (cf. [84] and refs. therein).

Appendix B.3. Meson-baryon cross sections

Appendix B.3.1. Non-resonant background cross sections in the resonance energy region

Besides the resonance cross sections, non-resonant cross-section contributions have been implemented in the collision term. The background cross sections denoted by σ^{BG} are chosen in such that the elementary cross-section data in the vacuum are reproduced. Background contributions are instantaneous in space-time, whereas the resonances propagate along their classical trajectories until they decay or interact with one or two nucleons in the nuclear medium.

One may decide not to propagate all know resonances, e.g. in order to speed up the simulation, cf. Appendix A. These resonances are then also not allowed to be produced in the collision term. We have to compensate for this by introducing additional background terms to the cross section as a direct interaction.

Additionally, we obtain a background term due to a lack of strength of the resonance cross sections, which do not describe the full experimentally observed cross section.

Appendix B.3.2. $\pi N \to X$

$\pi N \to \pi N$

In our model, the cross section for quasi-elastic pion-nucleon scattering is given by an incoherent sum of background and resonance contributions,

$$\sigma_{\pi N \to \pi N} = \sigma_{\pi N \to R \to \pi N} + \sigma^{\text{BG}}_{\pi N \to \pi N}. \tag{B.26}$$

Pion nucleon scattering can be categorized into four different isospin channels,

$$\sigma_{\pi^- n \to \pi^- n} = \sigma_{\pi^+ p \to \pi^+ p}, \tag{B.27}$$

$$\sigma_{\pi^- p \to \pi^0 n} = \sigma_{\pi^0 n \to \pi^- p} = \sigma_{\pi^+ n \to \pi^0 p} = \sigma_{\pi^0 p \to \pi^+ n}, \tag{B.28}$$

$$\sigma_{\pi^- p \to \pi^- p} = \sigma_{\pi^+ n \to \pi^+ n}, \tag{B.29}$$

$$\sigma_{\pi^0 n \to \pi^0 n} = \sigma_{\pi^0 p \to \pi^0 p}. \tag{B.30}$$

The cross sections in the individual channels are either connected by time-reversal or isospin symmetry. The first channel, eq. (B.27), is a pure isospin-$I = 3/2$-scattering process, whereas the other three channels are mixtures of $I = 1/2$ and $I = 3/2$. The cross section for the $I = 3/2$ channel, $\sigma_{\pi N \to \Delta \to \pi N}$, is given explicitly in [60] based on the resonance analysis by Manley and Saleski [64].

There are accurate data sets for the $\pi^+ p \to \pi^+ p$, $\pi^- p \to \pi^- p$ and $\pi^- p \to \pi^0 n$ for the first, second and third channel, eqs. (B.27)–(B.29), down to very low energies. Hence, we introduce a background term on top of our resonance contributions for a better description of these channels. The last channel, eq. (B.30), is inaccessible for experiment; therefore we can not introduce any background term. In this approach, we describe in a satisfying manner all available data, as can be seen in fig. B.53.

The cross sections on the neutron follow from isospin symmetry.

We include a realistic angular distribution for the elastic scattering of the pions [140]. Due to the *P*-wave nature of the $\Delta(1232)$ resonance, we assume for $\pi N \to \Delta \to \pi N$ in the resonance rest frame a distribution of the pion scattering angle, θ,[24] according to

$$f^\Delta(s, \theta) = \left(1 + 3\cos^2(\theta)\right) g(s, \theta), \tag{B.31}$$

---

[24]The angle, θ, is defined by the incoming and outgoing pion momenta. In the simulation, we must store for each Δ produced in a πN collision the momentum of the corresponding pion in the resonance-rest frame.
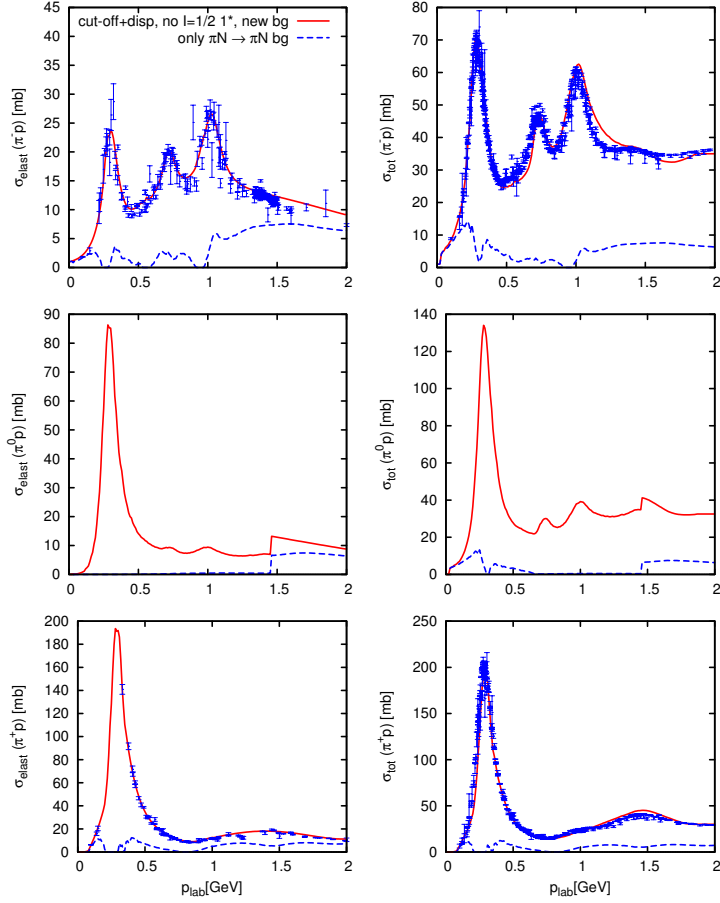
Figure B.53: (Color online) Elastic (left panels) and total (right panels) cross sections for the scattering of pions and protons. The solid curves show the results with our default parameters: all resonances besides the $I = 1/2$ 1*-resonances are included, the real parts of the self-energies are included in the propagators. The dashed curves show the background contributions. The data are from [129].

which is peaked in forward and backward direction. The function, $g(s, \theta)$, depending on Mandelstam s, parametrizes the energy dependence of the πN angular distribution. In a coherent calculation the angular distribution is generated by interference effects, which can not be accomplished by our transport model. In our ansatz we have to split the cross section in an incoherent way to preserve our semi-classical resonance picture. Therefore we take

$$g(s, \theta) = [\alpha - \cos(\theta)]^{\beta(m_\Delta - \sqrt{s})/m_\Delta} \tag{B.32}$$

with the Δ-pole mass, $m_\Delta = 1.232\,\text{GeV}$. For the background events we assume

$$f^{\text{BG}}(s, \theta) = g(s, \theta) . \tag{B.33}$$

The constants, $\alpha = 1.9$ and $\beta = 26.5$, are fitted to the angular distributions measured in the Crystal Ball [146] experiment; a comparison of our parametrization to this data is shown in fig. B.54.
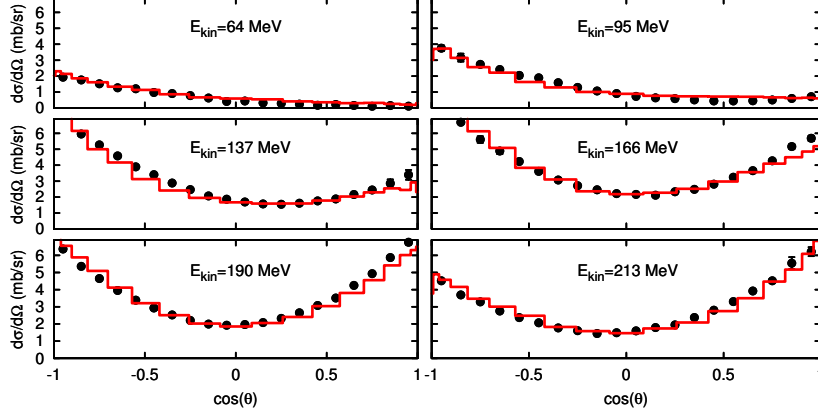
125

Figure B.54: (Color online) The angular distributions for the charge-exchange process, $\pi^- p \to \pi^0 n$, in the CM frame of pion and proton. The plots are labeled with the kinetic energies of the pions in the laboratory frame. The data are from [146].

$\pi N \to \pi\pi N$

The $\pi N \to \pi\pi N$ cross section is given by

$$\sigma_{\pi N \to N\pi\pi} = \sum_R \sigma_{\pi N \to R} \frac{\Gamma_{R \to N\pi\pi}}{\Gamma_{\text{tot}}}. \tag{B.34}$$

In fig. B.55 we show the model results for all pion proton channels: $\pi^- p \to \pi^0\pi^0 n$, $\pi^- p \to \pi^+\pi^- n$, $\pi^- p \to \pi^0\pi^- pX$, $\pi^+ p \to \pi^+\pi^+ n$, $\pi^+ p \to \pi^+\pi^0 p$. Obviously, calculations, where we include the $(I = 3/2)$-1*-resonances and exclude only the $(I = 1/2)$-1*-resonances, fit the data better than those, which neglect all 1*-resonance of the Manley analysis, especially in the $\pi^+ p \to \pi^+\pi^+ n$ and $\pi^+ p \to \pi^+\pi^0 p$ channels. For the first case we also see, that there is only a modest impact, whether we include real parts of the self-energy in the resonance propagators. We conclude that the choice to exclude only the $(I = 1/2)$-1*-resonances seems to fit the data better than the former choice to exclude all 1* resonances.

$\pi N \to \eta\Delta$

The mass differential cross section is given by the following expression

$$\frac{\mathrm{d}\sigma_{\pi N \to \eta\Delta}}{\mathrm{d}m_\Delta} = \left\langle 1\, I_z^\pi; \frac{1}{2}\, I_z^N \Big| \frac{3}{2}\, I_z^\Delta \right\rangle^2 \left| \mathcal{M}_{\pi N \to \eta\Delta} \right|^2 \frac{p_{\eta\Delta}(m_\Delta)}{s\, p_{\pi N}} \mathcal{A}_\Delta(m_\Delta), \tag{B.35}$$

where the matrix element is assumed to be a constant, $\left| \mathcal{M}_{\pi N \to \eta\Delta} \right|^2 = 7\,\mathrm{mb\,GeV}^2$. The corresponding total cross section is given by the integral of the r.h.s. of eq. (B.35) over the mass of the Δ resonance.

$\pi N \to \omega N$ and $\pi N \to \phi N$

The total cross section parametrizations $\sigma_{\pi^- p \to \omega n}$ and $\sigma_{\pi^- p \to \phi n}$ are adopted from Ref. [384] and Ref. [385], respectively. In the case of the ω production, the contributions from intermediate resonances $G_{17}(2190)$ and $P_{13}(1900)$ which have significant branching ratios to the $N\omega$ decay
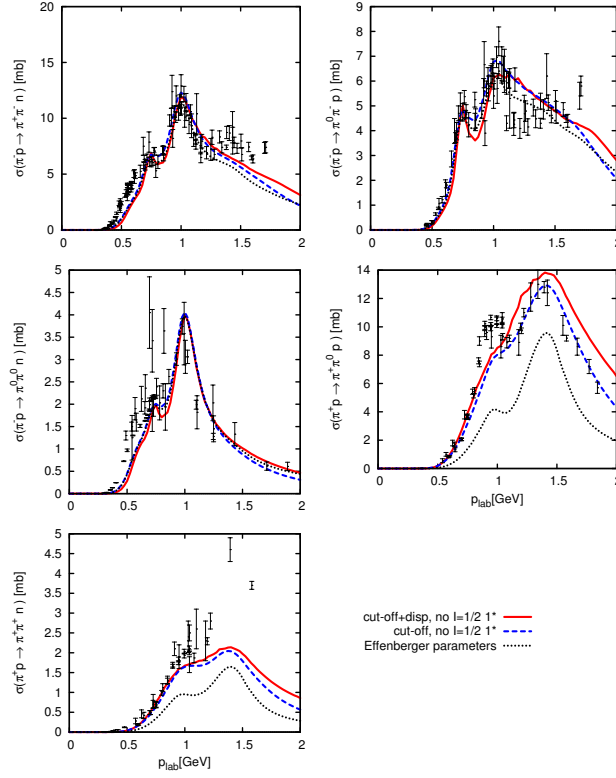
126

Figure B.55: (Color online) Cross sections for $\pi^- p \to \pi^0\pi^0 n$, $\pi^- p \to \pi^+\pi^- n$, $\pi^- p \to \pi^0\pi^- pX$, $\pi^+ p \to \pi^+\pi^+ n$, $\pi^+ p \to \pi^+\pi^0 p$. The solid line represents the full model in which only those 1*-resonances are not included which have isospin 1/2. The dashed curve neglects the effects of the dispersion relations and the dotted line represents the result according to the former choice of parameters [60].

channel (see table A.3) are subtracted from the parametrization of the total $\sigma_{\pi^- p \to \omega n}$ cross section such that

$$\sigma^{\mathrm{BG}}_{\pi^- p \to \omega n} = \sigma_{\pi^- p \to \omega n} - \sigma^{\mathrm{Resonances}}_{\pi^- p \to \omega n} . \tag{B.36}$$

For the ϕ production, there is no intermediate resonance contribution and we set

$$\sigma^{\mathrm{BG}}_{\pi^- p \to \phi n} = \sigma_{\pi^- p \to \phi n} . \tag{B.37}$$

The background cross sections for other charge channels are obtained from a simple isospin relation

$$\sigma^{\mathrm{BG}}_{\pi N_1 \to M N_2} = \left\langle 1\, I^\pi_z; \tfrac{1}{2}\, I^{N_1}_z | \tfrac{1}{2}\, I^{N_2}_z \right\rangle^2 \frac{3}{2} \sigma^{\mathrm{BG}}_{\pi^- p \to M n} , \quad M = \omega, \phi . \tag{B.38}$$

$\pi N \to \omega \pi N$ and $\pi N \to \phi \pi N$

We utilize the parametrizations of Ref. [385] for the inclusive cross sections $\sigma_{\pi^+ p \to \omega X}$ and $\sigma_{\pi^+ p \to \phi X}$. It is assumed, further, that the inclusive cross sections for the different charge states of initial particles are the same, i.e.,

$$\sigma_{\pi N \to M X} = \sigma_{\pi^+ p \to M X} , \quad M = \omega, \phi . \tag{B.39}$$

127

Then, the cross sections of the processes $\pi N \to \omega \pi N$ and $\pi N \to \phi \pi N$, summed over different charge states of the outgoing pion and nucleon, are obtained by the subtraction

$$\sigma_{\pi N \to M \pi N} = \sigma_{\pi N \to M X} - \sigma_{\pi^- p \to M n} , \quad M = \omega, \phi . \tag{B.40}$$

The probabilities for the different charge states of the outgoing particles are set equal to each other.

$\pi N \to \Sigma K$

We use a parametrization of Ref. [122] for the cross sections, $\sigma_{\pi^+ p \to K^+ \Sigma^+}$, $\sigma_{\pi^0 p \to K^+ \Sigma^0}$, $\sigma_{\pi^- p \to K^0 \Sigma^0}$, and $\sigma_{\pi^- p \to K^+ \Sigma^-}$. Assuming isospin symmetry and isospin-$I = \frac{1}{2}$ dominance in the intermediate resonance states we obtain $\sigma_{\pi^0 p \to K^0 \Sigma^+} = \sigma_{\pi^- p \to K^0 \Sigma^0}$. Channels with an initial neutron are defined by the isospin reflection symmetry from respective channels with initial proton.

$\pi N \to \Lambda K$

For the total cross section $\sigma_{\pi^- p \to \Lambda K^0}$, we again use the parametrization of Ref. [122]. Since a part of this cross section is caused by intermediate resonances ($P_{11}(1710)$ and $P_{11}(2100)$, see table A.3), we define the corresponding background cross section by subtracting the resonance contributions as

$$\sigma^{\text{BG}}_{\pi^- p \to \Lambda K^0} = \sigma_{\pi^- p \to \Lambda K^0} - \sigma^{\text{Resonances}}_{\pi^- p \to \Lambda K^0} . \tag{B.41}$$

The background cross sections of the other charge channels can be directly reconstructed by isospin relations since the total isospin of the final state is fixed to 1/2,

$$\sigma^{\text{BG}}_{\pi N \to \Lambda K} = \left\langle 1 \, I_z^\pi; \frac{1}{2} \, I_z^N \Big| \frac{1}{2} \, I_z^K \right\rangle^2 \frac{3}{2} \sigma^{\text{BG}}_{\pi^- p \to \Lambda K^0} . \tag{B.42}$$

$\pi N \to K \overline{K} N$

The cross section $\sigma_{\pi^- p \to p K^0 \overline{K}^-}$ is parametrized according to Ref. [386] as

$$\sigma_{\pi^- p \to p K^0 \overline{K}^-} = 1.121 \, \text{mb} \cdot \left(1 - \frac{s_0}{s}\right)^{1.86} \left(\frac{s_0}{s}\right)^2 \equiv \frac{1}{2} \sigma_0 \tag{B.43}$$

with $s_0 = (m_N + 2m_K)^2$. The cross sections of the other charge channels are obtained from the isospin symmetry of the K^* and π exchange diagram (see Fig. 1c in Ref. [386] and Ref. [60]) which gives:

$$\begin{aligned}
\sigma_{\pi^- p \to n K^0 \overline{K}^0} &= \sigma_0, & \sigma_{\pi^- p \to n K^+ \overline{K}^-} &= \sigma_0, \\
\sigma_{\pi^0 p \to n K^+ \overline{K}^0} &= \sigma_0, & \sigma_{\pi^0 p \to p K^0 \overline{K}^0} &= \frac{1}{4} \sigma_0, \\
\sigma_{\pi^0 p \to p K^+ \overline{K}^-} &= \frac{1}{4} \sigma_0, & \sigma_{\pi^+ p \to p K^+ \overline{K}^0} &= \frac{1}{2} \sigma_0 .
\end{aligned} \tag{B.44}$$

The πn cross sections are directly given by the the isospin reflection symmetry from the corresponding πp cross sections.

Process	a_i (mb)	Process	a_i (mb)
$\pi^- p \to \Lambda\, K^0\, \pi^0$	0.169	$\pi^+ p \to \Lambda\, K^+\, \pi^+$	0.217
$\to \Lambda\, K^+\, \pi^-$	0.140	$\to \Sigma^0\, K^+\, \pi^+$	0.0426
$\to \Sigma^0\, K^0\, \pi^0$	0.1	$\to \Sigma^+\, K^+\, \pi^0$	0.126
$\to \Sigma^0\, K^+\, \pi^-$	0.0724	$\to \Sigma^+\, K^0\, \pi^+$	0.0887
$\to \Sigma^-\, K^+\, \pi^0$	0.0520		
$\to \Sigma^-\, K^0\, \pi^+$	0.117		
$\to \Sigma^+\, K^0\, \pi^-$	0.0514		

Table B.9: Normalization factors for the fits to $\pi^{\pm} p \to \Sigma K\pi, \Lambda K\pi$ data.

$\pi N \to \Sigma K\pi,\ \Lambda K\pi$

In order to describe the strangeness production plus one pion channels, we performed a combined fit for all channels to experimental data [387] of the form

$$\sigma(s) = a_i\, A \left(\frac{s}{s_0} - 1\right)^B \left(\frac{s}{s_0}\right)^{-C} \quad , \qquad \sqrt{s_0} = \begin{cases}(1.750 + 0.100)\,\text{GeV} & \text{for} \quad \Lambda K\pi \\ (1.823 + 0.100)\,\text{GeV} & \text{for} \quad \Sigma K\pi\end{cases} \quad \text{(B.45)}$$

leading to the general constants,

$$A = 86.027 \quad , \qquad B = 2.197 \quad , \qquad C = 7.363 \quad , \tag{B.46}$$

and the process dependent normalization values, a_i, as listed in table B.9. The fit range was $p_{\text{lab}} < 3.5\,\text{GeV}$. The additional constant value of 100 MeV added to the threshold energies was introduced to achieve better numerical convergence.

Appendix B.3.3. $\pi\Delta \to X$

Besides resonance production channels, background contributions for ΛK and ΣK production are implemented according to [122].

Appendix B.3.4. $\rho N \to X$

Besides resonance-production channels, a πN background is introduced to absorb missing inelasticities above $\sqrt{s} > 1.8\,\text{GeV}$,

$$\sigma_{\rho N \to \pi N} = \sigma_{\text{tot, data}} - \sigma_{\text{tot, resonances}} \, . \tag{B.47}$$

Appendix B.3.5. $\eta N \to X$
$\eta N \to \pi N$

Additionally to resonance production, a πN background is defined for $\sqrt{s} > 2\,\text{GeV}$,

$$\sigma_{\eta N \to \pi N} = \sigma_{\text{tot, data}} - \sigma_{\text{tot, resonances}} \, . \tag{B.48}$$

In this approach, missing resonance strength is attributed to the πN channel.

Appendix B.3.6. $\eta\Delta \to X$

$\eta\Delta \to \pi N$

By applying the detailed balance relation eq. (181) to eq. (B.35), we get

$$\sigma_{\eta\Delta\to\pi N} = \frac{1}{2} \left\langle 1\, I_z^\pi; \frac{1}{2}\, I_z^N \Big| \frac{3}{2}\, I_z^\Delta \right\rangle^2 |\mathcal{M}_{\pi N\to\eta\Delta}|^2 \frac{p_{\pi N}}{s\, p_{\eta\Delta}} . \tag{B.49}$$

The factor $1/2$ is due to (2j+1)-terms in the cross sections and different spins in initial and final state.

Appendix B.3.7. $\omega/\phi N \to X$

The elastic $\sigma_{MN}^{\mathrm{el}}$ ($M = \omega, \phi$) and inelastic $\sigma_{MN}^{\mathrm{inel}}$ cross sections on nucleon are taken from Ref. [388] for ω-induced reactions and from Ref. [389] for ϕ-induced ones. In the case of the ωN elastic scattering, the resonance contribution is subtracted to get the background elastic scattering cross section. The background cross sections $\sigma_{MN\to\pi N}^{\mathrm{BG}}$ are obtained by detailed balance relations from the corresponding cross sections of the inverse reactions. Additionally, the $\pi\pi N$ channel is included as a background in order to describe the remaining part of inelastic cross sections:

$$\begin{aligned}
\sigma_{\omega N\to\pi\pi N}^{\mathrm{BG}} &= \sigma_{\omega N}^{\mathrm{inel}} - \sigma_{\omega N\to R}^{\mathrm{inel}} - \sigma_{\omega N\to\pi N}^{\mathrm{BG}} , \\
\sigma_{\phi N\to\pi\pi N}^{\mathrm{BG}} &= \sigma_{\phi N}^{\mathrm{inel}} - \sigma_{\phi N\to\pi N}^{\mathrm{BG}} ,
\end{aligned} \tag{B.50}$$

where $\sigma_{\omega N\to R}^{\mathrm{inel}} \equiv \sigma_{\omega N\to R} - \sigma_{\omega N\to R\to\omega N}$ is the resonance part of the ωN inelastic scattering cross section.

Appendix B.3.8. $KN \to X$

The kaon-nucleon interactions are described following Effenberger (see Appendix A.2.4 of [60]). The experimental elastic cross section $K^+p \to K^+p$ is parametrized as

$$\sigma_{K^+p\to K^+p} = \frac{a_0 + a_1 p + a_2 p^2}{1 + a_3 p + a_4 p^2} , \tag{B.51}$$

where p is the kaon momentum with respect to the nucleon-rest frame, $a_0 = 10.508\,\mathrm{mb}$, $a_1 = -3.716\,\mathrm{mb/\,GeV}$, $a_2 = 1.845\,\mathrm{mb/\,GeV^2}$, $a_3 = -0.764\,\mathrm{GeV^{-1}}$, $a_4 = 0.508\,\mathrm{GeV^{-2}}$. The K^+n elastic and charge-exchange cross sections are assumed each to be 50 % of K^+p elastic cross section,

$$\sigma_{K^+n\to K^+n} = \sigma_{K^+n\to K^0p} = \frac{1}{2}\sigma_{K^+p\to K^+p} . \tag{B.52}$$

The inelastic K^+N cross sections are obtained by a spline interpolation of the experimental data points for the total K^+N cross sections [112] at $p_{\mathrm{lab}} < 6\,\mathrm{GeV}/c$ after subtraction of the elastic and charge-exchange contributions. The inelastic K^+N cross section is assumed to be entirely composed of the $K\pi N$-outgoing channels. The charges of the outgoing kaon, pion and nucleon are randomly selected such that all charge combinations that are possible by charge conservation are equally probable. The K^0N cross sections for the different outgoing channels are equal to the cross sections of the corresponding isospin-symmetric K^+N-collision channels. The kinematics of the outgoing particles is chosen according to the isotropic angular distribution for the KN-final state or by the three-body phase-space sampling for the $K\pi N$-final state.
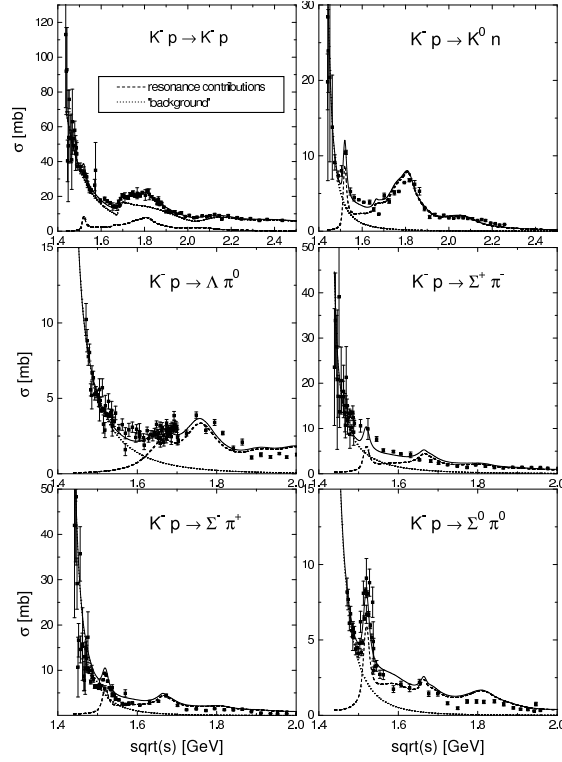
Figure B.56: The cross sections of elastic scattering, charge-exchange and hyperon production in $K^- p$ collisions. The total cross sections are shown as solid lines. The dashed lines represent the resonance contributions and the dotted lines the non-resonance background. The data are from [387]. Taken from [60].

Appendix B.3.9. $\overline{K}N \to X$

The antikaon-nucleon interaction is governed mostly by the $S = -1$ intermediate resonance excitation (see table A.4) according to eq. (176). On the other hand, the resonance contributions do not completely saturate the measured cross sections. In particular, at low invariant energies the background terms have to be included. This is especially important for the charge-neutral initial channels, $K^- p$ and $\overline{K^0} n$. In this case, the $\Lambda(1405)$ resonance, whose pole mass is only 30 MeV below the $\overline{K}N$ production threshold, determines the low-energy scattering. However, in our approach the explicit coupling of the $\Lambda(1405)$ resonance to the antikaon-nucleon channel is not included. Thus, the large cross sections of various $K^- p$ scattering channels at small invariant energies have to be considered as the non-resonant background.

The background terms have been parametrized by Effenberger [60]. In the case of a two-body outgoing channel $\alpha \equiv K^- p$, $\overline{K^0} n$, $\Lambda\pi^0$, $\Sigma^+\pi^-$, $\Sigma^-\pi^+$, $\Sigma^0\pi^0$,

$$\sigma^{\text{bg}}_{K^- p \to \alpha} = a_0 \frac{p_f}{p_i s} \left(\frac{a_1^2}{a_1^2 + p_f^2} \right)^{a_2} , \tag{B.53}$$

is used for the background cross section, where p_i and p_f are the c.m. momenta of the incoming

131

channel	a_0 [mb GeV^2]	a_1 [GeV]	a_2
$K^- p$	150	0.35	2
$\overline{K}^0 n$	100	0.15	2
$\Lambda \pi^0$	130	0.25	3
$\Sigma^+ \pi^-$	600	0.1	2
$\Sigma^- \pi^+$	5000	0.1	3
$\Sigma^0 \pi^0$	2500	0.1	3

Table B.10: Parameters of the non-resonant background cross sections for various two-body outgoing channels of $K^- p$ scattering.

and outgoing particles, respectively. The parameters a_j, j=0,1,2, are listed in table B.10 for the different outgoing channels α. For $K^- p \to K^- p$ elastic scattering, the parametrization eq. (B.53) is used only for invariant energies $\sqrt{s} < 1.7$ GeV. At higher $\sqrt{s}$, the spline interpolation of the experimental data is used to describe the broad maximum in the cross section at $\sqrt{s} \simeq 1.8$ GeV. As can be seen from fig. B.56, the sum of the resonance and background contributions provide a very good description of experimental data for the processes $K^- p \to K^- p$, $\overline{K}^0 n$, $\Lambda \pi^0$, $\Sigma^+ \pi^-$, $\Sigma^- \pi^+$ and $\Sigma^0 \pi^0$.

In order to describe the total $K^- p$ cross section at invariant energies $\sqrt{s}$ up to 2.2 GeV, one needs to take into account the channels with more than two particles in the final state. To this aim, the process $\overline{K} N \to Y^* \pi$ is implemented by assuming a constant matrix element for all hyperonic resonances,

$$\sigma_{\overline{K} N \to Y^* \pi} = C \frac{|\mathcal{M}|^2}{p_i s} \int\limits_{m_{\Lambda(\Sigma)} + m_\pi}^{\sqrt{s} - m_\pi} \mathrm{d}(\mu^2) \, p_f \mathcal{A}_{Y^*}(\mu) \,, \tag{B.54}$$

where the coefficient C is a combination of isospin-Clebsch-Gordan coefficients of the incoming (1,2) and outgoing (3,4) particles given by

$$C = \sum_I \left\langle I^1 I_z^1; I^2 I_z^2 | I I_z \right\rangle^2 \left\langle I^3 I_z^3; I^4 I_z^4 | I I_z \right\rangle^2 . \tag{B.55}$$

The total $K^- p$ cross section is well reproduced (see fig. B.57), if the value of the matrix element $|\mathcal{M}|^2 = 22$ mb GeV^2 is chosen. Applying eq. (B.54), only the hyperon resonances with masses larger than or equal to 1.6 GeV are taken into account. Using the parametrization eq. (B.54) and the detailed-balance relation eq. (180), one obtains the cross section for the inverse reaction, $\pi Y^* \to N \overline{K}$,

$$\sigma_{\pi Y^* \to N \overline{K}} = C \frac{2}{2 J_{Y^*} + 1} \frac{p_f}{p_i s} |\mathcal{M}|^2 . \tag{B.56}$$

The $K^- n$ elastic scattering is described in terms of the resonance contributions and a small constant background cross section

$$\sigma_{K^- n \to K^- n}^{\mathrm{BG}} = 4 \text{ mb} . \tag{B.57}$$

Since the isospin of the final state in the processes $K^- n \to \Lambda \pi^-$ and $K^- p \to \Lambda \pi^0$ is fixed ($I = 1$), we have the exact relation

$$\sigma_{K^- n \to \Lambda \pi^-}^{\mathrm{BG}} = 2 \sigma_{K^- p \to \Lambda \pi^0}^{\mathrm{BG}} . \tag{B.58}$$
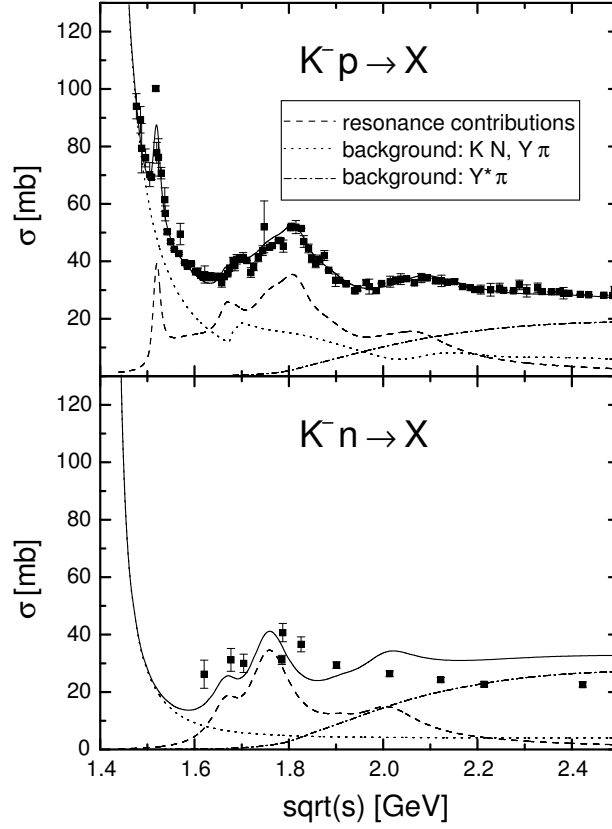
Figure B.57: The total cross sections (solid lines) of the K^-p and K^-n collisions with respective resonance contributions (dashed lines) and background contributions from $\overline{K}N \to \overline{K}N$, πY (dotted lines) and $\overline{K}N \to \pi Y^*$ (dash-dotted lines). The data are from [387]. Taken from [60].

For the $\Sigma\pi$-outgoing channel, we assume the background cross section,

$$\sigma^{\mathrm{BG}}_{K^-n \to \Sigma^-\pi^0} = \sigma^{\mathrm{BG}}_{K^-n \to \Sigma^0\pi^-} = \frac{1}{2}\left(\sigma^{\mathrm{BG}}_{K^-p \to \Sigma^-\pi^+} + \sigma^{\mathrm{BG}}_{K^-p \to \Sigma^+\pi^-}\right) . \tag{B.59}$$

The total K^-n cross section is shown in fig. B.57. One observes a fair agreement with the available experimental data.

The cross sections for $\overline{K}^0 N$ scattering are obtained isospin symmetry,

$$\sigma_{\overline{K}^0 p} = \sigma_{K^-n} , \quad \sigma_{\overline{K}^0 n} = \sigma_{K^-p} . \tag{B.60}$$

Finally, the cross sections for the $\pi Y \to \overline{K}N$ processes, important for heavy ion collisions, are directly obtained from the detailed-balance formula eq. (181). This results in values of about 4 mb for the isospin-averaged $\pi\Lambda \to \overline{K}N$ and $\pi\Sigma \to \overline{K}N$ cross sections at $\sqrt{s} < 2\,\mathrm{GeV}$.

Appendix B.3.10. Meson-Baryon Annihilation Processes

It is worthwhile to reemphasize, that the cross sections listed above are only used for low energies, cf. section 3.3.2. At higher energies, the final state decisions are done by event gen-
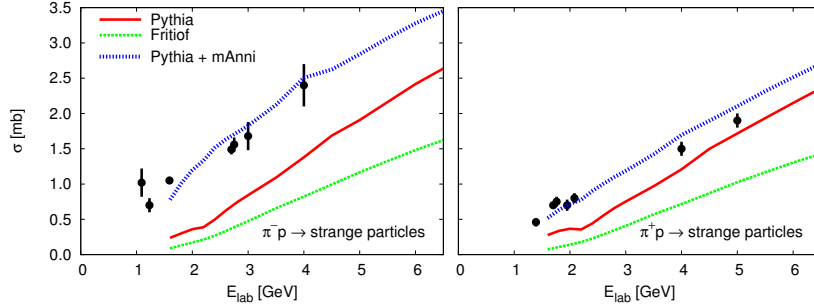
Figure B.58: The cross section of production of strange particles in πp collisions as function of the projectile energy. Only the high energy contributions are shown. The event generators PYTHIA (red solid) or FRITIOF (green dotted) underestimate the experimental data [387]. The contribution of the meson-baryon annihilation process on top of the PYTHIA contribution is shown as the blue dashed curve.

erators like PYTHIA. As developed in Ref. [127], we also have to take into account additionally quark-antiquark annihilation processes in meson-baryon collisions.

For this we split up the incoming hadrons into their quark content and check, whether an annihilation between a quark and its antiquark is possible. If so, we construct a string out of the remaining three quarks, which has the invariant mass of the incoming colliding hadron pair. This string decays according the string fragmentation used in PYTHIA.

The probability for these annihilation events is chosen such, that we we match the strangeness production in πp events, as shown in fig. B.58. We find

$$\text{Prob(annihilation)} = R_{\text{comb}} \cdot \left(a - b\sqrt{s}\right) \quad \text{with} \quad a = 0.6 \,, \; b = 0.1\,\text{GeV}^{-1} \tag{B.61}$$

as a suitable prescription, which is slightly different from what was used in Ref. [127]. Here R_{comb} is a combinatorial factor, which is 1, if only one quark-antiquark combination is possible, and 2, if there are, e.g., two quarks for the corresponding antiquark (e.g. for $\pi^+ p$, there is only one $\bar{d}d$ combination, while for $\pi^- p$ one finds two possibilities for $\bar{u}u$ annihilation).

Comparisons with experimental data for other final state channels, as, e.g., two pion production, sustain the findings of fig. B.58, that PYTHIA plus the annihilation prescription describes best all the data.

Appendix B.4. Meson-meson cross sections

In central heavy ion collisions at high energy a hot and dense medium consisting of baryons and mesons is produced. With increasing beam energy, the mesonic degrees of freedom become more and more important. Already at AGS energies ($E_{\text{lab}} \simeq 10\,A\text{GeV}$) the number of produced pions becomes comparable to the original number of nucleons in the colliding nuclei. In such a system, the meson-meson (mostly $\pi\pi$) collisions can not be neglected. The meson-meson collisions are in particular important for a realistic description of strangeness production in heavy ion collisions in kinetic models based on hadronic degrees of freedom [390, 127, 391].

The $\pi\pi$-elastic scattering and total cross sections are dominated by intermediate ρ and σ meson excitation via the resonance mechanism of eq. (176). Also other resonance channels of meson-meson collisions, e.g., $\rho\pi \to \phi$ and $K\pi \to K^*$ have to be considered (see table A.6 for all possible meson-meson collisions leading to a mesonic resonance excitation included in the

model). However, the resonance mechanism does not account for the process $\pi^+\pi^- \to K^+K^-$ which has a rather large cross section of about 1.5 mb near the threshold [392].

In Ref. [393], the cross sections of the processes, $\pi\pi \to K\overline{K}$, $\rho\rho \to K\overline{K}$, $\pi\rho \to K\overline{K}^*$, and $\pi\rho \to K^*\overline{K}$, were calculated on the basis of a kaon- and K^*-exchange model in the impulse approximation. We use the parametrization of the $\pi\pi \to K\overline{K}$ cross section from Ref. [394], which is based on these calculations,

$$\sigma_{\pi\pi \to K\overline{K}} = 6.075\,\text{mb} \cdot C \left(1 - \frac{(2m_K)^2}{s}\right)^{0.76}, \tag{B.62}$$

where the isospin-dependent factor C is given by eq. (B.55).

For simplicity, eq. (B.55) is also applied to evaluate the $\rho\rho \to K\overline{K}$, $\pi\rho \to K\overline{K}^*$ and $\pi\rho \to K^*\overline{K}$ cross sections since the isospins of the incoming particles are the same [127]. For other strangeness-production reactions involving two non-strange mesons in the incoming channel, $\pi\eta \to K\overline{K}$, $\pi\eta' \to K\overline{K}$, $\pi\omega \to K^*\overline{K} + K\overline{K}^*$, $\eta\eta \to K\overline{K}$, $\rho\eta \to K^*\overline{K} + K\overline{K}^*$, $\eta\omega \to K^*\overline{K} + K\overline{K}^*$, $\eta\eta' \to K\overline{K}$, $\rho\omega \to K\overline{K}$, $\rho\eta' \to K^*\overline{K} + K\overline{K}^*$, $\sigma\sigma \to K\overline{K}$, $\omega\omega \to K\overline{K}$, $\omega\eta' \to K^*\overline{K} + K\overline{K}^*$, $\eta'\eta' \to K\overline{K}$, a constant cross section of 2 mb is assumed. The respective back reactions are included, and their cross sections are calculated according to the detailed-balance relation eq. (181). The cross sections of reactions with a vector and a pseudoscalar meson in the initial channel and outgoing $K\overline{K}$, such as, e.g., $\rho\pi \to K\overline{K}$, are small due to P-wave suppression and are not included directly (see also discussions in [393, 391]). However, the latter reaction proceeds via an intermediate ϕ meson. The contributions from the processes involving a scalar σ meson and a pseudoscalar or vector meson in the initial channel either vanish due to parity violation (as, e.g., $\sigma\pi \to K\overline{K}$) or are small due to the p-wave suppression (as, e.g., $\sigma\rho \to K^*\overline{K} + K\overline{K}^*$) and are neglected as well.

Appendix C. Elementary ℓN reactions

Elementary interactions of leptons and photons with nucleons are treated differently than those of mesons and baryons. In this section we explain in detail our implementation of the corresponding cross sections.

In the region of intermediate lepton beam energies ($E_{\text{beam}} \sim 0.5\text{-}2\,\text{GeV}$), the cross section contains contributions from quasi-elastic (QE) scattering ($\ell N \to \ell' N'$), resonance (R) excitation ($\ell N \to \ell' R$) and direct, i.e., non-resonant, single-pion production ($\ell N \to \ell' \pi N'$) treated as background (1π BG). At higher energies, channels open up, which can not be described by resonance decays any more.

Thus we assume

$$\mathrm{d}\sigma_{\text{tot}} = \mathrm{d}\sigma_{\text{QE}} + \sum_R \mathrm{d}\sigma_R + \mathrm{d}\sigma_{1\pi\,\text{BG}} + \mathrm{d}\sigma_{2\pi\text{BG}} + \mathrm{d}\sigma_{\text{DIS}}. \tag{C.1}$$

The dynamics of the interaction is encoded in the absolute value of the matrix element squared, averaged (summed) over initial (final) spins,

$$\overline{|\mathcal{M}_{\text{QE,R,BG}}|^2} = C^2_{\text{EM,CC,NC}} L_{\mu\nu} H^{\mu\nu}_{\text{QE,R,BG}}, \tag{C.2}$$

with $C_{\text{EM}} = 4\pi\alpha/Q^4$ for electromagnetic (EM) interactions ($e^-N \to e^-X$), $C_{\text{CC}} = G_F \cos\theta_C/\sqrt{2}$ for charged-current (CC) weak interactions ($\nu_\ell N \to \ell^-X$) and $C_{\text{NC}} = G_F/\sqrt{2}$ for neutral-current (NC) ones ($\nu N \to \nu X$). Here, Q^2 is the four-momentum transfer; $\alpha \simeq 1/137$ the fine-structure

constant, $G_F = 1.16637 \cdot 10^{-5}\,\text{GeV}^{-2}$ the Fermi constant, and $\cos\theta_C = 0.9745$ the Cabibbo angle. The leptonic tensor is given by

$$L_{\mu\nu} = \frac{1+a}{2}\,\text{Tr}\left[(\slashed{k} + m_\ell)\tilde{l}_\mu(\slashed{k}' + m_{\ell'})l_\nu\right],\tag{C.3}$$

where $l_\mu = \gamma_\mu(1 - a\gamma_5)$ and $\tilde{l}_\mu = \gamma_0 l_\mu^\dagger \gamma_0$; k (k') denotes the four-momentum of the incoming (outgoing) lepton and m_ℓ $(m_{\ell'})$ the corresponding mass. The parameter a depends on the reaction process: $a = 0$ for EM processes and $a = 1$ for CC or NC neutrino scattering.

The hadronic currents in $H^{\mu\nu}_{\text{QE,R,BG}}$ have to be parametrized in terms of form factors and thus depend not only on the final state but also on the specific process, namely EM, CC, or NC.

In the following subsections we present a brief summary of our model; an extended discussion with all details can be found in [55, 58, 351].

Appendix C.1. Quasi-elastic scattering

The cross section for quasi-elastic scattering, $\ell(k)N(p) \to \ell'(k')N'(p')$, is given by

$$\frac{\mathrm{d}\sigma_{\text{QE}}}{\mathrm{d}\omega\,\mathrm{d}\Omega_{k'}} = \frac{|\boldsymbol{k}'|}{32\pi^2}\,\frac{\delta(p'^2 - M'^2)}{\sqrt{(k\cdot p)^2 - m_\ell^2 M^2}}\,\overline{|\mathcal{M}_{\text{QE}}|^2}\,,\tag{C.4}$$

with $M = \sqrt{p^2}$; $\omega = k^0 - k'^0$ is the energy transfer and $\Omega_{k'}$ is the solid angle between incoming and outgoing leptons.

The hadronic tensor, $H^{\mu\nu}_{\text{QE}}$, for quasi-elastic scattering is given by

$$H^{\mu\nu}_{\text{QE}} = \frac{1}{2}\,\text{Tr}\left[(\slashed{p} + M)\tilde{\Gamma}^\mu_{\text{QE}}(\slashed{p}' + M')\Gamma^\nu_{\text{QE}}\right],\tag{C.5}$$

with

$$\tilde{\Gamma}^\mu_{\text{QE}} = \gamma_0 \Gamma^{\mu\,\dagger}_{\text{QE}}\gamma_0.\tag{C.6}$$

Γ^μ_{QE} has a $V - A$ Dirac structure,

$$\Gamma^\mu_{\text{QE}} = \mathcal{V}^\mu_{\text{QE}} - \mathcal{A}^\mu_{\text{QE}},\tag{C.7}$$

with the vector part,

$$\mathcal{V}^\mu_{\text{QE}} = \mathcal{F}_1\gamma^\mu + \frac{\mathcal{F}_2}{2m_N}i\sigma^{\mu\alpha}q_\alpha,\tag{C.8}$$

and the axial-vector part,

$$-\mathcal{A}^\mu_{\text{QE}} = \mathcal{F}_A\gamma^\mu\gamma_5 + \frac{\mathcal{F}_P}{m_N}q^\mu\gamma_5.\tag{C.9}$$

Here, $q_\mu = p'_\mu - p_\mu$; $\mathcal{F}_i$ $(i = 1, 2)$ stands either for the CC form factors, F_i^V, for the NC form factors, $\tilde{F}_i^N$, or the EM form factors, F_i^N, with $N = p, n$; $\mathcal{F}_A$ for the CC form factor, F_A, and the NC form factor, $\tilde{F}_A^N$ (analogous for $\mathcal{F}_P$). All form factors depend on $Q^2 = -q^2$. Details on the form factors for QE scattering are given in Chapter 4 of Ref. [351].

Appendix C.2. Resonance excitation

This section is devoted to the second part in our general decomposition of the cross section given in eq. (C.1), namely the excitation of resonances $\sum_R d\sigma_R$.

The cross section for resonance excitation $\ell(k)N(p) \to \ell'(k')R(p')$ is given by

$$\frac{d\sigma_R}{d\omega \, d\Omega_{k'}} = \frac{|\mathbf{k}'|}{32\pi^2} \frac{\mathcal{A}(p'^2)}{\sqrt{(k \cdot p)^2 - m_\ell^2 M^2}} \, \overline{|\mathcal{M}_R|^2};$$ (C.10)

with $M = \sqrt{p^2}$ and the resonance-spectral function, $\mathcal{A}(p'^2)$, according to section 2.4.2.

The hadronic tensor for the excitation of a spin-1/2 resonance is given by

$$H_{1/2}^{\mu\nu} = \frac{1}{2} \operatorname{Tr}\left[(\slashed{p} + M)\tilde{\Gamma}_{1/2}^{\mu}(\slashed{p}' + M')\Gamma_{1/2}^{\nu}\right],$$ (C.11)

with $M' = \sqrt{p'^2}$ and

$$\tilde{\Gamma}_{1/2}^{\mu} = \gamma_0 \Gamma_{1/2}^{\mu}{}^{\dagger}\gamma^0.$$ (C.12)

For states with positive parity (e.g., $P_{11}(1440)$),

$$\Gamma_{1/2+}^{\mu} = \mathcal{V}_{1/2}^{\mu} - \mathcal{A}_{1/2}^{\mu},$$ (C.13)

and for states with negative parity (e.g., $S_{11}(1535)$),

$$\Gamma_{1/2-}^{\mu} = \left[\mathcal{V}_{1/2}^{\mu} - \mathcal{A}_{1/2}^{\mu}\right]\gamma^5,$$ (C.14)

where the vector part, $\mathcal{V}_{1/2}^{\mu}$, is given by

$$\mathcal{V}_{1/2}^{\mu} = \frac{\mathcal{F}_1}{(2m_N)^2}\left(Q^2\gamma^{\mu} + \slashed{q}q^{\mu}\right) + \frac{\mathcal{F}_2}{2m_N}i\sigma^{\mu\alpha}q_{\alpha}$$ (C.15)

and the axial part $\mathcal{A}_{1/2}^{\mu}$ by

$$-\mathcal{A}_{1/2}^{\mu} = \mathcal{F}_A\gamma^{\mu}\gamma_5 + \frac{\mathcal{F}_P}{m_N}q^{\mu}\gamma^5.$$ (C.16)

As in the QE case, $\mathcal{F}_i$ ($i = 1, 2$) stands either for the CC form factors, F_i^V, for the NC form factors, $\tilde{F}_i^N$, or the EM form factors, F_i^N, with $N = p, n$; analogous for $\mathcal{F}_A$ and $\mathcal{F}_P$.

The excitation of a spin-3/2 final state is described within a Rarita-Schwinger formalism, where the hadronic tensor is given by

$$H_{3/2}^{\mu\nu} = \frac{1}{2} \operatorname{Tr}\left[(\slashed{p} + M)\tilde{\Gamma}_{3/2}^{\alpha\mu}\Lambda_{\alpha\beta}\Gamma_{3/2}^{\beta\nu}\right],$$ (C.17)

with the spin-3/2 projector

$$\Lambda_{\alpha\beta} = -\left(\slashed{p}' + M'\right)$$
$$\times \left(g_{\alpha\beta} - \frac{2}{3}\frac{p_{\alpha}'p_{\beta}'}{M'^2} + \frac{1}{3}\frac{p_{\alpha}'\gamma_{\beta} - p_{\beta}'\gamma_{\alpha}}{M'} - \frac{1}{3}\gamma_{\alpha}\gamma_{\beta}\right),$$ (C.18)

and

$$\tilde{\Gamma}_{3/2}^{\alpha\mu} = \gamma_0 \Gamma_{3/2}^{\alpha\mu}{}^{\dagger}\gamma_0.$$ (C.19)

For states with positive parity as the $P_{33}(1232)$, we have

$$\Gamma^{\alpha\mu}_{3/2+} = \left[\mathcal{V}^{\alpha\mu}_{3/2} - \mathcal{A}^{\alpha\mu}_{3/2}\right]\gamma_5, \tag{C.20}$$

and for the negative-parity ones (e.g., $D_{13}(1535)$),

$$\Gamma^{\alpha\mu}_{3/2-} = \mathcal{V}^{\alpha\mu}_{3/2} - \mathcal{A}^{\alpha\mu}_{3/2}. \tag{C.21}$$

In terms of the form factors, the vector part is given by

$$\begin{aligned}
\mathcal{V}^{\alpha\mu}_{3/2} =& \frac{C_3^V}{m_N}(g^{\alpha\mu}\slashed{q} - q^\alpha\gamma^\mu) + \frac{C_4^V}{m_N^2}(g^{\alpha\mu}q\cdot p' - q^\alpha p'^\mu) \\
&+ \frac{C_5^V}{m_N^2}(g^{\alpha\mu}q\cdot p - q^\alpha p^\mu) + g^{\alpha\mu}C_6^V
\end{aligned} \tag{C.22}$$

and the axial part by

$$\begin{aligned}
-\mathcal{A}^{\alpha\mu}_{3/2} =& \left[\frac{C_3^A}{m_N}(g^{\alpha\mu}\slashed{q} - q^\alpha\gamma^\mu) + \frac{C_4^A}{m_N^2}(g^{\alpha\mu}q\cdot p' - q^\alpha p'^\mu)\right. \\
&\left. + C_5^A g^{\alpha\mu} + \frac{C_6^A}{m_N^2}q^\alpha q^\mu\right]\gamma_5.
\end{aligned} \tag{C.23}$$

As before, the calligraphic C stands either for the CC form factors, $C_i^{V,A}$, $i = 3,\ldots,6$, the electromagnetic transition form factors, C_i^N, with $N = p, n$, or the NC form factors, $\tilde{C}_i^{V,A\,N}$, as detailed in Table 5.5 in Ref. [351]. Note that current conservation implies $C_6^N = 0$.

Any formalism describing resonances with spins greater than 3/2 is highly complicated [395]. Thus, for simplification, we assume that all resonances with spin > 3/2 can be treated with the spin-3/2 formalism. This rough approximation introduces only small errors since the contribution of resonances beyond the Δ is small and soon overshadowed by the opening of DIS processes.

The electromagnetic/vector form factors can be fixed using helicity amplitudes extracted from electron scattering experiments. The explicit relations between the form factors and the helicity amplitudes are given in Appendix E of Ref. [351]. We use these relations to extract the form factors from the results of the recent MAID2005 analysis [396, 397, 398, 399] for the helicity amplitudes including their Q^2 dependences. In this analysis, 13 resonances with invariant masses of less than 2 GeV are included. They are listed in table C.11

Experimental information on the $N - R$ axial form factors is very limited. In QE case, Goldberger-Treiman relations allowing to express the nucleon weak axial coupling through the strong pion-nucleon coupling have been derived [400] from the condition of partially conserved axial current (PCAC). We follow this approach and apply PCAC and pion-pole dominance to derive the axial couplings for the resonances. The equations obtained in this way are sometimes called the off-diagonal Goldberger-Treiman relations. In the case of the Δ, we use the data to fit the Q^2 dependence. For higher-lying resonances, which have only a small effect on observables, we simply approximate the Q^2 dependence by a dipole form factor with axial mass $M_A = 1$ GeV. An extended discussion of axial form factors is given in [351].

The cross sections for photon-induced reactions are given by the limit $Q^2 \to 0$ of the above

name	spin	isospin	parity
$P_{33}(1232)$	3/2	3/2	+
$P_{11}(1440)$	1/2	1/2	+
$D_{13}(1520)$	3/2	1/2	-
$S_{11}(1535)$	1/2	1/2	-
$S_{31}(1620)$	1/2	3/2	-
$S_{11}(1650)$	1/2	1/2	-
$D_{15}(1675)$	5/2	1/2	-
$F_{15}(1680)$	5/2	1/2	+
$D_{33}(1700)$	3/2	3/2	-
$P_{13}(1720)$	3/2	1/2	+
$F_{35}(1905)$	5/2	3/2	+
$P_{31}(1910)$	1/2	3/2	+
$F_{37}(1950)$	7/2	3/2	+

Table C.11: Resonances included in the MAID analysis [397].

expressions,

$$
\begin{aligned}
\sigma_{\gamma N \to R} &= \frac{1}{4\sqrt{(q_\alpha p^\alpha)^2}} \frac{\mathrm{d}^4 p'}{(2\pi)^4} \, 2\pi \mathcal{A}_R(p'^2) \, \overline{|\mathcal{M}_R|^2} \, (2\pi)^4 \delta^4 \left(p + q - p'\right) \\
&= \frac{1}{4\sqrt{(q_\alpha p^\alpha)^2}} \, 2\pi \mathcal{A}_R(p'^2) \, \overline{|\mathcal{M}_R|^2} \Bigg|_{p+q=p'} ,
\end{aligned}
\tag{C.24}
$$

where q is the four-momentum of the real photon (with $q^2 = 0$); the averaged squared matrix element is given by

$$
\overline{|\mathcal{M}_R|^2} = -\frac{1}{2} H_R^{\mu\nu} g_{\mu\nu} .
\tag{C.25}
$$

As in the lepton case, we use helicity amplitudes extracted from the MAID analysis [397] to determine the contributions of individual resonances and to fix the form factors [55].

Appendix C.3. One-pion background

This section is devoted to the third term of eq. (C.1), i.e., non-resonant π production. The need for a one-π non-resonant background contribution, $\mathrm{d}\sigma_{1\pi\,\mathrm{BG}}$, is justified by the fact, that the pure resonance contributions underestimate the total one-π-production cross section in the isospin $1/2$ channels.

Recent progress has been achieved in models treating the one-π background as a sum of Feynman diagrams with a pion and a nucleon in the final state [401, 402, 403]. In this approach the process of Δ-resonance production with its following decay is just one of the considered diagrams (Δ pole), along with six others (crossed Δ, nucleon pole, crossed nucleon, contact term, pion pole and pion in flight). These six diagrams introduce new vertices, which can be described within various models for nucleon-meson interactions.

As one of the possibilities to account for the background contribution, in the GiBUU code we adopt the approach of Hernandez *et al.* [402], where the new vertices are described within the SU(2)-nonlinear σ model. The model is applied to electron and neutrino scattering on nucleons [404]. The ANL and BNL data for integrated cross sections and various one-differential

distributions [405, 406] are described with an accuracy which is of the same order of magnitude as the experimental uncertainties between different data sets.

The advantage of this theoretical approach is that it gives a clear picture of the underlying processes and their kinematics, and it takes interference effects into account explicitly. The disadvantage is related to the fact, that the new vertices mentioned above, as well as the relative signs of the various amplitudes, are not always known. In [404] it is shown, that the model gives good results for pion-nucleon invariant masses $W < 1.4\,\text{GeV}$. However, its extension to higher invariant masses, at least to the second resonance region, is not yet achieved and requires significant efforts.

Therefore, to obtain the background in the entire resonance region, that is up to $W < 2\,\text{GeV}$, we have adopted a phenomenological approach, described in detail in [55] and shortly summarized in the following. This approach starts from the cross sections, since the amplitudes are not available, and separates them into a background and a resonance contribution. We illustrate this first for electromagnetic processes. We use the measured unpolarized one-π-production cross section $\ell(k)N(p) \to \ell'(k')\pi(k_\pi)N(p')$ and subtract the theoretically deduced resonance contribution. The rest, which then includes the genuine background, but also the resonance-background interference terms, we use as one-π background, $\mathrm{d}\sigma_{1\pi\,\text{BG}}$. We thus obtain [58]

$$\frac{\mathrm{d}\sigma^{\text{V}}_{1\pi\,\text{BG}}}{\mathrm{d}\omega\mathrm{d}\Omega_{k'}\mathrm{d}\Omega_{k_\pi}} = \frac{\mathrm{d}\sigma^{\text{V}}_{N\pi}}{\mathrm{d}\omega\mathrm{d}\Omega_{k'}\mathrm{d}\Omega_{k_\pi}} - \sum_R \frac{\mathrm{d}\sigma^{\text{V}}_{\ell N\to\ell R\to\ell N\pi}}{\mathrm{d}\omega\mathrm{d}\Omega_{k'}\mathrm{d}\Omega_{k_\pi}}. \tag{C.26}$$

The superscript, V, denotes here, that in electromagnetic processes only the vector part of the current contributes.

The first term of the r.h.s. of eq. (C.26) denotes the measured one–pion production cross section $\mathrm{d}\sigma^{\text{V}}_{N\pi}$. For simplicity we obtain it from the MAID analysis [396, 397, 398, 399] (the MAID amplitudes are integrated into the GiBUU code).

The second term of the r.h.s. of eq. (C.26), the resonance contribution, is again obtained from the MAID analysis. In order to get the required angular distribution we assume that the resonances produced decay isotropically in their rest frame

$$\frac{\mathrm{d}\Gamma_{R\to N\pi}}{\mathrm{d}\Omega^{\text{cm}}_{k_\pi}} = \frac{\Gamma_{R\to N\pi}}{4\pi}\,. \tag{C.27}$$

Hence,

$$\begin{aligned}\frac{\mathrm{d}\sigma^{\text{V}}_{\ell N\to\ell R\to\ell N\pi}}{\mathrm{d}\omega\mathrm{d}\Omega_{k'}\mathrm{d}\Omega_{k_\pi}} &= \frac{\mathrm{d}\sigma^{\text{V}}_R}{\mathrm{d}\omega\mathrm{d}\Omega_{k'}}\frac{1}{\Gamma_R}\frac{\Gamma_{R\to N\pi}}{4\pi}\frac{\mathrm{d}\Omega^{\text{cm}}_{k_\pi}}{\mathrm{d}\Omega_{k_\pi}} \\ &= \frac{\mathrm{d}\sigma^{\text{V}}_R}{\mathrm{d}\omega\mathrm{d}\Omega_{k'}}\frac{1}{\Gamma_R}\frac{\Gamma_{R\to N\pi}}{4\pi}\frac{\sqrt{p'^2}k^2_\pi}{|\boldsymbol{k}^{\text{cm}}_\pi|\left(|\boldsymbol{k}_\pi|p'^0 - |\boldsymbol{p}'|k^0_\pi\cos\theta_\pi\right)}\,,\end{aligned} \tag{C.28}$$

where Γ_R is the total decay width of the resonance, $\theta_\pi = \measuredangle(\boldsymbol{k}_\pi, \boldsymbol{p}')$ and the vector part of the resonance production cross section has been introduced in the previous section. The quantity $\frac{\mathrm{d}\sigma^{\text{V}}_{1\pi\,\text{BG}}}{\mathrm{d}\omega\,\mathrm{d}\Omega_{k'}}$ can now be retrieved by an integration over the solid angle of the outgoing pion.

The background for neutrino reactions includes vector, axial, and interference contributions,

$$\mathrm{d}\sigma_{1\pi\,\text{BG}} = \mathrm{d}\sigma^{\text{V}}_{1\pi\,\text{BG}} + \mathrm{d}\sigma^{\text{A}}_{1\pi\,\text{BG}} + \mathrm{d}\sigma^{\text{V/A}}_{1\pi\,\text{BG}} = \mathrm{d}\sigma^{\text{V}}_{1\pi\,\text{BG}} + \mathrm{d}\sigma^{\text{non-V}}_{1\pi\,\text{BG}}. \tag{C.29}$$
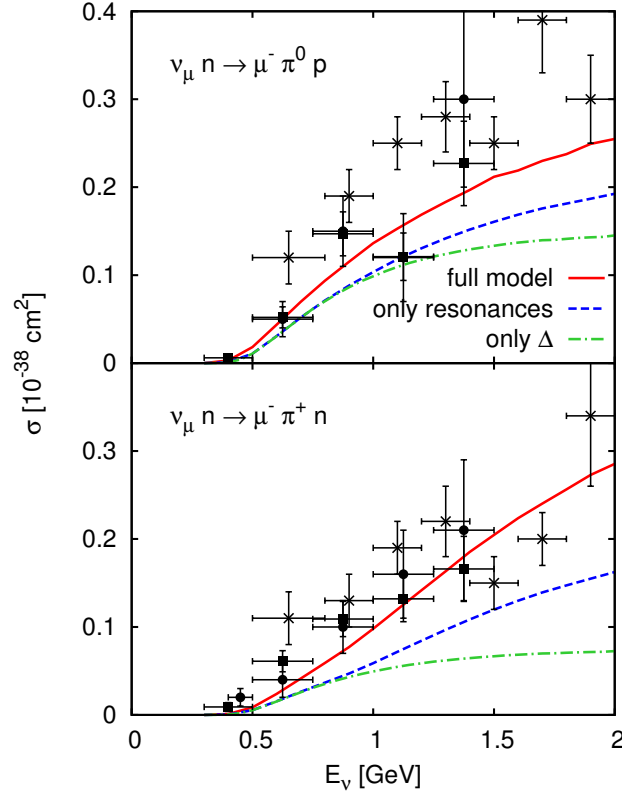
Figure C.59: (Color online) Total CC pion-production cross sections for the mixed isospin channels as a function of the neutrino energy compared to the pion-production data from ANL (Refs. [407] (•) and [405] (■)) and BNL ([406] (×)). The solid lines denote our full result including the non-resonant background following eq. (C.30) with $b^{p\pi^0} = 3$ and $b^{n\pi^+} = 1.5$. Furthermore, we show the results for pion production only through the excitation and the subsequent decay of all resonances (dashed lines) or through the Δ alone (dash-dotted lines). No cut on the invariant mass is applied (taken from [58]).

The vector part is fully determined by electron-scattering data as described above. The axial and the interference terms collected under the label "non-V" are fitted to the available data for neutrino reactions in the isospin-1/2 channels.

We assume that $d\sigma^V_{1\pi\,BG}$ and $d\sigma^{non-V}_{1\pi\,BG}$ have the same functional form, i.e.,

$$d\sigma_{1\pi\,BG} = d\sigma^V_{1\pi\,BG} + d\sigma^{non-V}_{1\pi\,BG} = (1 + b^{N\pi})\,d\sigma^V_{1\pi\,BG}, \tag{C.30}$$

where the global factor, $b^{N\pi}$, depends on the process. For CC reactions, $b^{p\pi^0} = 3$ for $vn \to \ell^- p\pi^0$, and $b^{n\pi^+} = 1.5$ for $vn \to \ell^- n\pi^+$ give a reasonable agreement with the ANL data. This is shown in fig. C.59. The background in the isospin-3/2 channel is neglected.

For NC reactions the data on one-π production are scarce. We find a good agreement with the data already without a non-resonant part. In view of this, we abstain from fitting the non-vector part to these data and neglect a NC background. More results on the one-π background are presented in [351, 58].

141

Appendix C.4. Two-pion photoproduction

Already in the 1960's and 70's, first extensive photon-induced $\pi\pi$ production experiments on elementary targets have been performed (cf. [408, 409, 410] and references therein). More recently, the TAPS [411, 412, 413, 414, 415], DAPHNE [416, 417], GDH [418, 419], and GRAAL [420] collaborations have been examining $\pi\pi$ production with high statistical accuracy. In fig. C.60, the most recent data sets are plotted as an overview over the relevant threshold region. Neutron data (see [55] for a detailed description of the experimental situation) have still large uncertainties, whereas the proton data seem to be reliable after a period of contradiction between different experiments. The lines represent our calculations as described below.

For the elementary two-pion-production process on the nucleon we apply the model of Nacher *et al.* [421], which is an updated version of a model developed by Tejedor *et al.* [422, 423]. This model provides a reliable input for the momentum distributions of the pions in the elementary process. It is based on a set of tree-level diagrams, which include the coupling of the nucleons, pions, photons and baryon resonances ($P_{33}(1232)$, $P_{11}(1440)$, $D_{13}(1520)$, and $P_{33}(1700)$).

Figure C.60 shows the result of this model for the total cross sections. Although the agreement of the model to data is quite good we scale the total cross section to the available data before analyzing the reaction in complex targets. Hence, for all channels besides $\gamma N \rightarrow N\pi^+\pi^-$ we directly use the data measured by the TAPS, DAPHNE, and the GDH&A2 collaborations [411, 412, 413, 414, 415, 416, 417, 418, 419, 425, 426, 424] to normalize the calculated cross sections, while we take the decay-mass and momentum distributions from theory. In the threshold regions of $\gamma p \rightarrow p\pi^0\pi^0$, $\gamma p \rightarrow p\pi^-\pi^+$, $\gamma n \rightarrow n\pi^0\pi^0$, and $\gamma n \rightarrow p\pi^0\pi^-$, where no data are available, we estimate the total cross section based on the three-particle-phase-space structure. We assume the matrix element $\mathcal{M}$ to be constant in this region and get

$$
\begin{aligned}
\sigma_{\text{threshold}} &= \frac{(2\pi)^4}{4m_N q_0}|\mathcal{M}|^2 \int \frac{\mathrm{d}^3\boldsymbol{k}_1}{2k_1^0(2\pi)^3}\frac{\mathrm{d}^3\boldsymbol{k}_2}{2k_2^0(2\pi)^3}\frac{\mathrm{d}^3\boldsymbol{p}\,'}{2p_0'(2\pi)^3}\delta^4\left[q+p-\left(p'+\sum_{i=1}^{2}k_i\right)\right] \\
&= \frac{(2\pi)^4}{4m_N q_0}|\mathcal{M}|^2 \times 16\,(2\pi)^7 \times \int \frac{\mathrm{d}m_{12}^2 \mathrm{d}m_{13}^2}{s},
\end{aligned}
\tag{C.31}
$$

where s is the Mandelstam s of the process; $\mathrm{d}m_{12}^2$ and $\mathrm{d}m_{13}^2$ are defined by

$$
\begin{aligned}
m_{12} &= (k_1 + k_2)^2, \\
m_{13} &= (k_1 + p\,')^2.
\end{aligned}
\tag{C.32}
$$

The value of $|\mathcal{M}|^2$ is now fixed by the value of the lowest available data point,

$$\sigma_{\text{threshold}}(\text{energy of lowest data point}) = \sigma(\text{lowest data point}) .$$

Table C.12 shows a compilation of the invariant matrix elements $|\mathcal{M}|^2$.

The solid line in the $\gamma n \rightarrow n\pi^+\pi^-$ panel in fig. C.60 shows the result of the model by Nacher *et al.* [421] with a slightly adjusted set of parameters. The solid lines in the other panels represent our fits and threshold estimates. Altogether, these six solid lines represent our elementary input cross sections.

Appendix C.5. Two-pion background

In the previous section we described some involved model, which fits the photoproduction data very accurately. However, this model is only applicable to photoproduction and was not
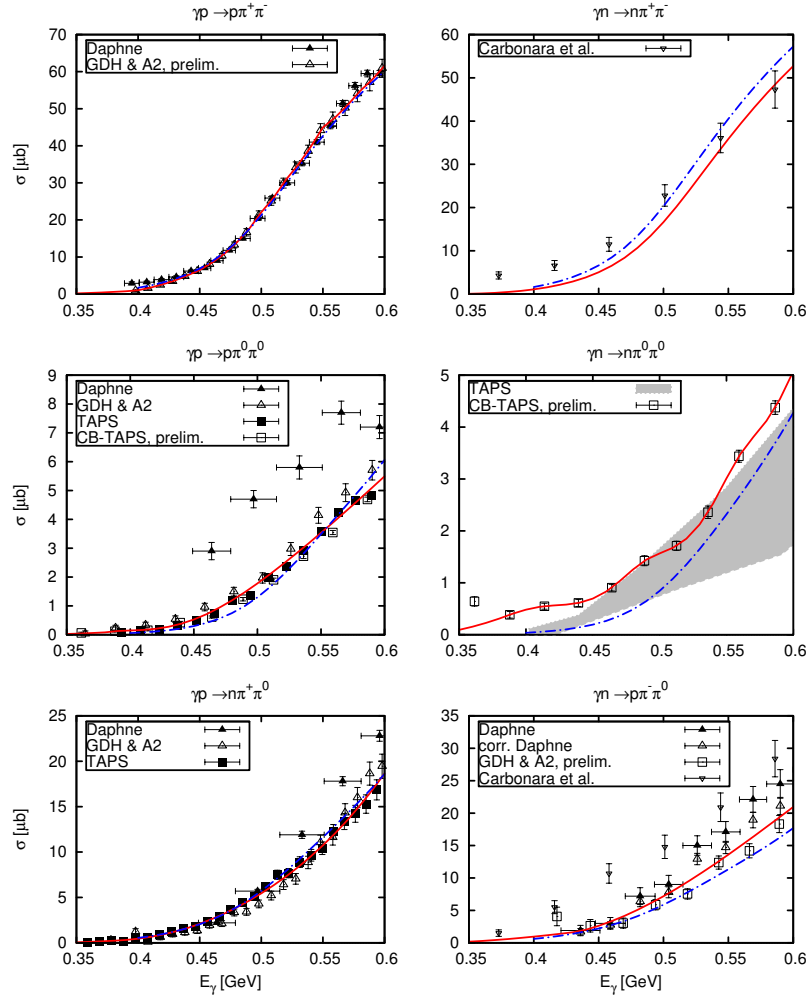
Figure C.60: (Color online) Different isospin channels for the reaction $\gamma N \to N\pi\pi$. For the error bars we added the systematical and statistical uncertainties ($\Delta^2 = \Delta^2_{\text{stat}} + \Delta^2_{\text{sys}}$) as quoted by the experiments. The data are taken from [410, 416, 417, 411, 412, 413, 414, 415, 418, 419]; preliminary data have been communicated by [424, 425, 426]. In the panel, representing $\gamma n \to n\pi^0\pi^0$, the shaded area shows the cross-section measurement by [415]. The solid line represents our parametrizations, which we use as input for the nuclear targets. The dotted-dashed curves show the result obtained with the original model of Nacher *et al.* [421, 427] based on Tejedor *et al.* [422, 423]. Taken from [55].

Channel	E_γ [MeV]	σ [μb]	$|\mathcal{M}|^2 \times (2\pi)^{11}$
$\gamma p \to p\pi^0\pi^0$	380	0.08128	4.871
$\gamma p \to p\pi^-\pi^+$	398	0.9083 [425]	34.74
$\gamma n \to n\pi^0\pi^0$	387.9	0.3840 [424]	18.60
$\gamma n \to p\pi^0\pi^-$	435	1.752	34.96

Table C.12: Parameters for the threshold estimation of the total cross section: For each channel, we show the lowest possible energy at which we can reliably estimate the cross section from experiment and the extracted cross section, σ. The fourth column shows the corresponding value of the threshold-matrix element $|\mathcal{M}|^2$.
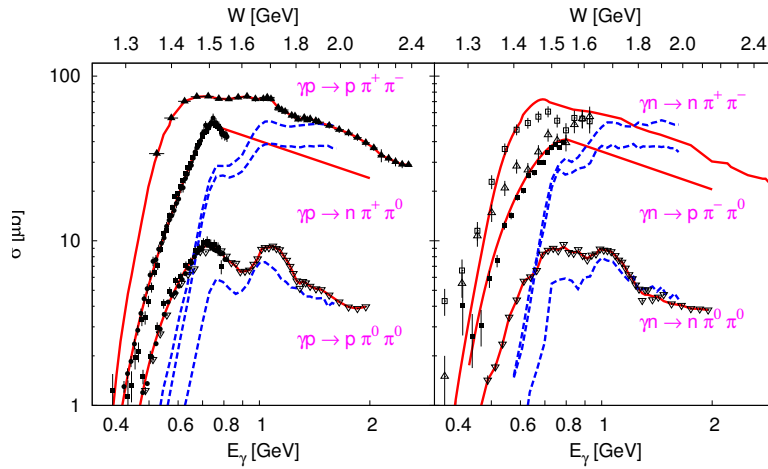

Figure C.61: (Color online) Total photoproduction cross section of two-pion channels as function of the photon energy (bottom axes) or center of momentum energy (top axes), respectively. The solid lines indicate the cross-section parametrizations implemented in GiBUU intended to describe the experimental data. The dashed lines show only resonance contribution. Experimental data are from Carbonara *et al.* ($\square$,$\triangle$ [410]), SAPHIR@ELSA ($\blacktriangle$ [428]), GDH&A2@Mainz ($\blacksquare$ [418, 419]), TAPS ($\bullet$ [414, 413]), CB-TAPS (preliminary) ($\triangledown$ [424]).

extended to nonzero Q^2 yet. In GiBUU, however, we need the description of two-π production in electron and neutrino reactions as well. Keeping also in mind, that eventually we want to study nuclear reactions, where resonances modify their properties and propagate out of the nucleus, we have to split the two-π cross section into a resonant and a background part.

For the elementary reaction, the resonances are to be described according to the general formalism as outlined in Appendix C.2. Then we can use experimental two-π data to extract the background.

Let us consider EM interactions at low energies, as studied in detail in [55]. In fig. C.61, we show the resonance contribution to the two-π photoproduction cross sections with various charge combinations in the final state. The data points are the same that were used in Appendix C.4. At $E_\gamma \lesssim 1$ GeV, all curves showing only the resonance contribution are below the data, because the resonance production with their following decays opens up only at higher energies. Thus, we
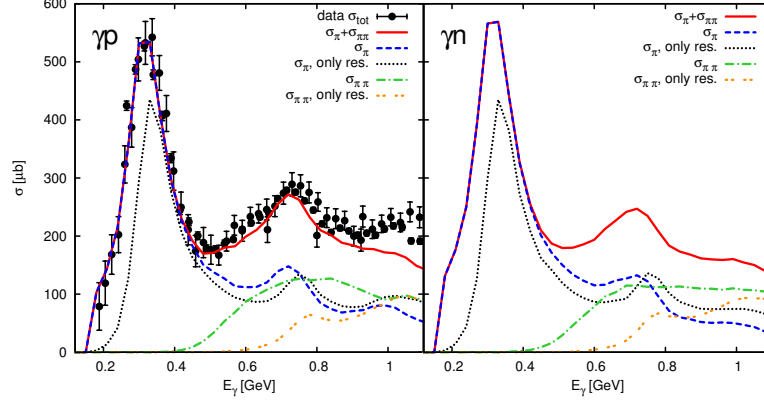
Figure C.62: (Color online) Photon-induced reactions on the proton (left panel) and the neutron (right panel) as a function of the incoming photon energy. The solid line shows the sum of single-π and double-π production for the full model, the dashed line shows the result for single-π and the dashed dotted one gives $\pi\pi$; dotted and double-dashed curves show the contributions of resonances. The data are taken from [374]. Taken from [55].

define the two-π background as

$$d\sigma_{2\pi BG} = d\sigma_{2\pi}^{exp} - \sum_R d\sigma_R|_{R \to 2\pi} \quad \text{for} \quad Q^2 = 0 \, \text{GeV}^2 \, . \tag{C.33}$$

This subtraction must be adjusted for all possible charge channels, $\pi^+\pi^-$, $\pi^0\pi^0$, and $\pi^0\pi^\pm$, independently and includes the resonance contributions of the following four channels

$$
\begin{aligned}
\gamma N &\to R \to \pi\Delta &\to N'\pi\pi \, , \\
\gamma N &\to R \to \pi P_{11}(1440) &\to N'\pi\pi \, , \\
\gamma N &\to R \to \rho N &\to N'\pi\pi \, , \\
\gamma N &\to R \to \sigma N &\to N'\pi\pi \, .
\end{aligned}
\tag{C.34}
$$

Given $\sigma_{\gamma N \to R}$, the evaluation of $\sigma_{\gamma N \to R \to N'\pi\pi}$ for a special $\pi\pi$-charge state involves a weighting with the partial decay widths for the intermediate $\pi\Delta$, $\pi P_{11}(1440)$, ρN, and σN channels and the relevant isospin Clebsch-Gordan factors. The distribution of the final-state momenta of the $\pi\pi$-background events are assumed to follow the phase space distribution.

As expected, with increasing photon energy, the background contribution vanishes. At $E_\gamma \gtrsim 1 \, \text{GeV}$ the resonance contribution even overestimates the full model calculations; here we set the background to zero.

The resulting two-π contributions are shown in fig. C.62 together with the total photoproduction cross section for both proton and neutron targets. Obviously, the total cross section is well described for $E_\gamma < 0.9 \, \text{GeV}$; the resonance contribution to $\pi\pi$ in this region is in fact small compared to the total $\pi\pi$-production cross section, especially at energies below 600 MeV.

In order to generalize this two-pion-background model from real photons to virtual photons, we assume for simplicity the same dependence as for the total cross section,

$$d\sigma_{2\pi BG}(\epsilon, Q^2) = d\sigma_{2\pi BG} \frac{d\sigma_{tot}(\epsilon, Q^2)}{d\sigma_{tot}(0, 0)} . \tag{C.35}$$
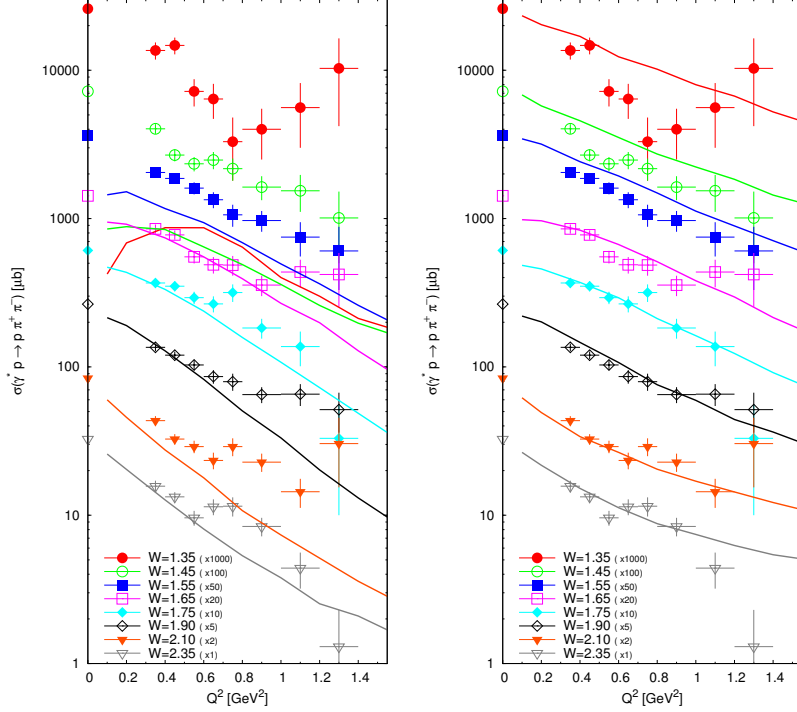
145

Figure C.63: (Color online) Cross section of $\gamma^* p \to p\pi^+\pi^-$ for $E_{\text{beam}} = 7.2\,\text{GeV}$ as function of Q^2 for different W bins. Both panels repeat the same experimental data [430], while lines show calculations only within the resonance prescription (left) and with inclusion of the two-pion background and the DIS contribution (right).

We use the cross-section parametrization of Bosted *et al.* [429]. We show a comparison of the Q^2 dependence of the channel $\gamma^* p \to p\pi^+\pi^-$ with experimental data in fig. C.63.

For neutrino-induced reactions (CC,NC), no experimental data are available yet to fix the two-pion background. Therefore we neglect it.

Appendix C.6. Deep-inelastic scattering

It is clear from phase-space considerations, that with increasing energy the multiplicity in the final state increases. We try to extrapolate the DIS prescription from the DIS regime ($W \to \infty$, $Q^2 \to \infty$) down to $W \simeq 1.6\,\text{GeV}$.

Conventionally, experimental results for electroproduction reactions are shown in the form of the cross section for virtual photons

$$\frac{1}{\Gamma_t} \frac{\mathrm{d}\sigma}{\mathrm{d}\Omega'\mathrm{d}E'} = \sigma_T + \varepsilon\sigma_L, \tag{C.36}$$

where Γ_t is the flux of the virtual photon field,

$$\Gamma_t = \frac{\alpha}{2\pi^2} \frac{E'}{E_e} \frac{W^2 - m_N^2}{2m_N Q^2} \frac{1}{1 - \varepsilon},$$

146

and ε is the degree of transverse polarization of the photon,

$$\varepsilon = \left[1 + 2 \left(1 + \frac{\nu^2}{Q^2} \right) \tan^2 \frac{\theta}{2} \right]^{-1} .$$

Figure C.64 compares the model description with the parametrization of the experimental data by Bosted *et al.* [429]. Here we perform a Rosenbluth separation both for the calculation and the data parametrization, relying on $\epsilon = 0.05$ and $\epsilon = 0.99$.

At the high-energy side, we use PYTHIA [110] for event generation. In former code versions, we had not been able to create events with PYTHIA down to the energy range of $W = 2 \, \text{GeV}$, since we ran into situations, where PYTHIA entered infinite loops in the calculation of diffractive events. This created a gap between the PYTHIA region and the resonance-model region. Parametrizations of cross sections for some known explicit channels and the FRITIOF model [370] for the unknown part had to be used to bridge the gap in the same spirit as described in Appendix C.8 for the case of real photons. In the present version of GiBUU we have modified the PYTHIA code such that the creation of diffractive events in a certain, low-energy parameter space is forbidden.

Nevertheless, PYTHIA is just a complex implementation of leading-order processes, as, e.g., DIS processes. In leading order, PYTHIA contains the corresponding standard formulae,

$$\frac{\mathrm{d}^2\sigma^{(\mu^- p \to \mu^- X)}}{\mathrm{d}x \, \mathrm{d}y} = 2\pi\alpha^2 \, \frac{2m_N E}{Q^4} \left[1 + (1-y)^2 \right] \sum e_i^2 \, x \left[q_i(x) + \overline{q}_i(x) \right], \tag{C.37}$$

$$\frac{\mathrm{d}^2\sigma^{(\nu_\mu p \to \mu^- X)}}{\mathrm{d}x \, \mathrm{d}y} = \frac{G_F^2}{2\pi} \, \frac{2m_N E}{(1 + Q^2/m_W^2)^2} \, 2x \left[d(x) + (1-y)^2 \overline{u}(x) \right], \tag{C.38}$$

$$\frac{\mathrm{d}^2\sigma^{(\overline{\nu}_\mu p \to \mu^+ X)}}{\mathrm{d}x \, \mathrm{d}y} = \frac{G_F^2}{2\pi} \, \frac{2m_N E}{(1 + Q^2/m_W^2)^2} \, 2x \left[(1-y)^2 u(x) + \overline{d}(x) \right] . \tag{C.39}$$

with

$$x = \frac{Q^2}{2m_N \nu}, \quad y = \frac{\nu}{E}, \quad \nu = E - E', \quad \cos\theta = 1 - \frac{Q^2}{2 \, E \, E'}$$

and $q(x)$ ($\overline{q}(x)$) standing for the parton distribution function of the quarks (antiquarks) inside the nucleon.

We use the Jacobian determinant,

$$\mathrm{d}x \, \mathrm{d}y = \frac{1}{2m_N \nu E} \, \mathrm{d}Q^2 \, \mathrm{d}\nu = \frac{E - \nu}{m_N \nu} \, \mathrm{d}E' \, \mathrm{d}\cos\theta, \tag{C.40}$$

to transform these analytic expressions to any desired variables. During the Monte Carlo integration over the results of PYTHIA these transformations are straightforward. By using PYTHIA we not only obtain the total cross sections, given by eq. (C.37), but also the complete hadronic final state of the event. Semi-exclusive events can thus be investigated.

Appendix C.7. Exclusive pion production

Until now we have just covered the inclusive particle production as provided by PYTHIA. But according to [272, 273, 433], also a detailed study of exclusive pion production is necessary at high energies.

The idea proposed in [272, 273, 433] is to treat exclusive meson production as an exclusive limit of semi-inclusive DIS. This is in spirit of the exclusive-inclusive connection [434]. In this
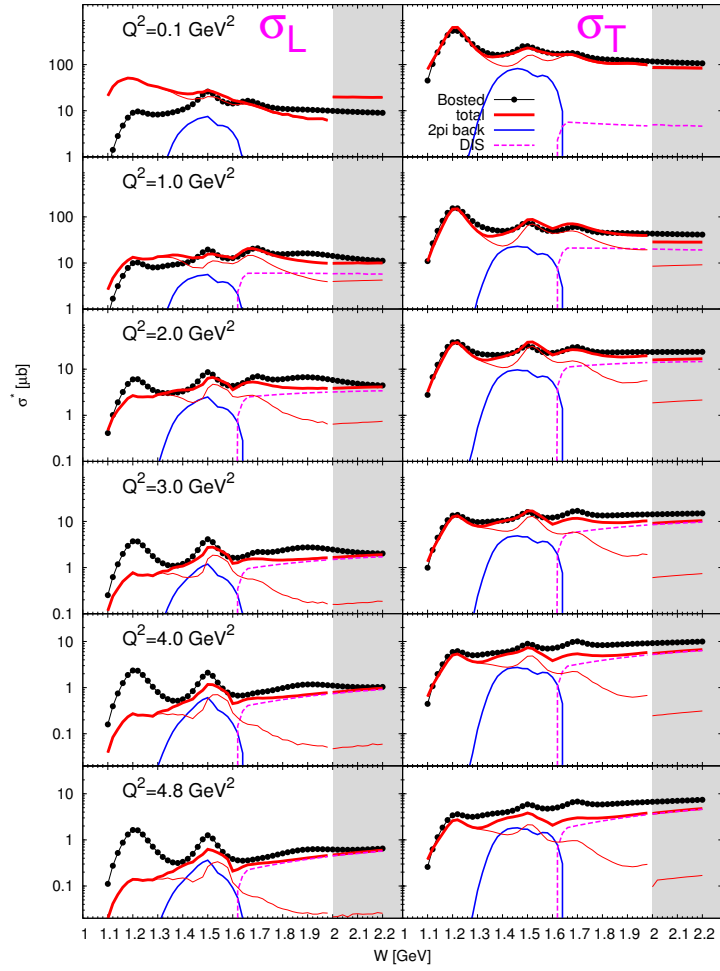
Figure C.64: (Color online) Rosenbluth separation done for $\epsilon_{1,2} = 0.05, 0.99$ for $Q^2 = 0.1$-$4.8\,\text{GeV}^2$ as function of W. The points show the data parametrization of Bosted *et al.* [429]. The thick solid line shows the sum of all contributions, resonances+1πBG (thin red), 2πBG (thin blue), and DIS (dashed magenta). The grey-shaded area is the high energy region $W > 2\,\text{GeV}$; there we have the VMD contribution instead of the resonance contribution (thin red).
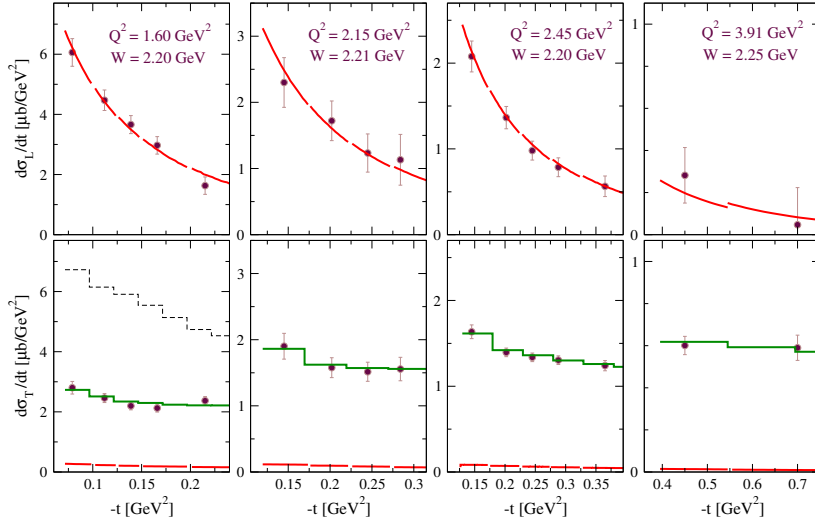
Figure C.65: (Color online) The longitudinal ($d\sigma_L/dt$, top panels), and the transverse ($d\sigma_T/dt$, bottom panels) differential cross sections of the reaction $p(\gamma^*, \pi^+)n$ at average values of $Q^2 = 1.60$ (2.45) GeV^2 [431] and $Q^2 = 2.15$ (3.91) GeV^2 [432]. The solid curves show the contribution of the hadron-exchange model and the histograms the contribution of the DIS pions. The discontinuities in the curves result from the different values of Q^2 and W for the various $-t$ bins. The dashed histogram in the lower left panel shows the contribution of the DIS pions for the average transverse momentum of partons $\sqrt{\langle k_t^2 \rangle} = 0.4$ GeV. Taken from Ref. [272].

case, the reaction mechanism consists of two components. The first one describes the soft production mediated by the exchange of meson-Regge trajectories. These peripheral processes are relevant for the photo production and low-Q^2 electro production. As the second, novel element, at large Q^2 the GiBUU model allows the direct interaction of virtual photons with partons followed by the fragmentation of excited color string into the meson-baryon channel. Details can be found in Ref. [272, 273, 433]. In fig. C.65 we show the results for the exclusive production of charged pions in the kinematics available at JLAB. As one can see, all longitudinal and transverse cross sections are very well described. The dashed curves describe the Regge-exchange contributions and dominate in the longitudinal channel. In the transverse channel the contributions of mesons are marginal. Here, the direct partonic interactions dominate the production mechanism. In fig. C.66 we show the comparison of the model results with new data from JLAB. As one can see, the model (solid curves) describes the cross section in a remarkably large Q^2 range up to $Q^2 \simeq 5$ GeV^2.

Note that this behavior is rather general and is also observed in other meson production processes. For instance, the string-breaking mechanism is effective in the transverse cross section and explains large cross sections in pseudoscalar $\pi^0(\eta)$ and ρ^0 production channels.

In fig. C.67 we show our results for the deep exclusive production of charged pions in the kinematics of the HERMES experiment. The two-component model describes again the data very well. At forward angles the Regge-exchange contributions again dominate. In the non-forward region the transverse partonic interactions are large and describe the measured cross sections very well.
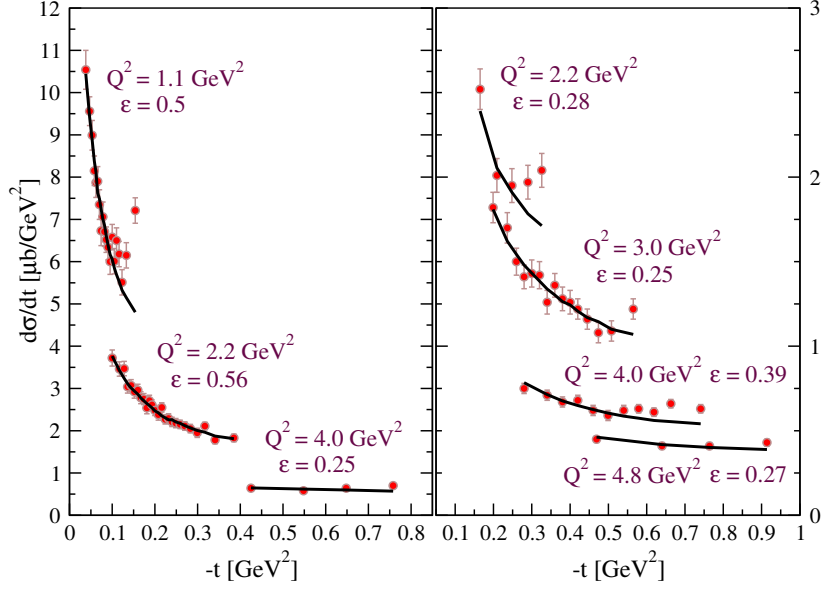
149

Figure C.66: (Color online) Differential cross section $d\sigma/dt = d\sigma_T/dt + \varepsilon d\sigma_L/dt$ of the reaction, $p(\gamma^*, \pi^+)n$, at JLAB. The solid curves are the model predictions. Taken from Ref. [272].

Appendix C.8. Vector-meson production

Exclusive vector-meson production plays a special role in lepton- or photon-induced reactions. In GiBUU this is usually treated within the PYTHIA model, which implements a vector-meson dominance (VMD) model.

The invariant amplitude for the process $\gamma^*h \to X$ can be expressed in terms of the on-shell vector-meson-scattering amplitude,

$$\mathcal{M}_{\gamma^*h \to X} = \sum_V \frac{e}{g_V} \frac{m_V^2}{Q^2 + m_V^2} \mathcal{M}_{Vh \to X} \quad . \tag{C.41}$$

Here, m_V denotes the mass of the vector meson, V, and $(e/g_V)^2$ gives the probability for the transitions $\gamma^* \to V$. One may use Pomeron–Reggeon parametrizations for the total hadronic cross section. Assuming an additive quark model, the total Vp cross sections can be parametrized as

$$\sigma_{\text{tot}}^{\rho^0 p} \simeq \sigma_{\text{tot}}^{\omega p} \simeq \frac{1}{2}\left(\sigma_{\text{tot}}^{\pi^+ p} + \sigma_{\text{tot}}^{\pi^- p}\right) = 13.63 \, s^\epsilon + 31.79 \, s^{-\eta} \tag{C.42}$$

$$\sigma_{\text{tot}}^{\phi p} \simeq \sigma_{\text{tot}}^{K^+ p} + \sigma_{\text{tot}}^{K^- p} - \sigma_{\text{tot}}^{\pi^+ p} = 10.01 \, s^\epsilon + 1.52 \, s^{-\eta} \tag{C.43}$$

Using eq. (C.41) in the optical theorem, one obtains the 'diagonal approximation', i.e., neglecting
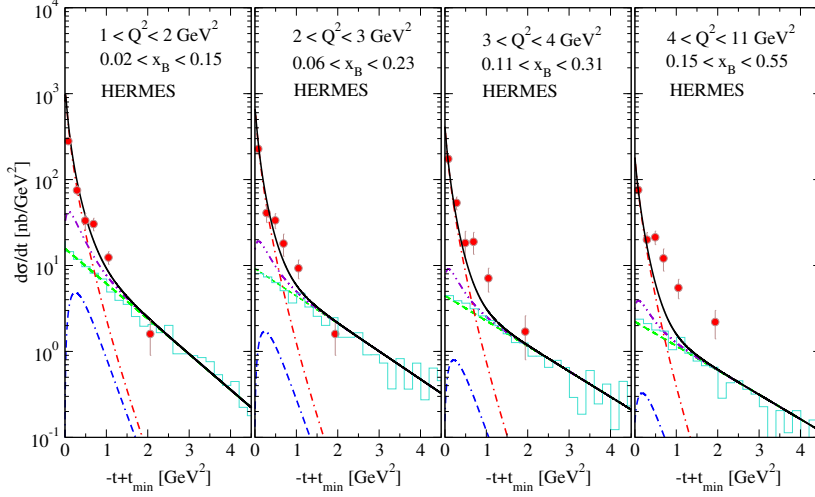
150

Figure C.67: (Color online) The differential cross section, $d\sigma/dt = d\sigma_T/dt + \epsilon d\sigma_L/dt$, of the exclusive reaction, $p(\gamma^*, \pi^+)n$, in the kinematics of the HERMES experiment. The solid curves are the model results. The dash-dotted curves correspond to the exchange of π-Regge trajectory and dash-dash-dotted curves to the exchange of ρ-Regge trajectory. The histograms and the dashed curves which just fit the histograms describe the partonic contributions in line of the DIS mechanism. The dot-dot-dashed curves are the contribution of the transverse cross section, $d\sigma_T/dt$, to the total unseparated response, $d\sigma/dt$. Taken from Ref. [433].

off-diagonal scattering $VN \rightarrow V'N$ with $V' \neq V$, [25]

$$\sigma^{\gamma^* p}_{\text{VMD}} = \sum_V \frac{e^2}{g_V^2} \sigma^{Vp}_{\text{tot}} \quad . \tag{C.44}$$

Comparing this with the total γp cross section, one realizes, that this VMD prescription describes 80 % of the total interaction [435]. In addition, the VMD contribution is dominated by the ρ^0 component of the photon. In order to achieve a full prescription of the photon interaction, one has to take into account some "generalized vector meson dominance" interactions, where the interaction of the photon is described with some higher excited $q\bar{q}$ states, and also direct interactions play a major role [435].

The model described above is rather simple and can be used for both real and virtual photons. Here, we are interested in the case of real photons. As discussed in section 4.3.4, modern photoproduction experiments allow to investigate the modification of meson properties in the nuclear medium. Thus, we need a more detailed description for the elementary input, which can be meaningfully extended to the in-medium case. So, for photo production we replace the PYTHIA treatment with the model described below.

In our model the exclusive cross sections for the photo production of vector mesons on a nucleon, i.e., $\gamma N \rightarrow VN$ (with $V = \rho^0, \omega, \phi$), are adjusted to experimental data with the ansatz [60]

$$\sigma_{\gamma N \rightarrow VN} = \frac{1}{p_i s} \int_0^{\mu_{max}} d(\mu^2) \left| \mathcal{M}_V(\sqrt{s}) \right|^2 p_f \mathcal{A}_V(\mu), \tag{C.45}$$

---

[25]Within this prescription one easily may implement medium modifications/shadowing effects by modifying the coupling constant, $\frac{e^2}{g_V^2}$, according to the spatial coordinate.
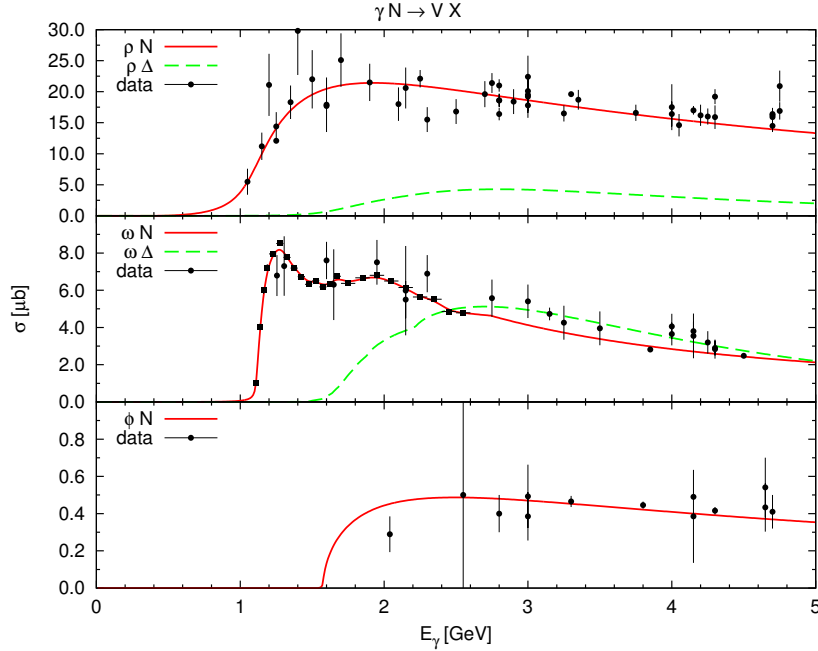
Figure C.68: (Color online) Photoproduction cross sections of vector mesons. Data taken from [129] and [436].

where we integrate over the mass, μ, of the vector meson, V, up to a maximum $\mu_{max} = \sqrt{s} - m_N$. Here $\sqrt{s}$ is the total energy available for the reaction. The center-of-mass momenta of the initial and final state are denoted by p_i and p_f, respectively:

$$p_i = \frac{1}{2\sqrt{s}} \left(s - m_N^2 \right) , \tag{C.46}$$

$$p_f = \frac{1}{2\sqrt{s}} \sqrt{\left(s - (m_N + \mu)^2 \right) \left(s - (m_N - \mu)^2 \right)} . \tag{C.47}$$

The spectral function of the vector meson is given by

$$\mathcal{A}_V(\mu) = \frac{1}{\pi} \frac{\mu \Gamma_V(\mu)}{(\mu^2 - M_V^2)^2 + (\mu \Gamma_V(\mu))^2} .$$

Here, M_V is the pole mass of the vector meson, and Γ_V its total width, which for an elementary reaction is just the vacuum decay width. However, it will include contributions from collisional broadening, when we describe vector meson production in the medium.

For the ρ^0 and ϕ mesons, constant matrix elements

$$|\mathcal{M}_\rho|^2 = 160 \, \mu b \cdot GeV^2 , \tag{C.48}$$

$$|\mathcal{M}_\phi|^2 = 4 \, \mu b \cdot GeV^2 \tag{C.49}$$

are sufficient to obtain a good fit of the data, cf. fig. C.68.

For the ω meson we use an $\sqrt{s}$-dependent matrix element. It can be directly obtained from a spline-fit to the SAPHIR data [437] for ω photoproduction on a proton. Using the fact, that in

the vacuum the ω spectral function is very narrow [62] and can be approximated by the Delta-function in eq. (C.45), we get

$$\left|\mathcal{M}_\omega(\sqrt{s})\right|^2 = \frac{p_i \, s \, \sigma_{\gamma N \to \omega N}^{exp}(s)}{\phi_2(s)},$$

where ϕ_2 stands for the two-body phase-space integral (in the vacuum). This matrix element is then used in eq. (C.45) together with the in-medium spectral function.

In order to describe the photoproduction of mesons with masses below the pole mass, we follow the idea of [229] and extend the matrix element to sub-threshold energies by defining a new invariant

$$Q(\mu) = \sqrt{s_0(M_V)} - \sqrt{s_0(\mu)} + \sqrt{s} \equiv \sqrt{s} + M_V - \mu. \tag{C.50}$$

Here $\sqrt{s_0(\mu)}$ is the threshold energy for the production of ω mesons of mass μ. With this definition one substitutes

$$\mathcal{M}(\sqrt{s}) \to \mathcal{M}[Q(\mu)] \quad .$$

In the vacuum $Q(\mu)$ is only nonzero in the vicinity of $Q(\mu) \approx \sqrt{s}$, since the ω is a very narrow state. At the same time, eq. (C.50) provides a reasonable prescription for the in-medium case (see Appendix D.4.2 for more details).

For the process $\gamma N \to V\Delta$ we use the following parametrization of the total cross section [289],

$$\sigma_{\gamma N \to V\Delta} = \frac{1}{p_i s} \int d(\mu_\Delta^2) p_f(\mu_\Delta) \mathcal{A}_\Delta(\mu_\Delta) \frac{A}{(\sqrt{s} - M)^2 + \Gamma^2/4}, \tag{C.51}$$

where the constants, A, M, and Γ, are fitted to the experimental cross section of Ref. [438], yielding $A = 47.3\,\mu\text{b}\,\text{GeV}^4$, $M = 2.3\,\text{GeV}$ and $\Gamma = 1.8\,\text{GeV}$ for the ω meson.

For both $\gamma N \to \omega N$ and $\gamma N \to \omega\Delta$, the angular dependence is usually modeled as an exponential,

$$\frac{d\sigma}{dt} \propto \exp(Bt) \tag{C.52}$$

While such a very forward peaked distribution gives a good description of the data at large photon energies, the experimental distributions turn out to be flatter at lower photon energies [436]. In [62] a more complicated tree-level model has been developed, which includes s-, t-, and u-channel nucleon diagrams and leads to a good description of ω-photoproduction data at low energies. In the GiBUU code one can switch between the two models.

The more inclusive vector-meson-production channels (beyond $\gamma N \to \omega N$ and $\gamma N \to \omega\Delta$) are described via FRITIOF [370], by assuming strict vector meson dominance (VMD) and converting the incoming photon into a ρ^0.

Appendix D. Numerical realization

This appendix introduces the special algorithms used for the GiBUU model. Appendix D.1 describes the numerical solution of the Vlasov part of the GiBUU-equation (71). Afterwards, in Appendix D.2, the concept of perturbative particles is explained. The way how the test particles are initialized before the propagation is described in Appendix D.3. In Appendix D.4 we give some details connected with the collision term, while in Appendix D.5 the final-state decision algorithm is detailed.

Appendix D.1. Vlasov term: Numerical treatment

The propagation of the test particles including mean fields, i.e., the numerical treatment of the Vlasov equation, is realized in the framework of the test-particle method, see the general eq. (89). In practice, however, the usage of δ functions produces numerical noise which has to be compensated by a large number of test particles per particle. An alternative and standard representation consists in the use of Gaussian-like functions in coordinate space with a width, L. This alternative representation leads to smooth densities and fields, even when using a rather small number of test particles. Furthermore, heavy-ion collisions are usually simulated in the CM-frame of the two colliding nuclei with the z-axis as the beam direction. In order to account for the relativistic contraction of the coordinate space in z-direction, the Gaussian distribution is Lorentz contracted along z and reads

$$\rho_i(\boldsymbol{r}) = \frac{\gamma}{(2\pi)^{3/2}L^3} \exp\left\{-\frac{[x - x_i(t)]^2}{2L^2} - \frac{[y - y_i(t)]^2}{2L^2} - \frac{[z - z_i(t)]^2\gamma^2}{2L^2}\right\} . \tag{D.1}$$

For hadron-induced reactions the simulations are performed in the rest frame of the target (laboratory system). Thus no Lorentz contraction is necessary. To ensure kinetic-energy conservation with an accuracy of better than 3 % for the studied reactions, the Hamilton equations of motion for the test particles are solved by using the $O(\Delta t^2)$ predictor-corrector method. This numerical method consists of two steps. First, one predicts in a one-step propagation the value of the quantity under consideration. This is the predictor step. This value is then corrected in the secondary corrector step. We apply this method to the Hamilton equations for the test particles: at given phase-space coordinates, $\boldsymbol{r}_i$, and momenta, $\boldsymbol{p}_i$, for a test particle with label i ($i = 1, \cdots, A \cdot N$) at time t the predictor step reads

$$\boldsymbol{r}_i{}^P = \boldsymbol{r}_i + \Delta t \frac{\partial H(\boldsymbol{r}_i, \boldsymbol{p}_i)}{\partial \boldsymbol{p}_i}, \tag{D.2}$$

$$\boldsymbol{p}_i{}^P = \boldsymbol{p}_i - \Delta t \frac{\partial H(\boldsymbol{r}_i, \boldsymbol{p}_i)}{\partial \boldsymbol{r}_i}, \tag{D.3}$$

where Δt is the time step. The single-particle Hamilton function is given by eq. (97) or eq. (128) for the non-relativistic or relativistic cases, respectively. The predictor step is performed for all test particles to obtain a predictor value for the phase-space distribution, f. With this f one then calculates the baryon current, $\boldsymbol{j}_i = \boldsymbol{j}(\boldsymbol{r}_i)$, and baryon density, $\rho_i = \rho(\boldsymbol{r}_i)$, needed for the determination of the Hamilton function and its derivatives. The latter quantities are calculated numerically. These values are then used for the corrector step, from which one obtains the phase-space distribution for the next time step,

$$\boldsymbol{r}_i{}^C = \boldsymbol{r}_i + \frac{1}{2}\Delta t \left[\frac{\partial H(\boldsymbol{r}_i, \boldsymbol{p}_i)}{\partial \boldsymbol{p}_i} + \frac{\partial H(\boldsymbol{r}_i{}^P, \boldsymbol{p}_i{}^P)}{\partial \boldsymbol{p}_i{}^P}\right], \tag{D.4}$$

$$\boldsymbol{p}_i{}^C = \boldsymbol{p}_i - \frac{1}{2}\Delta t \left[\frac{\partial H(\boldsymbol{r}_i, \boldsymbol{p}_i)}{\partial \boldsymbol{r}_i} + \frac{\partial H(\boldsymbol{r}_i{}^P, \boldsymbol{p}_i{}^P)}{\partial \boldsymbol{r}_i{}^P}\right]. \tag{D.5}$$

The technical parameters are therefore the size of shells, $\Delta \boldsymbol{r}$, the time step, Δt, and the number of test particles per nucleon, N. The value of the width of the Gaussians in coordinate space is the same as the step in the spatial grid. Note also that along the beam-axis the grid is contracted according to the relativistic γ-factor. These parameters are common to all hadronic processes.

Usually the values $\Delta r = 0.5$ fm and $\Delta t = 0.2$ fm/c are used. The number of test particles per nucleon varies according to the process considered. In heavy-ion collisions one uses $N = 200$, in hadron-induced reactions $N = 1000$, in high-energy photon- and electron-induced reactions $N = 200$, in pion-induced ones $N = 500$, and in neutrino-induced ones from $N = 500$ to $N = 2000$. Note, that the various cases listed above can run in parallel mode, which improves the statistics significantly.

Appendix D.2. Real and perturbative test particles

The test particles mentioned so far can all collide with each other. This is connected with a large computational effort.

However, there may be physics situations in which only very few particles are actively involved in a reaction and the remnant nucleus, involving all the other particles, stays close to its ground state and acts as a background for the propagation of the active particles. This may, e.g. be the case for low-energy πA or γA collisions. In this case the produced particles do not significantly affect the target configuration. This can also happen in heavy-ion collisions when rare events are considered [60]. One example is the production of Λ baryons in NN scattering. This process is so rare that the statistical information on this channel is very scarce in a conventional run. However, one can enforce production of an additional $N\Lambda K$ final state in each NN collision. These particles then are weighted with the production probability, $\sigma_{N\Lambda K}/\sigma_{\text{tot}}$. Thus one achieves large statistics - under the assumption that these rare events do not lead to an overall change of the particle flow which acts as a background to their propagation.

In both cases the active particles can scatter with the remnant without changing it too much. To exploit this situation we introduce two types of test particles The test particles, which represent the background nucleons, are called *real* test particles. For the particles participating actively in a reaction one defines another type of test particles, which are called *perturbative*. These perturbative test particles are only allowed to collide with a real one, but not among themselves. All products of collisions between real and perturbative testparticles are again represented by perturbative test particles thus allowing for a build-up of particle multiplicity. Perturbative particles are neglected in the calculation of the actual densities which are kept constant. For example, in πA collisions one may represent the initial-state pion by perturbative test particles. Thus, the target nucleus is unchanged, and all products of the collisions of the pion with the target nucleons are assigned to the perturbative regime.

Since the perturbative particles do not interact with each other and do not affect the real particles in a reaction one can also split a perturbative particle into n realizations (several perturbative particles) during a run. Each realization is given a corresponding weight, $1/n$. In this way, one simulates n possible final-state scenarios of the same perturbative particle during one run thus improving statistics significantly.

As an additional simplification for electron-, photon- and neutrino-induced reactions one could also freeze the groundstate configuration by not propagating any real testparticles.

Appendix D.3. Preparation of the initial configuration

Before starting the time evolution, the initial configuration of test particles has to be prepared. For different processes we use different, optimized prescriptions.

Appendix D.3.1. Heavy-Ion and hadron-induced (non perturbative) collisions

The initialization of heavy-ion collisions is straightforward in the GiBUU model since these event types cannot use the concept of perturbative test particles. Also $\pi+A$ and $p+A$ reactions can be run, as an option, in this mode. This is necessary when major excitation of the target nucleus, or even its break-up, is to be expected. For the initial configuration in these reactions, real test particles are distributed according to the phase-space distributions of the projectile and the target nucleus. The corresponding particles are separated in space by a given impact parameter in the direction perpendicular to the beam, i.e. in x-direction. In z-direction, the beam axis, the separation is adjusted such, that initially there is no overlap between the two distinct distributions for target and projectile. For the actual time evolution, the initial velocities of the test particles are aligned along the z-axis. Interactions are handled via the collision term in the propagation.

Minimum-bias calculations involving an average over all impact parameters are only possible by performing separate calculations with fixed values of the impact parameter and averaging the output afterwards.

Appendix D.3.2. Hadron-induced collisions (perturbative)

For reactions that can employ the perturbative test particle method one can simulate impact-parameter averages in one single run, since the actual impact does not influence the calculated density distribution.

In this method different weights can be assigned to every test particle. In the first step, for a given fixed impact parameter, every real projectile particle is simulated by $n \sim 25$ test particles (per ensemble), with each one of them being weighted by the factor $1/n$.

For a correct calculation of the total cross section, the test particles have to be initialized in a disc in the transverse plane (displaced by some value in the z-direction, see above) with the radius b_{max}. This value has to be chosen such, that within the geometrical interpretation of the cross section it is given by the spatial extension of the target nucleus plus the cross-section correction factor. Particles outside this radius do not interact with the nucleus.

The integral $\int_0^{b_{\mathrm{max}}} \mathrm{d}b\, b$ implies that most of the particles are placed close to the maximal impact parameter, b_{max}. Due to the density-falloff the interaction rate of these particles is very small. To overcome this problem the individual weighting of test particles is used, which allows for a drastic improvement of the numerics. In order to prevent many test particles passing the nucleus without interaction, we split the initial disc into an inner disk ($b < b_d$) and an outer ring ($b_d < b < b_{\mathrm{max}}$). In a first Monte Carlo choice, a test particle is assigned to the inner disc with probability $p_d \sim 0.7$, otherwise it is part of the outer ring. Then the impact parameter is chosen according to $\mathrm{d}b\, b$ between 0 and b_d or between b_d and b_{max}, respectively. The weight for every test particle is given by

$$w_i = \frac{1}{n} \begin{cases} \frac{\pi b_d^2}{p_d} & \text{for inner disk ,} \\ \frac{\pi (b_{\mathrm{max}}^2 - b_d^2)}{1 - p_d} & \text{for outer ring .} \end{cases} \tag{D.6}$$

Interactions are handled via the collision term in the usual propagation steps.

As an optional additional optimization, an abbreviation of the propagation of the projectile cloud onto the target nucleus is implemented. This is possible by first sorting the test particles of the target nucleus according to their z-coordinate. Then for every projectile test particle, an interaction on every target test particle is probed and the loop is stopped, when the collision rate suggests an interaction to happen. The projectile test particle is taken out of the particle vector and replaced by the final-state particles of this interaction. This optimization also allows for

testing some modified physics: In the case of very high energy proton-induced collisions, hard probes do not scale with $A^{2/3}$, but instead with A^1. This can be simulated by not quitting the loop over the target test particles after an interaction, but just continuing. This implies, that one projectile test particle may interact with more than one target test particle.

Appendix D.3.3. Lepton-induced collisions (perturbative)

In the case of collisions, induced by particles which are not directly propagated in the GiBUU model, as, e.g., electrons, photons, or neutrinos, initializations as described above are not possible. Instead, the incoming lepton is split into A test particles in every ensemble. Now every test particle interacts with one of the target test particles and produces some final state of particles, which now may be propagated by the GiBUU model. Only these test particles are inserted into the particle vector.

Since the final state at the leptonic vertex is not determined by the input variables, the weight assigned to every particle is given by $d\sigma/dE'\, d\Omega_k$. For photon-induced reactions, one may also divide this weight by the flux f_T, thus the weight is given by σ_{γ^*}. These details have to be respected in the corresponding analysis routines.

Appendix D.4. Collision term

Appendix D.4.1. Ensemble Techniques

To point out the connection between our numerical implementation and the underlying BUU equation, we focus on the loss term of BUU. We will not elaborate on the gain term, I_{gain}, which describes the production of particles. However, its numerical implementation is analogous to the loss term since both are related by detailed balance.

As shown in [138], in terms of the test-particle ansatz eq. (89) the loss term eq. (187) reads

$$
\Delta t\, C_{\text{loss}}(\boldsymbol{r}, t, \boldsymbol{p}_A) = \lim_{N\to\infty} \frac{(2\pi)^4}{gN} \sum_{i=1}^{n(t)} \sum_{\substack{j=1 \\ j\neq i}}^{n(t)} \delta(p_A^0 - p_i^0)\delta(\boldsymbol{p}_A - \boldsymbol{p}_i)\delta(\boldsymbol{r} - \boldsymbol{r}_i)
$$

$$
\times \lim_{N\to\infty} \frac{1}{\sigma_{ij}} \int d\Omega_{\text{CM}}\, \mathcal{P}_a \mathcal{P}_b \frac{d\sigma_{ij\to ab}}{d\Omega_{\text{CM}}} \sigma_{ij} \Delta t\, v_{ij} \frac{1}{N} \delta(\boldsymbol{r} - \boldsymbol{r}_j) \tag{D.7}
$$

$$
= \lim_{N\to\infty} \frac{(2\pi)^4}{gN} \sum_{i=1}^{n(t)} \sum_{\substack{j=1 \\ j\neq i}}^{n(t)} \delta(p_A - p_i)\delta(\boldsymbol{r} - \boldsymbol{r}_i)\overline{\mathcal{P}_a \mathcal{P}_b} \int_{\Delta V_{ij}} \delta(\boldsymbol{r}\,' - \boldsymbol{r}_j) d^3 r',
$$

where σ_{ij} and v_{ij} are the total interaction cross section and the relative velocities of the test particles, i, j, and $\mathcal{P}_{a,b}$ are the usual Pauli blocking factors for particles a and b. The volume, $\Delta V_{ij} = \sigma_{ij}\Delta t\, v_{ij}/N$, is an infinitesimal volume in the vicinity of $\boldsymbol{r}_i$ and defines the locality of the scattering process of two test particles. The term,

$$
\overline{\mathcal{P}_a \mathcal{P}_b} = \frac{1}{\sigma_{ij}} \int d\Omega_{\text{CM}}\, \mathcal{P}_a \mathcal{P}_b \frac{d\sigma_{ij\to ab}}{d\Omega_{\text{CM}}}, \tag{D.8}
$$

denotes the blocking of the final state averaged over its angular distribution. We have excluded self interactions – therefore a test particle cannot scatter with itself.

The time step, Δt, is chosen such that the average distance traveled by the particles during Δt is less than their mean free path. Therefore, ΔV_{ij} is so small that a particle has no more than one scattering partner at a given time step.

157

The kind of simulation for the two-body processes, which we have described above, is called a *full-ensemble calculation*. There exists a common simplification to this method: *the parallel-ensemble method* [90]. In this scheme, one performs $\tilde{N}$ calculations in parallel, each of which includes only one single ensemble ($N = 1$). The densities used in each parallel run are the averaged densities of all $\tilde{N}$ parallel runs. Therefore the propagation part basically stays the same, whereas the collision term gets very much simplified.

Note that the only justification for this simplification is a great gain in computation time. In the full-ensemble method, the propagation part scales according to the number of test particles per nucleon, N, whereas the two-body collision term scales with N^2 – therefore the computation time is $O(N^2)$. In the parallel-ensemble method $\tilde{N}$ runs are performed, which results in $O(\tilde{N})$ computation time. Thus there is a linear scaling in a parallel-ensemble run, but a quadratic one in a full-ensemble run.

The major drawback of the parallel-ensemble scheme is the non-locality of the collisions. As a showcase, let us consider the pion-nucleon interaction. There the maximum cross section amounts to roughly 200 mb. This leads to a maximal impact parameter of two test particles of $\sqrt{200\,\text{mb}/\pi} \simeq 2.52$ fm. Hence, the parallel-ensemble scheme may lead to large non-localities whereas the underlying BUU collision term is strictly local.

In pioneering works it has been shown by Welke *et al.* [439] and Lang *et al.* [440], that the parallel-ensemble scheme is a good approximation to the full-ensemble scheme under the conditions of high-energy heavy-ion collisions. However, it is still an open question, whether this also applies to more surface sensitive processes such as, e.g., pion double-charge exchange in nuclei. We will discuss this problem together with our numerical results.

The so-called *local-ensemble method*, which has been first applied to heavy-ion collisions by Lang *et al.* [440], is a method allowing for a full-ensemble run which is less time consuming than the standard algorithm. Here one divides position space into small cubical boxes, V_i, with equal volumes, ΔV. The loss term is then represented by

$$\Delta t\, C_{\text{loss}}(\boldsymbol{r}, t, \boldsymbol{p_A}) = \lim_{N \to \infty} \frac{(2\pi)^4}{gN} \sum_{i=1}^{n(t)} \sum_{\substack{j=1 \\ j \neq i}}^{n(t)} \delta(p_A - p_i)\delta(\boldsymbol{r} - \boldsymbol{r}_i)$$

$$\times \overline{\mathcal{P}_a\mathcal{P}_b}\Delta V_{ij}\frac{1}{\Delta V} \int_{V_A} \text{d}^3\boldsymbol{r}'\delta(\boldsymbol{r}' - \boldsymbol{r}_j), \tag{D.9}$$

where V_A is the box in which the particle A is situated. Now the whole expression $\overline{\mathcal{P}_a\mathcal{P}_b}\Delta V_{ij}/\Delta V$ is interpreted as the probability that an interaction takes place. If there are n test articles within one box, then there are $n(n-1)/2$ possible scattering events. One now chooses randomly only $n/2$ collision pairs out of the possible pairs. To conserve the overall reaction rate one has to rescale the collision probability by the factor

$$\frac{\text{number of possible collisions}}{\text{number of collisions}} = \frac{n(n-1)/2}{n/2}. \tag{D.10}$$

Finally, we obtain the probability that a chosen collision takes place as

$$P = \frac{n(n-1)/2}{n/2}\overline{\mathcal{P}_a\mathcal{P}_b}\Delta V_{ij}\frac{1}{\Delta V}. \tag{D.11}$$

This method is faster than the original full-ensemble method, since one can effectively order all test particles into the cells before one simulates the collision term. Afterwards only such test

particles need to be correlated/compared which are within one cell. In the limit of $\Delta V \to 0$ and $N \to \infty$ this corresponds to a full-ensemble calculation. The only drawback is that one has to adjust beforehand the parameters ΔV and Δt such, that $P \leq 1$ for all boxes. Therefore, one has to roughly estimate the mean value of n by the nuclear matter density ($\bar{n} \approx \rho \Delta V N$) and the cross section by some meaningful average value. Larger numbers of N lead to better estimates of n, while low N can lead to huge fluctuations in n. Typical volumes for $N \approx$ 300-1500 are[26] $\Delta V = (0.25\text{-}1.0\,\text{fm})^3$.

We have implemented all three algorithms (parallel-, full-, and local-ensemble method) within our model. The influence on the results is shown, e.g., in section 4.1.1 for the pionic double-charge exchange in πA scattering.

Appendix D.4.2. Determination of in-medium cross sections

In section 3.3.4 we have discussed the problem that arises when using free vacuum cross sections for collisions, where the colliding particles are inside the nuclear medium and experience potentials. There we have given three prescriptions for converting the actual invariant energy, $s^* = (p_1^* + p_2^*)^2$, into a free value at which the free cross section is read off. We recall, that $p_{1,2}^*$ are the kinetic four-momenta of colliding particles. For the calculations with nonrelativistic potentials, the kinetic and canonical four-momenta are the same, $p^* = p$. However, in the RMF-mode calculations, they differ by the vector field (cf. eq. (138)).

All the existing codes, in particular those for heavy-ion reactions, use a recipe how to achieve this, but this is never spelled out, nor justified. Since the possible prescriptions used contain some degree of arbitrariness which may affect the physics result, we discuss this point here in some more detail.

In order to illustrate the different ways of the calculation of the "free" invariant energy, let us consider the simple case of a momentum-independent scalar field acting on nucleons. This leads to

$$E = \sqrt{m_N^{*\,2} + \boldsymbol{p}^2} \tag{D.12}$$

for the dispersion relation for the nucleon.

As two representative examples, we will discuss NN and γN collisions. The total invariant in-medium c.m. energy squared is calculated as

$$s^* = \begin{cases} \left(\sqrt{m_N^{*\,2} + p_{\text{lab}}^2} + m_N^* \right)^2 - p_{\text{lab}}^2 & \text{for NN collision,} \\ (p_{\text{lab}} + m_N^*)^2 - p_{\text{lab}}^2 & \text{for } \gamma\text{N collision .} \end{cases} \tag{D.13}$$

Applying eq. (189) in the laboratory frame results in

$$s_{\text{free}}\big|_{\text{lab}} = \begin{cases} \left(\sqrt{m_N^2 + p_{\text{lab}}^2} + m_N \right)^2 - p_{\text{lab}}^2 & \text{for NN collision,} \\ (p_{\text{lab}} + m_N)^2 - p_{\text{lab}}^2 & \text{for } \gamma\text{N collision .} \end{cases} \tag{D.14}$$

Now, if one uses the same relation eq. (189) in the c.m. frame of the colliding particles, one obtains

$$\sqrt{s_{\text{free}}}\big|_{\text{cm}} = \begin{cases} 2\sqrt{q^2 + m_N^2} & \text{for NN collision,} \\ q + \sqrt{q^2 + m_N^2} & \text{for } \gamma\text{N collision ,} \end{cases} \tag{D.15}$$

---

[26]The default in our code is chosen to be $(0.5\,\text{fm})^3$. If events occur with $P > 1$, then the calculation must be repeated with a smaller time-step size, Δt.
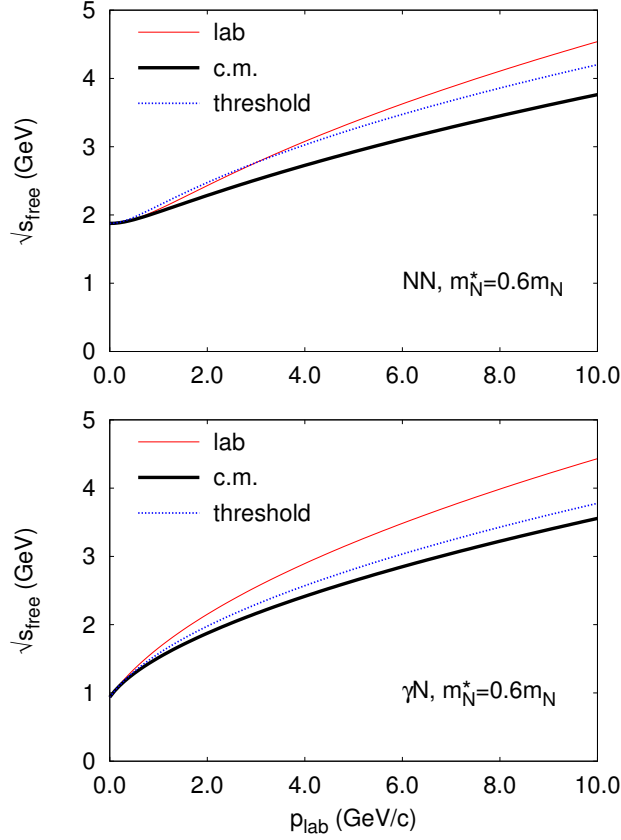
Figure D.69: (Color online) The "free" invariant energy calculated from eq. (189) in the laboratory (cf. eq. (D.14)) and c.m. (cf. eq. (D.15)) frames as well as from eq. (191) as a function of the laboratory momentum for NN (upper panel) and γN (lower panel) collisions. The nucleon effective mass is chosen as $m_N^* = 0.6m_N$ corresponding to the nuclear matter at the saturation density. See text for details.

where $q = \sqrt{s^*/4 - m_N^{*\,2}}$ and $q = (s^* - m_N^{*\,2})/2\sqrt{s^*}$ are the c.m. momenta of the colliding particles for NN and γN collisions, respectively. Finally, using the relation eq. (191), we obtain

$$\sqrt{s_{\text{free}}}\,\Big|_{\text{threshold}} = \begin{cases} \sqrt{s^*} - 2(m_N^* - m_N) & \text{for NN collision,} \\ \sqrt{s^*} - (m_N^* - m_N) & \text{for } \gamma\text{N collision .} \end{cases} \tag{D.16}$$

Figure D.69 shows the laboratory momentum dependence of $\sqrt{s_{\text{free}}}$ calculated by the different recipes explained above. One sees that the difference between various prescriptions grows with beam momentum reaching $\sim 20\%$ at $10\,\text{GeV}/c$.

In the RMF mode, the "free" invariant energy is always calculated by using eq. (191). The latter respects the in-medium particle production thresholds, as we show below. Let us assume, for simplicity, that the sum of vector fields is the same for initial and final particles, i.e., $V_1 + V_2 = \sum_{i=1'}^{N'} V_i$. Then, the difference of the canonical four-momenta which appears in the energy-momentum conserving δ-function of eq. (188) can be replaced by the difference of the kinetic

160

four-momenta, and, therefore,

$$d\sigma^*_{12\to 1'2'\dots N'} \propto d\Phi_N(p_1^* + p_2^*; p_{1'}^*, p_{2'}^*, \dots, p_{N'}^*),\tag{D.17}$$

where we have assumed that the outgoing particles are on their (Dirac) mass shells, $p_i^{*2} = m_i^{*2}$, $i = 1', \dots, N'$, and the N-body phase-space-volume element is defined according to Ref. [129] as

$$d\Phi_N(\mathcal{P}; p_1, p_2, \dots, p_N) = \delta^{(4)}(\mathcal{P} - p_1 - p_2 - \cdots - p_N)$$
$$\times \frac{d^3 p_1}{(2\pi)^3 2 p_1^0} \frac{d^3 p_2}{(2\pi)^3 2 p_2^0} \cdots \frac{d^3 p_N}{(2\pi)^3 2 p_N^0}.\tag{D.18}$$

The in-medium threshold condition follows immediately from eq. (D.17),

$$Q^* > 0,\tag{D.19}$$

with $Q^* = \sqrt{s^*} - \sum_{i=1'}^{N'} m_i^*$ being the in-medium excess energy and $s^* = (p_1^* + p_2^*)^2$. Defining now the "free" invariant energy as

$$\sqrt{s_{\text{free}}} = Q^* + \sum_{i=1'}^{N'} m_i = \sqrt{s^*} - \sum_{i=1'}^{N'} (m_i^* - m_i)\tag{D.20}$$

leads to the evaluation of the vacuum cross section at the in-medium excess energy, which obviously respects the true in-medium threshold condition eq. (D.19). Unfortunately, the definition eq. (D.20) is channel dependent and is hard to apply in practice. In most cases, the final-state particles are not known until the actual simulation of a given two-body collision is done. Thus, we further assume that the sum of scalar fields is the same for initial and final particles, i.e., $S_1 + S_2 = \sum_{i=1'}^{N'} S_i$, which allows us to rewrite eq. (D.20) as

$$\sqrt{s_{\text{free}}} = \sqrt{s^*} - (m_1^* - m_1) - (m_2^* - m_2).\tag{D.21}$$

We recall here the definition of the Dirac effective mass according to eq. (139). The expression (D.21) is used in the RMF-mode calculations. In the present RMF implementation, the conditions $V_1 + V_2 = \sum_{i=1'}^{N'} V_i$ and $S_1 + S_2 = \sum_{i=1'}^{N'} S_i$ used in the derivation of eq. (D.21) are fulfilled, since the coupling constants of all baryons with the meson fields are chosen equal to the nucleon-meson coupling constants, while the mean-field potentials acting on mesons are neglected. The only exception is the baryon-antibaryon annihilation into mesons (see section 4.1.3).

Appendix D.4.3. Pauli blocking

The phase-space distribution, $f_i(\mathbf{r}, \mathbf{p})$, which enters in the Pauli blocking factor, $1 - f_i(\mathbf{r}, \mathbf{p})$, is calculated by counting the number of test particles in the phase-space volume element composed of small spherical volumes ΔV_r with radius r_r centered at $\mathbf{r}$ in coordinate space and ΔV_p with radius r_p centered at $\mathbf{p}$ in momentum space,

$$f_i(\mathbf{r}, \mathbf{p}) = \sum_{j:\, \mathbf{p}_j \in \Delta V_p} \frac{1}{\kappa (2\pi\sigma^2)^{3/2}} \int_{\Delta V_r, |\mathbf{r}-\mathbf{r}_j|<r_c} d^3 r \, \exp\left\{-\frac{(\mathbf{r}-\mathbf{r}_j)^2}{2\sigma^2}\right\},\tag{D.22}$$

where

$$\kappa = \frac{2\,\Delta V_r\,\Delta V_p\,N}{(2\pi)^3}\,\frac{4\pi}{(2\pi\sigma^2)^{3/2}}\int\limits_0^{r_c}\mathrm{d}r\,r^2\exp\left\{-\frac{r^2}{2\sigma^2}\right\}\tag{D.23}$$

is a normalization factor. In eq. (D.22), the sum is taken over all test particles, j, of the type $i = p, n$ whose momenta belong to the volume ΔV_p. In coordinate space, the test particles are represented by Gaussians of the width, σ, cut off at the radial distance r_c, in a similar way as done for the folding of the density fields with Gaussians, see Appendix D.1. The default values of parameters are $r_p = 80\,\mathrm{MeV}/c$, $r_r = 1.86\,\mathrm{fm}$, $\sigma = 1\,\mathrm{fm}$, $r_c = 2.2\,\mathrm{fm}$. This set of parameters is a compromise between the quality of the Pauli blocking in the ground state and the smallness of statistical fluctuations in the case of simulations with $N \sim 200$ test particles per nucleon. Typically, this is sufficient in accuracy for modeling heavy-ion collisions at beam energies above $\sim 100\,A\mathrm{MeV}$.

However, for small-amplitude dynamics near the nuclear ground state, like the giant monopole resonance vibrations studied in Ref. [86], the accuracy provided by eqs. (D.22) and (D.23) is not sufficient, when the default parameters are used. The main reason is the constant, i.e., momentum-independent radius, r_p, which introduces a spurious temperature of the order of several MeV. To reduce this effect, we have introduced a position- and momentum-dependent radius of the momentum-space volume ΔV_p by $r_p(\mathbf{r}, |\mathbf{p}|) = \max[20\,\mathrm{MeV}/c, p_{F,i}(\mathbf{r}) - |\mathbf{p}|]$, which provides a sharper Fermi surface. This allows us to use the reduced parameters also in coordinate space, $r_r = 0.9 - 1.86\,\mathrm{fm}$, $\sigma = 0.5\,\mathrm{fm}$, $r_c = 1.1\,\mathrm{fm}$.

Appendix D.5. Final-state decisions for hadron-hadron scattering events

The final-state decision is straight forward in the case of resonance production. If there are two or three particles in the final state, the treatment is more involved. First, in Appendix D.5.1–Appendix D.5.3, we discuss the treatment in the vacuum. Then the medium corrections are discussed.

Appendix D.5.1. Resonance production

In the case of resonance production we obtain the final mass of the resonance by eqs. (205) and (206), which completely fixes the kinematics.

Appendix D.5.2. Two-body final states : $X \to cd$ in the vacuum

The general definition of the cross section for $2 \to n$ reactions is given by (see, e.g., [129])

$$\mathrm{d}\sigma_{a\,b\to f_1,f_2,f_3,\ldots,f_n} = \mathrm{d}\Phi_n\,(2\pi)^4\,\mathcal{S}_{\mathrm{final}}\frac{|\mathcal{M}_{ab\to f_1,\ldots,f_n}|^2}{4I_{ab}},\tag{D.24}$$

where $\mathrm{d}\Phi_n$ denotes the n-particle phase space of the final-state particles,

$$\mathrm{d}\Phi_n = \delta^{(4)}\left(p_a + p_b - \sum_{i=1}^{n} p_{f_i}\right)\prod_{i=1}^{n}\frac{\mathrm{d}^3\mathbf{p}_i}{(2\pi)^3 2E_i},\tag{D.25}$$

$\mathcal{S}_{\mathrm{final}}$ stands for the symmetry factor of the final state, and

$$I_{ab} = \sqrt{(p_a \cdot p_b)^2 - m_a^2 m_b^2}\tag{D.26}$$

represents the invariant flux factor of the particles, a and b. In the center-mass (CM) frame this flux factor reads

$$I_{ab} = p_{\text{cm}} \sqrt{s}, \tag{D.27}$$

with the CM momentum, p_{CM}, of the particles, a and b. It can be shown (see, e.g., [61, cf. especially Section 4.7] [27]), that one can express the cross section for the production of unstable particles c and d in the final state by

$$\frac{\mathrm{d}\sigma_{ab\to cd}}{\mathrm{d}\mu_c\,\mathrm{d}\mu_d\,\mathrm{d}\Omega}(s) = \frac{1}{64\pi^2}\frac{p_{cd}}{s}\frac{1}{p_{ab}}2\mu_c\mathcal{A}_c(\mu_c, p_c(\mu_c,\Omega))2\mu_d\mathcal{A}_d(\mu_d, p_d(\mu_d,\Omega))\,|\mathcal{M}_{ab\to cd}(s)|^2, \tag{D.28}$$

with p_{ab} and p_{cd} denoting the CM momenta of the $a\,b$ and the $c\,d$-system, respectively. Equations (B.6) and (B.10) are specializations of this expression. Here, one has to assume that the matrix element depends on s only. In the vacuum the spectral functions depend on the squares, $\mu^2 = p^\nu p_\nu$, only, while in the medium, in general, they are functions of the four momenta.

We want to use a Monte-Carlo method to choose the final state. In eq. (D.28), we note that the two-particle final state depends both on the masses of the outgoing particles and their directions of motion. The Mandelstam variable, s, and p_{ab} are determined by the initial state. Thus we choose the masses, μ_c and μ_d, at the same time as we choose the angles, Ω.

The transformed random number, y,

$$y(\mu) = 2\arctan\left[2\frac{\mu - M^0}{\Gamma^0}\right], \qquad , \qquad \mathrm{d}y = \mathrm{d}\mu\frac{\Gamma_0}{(\mu - M^0)^2 + \left(\frac{\Gamma_0}{2}\right)^2} \tag{D.29}$$

is distributed according to a Cauchy-Lorentz distribution, which leads to the the function,

$$\frac{\mathrm{d}\sigma_{ab\to cd}}{\mathrm{d}y_c\,\mathrm{d}y_d\,\mathrm{d}\Omega}(s) \propto \frac{1}{s}\frac{p_{cd}}{p_{ab}}\frac{\mu_c\mathcal{A}_c(\mu_c, p_c(\mu_c,\Omega))}{\frac{dy_c}{d\mu_c}}\frac{\mu_d\mathcal{A}_d(\mu_d, p_d(\mu_d,\Omega))}{\frac{dy_d}{d\mu_d}}\,|\mathcal{M}_{ab\to cd}(s)|^2, \tag{D.30}$$

smoother than the original function eq. (D.28), which is advantageous for the application of a rejection method. For $y_{c,d}$ one has to insert the values at the pole position in the vacuum $M^0_{c,d}$ and $\Gamma^0_{c,d}$ of particle c and d.

For the rejection procedure, we choose y_c, y_d, and Ω according to a flat distribution. The probability that a random ensemble, (y_c, y_d, Ω), will be accepted is then given by

$$P_{\text{accept}}(y_c, y_d, \Omega) = \frac{p_{cd}\mu_c\mathcal{A}_c(\mu_c, p_c(\mu_c,\Omega))\mu_d\mathcal{A}_d(\mu_d, p_d(\mu_d,\Omega))\frac{\mathrm{d}\mu_c}{\mathrm{d}y_c}\frac{\mathrm{d}\mu_d}{\mathrm{d}y_d}}{\left(p_{cd}\mu_c\mathcal{A}_c\mu_d\mathcal{A}_d\frac{\mathrm{d}\mu_c}{\mathrm{d}y_c}\frac{\mathrm{d}\mu_d}{\mathrm{d}y_d}\right)_{\max}}. \tag{D.31}$$

The maximal value in the denominator is actually hard to find. We parameterize it by

$$\left(p_{cd}\mu_c\mathcal{A}_c\mu_d\mathcal{A}_d\frac{\mathrm{d}\mu_c}{\mathrm{d}y_c}\frac{\mathrm{d}\mu_d}{\mathrm{d}y_d}\right)_{\max} = Q_{cd}\max\{p_{cd}^{\text{vac}}\}. \tag{D.32}$$

The dimensionless factor, Q, is of the order of 10 and depends on the outgoing particles. It has to be readjusted if one introduces medium effects.[28]

---

[27] Note that [61] uses a slightly different convention for the spectral function which differs by a factor $2m$ from the one used in this work.

[28] Recently, we started to implement a method of additionally slicing the mass range into smaller regions, where one optimizes the rejection method. In addition, the maximal values are then precalculated.

Appendix D.5.3. Three body final states : $X \rightarrow cde$ in the vacuum

For a three-particle final state one obtains in analogy to eq. (D.28) the complicated structure,

$$\frac{d\sigma_{ab \rightarrow cde}}{d\mu_c \, d\mu_d \, d\mu_e \, d|\boldsymbol{p}_c| \, d\Omega_c \, d|\boldsymbol{p}_d| \, d\phi_d}(s) = \frac{1}{8 \, (2\pi)^5} \frac{1}{p_{ab} \sqrt{s}} \frac{|\boldsymbol{p}_c| \, |\boldsymbol{p}_d|}{E_c E_d} 2\mu_c \mathcal{A}_c(\mu_c, p_c)$$
$$\times 2\mu_d \mathcal{A}_d(\mu_d, p_d) 2\mu_e \mathcal{A}_e(\mu_e, p_e) |\mathcal{M}_{ab \rightarrow cde}(s)|^2 \ . \tag{D.33}$$

Here, $\boldsymbol{p}_{c,d}$ denote the CM momenta of the particles, c and d. The CM momentum of e is given by total momentum conservation,

$$\boldsymbol{p}_c + \boldsymbol{p}_d + \boldsymbol{p}_e = 0. \tag{D.34}$$

In analogy to the two-particle final state, we apply the variable transformation eq. (D.29) to eq. (D.33) and obtain

$$\frac{d\sigma_{ab \rightarrow cde}}{dy_c \, dy_d \, dy_e \, d|\boldsymbol{p}_c| \, d\Omega_c \, d|\boldsymbol{p}_d| \, d\phi_d}(s) \propto \frac{1}{p_{ab} \sqrt{s}} \frac{|\boldsymbol{p}_c| \, |\boldsymbol{p}_d|}{E_c E_d} \mu_c \mathcal{A}_c(y_c, p_c) \mu_d \mathcal{A}_d(y_d, p_d)$$
$$\times \mu_e \mathcal{A}_e(y_e, p_e) |\mathcal{M}_{ab \rightarrow cde}(s)|^2 \frac{d\mu_c}{dy_c} \frac{d\mu_d}{dy_d} \frac{d\mu_e}{dy_e}. \tag{D.35}$$

Hence, we need to choose y_c, y_d, y_e, $|\boldsymbol{p}_c|$, Ω_c, ϕ_d, and $|\boldsymbol{p}_d|$ independently of each other. The limits for the y_i are given by the smallest and largest possible masses. The absolute values of the momenta, $|\boldsymbol{p}_i|$, are limited by energy conservation, $|\boldsymbol{p}_i| < \sqrt{s}$. The value of Ω_c is determined by choosing a random $\cos\theta \in [-1, 1]$ and $\phi \in [0, 2\pi]$.

The Monte Carlo probability to accept an event configuration is given by

$$p_{\text{accept}} = \frac{\mu_c \mu_d \mu_e \frac{|\boldsymbol{p}_c| |\boldsymbol{p}_d|}{E_c E_d} \mathcal{A}_c(y_c, p_c) \mathcal{A}_d(y_d, p_d) \mathcal{A}_e(y_e, p_e) \frac{d\mu_c}{dy_c} \frac{d\mu_d}{dy_d} \frac{d\mu_e}{dy_e}}{m}, \tag{D.36}$$

where the factor m in the denominator is chosen such, that it is larger than the maximum of the numerator.

Appendix D.5.4. Medium Corrections

In the medium we have more complicated dispersion relations. Therefore also the phase-space factors differ from the ones used above. Already in [60] possibilities to implement the right phase-space factors for ΔN and NN scattering have been discussed. Our treatment does not include such modifications, but preserves the energy in the medium for all collisions. We use the following algorithm:

1. Evaluate s_{vacuum}.
2. Do the final-state decision with vacuum kinematics assuming $s = s_{\text{vacuum}}$.
3. Correct the final state by scaling the final-state momenta by a factor, x, in the CM frame.

The last point needs special discussion. In the CM frame, energy and momentum conservation in step 2 result in a solution for the momenta $\boldsymbol{p}_i$, which obeys

$$\sum_i \sqrt{\left(p_i^{\text{CM}}\right)^2 + (m_i)^2} = \sqrt{s_{\text{vacuum}}} \quad , \qquad \sum_i \boldsymbol{p}_i^{\text{CM}} = 0. \tag{D.37}$$

Now we want to define the four momenta, q_i, in the medium. Momentum and energy conservation demand

$$\sum_i q_i^0(\boldsymbol{q}_i) = \sqrt{s} \qquad , \qquad \sum_i \boldsymbol{q}_i = 0. \tag{D.38}$$

The zeroth components of q_i are, due to the potentials, highly non-trivial functions of the vector components, $\boldsymbol{q}_i$. Hence we use the following recipe: Using the vacuum result for $\boldsymbol{p}_i$ we choose

$$\forall i: \quad \boldsymbol{q}_i = x\boldsymbol{p}_i, \tag{D.39}$$

where the scaling factor, x, is fixed by eq. (D.38). Since all momenta are scaled by the same factor, momentum conservation is fulfilled trivially.

Appendix D.6. Coding

The numerical implementation of the GiBUU model is based on Fortran2003 using modern programming paradigms and a version control management (Subversion). See the GiBUU website [23] and Section 3.1 and Appendix C in the dissertation of O. Buss [55] for detailed information on the current code structure and its programming history. The code runs and has been tested with numerous compilers on different platforms, details are given on our website [23]. At this website, one also finds information about program options and a documentation of the parameters. The GiBUU code is open source under the GPL license [441] and can be downloaded after registration [23].

References

[1] R. Serber, Phys. Rev. 72 (1947) 1114–1115.
[2] N. Metropolis, R. Bivins, M. Storm, J. Miller, G. Friedlander, et al., Phys. Rev. 110 (1958) 204–219.
[3] H. W. Bertini, Phys. Rev. 131 (1963) 1801–1821.
[4] J. Cugnon, Phys. Rev. C 22 (1980) 1885–1896.
[5] P. Carruthers, F. Zachariasen, Rev.Mod.Phys. 55 (1983) 245.
[6] G. Bertsch, H. Kruse, S. Gupta, Phys. Rev. C 29 (1984) 673–675.
[7] H. Stöcker, W. Greiner, Phys. Rept. 137 (1986) 277–392.
[8] W. Bauer, G. Bertsch, W. Cassing, U. Mosel, Phys. Rev. C 34 (1986) 2127–2133.
[9] G. Bertsch, S. Das Gupta, Phys.Rept. 160 (1988) 189–233.
[10] P. Danielewicz, G. Bertsch, Nucl. Phys. A 533 (1991) 712–748.
[11] W. Cassing, V. Metag, U. Mosel, K. Niita, Phys. Rept. 188 (1990) 363–449.
[12] S. Teis, W. Cassing, M. Effenberger, A. Hombach, U. Mosel, G. Wolf, Z. Phys. A 356 (1997) 421–435.
[13] J. Aichelin, Phys. Rept. 202 (1991) 233–360.
[14] C. Hartnack, et al., Eur. Phys. J. A 1 (1998) 151–169.
[15] Q. Li, J. Wu, C. Ko, Phys. Rev. C 39 (1989) 849–852.
[16] B. Blaettel, V. Koch, U. Mosel, Rept. Prog. Phys. 56 (1993) 1–62.
[17] S. Bass, M. Belkacem, M. Bleicher, M. Brandstetter, L. Bravina, et al., Prog.Part.Nucl.Phys. 41 (1998) 255–369.
[18] E. Santini, M. Cozma, A. Faessler, C. Fuchs, M. Krivoruchenko, et al., Phys. Rev. C 78 (2008) 034910.
[19] W. Ehehalt, W. Cassing, Nucl. Phys. A 602 (1996) 449–486.
[20] E. Kolomeitsev, C. Hartnack, H. Barz, M. Bleicher, E. Bratkovskaya, et al., J. Phys. G 31 (2005) S741–S758.
[21] L. L. Salcedo, E. Oset, M. J. Vicente Vacas, C. Garcia-Recio, Nucl. Phys. A 484 (1988) 557.
[22] A. Hombach, A. Engel, S. Teis, U. Mosel, Z. Phys. A 352 (1995) 223–230.
[23] GiBUU website, 2011. http://gibuu.physik.uni-giessen.de/GiBUU/.
[24] L. Kadanoff, G. Baym, Quantum Statistical Mechanics, Addison Wesley Publishing Company, 1994.
[25] W. Botermans, R. Malfliet, Phys. Rept. 198 (1990) 115–194.
[26] J. S. Schwinger, J. Math. Phys. 2 (1961) 407–432.
[27] L. V. Keldysh, Zh. Eksp. Teor. Fiz. 47 (1964) 1515–1527.

[28] E. Calzetta, B. L. Hu, Phys. Rev. D 37 (1988) 2878.
[29] E. A. Calzetta, B. L. Hu, Nonequilibrium Quantum Field Theory, Cambridge University Press, Cambridge, New York, Melbourne, Madrid, Cape Town, Singapore, Sao Paulo, Delhi, 2008.
[30] E. Lifshitz, L. Pitaevskii, Physical Kinetics, Pergamon, New York, 1981.
[31] P. Danielewicz, Ann. Phys. 152 (1984) 239–304.
[32] B. D. Serot, J. D. Walecka, Int. J. Mod. Phys. E 6 (1997) 515–631.
[33] C. J. Horowitz, B. D. Serot, Nucl. Phys. A464 (1987) 613.
[34] W. Cassing, S. Juchem, Nucl. Phys. A 665 (2000) 377–400.
[35] J. M. Luttinger, J. C. Ward, Phys. Rev. 118 (1960) 1417–1427.
[36] G. Baym, Phys. Rev. 127 (1962) 1391–1401.
[37] Y. B. Ivanov, J. Knoll, D. N. Voskresensky, Nucl. Phys. A 657 (1999) 413–445.
[38] Y. B. Ivanov, J. Knoll, D. N. Voskresensky, Nucl. Phys. A 672 (2000) 313–356.
[39] J. Knoll, Y. B. Ivanov, D. N. Voskresensky, Annals Phys. 293 (2001) 126–146.
[40] Y. B. Ivanov, J. Knoll, D. N. Voskresensky, Phys. Atom. Nucl. 66 (2003) 1902–1920.
[41] S. Leupold, Nucl. Phys. A 672 (2000) 475–500.
[42] W. Cassing, Eur. Phys. J. ST 168 (2009) 3–87.
[43] J. Berges, S. Borsanyi, Phys. Rev. D 74 (2006) 045022.
[44] S. Juchem, Nonequilibrium Quantum-Field Dynamics and Off-Shell Transport, Ph.D. thesis, JLU Giessen, 2003.
[45] J. M. Cornwall, R. Jackiw, E. Tomboulis, Phys. Rev. D 10 (1974) 2428–2445.
[46] H. van Hees, J. Knoll, Phys. Rev. D 66 (2002) 025028.
[47] A. Arrizabalaga, J. Smit, Phys. Rev. D 66 (2002) 065014.
[48] S. R. de Groot, W. A. van Leeuwen, C. G. van Weert, Relativistic kinetic theory: principles and applications, North-Holland Publ. Comp., Amsterdam, New York, Oxford, 1980.
[49] C. Greiner, K. Wagner, P. G. Reinhard, Phys. Rev. C 49 (1994) 1693–1701.
[50] S. Mrowczynski, P. Danielewicz, Nucl. Phys. B 342 (1990) 345–380.
[51] J. D. Bjorken, S. D. Drell, Relativistische Quantenmechanik, Bibliographisches Institut, Mannheim, 1967.
[52] G. Mao, L. Neise, H. Stoecker, W. Greiner, Phys. Rev. C 59 (1999) 1674–1699.
[53] C. Fuchs, A. Faessler, M. El-Shabshiry, Phys. Rev. C 64 (2001) 024003.
[54] K. Hagiwara, et al., Phys. Rev. D 66 (2002) 010001.
[55] O. Buss, Photon- and pion-induced nuclear reactions in a transport approach, Ph.D. thesis, Justus-Liebig-Universität Gießen, 2008. Available online at `http://theorie.physik.uni-giessen.de/`.
[56] E. Oset, L. L. Salcedo, Nucl. Phys. A 468 (1987) 631.
[57] W. Ehehalt, W. Cassing, A. Engel, U. Mosel, G. Wolf, Phys. Rev. C 47 (1993) 2467–2469.
[58] T. Leitner, O. Buss, L. Alvarez-Ruso, U. Mosel, Phys. Rev. C 79 (2009) 034601.
[59] M. Effenberger, U. Mosel, Phys. Rev. C 60 (1999) 051901.
[60] M. Effenberger, Eigenschaften von Hadronen in Kernmaterie in einem vereinheitlichten Transportmodell, Ph.D. thesis, Justus-Liebig-Universität Gießen, 1999. Available online at `http://theorie.physik.uni-giessen.de/`.
[61] J. Lehr, In-Medium-Eigenschaften von Nukleonen und Nukleonenresonanzen in einem semiklassischen Transportmodell, Ph.D. thesis, Justus-Liebig-Universität Gießen, 2003. Available online at `http://theorie.physik.uni-giessen.de/`.
[62] P. Mühlich, Mesons in Nuclei and Nuclear Reactions with Elementary Probes, Ph.D. thesis, Justus-Liebig-Universität Gießen, 2007. Available online at `http://theorie.physik.uni-giessen.de/`.
[63] A. B. Larionov, U. Mosel, Phys. Rev. C 66 (2002) 034902.
[64] D. M. Manley, E. M. Saleski, Phys. Rev. D 45 (1992) 4002–4033.
[65] C. Amsler, et al., Phys. Lett. B 667 (2008) 1.
[66] K. Gallmeister, T. Falter, Phys. Lett. B 630 (2005) 40–48.
[67] T. Falter, W. Cassing, K. Gallmeister, U. Mosel, Phys. Rev. C 70 (2004) 054609.
[68] S. Leupold, V. Metag, U. Mosel, Int. J. Mod. Phys. E 19 (2010) 147–224.
[69] R. Varga, Matrix Iterative Analysis, Prentice Hall, New Jersey, 1962.
[70] S. Teis, Transporttheoretische Beschreibung von relativistischen Schwerionenkollisionen bei SIS-Energien, Ph.D. thesis, Justus-Liebig-Universität Gießen, 1997. Available online at `http://theorie.physik.uni-giessen.de/`.
[71] G. M. Welke, M. Prakash, T. T. S. Kuo, S. D. Gupta, C. Gale, Phys. Rev. C 38 (1988) 2101.
[72] M. Prakash, et al., Phys. Rept. 280 (1997) 1–77.
[73] E. Chabanat, J. Meyer, P. Bonche, R. Schaeffer, P. Haensel, Nucl. Phys. A 627 (1997) 710–746.
[74] A. B. Larionov, W. Cassing, C. Greiner, U. Mosel, Phys. Rev. C 62 (2000) 064611.
[75] T. E. O. Ericson, W. Weise, Pions and Nuclei, Clarendon Press, Oxford, 1988.
[76] W. Peters, H. Lenske, U. Mosel, Nucl. Phys. A 640 (1998) 89–113.

[77] E. Friedman, A. Gal, Phys. Rept. 452 (2007) 89–153.

[78] G. A. Lalazissis, J. Konig, P. Ring, Phys. Rev. C 55 (1997) 540–543.

[79] A. B. Larionov, O. Buss, K. Gallmeister, U. Mosel, Phys. Rev. C 76 (2007) 044909.

[80] T. Gaitanos, H. Lenske, U. Mosel, Phys. Lett. B 663 (2008) 197–201.

[81] W. Greiner, B. Müller, Quantum Mechanics: Symmetries, Springer-Verlag, Berlin/Vienna/New York, 2001.

[82] N. Bogoliubov, D. Shirkov, Quantum Fields, Benjamin, London, 1982.

[83] Y. B. Ivanov, Nucl. Phys. A 474 (1987) 669–692.

[84] A. B. Larionov, I. N. Mishustin, L. M. Satarov, W. Greiner, Phys. Rev. C 78 (2008) 014604.

[85] K. Weber, et al., Nucl. Phys. A 515 (1990) 747–760.

[86] T. Gaitanos, A. B. Larionov, H. Lenske, U. Mosel, Phys. Rev. C 81 (2010) 054316.

[87] E. D. Cooper, S. Hama, B. C. Clark, R. L. Mercer, Phys. Rev. C 47 (1993) 297–311.

[88] W. Scheid, R. Ligensa, W. Greiner, Phys. Rev. Lett. 21 (1968) 1479–1482.

[89] J. Aichelin, C. M. Ko, Phys. Rev. Lett. 55 (1985) 2661–2663.

[90] G. F. Bertsch, S. D. Gupta, Phys. Rep. 160 (1988) 189–233.

[91] V. N. Russkikh, Y. B. Ivanov, Y. E. Pokrovsky, P. A. Henning, Nucl. Phys. A 572 (1994) 749–790.

[92] T. Maruyama, W. Cassing, U. Mosel, S. Teis, K. Weber, Nucl. Phys. A 573 (1994) 653–675.

[93] C. Fuchs, T. Gaitanos, H. Wolter, Phys. Lett. B 381 (1996) 23.

[94] P. K. Sahu, A. Hombach, W. Cassing, M. Effenberger, U. Mosel, Nucl. Phys. A 640 (1998) 493–504.

[95] A. Hombach, W. Cassing, S. Teis, U. Mosel, Eur. Phys. J. A 5 (1999) 157–172.

[96] P. Danielewicz, Nucl. Phys. A 673 (2000) 375–410.

[97] C. Fuchs, A. Faessler, E. Zabrodin, Y.-M. Zheng, Phys. Rev. Lett. 86 (2001) 1974–1977.

[98] P. Danielewicz, R. Lacey, W. G. Lynch, Science 298 (2002) 1592–1596.

[99] T. Klahn, et al., Phys. Rev. C 74 (2006) 035802.

[100] J. P. Blaizot, Phys. Rept. 64 (1980) 171.

[101] M. M. Sharma, Nucl. Phys. A 816 (2009) 65–88.

[102] M. Jaminon, C. Mahaux, P. Rochus, Nucl. Phys. A 365 (1981) 371–391.

[103] C. Gale, G. M. Welke, M. Prakash, S. J. Lee, S. Das Gupta, Phys. Rev. C 41 (1990) 1545–1552.

[104] C. W. De Jager, H. De Vries, C. De Vries, Atom. Data Nucl. Data Tabl. 14 (1974) 479–508.

[105] B. Steinmüller, Eine neue Initialisierung des Atomkerns fuer GiBUU, Diploma thesis, Justus-Liebig-Universität Gießen, 2007. Available online at http://theorie.physik.uni-giessen.de/.

[106] G. Batko, J. Randrup, T. Vetter, Nucl. Phys. A 536 (1992) 786–822.

[107] C. Greiner, S. Leupold, J. Phys. G 27 (2001) L95–L102.

[108] W. Cassing, Nucl. Phys. A 700 (2002) 618–646.

[109] M. Post, Hadronic Spectral Functions in Nuclear Matter, Ph.D. thesis, Justus-Liebig-Universität Gießen, 2004. Available online at http://theorie.physik.uni-giessen.de/.

[110] T. Sjostrand, S. Mrenna, P. Skands, JHEP 05 (2006) 026.

[111] K. Gallmeister, U. Mosel, Nucl. Phys. A 826 (2009) 151–160.

[112] A. Baldini, V. Flaminio, W. G. Moorhead, D. R. O. Morrison, H. Schopper, (Ed.), Landolt-Börnstein, New Series, Springer Verlag Berlin, Germany 1/12B (1988).

[113] V. P. Andreev, et al., Z. Phys. A 329 (1988) 371–373.

[114] M. Daum, M. Finger, J. Finger, M., J. Franz, F. Heinsius, et al., Eur. Phys. J. C 23 (2002) 43–59.

[115] J. G. Hardie, et al., Phys. Rev. C 56 (1997) 20–37.

[116] T. Tsuboyama, N. Katayama, F. Sai, S. S. Yamamoto, Nucl. Phys. A 486 (1988) 669–686.

[117] F. Shimizu, Y. Kubota, H. Koiso, F. Sai, S. Sakamoto, S. S. Yamamoto, Nucl. Phys. A 386 (1982) 571.

[118] A. Bondar, et al., Phys. Lett. B 356 (1995) 8–12.

[119] B. Ter Haar, R. Malfliet, Phys. Rev. C 36 (1987) 1611–1620.

[120] V. Dmitriev, O. Sushkov, C. Gaarde, Nucl. Phys. A 459 (1986) 503–524.

[121] S. Huber, J. Aichelin, Nucl. Phys. A 573 (1994) 587–625.

[122] K. Tsushima, S. W. Huang, A. Faessler, Austral. J. Phys. 50 (1997) 35–43.

[123] K. Tsushima, A. Sibirtsev, A. W. Thomas, Phys. Rev. C 59 (1999) 369–387.

[124] C. Fuchs, Prog. Part. Nucl. Phys. 56 (2006) 1–103.

[125] S. A. Kulagin, R. Petti, Nucl. Phys. A 765 (2006) 126–187.

[126] S. A. Kulagin, R. Petti, Phys. Rev. D 76 (2007) 094023.

[127] M. Wagner, A. B. Larionov, U. Mosel, Phys. Rev. C 71 (2005) 034910.

[128] V. R. Pandharipande, S. C. Pieper, Phys. Rev. C 45 (1992) 791–798.

[129] K. Nakamura, et al., J. Phys. G 37 (2010) 075021.

[130] G. I. Kopylov, Nuclear Physics 37 (1962) 425 – 437.

[131] D. Persram, C. Gale, Phys. Rev. C 65 (2002) 064611.

[132] B.-A. Li, L.-W. Chen, Phys. Rev. C 72 (2005) 064611.

[133] K. Gallmeister, U. Mosel, Nucl. Phys. A 801 (2008) 68–79.
[134] J. G. Messchendorp, et al., Phys. Rev. Lett. 89 (2002) 222302.
[135] F. Bloch, et al., Eur. Phys. J. A 32 (2007) 219.
[136] L. L. Salcedo, E. Oset, M. J. Vicente-Vacas, C. Garcia-Recio, Nucl. Phys. A 484 (1988) 557–592.
[137] A. Engel, W. Cassing, U. Mosel, M. Schafer, G. Wolf, Nucl. Phys. A 572 (1994) 657–681.
[138] O. Buss, L. Alvarez-Ruso, A. B. Larionov, U. Mosel, Phys. Rev. C 74 (2006) 044610.
[139] O. Buss, L. Alvarez-Ruso, P. Mühlich, U. Mosel, Ricerca scientifica ed Educazione Permanente Supplemento n.125 (2006). Proceedings of the XLIV international winter meeting on nuclear physics (Bormio, Italy).
[140] O. Buss, L. Alvarez-Ruso, P. Muehlich, U. Mosel, Eur. Phys. J. A 29 (2006) 189–207.
[141] O. Buss, L. Alvarez-Ruso, A. B. Larionov, U. Mosel, arXiv:nucl-th/0703060.
[142] R. A. Mehrem, H. M. A. Radi, J. O. Rasmussen, Phys. Rev. C 30 (1984) 301–304.
[143] A. A. Carter, J. R. Williams, D. V. Bugg, P. J. Bussey, D. R. Dance, Nucl. Phys. B 26 (1971) 445–460.
[144] D. Davidson, T. Bowen, P. K. Caldwell, E. W. Jenkins, R. M. Kalbach, D. V. Petersen, A. E. Pifer, R. E. Rothschild, Phys. Rev. D 6 (1972) 1199–1202.
[145] B. J. Kriss, et al., Phys. Rev. C 59 (1999) 1480–1487.
[146] M. E. Sadler, et al., Phys. Rev. C 69 (2004) 055206.
[147] A. S. Carroll, et al., Phys. Rev. C 14 (1976) 635–638.
[148] A. S. Clough, et al., Nucl. Phys. B 76 (1974) 15.
[149] C. Wilkin, et al., Nucl. Phys. B 62 (1973) 61–85.
[150] D. Ashery, I. Navon, G. Azuelos, H. K. Walter, H. J. Pfeiffer, F. W. Schlepütz, Phys. Rev. C 23 (1981) 2173–2185.
[151] E. Friedman, A. Goldring, R. R. Johnson, O. Meirav, D. Vetterli, P. Weber, A. Altman, Phys. Lett. B 257 (1991) 17–20.
[152] K. Nakai, T. Kobayashi, T. Numao, T. A. Shibata, J. Chiba, K. Masutani, Phys. Rev. Lett. 44 (1980) 1446–1449.
[153] H. Byfield, J. Kessler, L. M. Lederman, et al., Phys. Rev. 86 (1952) 17–21.
[154] W. R. Gibbs, M. J. Leitch (Eds.), Proceedings of the second LAMPF International Workshop on Pion-Nucleus Double Charge Exchange, World Scientific, 1990.
[155] F. Becker, C. Schmit, Nucl. Phys. B 18 (1970) 607–624.
[156] W. R. Gibbs, B. F. Gibson, A. T. Hess, G. J. Stephenson, Phys. Rev. C 15 (1977) 1384–1395.
[157] M. J. Vicente, E. Oset, L. L. Salcedo, C. Garcia-Recio, Phys. Rev. C 39 (1989) 209–215.
[158] M. Alqadi, W. R. Gibbs, Phys. Rev. C 65 (2002) 044609.
[159] B. M. Abramov, et al., Nucl. Phys. A 723 (2003) 389–407.
[160] A. P. Krutenkova, et al., Phys. Rev. C 72 (2005) 037602.
[161] M. Yuly, et al., Phys. Rev. C 55 (1997) 1848–1868.
[162] S. A. Wood, et al., Phys. Rev. C 46 (1992) 1903–1921.
[163] J. Hüfner, M. Thies, Phys. Rev. C 20 (1979) 273–285.
[164] P. A. M. Gram, et al., Phys. Rev. Lett. 62 (1989) 1837–1839.
[165] J. Aichelin, G. Bertsch, Phys. Rev. C 31 (1985) 1730.
[166] W. Bauer, G. Bertsch, W. Cassing, U. Mosel, Phys. Rev. C 34 (1986) 2127.
[167] J. J. Molitoris, H. Stoecker, Phys. Rev. C 32 (1985) 346–348.
[168] C. Gregoire, B. Remaud, F. Sebille, L. Vinet, Y. Raffray, Nucl. Phys. A 465 (1987) 317.
[169] A. Bonasera, G. Burgio, M. D. Toro, Phys. Lett. B 221 (1989) 233.
[170] A. Bonasera, F. Gulminelli, J. Molitoris, Phys. Rep. 243 (1994) 1.
[171] T. Gaitanos, C. Fuchs, H. Wolter, Phys. Lett. B 609 (2005) 241.
[172] M. G. Catanesi, et al., Astropart. Phys. 29 (2008) 257–281.
[173] M. G. Catanesi, et al., Phys. Rev. C 77 (2008) 055207.
[174] M. G. Catanesi, et al., Nucl. Phys. B 732 (2006) 1–45.
[175] D. Garreta, et al., Phys. Lett. B 135 (1984) 266 – 270.
[176] D. Garreta, et al., Phys. Lett. B 149 (1984) 64.
[177] K. Nakamura, et al., Phys. Rev. Lett. 52 (1984) 731–734.
[178] E. Friedman, A. Gal, J. Mares, Nucl. Phys. A 761 (2005) 283–295.
[179] T. Buervenich, et al., Phys. Lett. B 542 (2002) 261–267.
[180] I. N. Mishustin, L. M. Satarov, T. J. Buervenich, H. Stoecker, W. Greiner, Phys. Rev. C 71 (2005) 035201.
[181] J. Rafelski, Phys. Lett. B 91 (1980) 281.
[182] A. S. Iljinov, V. I. Nazaruk, S. E. Chigrinov, Nucl. Phys. A 382 (1982) 378 – 400.
[183] M. Cahay, J. Cugnon, P. Jasselette, J. Vandermeulen, Phys. Lett. B 115 (1982) 7–10.
[184] M. R. Clover, R. M. DeVries, N. J. DiGiacomo, Y. Yariv, Phys. Rev. C 26 (1982) 2138–2151.
[185] Y. Golubeva, A. Iljinov, A. Botvina, N. Sobolevsky, Nucl. Phys. A 483 (1988) 539 – 564.
[186] J. Rafelski, B. Muller, Phys. Rev. Lett. 48 (1982) 1066.

[187] J. Cugnon, J. Vandermeulen, Phys. Lett. B 146 (1984) 16–20.

[188] G. Bendiscioli, T. Bressani, L. Lavezzi, A. Panzarasa, P. Salvini, Nucl. Phys. A 815 (2009) 67–88.

[189] The PANDA Collaboration, M. F. M. Lutz, B. Pire, O. Scholten, R. Timmermans, arXiv:0903.3905 (2009).

[190] A. B. Larionov, I. N. Mishustin, L. M. Satarov, W. Greiner, Phys. Rev. C 82 (2010) 024602.

[191] R. J. Glauber, G. Matthiae, Nucl. Phys. B 21 (1970) 135–157.

[192] R. J. Abrams, et al., Phys. Rev. D 4 (1971) 3235–3244.

[193] S. P. Denisov, et al., Nucl. Phys. B 61 (1973) 62–76.

[194] A. S. Carroll, et al., Phys. Lett. B 80 (1979) 319.

[195] A. B. Larionov, I. A. Pshenichnov, I. N. Mishustin, W. Greiner, Phys. Rev. C 80 (2009) 021601.

[196] P. L. McGaughey, et al., Phys. Rev. Lett. 56 (1986) 2156–2159.

[197] S. Teis, W. Cassing, T. Maruyama, U. Mosel, Phys. Rev. C 50 (1994) 388–405.

[198] M. Colonna, J. Rizzo, P. Chomaz, M. Di Toro, Nucl. Phys. A 805 (2008) 454–461.

[199] F. Rejmund, et al., Nucl. Phys. A 683 (2001) 540–565.

[200] J. Benlliure, et al., Nucl. Phys. A 683 (2001) 513–539.

[201] W. Reisdorf, H. G. Ritter, Ann. Rev. Nucl. Part. Sci. 47 (1997) 663–709.

[202] A. Boudard, J. Cugnon, S. Leray, C. Volant, Phys. Rev. C 66 (2002) 044615.

[203] K. Abdel-Waged, Phys. Rev. C 74 (2006) 034601.

[204] J. P. Bondorf, A. S. Botvina, A. S. Ilinov, I. N. Mishustin, K. Sneppen, Phys. Rept. 257 (1995) 133–221.

[205] S. G. Mashnik, Eur. Phys. J. Plus 126 (2011) 49.

[206] D. Henzlova, et al., Phys. Rev. C 78 (2008) 044616.

[207] T. Gaitanos, H. Lenske, U. Mosel, Phys. Lett. B 675 (2009) 297–304.

[208] M. Wakai, Nucl. Phys. A 547 (1992) 89c–94c.

[209] T. Hatsuda, S. H. Lee, Phys. Rev. C 46 (1992) 34–38.

[210] T. Hatsuda, S. H. Lee, H. Shiomi, Phys. Rev. C 52 (1995) 3364–3372.

[211] R. S. Hayano, T. Hatsuda, Rev. Mod. Phys. 82 (2010) 2949.

[212] R. Rapp, J. Wambach, H. van Hees, arXiv:0901.3289. Published in Landolt-Börnstein, Volume I/23, 4-1 (2010).

[213] I. Tserruya, arXiv:0903.0415. Published in Landolt-Börnstein, Volume I/23, 4-43 (2010).

[214] M. Naruki, et al., Phys. Rev. Lett. 96 (2006) 092301.

[215] R. Muto, et al., Phys. Rev. Lett. 98 (2007) 042501.

[216] I. Frohlich, et al., Int.J.Mod.Phys. A 24 (2009) 317–326.

[217] G.-Q. Li, C. Ko, Nucl. Phys. A 582 (1995) 731–748.

[218] G. Wolf, W. Cassing, U. Mosel, M. Schaefer, Phys. Rev. C 43 (1991) 1501–1503.

[219] J. Weil, K. Gallmeister, U. Mosel, arXiv:1105.0314.

[220] A. Rustamov, AIP Conf.Proc. 1257 (2010) 736–740.

[221] Q. Wan, F. Iachello, Int. J. Mod. Phys. A 20 (2005) 1846–1849.

[222] M. Weber, Int.J.Mod.Phys. A 26 (2011) 737–740.

[223] M. Weber, Dielektronen-Spektroskopie in kalter Kernmaterie, Ph.D. thesis, Technische Universität München, 2011. Available online at http://mediatum.ub.tum.de/node?id=1007264.

[224] M. Gazdzicki, D. Röhrich, Z. Phys. C 71 (1996) 55.

[225] M. I. Gorenstein, M. Gazdzicki, K. A. Bugaev, Phys. Lett. B 567 (2003) 175–178.

[226] E. L. Bratkovskaya, S. Soff, H. Stoecker, M. van Leeuwen, W. Cassing, Phys. Rev. Lett. 92 (2004) 032302.

[227] I. C. Arsene, et al., Phys. Rev. C 75 (2007) 034902.

[228] A. Lang, W. Cassing, U. Mosel, K. Weber, Nucl. Phys. A 541 (1992) 507.

[229] A. B. Larionov, U. Mosel, Nucl. Phys. A 728 (2003) 135–164.

[230] B. B. Back, et al., Phys. Rev. C 66 (2002) 054901.

[231] T. Anticic, et al., Phys. Rev. C 69 (2004) 024902.

[232] A. S. Khvorostukin, V. V. Skokov, V. D. Toneev, K. Redlich, Eur. Phys. J. C 48 (2006) 531–543.

[233] H. Petersen, J. Steinheimer, G. Burau, M. Bleicher, H. Stocker, Phys. Rev. C 78 (2008) 044901.

[234] A. Andronic, P. Braun-Munzinger, J. Stachel, Phys. Lett. B 673 (2009) 142–145.

[235] L. Satarov, M. Dmitriev, I. Mishustin, Phys. Atom. Nucl. 72 (2009) 1390–1415.

[236] L. Ahle, et al., Phys. Lett. B 476 (2000) 1–8.

[237] S. V. Afanasiev, et al., Phys. Rev. C 66 (2002) 054902.

[238] V. Friese, et al., J. Phys. G 30 (2004) S119–S128.

[239] L. Ahle, et al., Phys. Lett. B 490 (2000) 53–60.

[240] A. Mischke, et al., J. Phys. G 28 (2002) 1761–1768.

[241] A. Mischke, et al., Nucl. Phys. A 715 (2003) 453–457.

[242] S. Ahmad, et al., Phys. Lett. B 382 (1996) 35–39.

[243] C. Pinkenburg, Nucl. Phys. A 698 (2002) 495–498.

[244] F. Antinori, et al., Nucl. Phys. A 661 (1999) 130–139.

[245] T. Bauer, R. Spital, D. Yennie, F. Pipkin, Rev. Mod. Phys. 50 (1978) 261.
[246] T. Falter, U. Mosel, Phys. Rev. C 66 (2002) 024608.
[247] T. Falter, K. Gallmeister, U. Mosel, Phys. Rev. C 67 (2003) 054606.
[248] O. Benhar, D. Day, I. Sick, Rev. Mod. Phys. 80 (2008) 189–224.
[249] J. Delorme, P. A. Guichon, Phys. Lett. B 263 (1991) 157–163.
[250] M. Dekker, P. Brussaard, J. Tjon, Phys. Rev. C 51 (1995) 1393–1407.
[251] A. Gil, J. Nieves, E. Oset, Nucl. Phys. A 627 (1997) 543–598.
[252] A. Gil, J. Nieves, E. Oset, Nucl. Phys. A 627 (1997) 599–619.
[253] S. Boffi, C. Giusti, F. D. Pacati, M. Radici, Electromagnetic response of atomic nuclei, Oxford University Press, Oxford, Great Britain, 1996.
[254] O. Benhar, N. Farina, H. Nakamura, M. Sakuda, R. Seki, Phys. Rev. D 72 (2005) 053005.
[255] H. Nakamura, M. Sakuda, T. Nasu, O. Benhar, Phys. Rev. C 76 (2007) 065208.
[256] J. Nieves, M. Valverde, M. J. Vicente Vacas, Phys. Rev. C 73 (2006) 025504.
[257] A. Meucci, F. Capuzzi, C. Giusti, F. D. Pacati, Phys. Rev. C 67 (2003) 054601.
[258] A. Meucci, C. Giusti, F. D. Pacati, Nucl. Phys. A 744 (2004) 307–322.
[259] A. V. Butkevich, S. A. Kulagin, Phys. Rev. C 76 (2007) 045502.
[260] M. C. Martinez, P. Lava, N. Jachowicz, J. Ryckebusch, K. Vantournhout, J. M. Udias, Phys. Rev. C 73 (2006) 024607.
[261] C. Praet, O. Lalakulich, N. Jachowicz, J. Ryckebusch, Phys. Rev. C 79 (2009) 044603.
[262] H. Nakamura, R. Seki, Nucl. Phys. Proc. Suppl. 112 (2002) 197.
[263] J. S. O'Connell, et al., Phys. Rev. Lett. 53 (1984) 1627–1629.
[264] J. Lehr, M. Effenberger, H. Lenske, S. Leupold, U. Mosel, Phys. Lett. B 483 (2000) 324–330.
[265] J. Lehr, H. Lenske, S. Leupold, U. Mosel, Nucl. Phys. A 703 (2002) 393–408.
[266] F. Froemel, H. Lenske, U. Mosel, Nucl. Phys. A 723 (2003) 544–556.
[267] O. Benhar, P. Coletti, D. Meloni, Phys. Rev. Lett. 105 (2010) 132301.
[268] O. Benhar, D. Meloni, Phys. Rev. Lett. 97 (2006) 192301.
[269] M. Anghinolfi, et al., J. Phys. G 21 (1995) L9–L15.
[270] M. Anghinolfi, et al., Nucl. Phys. A 602 (1996) 405–422.
[271] B. Clasie, et al., Phys. Rev. Lett. 99 (2007) 242502.
[272] M. M. Kaskulov, K. Gallmeister, U. Mosel, Phys. Rev. D 78 (2008) 114022.
[273] M. M. Kaskulov, K. Gallmeister, U. Mosel, Phys. Rev. C 79 (2009) 015207.
[274] A. Airapetian, et al., Eur. Phys. J. C 20 (2001) 479–486.
[275] A. Airapetian, et al., Phys. Lett. B 577 (2003) 37–46.
[276] A. Airapetian, et al., Nucl. Phys. B 780 (2007) 1–27.
[277] J. Ashman, et al., Z. Phys. C 52 (1991) 1–12.
[278] Y. Dokshitzer, V. Khoze, A. Mueller, S. Troyan, Basics of perturbative QCD, Editions Frontiers, Saclay, 1991.
[279] G. R. Farrar, H. Liu, L. L. Frankfurt, M. I. Strikman, Phys. Rev. Lett. 61 (1988) 686–689.
[280] A. Larson, G. A. Miller, M. Strikman, Phys. Rev. C 74 (2006) 018201.
[281] K. Hafidi, AIP Conf. Proc. 870 (2006) 669–672.
[282] B. Z. Kopeliovich, J. Nemchik, E. Predazzi, A. Hayashigaki, Nucl. Phys. A 740 (2004) 211–245.
[283] B. Z. Kopeliovich, J. Nemchik, I. Schmidt, Nucl. Phys. A 782 (2007) 224–233.
[284] E. Wang, X.-N. Wang, Phys. Rev. Lett. 89 (2002) 162301.
[285] M. Effenberger, A. Hombach, S. Teis, U. Mosel, Nucl. Phys. A 614 (1997) 501–520.
[286] M. Effenberger, U. Mosel, Phys. Rev. C 62 (2000) 014605.
[287] J. Lehr, M. Effenberger, U. Mosel, Nucl. Phys. A 671 (2000) 503–531.
[288] P. Mühlich, T. Falter, C. Greiner, J. Lehr, M. Post, et al., Phys. Rev. C 67 (2003) 024605.
[289] P. Mühlich, T. Falter, U. Mosel, Eur. Phys. J. A 20 (2004) 499–508.
[290] B. Krusche, J. Lehr, J. Ahrens, J. Annand, R. Beck, et al., Eur. Phys. J. A 22 (2004) 277–291.
[291] P. Mühlich, U. Mosel, Nucl. Phys. A 773 (2006) 156–172.
[292] T. Mertens, et al., Eur. Phys. J. A 38 (2008) 195–207.
[293] M. Wood, et al., Phys.Rev. C 78 (2008) 015201.
[294] E. A. Arakelian, et al., Sov. J. Nucl. Phys. 38 (1983) 589.
[295] A. K. Ananikyan, et al., Sov. J. Nucl. Phys. 46 (1987) 208.
[296] T. Frommhold, et al., Phys. Lett. B 295 (1992) 28–31.
[297] T. Frommhold, et al., Z. Phys. A 350 (1994) 249–261.
[298] N. Bianchi, et al., Phys. Lett. B 299 (1993) 219–222.
[299] N. Bianchi, et al., Phys. Lett. B 309 (1993) 5–9.
[300] N. Bianchi, et al., Phys. Rev. C 48 (1993) 1785–1790.
[301] N. Bianchi, et al., Phys. Lett. B 325 (1994) 333–336.

[302] N. Bianchi, et al., Phys. Rev. C 54 (1996) 1688–1699.
[303] V. Muccifora, et al., Phys. Rev. C 60 (1999) 064616.
[304] C. Cetina, et al., Phys. Rev. Lett. 84 (2000) 5740–5743.
[305] C. Cetina, et al., Phys. Rev. C 65 (2002) 044622.
[306] R. C. Carrasco, E. Oset, Nucl. Phys. A 536 (1992) 445–508.
[307] L. A. Kondratyuk, M. I. Krivoruchenko, N. Bianchi, E. De Sanctis, V. Muccifora, Nucl. Phys. A 579 (1994) 453–471.
[308] M. Effenberger, A. Hombach, S. Teis, U. Mosel, Nucl. Phys. A 613 (1997) 353–370.
[309] R. Rapp, M. Urban, M. Buballa, J. Wambach, Phys. Lett. B 417 (1998) 1–6.
[310] R. Rapp, J. Wambach, Adv. Nucl. Phys. 25 (2000) 1.
[311] M. Hirata, N. Katagiri, K. Ochi, T. Takaki, Phys. Rev. C 66 (2002) 014612.
[312] A. S. Ilinov, et al., Nucl. Phys. A 616 (1997) 575–605.
[313] I. A. Pshenichnov, et al., Eur. Phys. J. A 24 (2005) 69–84.
[314] S. G. Mashnik, M. I. Baznat, K. K. Gudima, A. J. Sierk, R. E. Prael, arXiv:nucl-th/0503061.
[315] A. Deppman, et al., Phys. Rev. C 66 (2002) 067601.
[316] A. Deppman, et al., J. Phys. G 30 (2004) 1991–2002.
[317] A. Deppman, et al., Phys. Rev. C 73 (2006) 064607.
[318] R. Nasseripour, et al., Phys. Rev. Lett. 99 (2007) 262302.
[319] P. Mühlich, U. Mosel, Nucl. Phys. A 765 (2006) 188–196.
[320] J. Lehr, M. Post, U. Mosel, Phys. Rev. C 68 (2003) 044601.
[321] B. Krusche, et al., Eur. Phys. J. A 22 (2004) 347–351.
[322] K. G. Fissum, et al., Phys. Rev. C 53 (1996) 1278–1289.
[323] B. Krusche, et al., Phys. Lett. B 526 (2002) 287–294.
[324] E. G. Drukarev, E. M. Levin, Nucl. Phys. A 511 (1990) 679–700.
[325] T. D. Cohen, R. J. Furnstahl, D. K. Griegel, Phys. Rev. C 45 (1992) 1881–1893.
[326] R. Brockmann, W. Weise, Phys. Lett. B 367 (1996) 40–44.
[327] V. Bernard, U. G. Meissner, I. Zahed, Phys. Rev. Lett. 59 (1987) 966.
[328] T. Hatsuda, T. Kunihiro, H. Shimizu, Phys. Rev. Lett. 82 (1999) 2840–2843.
[329] F. Bonutti, et al., Phys. Rev. Lett. 77 (1996) 603.
[330] F. Bonutti, et al., Nucl. Phys. A 677 (2000) 213.
[331] R. Gregor, Modifikation von Pionenpaaren in Kernmaterie, Ph.D. thesis, JLU Giessen, 2007.
[332] L. Roca, E. Oset, M. J. Vicente Vacas, Phys. Lett. B 541 (2002) 77–86.
[333] P. Mühlich, L. Alvarez-Ruso, O. Buss, U. Mosel, Phys. Lett. B 595 (2004) 216–222.
[334] L. Alvarez-Ruso, P. Mühlich, O. Buss, U. Mosel, Int. J. Mod. Phys. A 20 (2005) 578–580.
[335] O. Buss, L. Alvarez-Ruso, P. Mühlich, U. Mosel, R. Shyam, arXiv:nucl-th/0502031.
[336] M. Effenberger, E. L. Bratkovskaya, U. Mosel, Phys. Rev. C 60 (1999) 044614.
[337] F. Riek, R. Rapp, T.-S. Lee, Y. Oh, Phys. Lett. B 677 (2009) 116–120.
[338] F. Riek, R. Rapp, Y. Oh, T.-S. Lee, Phys. Rev. C 82 (2010) 015202.
[339] M. Nanova, et al., Eur. Phys. J. A 47 (2011) 16.
[340] M. Kotulla, et al., Phys. Rev. Lett. 100 (2008) 192302.
[341] D. Trnka, et al., Phys. Rev. Lett. 94 (2005) 192303.
[342] M. Nanova, et al., Phys. Rev. C 82 (2010) 035209.
[343] K. Gallmeister, M. Kaskulov, U. Mosel, P. Mühlich, Prog. Part. Nucl. Phys. 61 (2008) 283–289.
[344] U. Mosel, S. Leupold, V. Metag, Prog. Theor. Phys. Suppl. 186 (2010) 260–269.
[345] B. Aubert, et al., Phys. Rev. D 70 (2004) 112006.
[346] J. Lehr, U. Mosel, Phys. Rev. C 64 (2001) 042202.
[347] M. Kaskulov, E. Hernandez, E. Oset, Eur. Phys. J. A 31 (2007) 245–254.
[348] NUINT09, 6th International Workshop on Neutrino-Nucleus Interactions in the Few-GeV Region (NUINT09), May 17-22, 2009, Sitges, Spain, 2009. `http://nuint09.ifae.es/Agenda.html`.
[349] T. Leitner, L. Alvarez-Ruso, U. Mosel, Phys. Rev. C 73 (2006) 065502.
[350] T. Leitner, L. Alvarez-Ruso, U. Mosel, Phys. Rev. C 74 (2006) 065502.
[351] T. Leitner, Neutrino-nucleus interactions in a coupled-channel hadronic transport model, Ph.D. thesis, Justus-Liebig-Universität Gießen, 2009. Available online at `http://theorie.physik.uni-giessen.de/`.
[352] J. Marteau, J. Delorme, M. Ericson, arXiv:hep-ph/9906449.
[353] M. Martini, M. Ericson, G. Chanfray, J. Marteau, Phys. Rev. C 80 (2009) 065501.
[354] M. Martini, M. Ericson, G. Chanfray, J. Marteau, Phys. Rev. C 81 (2010) 045502.
[355] J. Nieves, I. Ruiz Simo, M. Vicente Vacas, Phys. Rev. C 83 (2011) 045501.
[356] T. Leitner, U. Mosel, Phys. Rev. C 81 (2010) 064614.
[357] T. Leitner, U. Mosel, Phys. Rev. C 82 (2010) 035503.

[358] A. A. Aguilar-Arevalo, et al., Phys. Rev. Lett. 100 (2008) 032301.
[359] D. Boer, M. Diehl, R. Milner, R. Venugopalan, W. Vogelsang, et al., arXiv:1108.1713.
[360] Z.-W. Lin, C. M. Ko, B.-A. Li, B. Zhang, S. Pal, Phys. Rev. C 72 (2005) 064901.
[361] W. Cassing, E. Bratkovskaya, Phys.Rev. C78 (2008) 034919.
[362] M. Berlowski, C. Bargholtz, M. Bashkanov, D. Bogoslawsky, A. Bondar, et al., Phys. Rev. D 77 (2008) 032004.
[363] T. Browder, et al., Phys. Rev. D 56 (1997) 5359–5365.
[364] L. G. Landsberg, Phys. Rept. 128 (1985) 301–376.
[365] B. Spruck, Optimierung des Pionenstrahls zum HADES Detektor und Bestimmung des Eta-Formfaktors in Proton-Proton Reaktionen bei 2.2 GeV, Ph.D. thesis, Justus-Liebig-Universität Gießen, 2008. Available online at http://geb.uni-giessen.de/geb/volltexte/2008/6667/.
[366] C. Terschlusen, S. Leupold, Phys. Lett. B 691 (2010) 191–201.
[367] E. L. Bratkovskaya, W. Cassing, Nucl. Phys. A 619 (1997) 413–446.
[368] R. Arnaldi, et al., Phys. Lett. B 677 (2009) 260–266.
[369] M. I. Krivoruchenko, A. Faessler, Phys. Rev. D 65 (2002) 017502.
[370] H. Pi, Comput. Phys. Commun. 71 (1992) 173–192.
[371] L. Montanet, et al., Phys. Rev. D 50 (1994) 1173–1814.
[372] J. Cugnon, J. Vandermeulen, D. L'Hote, Nucl. Instrum. Meth. B 111 (1996) 215–220.
[373] C. Gale, J. Kapusta, Phys. Rev. C 35 (1987) 2107–2116.
[374] W.-M. Yao, et al., J. Phys. G 33 (2006) 1–1232.
[375] M. Effenberger, Gammaabsorption an Kernen, Diploma thesis, Justus-Liebig-Universität Gießen, 1996.
[376] V. Pascalutsa, M. Vanderhaeghen, Phys. Lett. B 636 (2006) 31–39.
[377] J. Cugnon, J. Vandermeulen, Ann. Phys. (France) 14 (1989) 49–88.
[378] T. Armstrong, et al., Phys. Rev. D 36 (1987) 659–673.
[379] C. B. Dover, T. Gutsche, M. Maruyama, A. Faessler, Prog. Part. Nucl. Phys. 29 (1992) 87–174.
[380] C. Ghesquiere, 1974. In: Proc. Symp. on Antinucleon-Nucleon Interactions (Liblice, 1974), ed. L. Montanet.
[381] L. A. Kondratyuk, M. G. Sapozhnikov, Sov. J. Nucl. Phys. 46 (1987) 56.
[382] I. A. Pshenichnov, Statistical description of the reactions of multiple meson production on nuclei (in Russian), Ph.D. thesis, INR Moscow, 1998.
[383] E. S. Golubeva, A. S. Iljinov, B. V. Krippa, I. A. Pshenichnov, Nucl. Phys. A 537 (1992) 393–417.
[384] J. Cugnon, P. Deneye, J. Vandermeulen, Phys. Rev. C 41 (1990) 1701–1718.
[385] A. Sibirtsev, W. Cassing, U. Mosel, Z. Phys. A 358 (1997) 357–367.
[386] A. A. Sibirtsev, W. Cassing, C. M. Ko, Z. Phys. A 358 (1997) 101–106.
[387] A. Baldini, V. Flaminio, W. G. Moorhead, D. R. O. Morrison, H. Schopper, (Ed.), Landolt-Börnstein, New Series, Springer Verlag Berlin, Germany 1/12A (1988).
[388] G. I. Lykasov, W. Cassing, A. Sibirtsev, M. V. Rzyanin, Eur. Phys. J. A 6 (1999) 71–81.
[389] Y. S. Golubeva, L. A. Kondratyuk, W. Cassing, Nucl. Phys. A 625 (1997) 832–854.
[390] H. Weber, E. L. Bratkovskaya, W. Cassing, H. Stoecker, Phys. Rev. C 67 (2003) 014904.
[391] B. Tomasik, E. E. Kolomeitsev, arXiv:nucl-th/0512088.
[392] J. Petersen, The pi pi Interaction, 1977. CERN-77-04, Lectures given in Academic Training Program of CERN, 1975-1976.
[393] G. E. Brown, C. M. Ko, Z. G. Wu, L. H. Xia, Phys. Rev. C 43 (1991) 1881–1892.
[394] W. Cassing, E. L. Bratkovskaya, U. Mosel, S. Teis, A. Sibirtsev, Nucl. Phys. A 614 (1997) 415–432.
[395] V. Shklyar, H. Lenske, U. Mosel, G. Penner, Phys. Rev. C 71 (2005) 055206.
[396] L. Tiator, private communication, 2007.
[397] MAID, 2011. http://www.kph.uni-mainz.de/MAID.
[398] L. Tiator, S. Kamalov, arXiv:nucl-th/0603012.
[399] D. Drechsel, S. S. Kamalov, L. Tiator, Eur. Phys. J. A 34 (2007) 69–97.
[400] G. L. Fogli, G. Nardulli, Nucl. Phys. B 160 (1979) 116.
[401] T. Sato, D. Uno, T. S. H. Lee, Phys. Rev. C 67 (2003) 065201.
[402] E. Hernandez, J. Nieves, M. Valverde, Phys. Rev. D 76 (2007) 033005.
[403] C. Barbero, G. Lopez Castro, A. Mariano, Phys. Lett. B 664 (2008) 70–77.
[404] O. Lalakulich, T. Leitner, O. Buss, U. Mosel, Phys. Rev. D 82 (2010) 093001.
[405] G. M. Radecky, et al., Phys. Rev. D 25 (1982) 1161.
[406] T. Kitagaki, et al., Phys. Rev. D 34 (1986) 2554–2565.
[407] S. J. Barish, et al., Phys. Rev. D 19 (1979) 2521.
[408] M. G. Hauser, Phys. Rev. 160 (1967) 1215–1227.
[409] Aachen-Berlin-Bonn-Hamburg-Heidelberg-Munich Collaboration, Phys. Rev. 175 (1968) 1669–1696.
[410] F. Carbonara, et al., Nuovo Cim. A 36 (1976) 219–234.
[411] F. Harter, et al., Phys. Lett. B 401 (1997) 229–233.

[412] M. Wolf, et al., Eur. Phys. J. A 9 (2000) 5–8.

[413] M. Kotulla, et al., Phys. Lett. B 578 (2004) 63–68.

[414] W. Langgartner, et al., Phys. Rev. Lett. 87 (2001) 052001.

[415] V. Kleber, et al., Eur. Phys. J. A 9 (2000) 1–4.

[416] A. Zabrodin, et al., Phys. Rev. C 55 (1997) 1617–1620.

[417] A. Braghieri, et al., Phys. Lett. B 363 (1995) 46–50.

[418] J. Ahrens, et al., Phys. Lett. B 551 (2003) 49–55.

[419] J. Ahrens, et al., Phys. Lett. B 624 (2005) 173–180.

[420] Y. Assafiri, et al., Phys. Rev. Lett. 90 (2003) 222001.

[421] J. C. Nacher, E. Oset, M. J. Vicente, L. Roca, Nucl. Phys. A 695 (2001) 295–327.

[422] J. A. Gomez Tejedor, M. J. Vicente-Vacas, E. Oset, Nucl. Phys. A 588 (1995) 819–828.

[423] J. A. Gomez Tejedor, E. Oset, Nucl. Phys. A 600 (1996) 413–435.

[424] I. Jaegele, 2007. private communication.

[425] J. Ahrens, et al., Eur. Phys. J. A 34 (2007) 11–21.

[426] P. Pedroni, 2007. Private communications.

[427] L. Alvarez-Ruso, 2005. Private communications.

[428] C. Wu, et al., Eur. Phys. J. A 23 (2005) 317–344.

[429] M. E. Christy, P. E. Bosted, Phys. Rev. C 81 (2010) 055213.

[430] P. Joos, et al., Nucl. Phys. B 113 (1976) 53.

[431] T. Horn, et al., Phys. Rev. Lett. 97 (2006) 192001.

[432] T. Horn, et al., Phys. Rev. C 78 (2008) 058201.

[433] M. M. Kaskulov, U. Mosel, Phys. Rev. C 80 (2009) 028202.

[434] J. D. Bjorken, J. B. Kogut, Phys. Rev. D 8 (1973) 1341.

[435] T. Falter, Nuclear reactions of high energy protons, photons and leptons, Ph.D. thesis, Justus-Liebig-Universität Gießen, 2004. Available online at `http://theorie.physik.uni-giessen.de/`.

[436] J. Barth, et al., Eur. Phys. J. A 18 (2003) 117–127.

[437] J. Barth, Photoproduktion der Vektormesonen ω(782) und ϕ(1020) am Proton von der Erzeugungsschwelle bis zu einer Photon-Energie von 2.6 GeV, Ph.D. thesis, Friedrich-Wilhelms-Universität Bonn, 2002.

[438] D. P. Barber, et al., Z. Phys. C 26 (1984) 343–351.

[439] G. Welke, R. Malfliet, C. Grégoire, M. Prakash, E. Suraud, Phys. Rev. C 40 (1989) 2611–2620.

[440] A. Lang, H. Babovsky, W. Cassing, U. Mosel, H.-G. Reusch, K. Weber, Journal of Comp. Phys. 106 (1993) 391–396.

[441] gpl, GPL website, `http://www.gnu.org/copyleft/gpl.html`, 2007.